The Role of Boundary Conditions on the Stability of Confined Active Matter

A Numerical Instability Analysis on
Momentum-Conserving Active Matter

MATTHEW SPARKES

PH.D.

University of York

Mathematics Department

June 2022

Abstract

Active matter is comprised of active particles whose underlying property is their ability to exert mechanical stresses on their environment by the conversion of stored or ambient free-energy. At sufficient particle number density, orientational order emerges due to steric, mechanical or behavioural mechanisms, generating collective motion in motile suspensions. On micrometre length scales, active particles such as bacteria can be categorised by their swimming type: 'extensile' swimmers push themselves through their medium using flagellum, whereas 'contractile' swimmers pull themselves. Activity drives an instability in ordered extensile (contractile) suspensions due to bend (splay) deformations in the suspension orientation (director) which generate active flow and enhance the director perturbation by shear-induced torque. This work comprises a two-part comprehensive extension to this fundamental instability in both 2D and 3D, and both unbounded and confined regimes. Active flow propagates in the same plane as the deformation that caused it, and in part one of this work, we show this causes a de-coupling of the governing equations in the unbounded 3D regime, resulting in the dominance of bend modes for extensile suspensions. Our main result concerns a new chirality term in the Jeffrey orbit equations which re-couples the governing equations by rotating the director out-of-plane from activity induced shear, and in an imposed-shear regime, enhances the instability growth rate by up to 10% versus the unbounded regime when alignment-to-shear and chiral-rotation effects are both present. In part two, we connect bulk growth rates to regimes of weak and strong confinement and show the critical confinement length h^c to suppress growth in 2D regime is related to the wavelength of maximum growth in the unbounded regime, and show further that alternative boundary conditions can reduce this critical value by an order of magnitude. The culmination of this work is the exploration of alternative steady states and boundary conditions for the suspension orientation: the effects of rotating the suspension relative to the boundaries, investigating torque-free boundary conditions, imposing a 'swimmer slip' condition on the substrate, and the effects of inclination. We find regimes for which alignment-to-shear is *stabilising*, regimes where alignment-to-shear is *de-stabilising*, and predict new steady states using a steady torque-balanced equation for the director. This work invites discussion on appropriate boundary conditions for active matter by providing insight into the dynamics of 3D regimes of confinement, with experimentally realisable predictions for low Reynolds number suspensions. As part of an ongoing research narrative, this work utilises a robust codebase, broadly extendable to new regimes of interest, and will be published at a later date.

Author's Declaration

This thesis is a product of my research between September 2018 and June 2022, conducted in the Department of Mathematics at the University of York, United Kingdom.

The material presented is a presentation of my own original work, and I am its sole author. All sources are acknowledged as References. This work has not previously been submitted for an award at this, or any other, University.

Acknowledgements

I would like to express my sincere gratitude to my supervisors, Dr. Mitya Pushkin, whose enthusiasm and support always lifted my spirits, and Prof. Martin Bees, whose insight help refine this thesis. This work would not have been accomplished without you both, with your kind and generous support.

I am truly indebted to my family, who humour my erratic attempts at explaining any and all fluid-related phenomena I come across, and to my wife Katie, who selflessly sat with me for hours on end to keep me company whilst writing and finishing this work.

Contents

List of Figures

Nomenclature

Notation	Symbol	Description
alpha	α	swimmer activity, $\alpha = -f_\alpha c(d + d')/2$
b, bold	$\boldsymbol{b}$	body moment acting on a fluid element
c	c	scalar field for the local swimmer concentration
D	D	director diffusivity, $D = \frac{K}{\zeta_r}$
delta	δ	dirac delta
delta, bold	$\boldsymbol{\delta}$	identity matrix
E, bold	$\boldsymbol{E}$	flow rate of strain, $E_{ij} = \frac{1}{2}(\partial_i u_j + \partial_j u_i)$
epsilon	ϵ	small parameter, used for linearisation of governing equations
eta	η	dimensionless number comparing rotational diffusivity to rotation due to active shear $\eta = \frac{L^2\|\alpha\|}{D\mu}$
f, a	f_α	Force-dipole strength of an active swimmer, approximated using the swimmer velocity such that $f_\alpha \sim v_p \mu \hat{d}$ where $\hat{d}$ is the swimmer dipole length
F, bold	$\boldsymbol{F}$	general force

Notation	**Symbol**	**Description**
F, curly	$\mathcal{F}$	Frank free energy
f, d	f_d	Frank free energy integrand
f, k	f_k	general fourier mode
g	g	gravitational field strength
g, bold	$\boldsymbol{g}$	body force acting on a fluid element
gamma	γ	dimensionless number comparing active shear to gravitational shear, $\gamma = \frac{\rho g L}{\lvert\alpha\rvert}$
h	h	dimensionless confinement length of channel and film
h, c	h^c	confinement length for which the fundamental instability is suppressed by confinement
h, straight	h	molecular field (static equilibrium condition on director)
K	K	elasticity coefficient for director deformations
k	k	amplitude of perturbation wavevector, $k = \lvert\boldsymbol{k}\rvert$
k, bold	$\boldsymbol{k}$	perturbation wavevector for Fourier modes, such that $f = f_k \exp(i\boldsymbol{k} \cdot \boldsymbol{x} - i\omega t)$
k, c	k^c	wavenumber associated with a bifurcation in the associated eigenmodes
k, m	k^m	wavenumber associated with maximum eigenmode growth rate
L	L	characteristic length scale, set to elasticity/active shear balancing, $L^2 = \frac{D\mu}{\lvert\alpha\rvert}$
l, bold	$\boldsymbol{l}$	surface moment acting on a fluid element
lambda, 1	λ_1	parameter measuring swimmer alignment to shear
lambda, 1, -	λ_1^{-}	shorthand notation, $\lambda_1^{-} = \frac{1}{2}(\lambda_1 - 1)$
lambda, 1, +	λ_1^{+}	shorthand notation, $\lambda_1^{+} = \frac{1}{2}(\lambda_1 + 1)$

Notation	**Symbol**	**Description**
lambda, 2	λ_2	parameter measuring swimmer rotation due to chiral effects
lambda, m	λ_m	mean-free path of particles
laplacian	∇^2	laplacian operator, $\partial_x^2 + \partial_y^2 + \partial_z^2$
mu	μ	parameter measuring fluid viscosity
mu, k	μ_k	kinematic fluid viscosity
n, bold	$\boldsymbol{n}$	outward normal to a surface
nabla	∇	the gradient operator, $(\partial_x, \partial_y, \partial_z)$
omega	ω	the complex wave-frequency for a Fourier mode of the form $f = f_k \exp(\boldsymbol{k} \cdot \boldsymbol{x} - i\omega t)$
omega, +	ω^+	eigenvalue associated with unstable eigenmodes
omega, -	ω^-	eigenvalue associated with stable eigenmodes
Omega, bold	$\boldsymbol{\Omega}$	flow vorticity , $\Omega_{ij} = \frac{1}{2}(\partial_i u_j - \partial_j u_i)$
omega, i	ω_i	the imaginary part of the complex wave-frequency
omega, r	ω_r	the real part of the complex wave-frequency
P	P	flow pressure, force per unit area
P, A	P_A	atmospheric pressure constant
p, bold	$\boldsymbol{p}$	a unit vector describing the local average orientation of active particles
phi	ϕ	azimuthal angle of director, measured from the x-axis
psi	ψ	2D stream function
q	q	perturbation wavevector angle, where $\boldsymbol{k} = k(\cos q\ , 0\ , \sin q)$ in 2D
R, bold	$\boldsymbol{R}$	grand resistance tensor for active particles

Notation	**Symbol**	**Description**
rho	ρ	scalar field for fluid density
S	S	scalar order parameter for director
s, a	s^α	sign of activity, $s^\alpha = \frac{\alpha}{\lvert\alpha\rvert}$
S, bold	$\boldsymbol{S}$	fluid stresslet
sigma, bold	$\boldsymbol{\sigma}$	stress tensor acting on fluid
sigma, bold, alpha	$\boldsymbol{\sigma}^\alpha$	active part of stress tensor acting on fluid
sigma, bold, v	$\boldsymbol{\sigma}^v$	viscous part of stress tensor acting on fluid
T	T	characteristic time scale, set to activity driven shear $T = \frac{\mu}{\lvert\alpha\rvert}$
t	t	non-dimensionalised time
T, bold	$\boldsymbol{T}$	generalised torque
t, bold	$\boldsymbol{t}$	surface force acting on a fluid element
theta	θ	radial angle of director, measured from the x-axis
u, bold	$\boldsymbol{u}$	vector field describing fluid velocity
v, bold	$\boldsymbol{v}$	swimmer velocity
v, p	v_p	the self-propulsion velocity of swimmers
vartheta	ϑ	dimensionless number comparing motility to active shear, $\vartheta = \frac{v_p \mu}{\lvert\alpha\rvert L}$
w, bold	$\boldsymbol{w}$	swimmer angular velocity
x, bold	$\boldsymbol{x}$	non-dimensionalised spatial coordinates, Cartesian
xi	ξ	dimensionless number comparing elastic to viscous damping, $\xi = \frac{\rho D}{\mu}$
zeta	ζ	swimmer drag coefficient, context dependent

1 | Introduction

1.1 Active Matter

Active matter is comprised of active, self-propelled particles (SPPs), suspended in a medium.[9–13] The underlying property of these particles is their ability to exert mechanical *stresses* on their environment by converting stored or ambient *free-energy* into self-propulsion. The diversity of SPPs is vast and active matter systems constitute a large breadth of length scales, crossing the disciplines of Biology, Physics and Chemistry. SPPs can be biological units, ranging from decimetre length scales, such as flocking starlings or sardines[14] (FIGURE 1.1), to micrometer scales such as bacteria[15–17] (FIGURE 1.2B); mechanically vibrated granular rods span centimetre length scales;[18–20] and chemically driven *phoretic* swimmers such as 'Janus' particles (FIGURE 1.2A) exist on the nanometre scale.[21–23] Active particles can be broadly categorised by their polarity: microswimmers and phoretic swimmers are *polar* with head-tail structure, and form *polar active matter*, whereas rods and disks are *apolar* and form *nematic active matter*.

A ubiquitous goal of active matter research is to be able to quantify observed macroscopic phenomena by understanding active matter's principle mechanisms: the role of environment and confinement, the effect of swimmer geometry and propulsion mechanisms, the strength and nature of coupling between active units and their medium, the extent of momentum-damping, or the influence of external alignment factors, which could be behavioural, mechanical or chemical in nature. Active mat-

FIGURE 1.1: Collective motion governed by behavioural mechanisms in active matter. LEFT: A starling murumuration flies in intricate and complex patterns, sometimes consisting of thousands of birds.*[1] Starlings showcase large number fluctuations in flocking governed by nearest-neighbour alignment rules. RIGHT: A closely packed shoal of sardines.†[2] The elongated nature of sardines make them an excellent exhibition of possible deformations in the local swimmer orientation, such as bend and splay.

ter research has led to many exciting practical developments, including new 'active' materials with manufactured properties such as self-healing,[24,25] overcoming longstanding therapeutic challenges,[26] or the emergence of adaptive biomaterials[27] — which could be achieved either by intelligent SPP design, modifications to their environment, or their medium.

In the medical field of therapeutics, active particles are being utilised to overcome longstanding challenges in targeted drug delivery. The delivery of orally administered drugs, such as insulin, is hindered by the tight cell junctions in the *gastrointestinal epithelial lining* (GI). Traditional drug delivery, mediated by passive particles, cannot overcome the thick inner mucus lining of the colon, which acts as a mechanical barrier for foreign biomatter by a constant shedding of the mucus layer; *viscoelastic* swimmers which respond favourably to shear gradients close to a boundary could

---

*Image reproduced under *CC BY-NC-ND 2.0* licence.[1]

†Image reproduced with authors permission.[2]

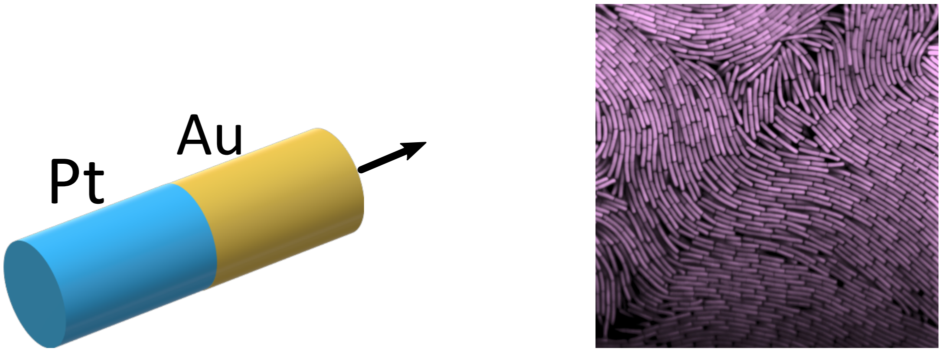

Figure 1.2: Left: Novel 'Janus' particles move under their own self-propulsion by inducing inhomogeneity in a chemical field. In this configuration, the platinum end of the rod acts as a catalyst in the $H_2O_2 \rightarrow H_2O + O_2$ decomposition; the resulting concentration difference causes diffusion toward the inert gold end of the rod. Right: Confocal (false-colour) microscopy demonstrating *Bacillus subtilis* as an exemplar bacterial active matter suspension displaying collective motion and structural defects.[*][3]

be used to navigate the biomechanical defences of the colon, where their passive counterparts cannot.[26] Examples of self-healing matter can be found in bundles of *micotubules* close to their packing fraction, where the particles undergo continuous extension, buckling, fracturing and self-healing, generating strong internal flows up to three times of their own propulsion velocity;[27] active stresses in a droplet, in combination with *Marangoni* stresses at an interface,[28] can create droplets capable of self-propulsion;[24] suspensions of motile, extensile (contractile) active units produce apparent *shear thickening* (*thinning*), due to coupling between elastic stresses in the director, activity driven shear and motility driven local stress in the fluid.[25]

An underlying theme of active matter is the existence of a *phase transition* from a disordered *isotropic phase* to an ordered *anisotropic phase*. Here, *phase* refers to a homogeneous state of matter, e.g. gas, liquid, solid or *crystaline* and *isotropic* (*anisotropic*) refers to a physical property which is invariant (variant) under rotation. A simple, intuitive example of the isotropic-anisotropic phase transition can

---

[*] Image reproduced under *CC BY-NC-ND 2.0* licence.[3]

be gleaned from the behaviour of a herd of sheep. When unharassed and far from their *packing fraction*, the herd exhibits a disordered isotropic phase; the sheep have no preferential direction and are uniformly distributed across an appropriate spatial average. When spooked, herded or packed close together, the sheep are in an ordered anisotropic phase, the rotational symmetry of the flock has been broken by some environmental stimulus and there exists a local preferential direction. To go between these states, an isotropic-anisotropic phase transition must occur — in the example of sheep, orientational order occurs due to a behavioural mechanism, *e.g.* safety in numbers.

Significant literature has been devoted to uncovering the general mechanisms which break rotational symmetry in the isotropic-anisotropic phase transition for active matter. Early works by Viscek[29] and Toner-Tu[14] demonstrated this phase transition occurs by only employing noisy, nearest-neighbour velocity alignment rules, as would be appropriate for a herd of sheep, or flock of birds. Cates and Taileur[30] invoke *motility* (particle activity leading to self-propulsion) and *steric* interactions (non-binding particle-particle interactions such as volume exclusion) as an underlying mechanism — collisions between particles temporarily reduces their self-propulsion velocity, leading to particle accumulation and collective motion. Simha and Ramaswamy[31] show that rotational symmetry is broken through particle interaction by long-range hydrodynamic forces (particle interactions mediated by induced flow) and *entropic* elasticity (elastic-like forces due to system tendency toward entropically favourable states).

Attempts to generalize active matter using ‘thermodynamic-like’ descriptions by entropy production arguments are also successful in predicting the isotropic-anisotropic phase transition.[32,33] An insightful model by Takatori *et al.*[34] drew analogy of SPPs to passive Brownian particles to give an intuitive insight to the emergence of collective motion. A lone Brownian particle exhibits random walk behaviour due to *Brownian motion*; similarly, ‘run-and-tumble’ bacteria, such as *Escherichia coli* (Figure 1.3) undergo ‘runs’ of uniform swimming punctuated by tumble events where the bacteria randomly reorientates.[35] On sufficient spatial-temporal averaging, this motion is analogous to Brownian particle motion — the distinction being that the time between reorientation events for run-and-tumble swimmers is negatively biased toward an increase in bacteria concentration. By this language, Takatori *et al.* demonstrate that run-and-tumble bacteria suspensions undergo '*phase separation*' into a coexistence of dilute-dense phases, analogous to first-order gas-liquid phase transitions.

In all the discussed cases, regardless of the mechanism driving the isotropic-anisotropic phase transition, active matter as a living material is fundamentally always out-of-equilibrium. This arises due to the presence of SPPs in three ways: firstly, local energy dispersion results in a local stress field, which generates hydrodynamic stresses in the medium — irrespective of fluid flow or particle motility. Secondly, SPPs are force-free, they can only move by momentum exchange with their surroundings. A suspension of force-free swimmers can be compared to an internal body force,[36] which — unlike the sedimentation of spheres, whose motion is driven by external body forces (i.e. gravity) — increases the degrees of freedom of the system. Thirdly, particle orientation is self-determined and coupled to both local fluid flow and neighbouring particle orientation. Active matter is a close relative of *soft matter*, which is well described by close-to-equilibrium arguments in *thermodynamics* — conversely, these rudimentary properties of active matter yield a highly non-equilibrium system,

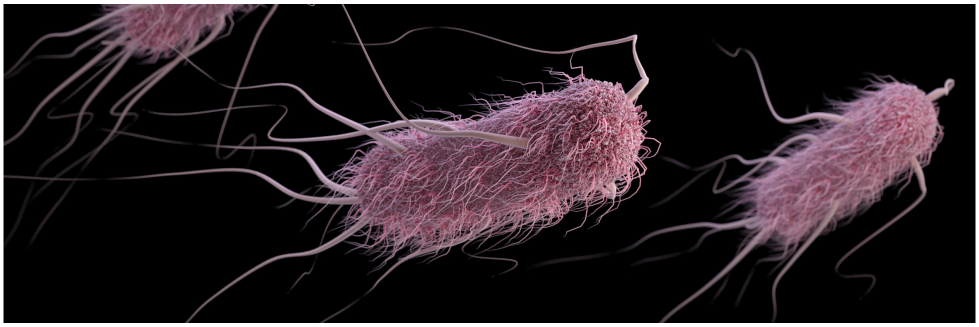

FIGURE 1.3: A computer-generated image of a group of *Escherichia coli.*[4] *E. coli* is an exemplar rod-like bacteria which demonstrates 'run-and-tumble' behaviour – periods of 'runs' punctuated by 'tumbles' where the bacteria randomly reorientates.

rendering it prone to wide range of unique phenomena. In the ordered anisotropic phase, studies on active matter reveal a rich variety of phase transitions, instabilities, wave propagation, jets and vortices, defect formation, and turbulence, amongst many other anomalies.[31, 37–41]

The quantitative analysis, description and prediction of active matter phenomena is actualized by sound Mathematical models — which in turn must be appropriate for the nature of the system they are modelling. Active matter models can be broadly split in two regimes based on the nature of the momentum dissipation of the medium: where *hydrodynamic* interactions between SPPs are important, momentum conservation arguments must be considered, which is referred to as ‘wet’ active matter; if the medium can considered inert, providing only friction, particle kinematics are *overdamped* and can be modelled without momentum conservation, referred to as ‘dry’ active matter. The terms wet and dry refer only to the type of model typically used, they are not a reference to the nature of the medium — some active matter systems could be modelled by either approach. Vibrated granular rods[42] and migrating animal herds[43] are examples of systems which could be modelled as dry active matter; swarming bacteria suspensions[44] and Janus nanoswimmers[21] are examples of systems which could be modelled as wet active matter.

In Section 1.2, I derive the governing equations for a coarse-grained description of momentum-conserving active matter, suitable for a wet active matter regime where appropriate modelling of the suspension medium and hydrodynamic interactions between SPPs (from here on referred to as swimmers or microswimmers) are important. In this regime, it is important to address the discrete nature of microswimmers: when is it permissible to employ a continuum description of active matter? If we consider the kinematics of a fluid, over spatial-intervals on the same order of magnitude of its molecular constituents, the fluid spatial-temporal evolution is dictated by the thermal fluctuations of, and collisions between, individual molecules. The ‘finiteness’ of the fluid on such a length scale is unavoidable. For spatial-intervals orders of magnitude above the molecular dimensions, the details of intermolecular interactions can be neglected in favour of averaged macroscopic properties such as pressure (force per unit area due to intermolecular collisions) and stress (force per unit area due to intermolecular resistance to deformation, which are well defined in a continuum limit.

The question of continuity then, is captured by the relationship between the length scale of interest and the interaction between particles. The Knudsen number is the ratio of these properties, defined as

$$\mathrm{Kn} = \frac{\lambda_m}{L} = \frac{\textit{mean-free path}}{\textit{length scale}}.$$

Here, λ_m is the mean-free path, defined as the average distance between successive impacts between particles. The length scale, which is the scale of phenomena we're interested in investigating, we are free to set at our own will. A continuum model is appropriate when our length scale of interest is an order of magnitude above the mean-free path, i.e. $\mathrm{Kn} < 0.1$. For water molecules, $\lambda_m \approx 0.25$nm, and measurements of flow around even the smallest bacteria, such as *Pelagibacter ubique* with an average cell diameter of 200nm,[45] have a Knudsen number of $\mathrm{Kn} \approx 10^{-3}$. Consequently, fluid velocity will always be modelled by a continuous vector field, in this work denoted $\boldsymbol{u}(\boldsymbol{x}, t)$ (Section 1.2.1), whose spatial-temporal evolution is governed by classical Newtonian mechanics generalised to infinitesimal fluid elements.

The generalisation of these principles to active matter is not clear-cut; the mean-free path of microswimmers can be difficult to determine. A didactic case occurs when the mechanism for the isotropic-anisotropic phase transition is motility, as Cates and Taileur[30] demonstrate. In a dilute-phase, the mean-free path could be large (relative to swimmer size) due to the distance between particles, yet the self-propulsive nature of microswimmers increases the rate of successive collisions, effectively reducing the mean-free path. As an isotropic-anisotropic phase transition occurs, relative particle-particle displacement decreases, increasing interaction probability. However, successive collisions between swimmers reduces the self-propulsion velocity, which therefore increases the interaction time-scale — consequently, the notion of a mean-free path becomes difficult to find deterministically. The dynamic characteristics of the mean-free path for swimmers in active matter is not only cause of complexities — many interesting phenomena of active matter occur at intermediate length scales, such as boundary layer phenomena, thin-films, or defect formation. Accordingly, appropriate care must be taken when applying a continuum model that has been developed to understand long-wavelength behaviour to localised phenomena, such as boundary phenomenon. Microswimmers exhibit niche behaviour at boundaries: collisions with a boundary temporarily decrease swimmer motility, leading to swimmer accumulation and trapping;[46,47] boundaries can be a source of strong surface energy, exerting a preferential alignment orientation on the suspension;[48] and swimmers can 'slip' along a boundary, where orientation assumes a different direction to their trajectory[49] (Figure 1.4).

A pragmatic approach to a continuum description of active matter might invoke the tools of statistical mechanics. Microscopic description of swimmers, as well as their interactions with their medium, can be coarse-grained to produce long-wavelength, long-time behaviour. In doing so, a natural order parameter known as the director emerges, describing the local average orientation of swimmers. In the ordered anisotropic phase, the director is a unit vector,* in this work denoted by $\boldsymbol{p}(\boldsymbol{x}, t)$

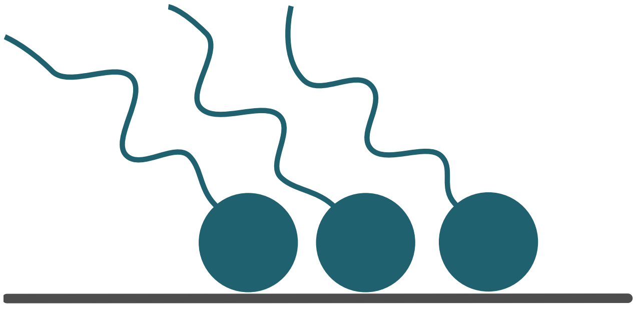

Figure 1.4: Microswimmers near a boundary can display a 'slip' behavioural mechanism, where swimmer orientation assumes a different direction to their trajectory.

---

[*] The director can be defined in the isotropic phase too, but will no longer be a unit vector

(Section 1.2.2). Its spatial-temporal evolution is governed by macroscopic principles, coarse-grained from microscopic particle-particle interactions — analogous to the emergence of macroscopic principles in a fluid, such as pressure and strain. With careful treatment, coarse-graining is a powerful approach to a continuum model. However this becomes inevitably intensive (and numerically expensive, if producing simulations) as swimmer models become more detailed, swimmer volume fraction increases, or particle interaction becomes stronger — analytical solutions quickly become impossible, or at best very difficult, to solve.

An alternative approach starts with writing down all the conserved fields — physical quantities which must be conserved by the laws of physics — and using the laws of conservation of mass, momentum and energy to derive the governing hydrodynamic equations. The choice of these fields is restricted to those which are 'slow variables'.[50] When a system is disturbed from equilibrium, the perturbation which caused the disturbance has an associated wavelength. A slow variable is one whose relaxation time is proportional to this wavelength; in particular, whose relaxation time is unbounded as the wavelength approaches infinity. The most general treatment of ordered anisotropic fluids by this phenomenological approach is found in liquid-crystal literature. The appropriation of this language for active matter was first made by Simha *et al.*[31] and has since been widely utilised as a continuum approach.

In this thesis, I establish the continuum, coarse-grained governing equations for momentum-conserving active matter by writing down the relevant continuum fields, applying hydrodynamic conservation laws to the suspension (Section 1.2.1), and determine director alignment with contributions from liquid-crystal literature to calculate the bulk and surface torques acting on the suspension (Section 1.2.2). Following a linear stability analysis around a constant steady state solution, in Chapter 2 I establish the instability mechanism for the unbounded 2D regime by deriving a fun-

---

to account for varying order. The inclusion of defects in the director requires a generalisation to Q-tensor theory, common to liquid-crystal literature.

damental instability known as the Stokesian active matter instability, established in literature by Simha *et al.*[31] and Sankararman *et al.*[51] In Chapter 3, I extend this analysis to the unbounded 3D regime where I illustrate that a de-coupling of the governing equations leads to the dominance of bend modes for an extesile suspension. The main result of this work follows in Section 3.3.2, where I consider a recent development for the inclusion of chirality into the Jeffrey orbit equations which recouples the governing equations and present a new regime of instability consisting of travelling twist-bend modes and an enhanced disturbance growth rate under imposed shear.

Hereafter, I introduce a numerical element to the analysis in the second part of this work by solving the linearised governing equations in an instability analysis as an eigenvalue problem in MATLAB, and I explore the consequences of imposing confinement on the fundamental instability by considering a channel and film regime in Chapter 4. After connecting the growth rates of unbounded regime and regimes of weak, intermediate and strong confinement in Section 4.6, I show in Section 4.7 that a 3D regime will always be less stable than a 2D regime by virtue of the de-coupling mechanism discussed in Chapter 2, and continue the narrative concerning chirality in Section 4.8. In Section 4.9, I illustrate that the choice of boundary conditions can greatly impact the growth rate of regimes under strong confinement and can reduce the critical confinement length needed to suppress the instability growth rate by an order of magnitude. The culmination of this work explores the instability growth rate of alternative steady states, either by imposing specific boundary conditions, or by imposing flow, such as in an inclined plane, which I detail in Chapter 5. Finally in Chapter 6, I discuss possible future avenues of exploration by the inclusion of stresses unique to polar active matter, the modelling of defects in the nematic phase, the consequences of having a non-uniform distribution of orientations, and extensions to the discussed regimes.

1.2 Governing Equations

The conserved fields for a wet active matter suspension of active, motile particles read,

$\rho(\boldsymbol{x}, t)$	fluid density,
$\boldsymbol{u}(\boldsymbol{x}, t)$	fluid velocity,
$c(\boldsymbol{x}, t)$	suspension concentration,
$\boldsymbol{p}(\boldsymbol{x}, t)$	suspension orientation.

The fields are all functions of position $\boldsymbol{x}$ and time t. The isotropic fluid and anisotropic swimmer suspension fields permeate — that is, they individually obey mass and momentum conservation laws and occupy the same domain. The fluid, whose governing equations are derived in Section 1.2.1, is governed by modified *Navier-Stokes* equations (1.18a, 1.18b) and the fluid contributes to swimmer suspension kinematics by *advection*, rotation due to *vorticity*, and alignment to *shear* gradients, and the suspension concentration and orientation can be defined from volume-averaged quantities over microswimmers with local orientation and position (1.19a–1.19c).

In the microswimmer suspension, whose governing equations are derived in Section 1.2.2, individual swimmers are assumed to be neutrally buoyant and axisymmetric, with a geometric parameter λ_1 measuring their alignment to local shear and a second new geometric parameter[52] λ_2 governing chirality (discussed in Section 3.2). Microswimmers interact with one another in two ways: hydrodynamic interactions are governed by a forcing term in the Navier-Stokes equations of the form $\boldsymbol{pp}$ commonly known as the *active stress* tensor[31] and a non-equilibrium motility stress of the form $\partial_i p_j + \partial_j p_i$ —both terms couple the swimmer orientation to fluid flow; *steric* interactions are modelled through a suspension elasticity term which is derived from a free energy functional, equation (1.32). The swimmer suspension also exerts stress due to swimmer polarity, self-advection from self-propulsion and thermodynamic contributions.[53] However, these terms come in at next-to-leading order spatial gradients, and can be neglected for an initial hydrodynamic instability analysis (Chapter 2). The mechanical stress contributions due to a suspension of passive particles broadly fall under *rheological* studies and are omitted in this work.

1.2.1 Hydrodynamics

The equations which govern all fluid mechanics are derived from the conservation principles of mass, linear momentum and angular momentum. Our derivation follows from fundamental principles in the Eulerian frame of reference, and a similar derivation can be found in any good fluid dynamics textbook, such as *Elementary fluid dynamics, Acheson*.[54] By the principle of conservation of mass, the rate-of-change of mass in a fixed volume V is proportional to the mass-flux on the volume boundary S (Figure 1.5),

$$\frac{\partial}{\partial t}\int_V \rho \, \mathrm{d}V + \int_S \rho \boldsymbol{u} \cdot \boldsymbol{n} \, \mathrm{d}S = 0. \tag{1.1}$$

Here $\boldsymbol{n}$ denotes the outward unit normal (Figure 1.5). Use of the *divergence theorem* allows us to write the surface integral as a volume integral, and we can bring the

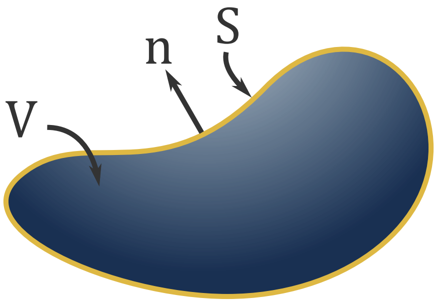

FIGURE 1.5: A fixed volume of fluid of volume V with surface boundary S and unit normal $\boldsymbol{n}$ pointing out of the volume.

time derivative inside the volume integral by utilising *Reynolds transport theorem*,

$$\int_V \frac{\partial}{\partial t}\rho + \nabla \cdot \Big(\rho \boldsymbol{u}\Big)\,\mathrm{d}V = 0. \tag{1.2}$$

Since (1.2) must hold for any fixed volume, we can reduce it to point form and write,

$$\frac{\partial \rho}{\partial t} + \nabla \cdot \rho \boldsymbol{u} = 0. \tag{1.3}$$

This is the statement of mass conservation for a fluid. When ρ is constant throughout the fluid, equation (1.3) reduces to the incompressibility constraint

$$\nabla \cdot \boldsymbol{u} = 0, \tag{1.4}$$

which holds for all regimes considered in this work. The momentum conservation laws state that the rate-of-change of momentum is balanced by the sum of the forces acting on the fluid, which can be generalised as,

$\boldsymbol{g}$	External body force per unit mass,
$\boldsymbol{b}$	External body moment per unit mass,
$\boldsymbol{t}$	Surface force per unit area,
$\boldsymbol{l}$	Surface moment per unit area.

As a consequence of the *Euler-Cauchy stress principle*, the surface force and surface moment can be expressed as functions of the stress tensor $\boldsymbol{\sigma}$ and couple stress tensor $\boldsymbol{\pi}$ respectively,

$$\boldsymbol{t} = \boldsymbol{n} \cdot \boldsymbol{\sigma}, \qquad \boldsymbol{l} = \boldsymbol{n} \cdot \boldsymbol{\pi}. \tag{1.5}$$

The equation for linear momentum balance reads,

$$\frac{\mathrm{d}}{\mathrm{d}t} \int_V \rho \boldsymbol{u} \, \mathrm{d}V = \rho \int_V \boldsymbol{g} \, \mathrm{d}V + \int_S \boldsymbol{t} \, \mathrm{d}S, \tag{1.6}$$

Rewriting the surface integral using equation (1.5) gives,

$$\begin{aligned} \int_S \boldsymbol{t} \, \mathrm{d}S &= \int_S \boldsymbol{n} \cdot \boldsymbol{\sigma} \, \mathrm{d}S \\ &= \int_V \nabla \cdot \boldsymbol{\sigma} \, \mathrm{d}V, \end{aligned} \tag{1.7}$$

where we have used the divergence theorem in the final step. We can again bring the time derivative inside the integral on the left hand side of (1.6) by utilising *Reynolds transport theorem* and the incompressibility of $\boldsymbol{u}$. With the contribution from (1.7), equation (1.6) can be reduced to point form and we obtain the linear momentum balance equation,

$$\rho\Big(\frac{\partial \boldsymbol{u}}{\partial t} + (\boldsymbol{u} \cdot \nabla)\boldsymbol{u}\Big) = \rho \boldsymbol{g} + \nabla \cdot \boldsymbol{\sigma}. \tag{1.8}$$

The differential form on the left-hand side is commonly known as the material derivative,

$$\frac{\mathrm{d}}{\mathrm{d}t} = \frac{\partial}{\partial t} + (\boldsymbol{u} \cdot \nabla). \tag{1.9}$$

The material derivative describes the transport of a physical quantity, such as heat or matter, in the presence of the background flow $\boldsymbol{u}$. When applied to the vectorial field $\boldsymbol{u}$, it describes the acceleration of a fluid element from the frame of reference of a fluid particle. The first term describes changes of the local (i.e. fixed point in space) flow field in time. The second term, known as the inertia term, describes the 'spatial' acceleration of the fluid. When applied to a scalar quantity, such as density or concentration, the second term describes advection due to the flow.

The linear momentum equation (1.8) is the fluidic equivalent of Newton's second law. To complete an equation of motion from equation (1.8) requires a *constitutive relation* between the *kinetic* and *kinematic* qualities of a fluid. A fluid will always deform when subjected to stress - for a Newtonian fluid, the relationship between the viscous stress $\boldsymbol{\sigma}^v$ and velocity gradients is linear, and the Newtonian Constitutive equation is written as,†

$$\boldsymbol{\sigma}^v = -P\boldsymbol{\delta} + 2\mu\boldsymbol{E}, \tag{1.10}$$

where P is fluid pressure, the normal stress exerted between bodies of a fluid; $\boldsymbol{\delta}$ is the Kronecker delta, μ is dynamic *viscosity*, which governs dissipation of momentum between neighbouring regions of fluid; and $\boldsymbol{E}$ is the rate-of-strain tensor, the symmetric component of the velocity gradient tensor $\nabla\boldsymbol{u}$ which is written,

$$\boldsymbol{E} = \frac{1}{2}\Big(\nabla\boldsymbol{u} + (\nabla\boldsymbol{u})^T\Big). \tag{1.11}$$

The resulting equation by substitution of (1.10) into (1.8) is the *Navier-Stokes* equation,

$$\rho\Big(\frac{\partial\boldsymbol{u}}{\partial t} + (\boldsymbol{u}\cdot\nabla)\boldsymbol{u}\Big) = -\nabla P + \mu\nabla^2\boldsymbol{u} + \rho\boldsymbol{g}. \tag{1.12}$$

---

† Here, incompressibility of the fluid has been assumed.

The first term on the right-hand side represents pressure forces, the second term represents viscous forces and the final term is the body force, typically gravity in this work. The presence of a suspension of swimming microorganisms in a viscous fluid also induces hydrodynamic stress, which acts like a forcing term in the Navier-Stokes equation. A simplistic model which captures forcing effects can be built from elementary solutions to the *Stokes* equation, equation (1.14), which describes highly viscous flows. Viscous flows are characterised by the dimensionless *Reynolds* number which describes the relationship between the inertia and viscous term in the Navier-Stokes equation,

$$\mathrm{Re} = \frac{\textit{Inertia forces}}{\textit{Viscous forces}} = \frac{\rho U L}{\mu}, \tag{1.13}$$

for velocity and length scales U and L. High Reynold number flows ($\mathrm{Re} \gg 1$) correspond to regimes where inertia forces dominate, such as aviation aerodynamics which are typically turbulent. Low Reynold number flows ($\mathrm{Re} \ll 1$) correspond to regimes where viscous forces dominate, such as coiling honey, and are typically steady. An exemplar microswimmer, such as *B. subtilis*, with a characteristic length of $\sim 4\mu$m and swim speed of $\sim 20\mu$m (see Section 2.2.1 for parameter ranges) yields a Reynolds number in water of $\mathrm{Re} \approx 10^{-4}$. Consequently, the inertia terms for the flow around microswimmers can be neglected, and the Navier-Stokes equation can be replaced by the steady Stokes equation,

$$\nabla \cdot \boldsymbol{\sigma}^{v} = 0. \tag{1.14}$$

In our initial analysis, we omit the externally-imposed body force $\rho\boldsymbol{g}$ which would appear on the right-hand side of equation (1.14). Microswimmers are typically neutrally buoyant, but gravitational forces can cause a re-orientation phenomenon known as *geotaxis* when the hydrodynamic center and the center-of-mass of a microswimmer are located in different places, causing a re-orientation along the direction of the ap-

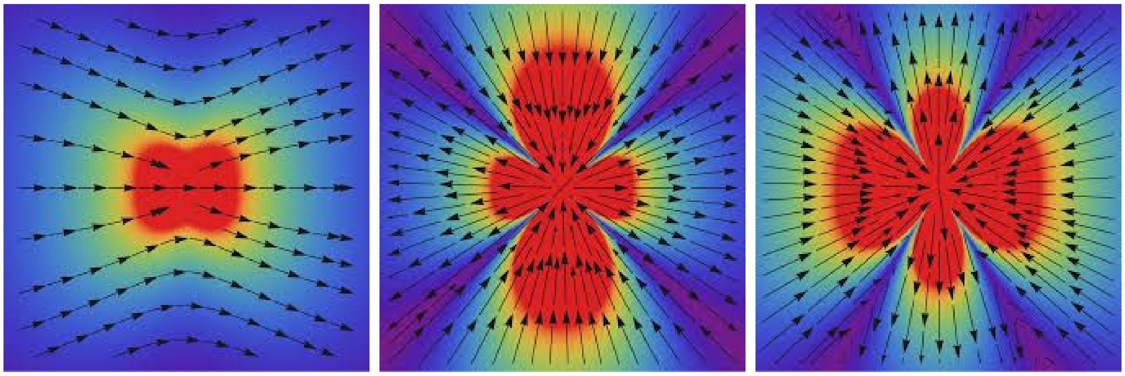

FIGURE 1.6: Elementary solutions of the Stokes equation (1.14). Reproduced from Kos *et al.*, 2018*.[5] LEFT: The fluidic response to a point force, otherwise known as a Stokeslet. Viscosity drags along fluid adjacent to the point force, where the fluid velocity spatial decay is proportional to $1/r^2$. MIDDLE: The flow field resulting from a dipole of two opposing forces (corresponding to active units orientated in the y-axis, exerting contractile stress such as a 'puller' swimmer). RIGHT: The flow field resulting from a dipole of two forces facing away from one another (corresponding to active units orientated in the y-axis, exerting extensile stresses such as a 'pusher' swimmer).

plied gravitational field.[55] This re-orientation effect can produce plumes of up-welling (gravitaxis) or down-welling bacteria (gyrotaxis),[56] however, as we are interested in activity-driven phenomena, we choose to omit this effect (which would have appeared as a separate term for the director in Section 1.2.2). Gravitationally-induced flows are typically an order-of-magnitude larger than microswimmer activity-driven flows (see Section 2.2.1 for further parameter analysis), and the corresponding shear-induced torque can be the dominant mechanism for re-orientation in swimmer suspensions when confinement effects are small. These effects are included with shear-induced torque acting on the suspension in Section 1.2.2 and specifically addressed in Chapter 5.

Equation (1.14) expresses a time-independent force-balance in viscous fluids; its response to a point force $\delta(\boldsymbol{x})\boldsymbol{f}(\boldsymbol{x})$, where $\delta(\boldsymbol{x})$ is the Dirac delta function, has an

---

*Figure reproduced under MDPI Open Access licence.

elementary solution called a stokeslet (Figure 1.6, LEFT): the dominant flow is along the axis of the direction of $f(\boldsymbol{x})$, but is also constituted of a component perpendicular to the direction of $f(\boldsymbol{x})$ as fluid is dragged along due to viscous effects. In a far-field approximation, we can approximate a microswimmer by two point forces: the first represents the drag of the microswimmer, which is largest around the body or head of the microswimmer, and the second represents the thrust exerted on the fluid by the swimmer flagella. The relative position of these two forces broadly categorises the type of microswimmer we have: when the microswimmer flagella are located in front of the body, we have a 'puller' microswimmer, when the flagella are located behind the microswimmer head, we have a 'pusher' microswimmer. This minimalist description is known as the far-field 'dipole' approximation for microswimmers and captures the fundamental flow field around the swimmer: corrections to the resultant flow field can be achieved by considering higher multipole expansions.[57] The flow fields for the dipole solutions are also called 'stresslets', and depend only on whether the swimmer is a 'pusher' or a 'puller' (corresponding flow fields in Figure 1.6, MIDDLE and RIGHT). The full derivation and explicit forms can be found in any good text book on microhydrodynamics, such as Kim & Karrila.[58]

In this work, we are interested in the net flow-field arising from a suspension of swimming microorganisms. The minimalistic dipole description of a microswimmer is an ideal first-order approximation to this flow-field as corrections from higher multipole expansions are small when averaging over the swimmer suspension. To form the active stress tensor, we idealise a suspension of stresslets where the a^{th} swimmer has position $\boldsymbol{r}_a$, orientation $\boldsymbol{\nu}_a$ and, equal and opposite poles of strength f_α located at $\boldsymbol{r}_a + d\boldsymbol{\nu}_a$ and $\boldsymbol{r}_a - d'\boldsymbol{\nu}_a$ (Figure 1.7). The force density of these rods at $\boldsymbol{x}$ is given by,

$$\boldsymbol{F}_\alpha(\boldsymbol{x}) = \sum_a f_\alpha \boldsymbol{\nu}_a \Big(\delta\Big(\boldsymbol{x} - (\boldsymbol{r}_a + d\boldsymbol{\nu}_a)\Big) - \delta\Big(\boldsymbol{x} - (\boldsymbol{r}_a - d'\boldsymbol{\nu}_a)\Big)\Big) \tag{1.15}$$

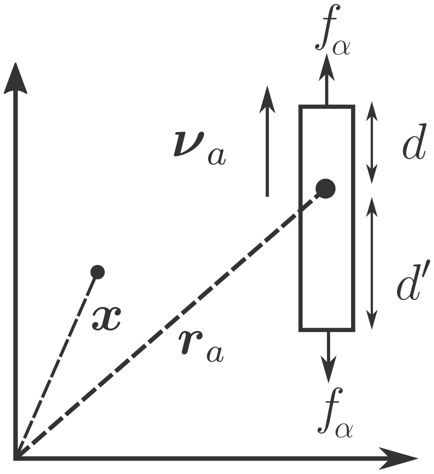

FIGURE 1.7: A collection of idealised dipole microswimmers. The a^{th} microswimmers location is given by $\boldsymbol{r}_a$ with orientation $\boldsymbol{\nu}_a$. The microswimmer idealised as a rod has equal and opposite forces located at $\boldsymbol{r}_a + d\boldsymbol{\nu}_a$ and $\boldsymbol{r}_a - d'\boldsymbol{\nu}_a$.

Expansion of the dirac delta function around swimmer position $\boldsymbol{r}_a$ gives,

$$\boldsymbol{F}_\alpha(\boldsymbol{x}) = -f_\alpha(d+d')\nabla \cdot \sum_a \boldsymbol{\nu}_a\boldsymbol{\nu}_a\delta\Big(\boldsymbol{x} - \boldsymbol{\nu_a}\Big) + \mathcal{O}\Big(\nabla\nabla\Big). \tag{1.16}$$

Here, $\mathcal{O}\Big(\nabla\nabla\Big)$ represents higher order derivatives in the Taylor expansion. Coarse-graining this summation[16] gives us the divergence of the active stress tensor $\boldsymbol{\sigma}^\alpha$ such that,

$$\boldsymbol{\sigma}^\alpha = \alpha\boldsymbol{p}\boldsymbol{p}, \tag{1.17}$$

where individual swimmer orientation $\boldsymbol{\nu}_a$ has been coarse-grained to an averaged swimmer orientation term $\boldsymbol{p}(\boldsymbol{x}, t)$ and the swimmer number density is contained within the activity term $\alpha = -f_\alpha\hat{d}c(\boldsymbol{x}, t)$, where $\hat{d} = (d{+}d')/2$ and $\alpha < 0$ corresponds to pusher swimmers exerting tensile stress on the fluid, and $\alpha > 0$ corresponds to puller swimmers exerting contractile stresses on the fluid. Here, the averaged swimmer orientation $\boldsymbol{p}$ can be well-determined by moments about a probability density function for the swimmer orientation and position, which is discussed further in the governing equations for the suspension (Section 1.2.2). For a fluid of viscosity μ, the dipole strength can be evaluated by $f_\alpha \sim v_p \mu \hat{d}$, where v_p is the microswimmer speed, and takes values in the range of $f_\alpha \in [0.1, 10]$pN (detailed in Section 2.2.1). Finally, defining the total stress as $\boldsymbol{\sigma} = \boldsymbol{\sigma}^v + \boldsymbol{\sigma}^\alpha$, this allows us to write down the governing equations for the active matter hydrodynamics as,

$$\nabla \cdot \boldsymbol{u} = 0, \tag{1.18a}$$

$$\rho\Big(\frac{\partial \boldsymbol{u}}{\partial t} + (\boldsymbol{u} \cdot \nabla)\boldsymbol{u}\Big) = -\nabla P + \mu \nabla^2 \boldsymbol{u} + \rho \boldsymbol{g} + \alpha \nabla \cdot \boldsymbol{p}\boldsymbol{p}. \tag{1.18b}$$

1.2.2 Swimmer Suspension

Next, we turn our attention to the continuum fields for the spatial and orientational configurations of the swimmer suspension , which are well defined by the moments of the probability density function $\mathcal{P}(\boldsymbol{x}, \boldsymbol{\nu}, t)$ describing the probability of finding a particle at point $\boldsymbol{x}$, with orientation $\boldsymbol{\nu}$, at time t, such that,

$$c(\boldsymbol{x}, t) = \int_{\mathsf{S}} \mathcal{P}(\boldsymbol{x}, \boldsymbol{\nu}, t) \, \mathrm{d}\boldsymbol{\nu}, \tag{1.19a}$$

$$\boldsymbol{m}(\boldsymbol{x}, t) = \int_{\mathsf{S}} \mathcal{P}(\boldsymbol{x}, \boldsymbol{\nu}, t) \boldsymbol{\nu} \, \mathrm{d}\boldsymbol{\nu}, \tag{1.19b}$$

$$\boldsymbol{Q}(\boldsymbol{x}, t) = \int_{\mathsf{S}} \mathcal{P}(\boldsymbol{x}, \boldsymbol{\nu}, t) \Big(\boldsymbol{\nu}\boldsymbol{\nu} - \frac{\boldsymbol{\delta}}{3}\Big) \, \mathrm{d}\boldsymbol{\nu}. \tag{1.19c}$$

where integrands are evaluated over S, the unit sphere of all possible orientations. Then, the zeroth moment corresponds to the concentration $c(\boldsymbol{x}, t)$ of swimmers, the first moment corresponds to the unnormalized polarisation $\boldsymbol{m}(\boldsymbol{x}, t) = S(\boldsymbol{x}, t)\boldsymbol{p}(\boldsymbol{x}, t)$, where $\boldsymbol{p}(\boldsymbol{x}, t)$ is a unit vector describing the average orientation of particles and $S(\boldsymbol{x}, t)$ is a scalar order parameter describing the order strength. The second moment gives the unnormalized tensorial order parameter $\boldsymbol{Q}(\boldsymbol{x}, t)$ which describes the deviation away from the isotropic state.

A full, dynamical description of an active matter suspension capable of predicting isotropic-anisotropic phase transitions would require solving the *Smoluchowski equations* for the probability density function $\mathcal{P}(\boldsymbol{x}, \boldsymbol{\nu}, t)$. However, since we are interested in the stability of the ordered anisotropic phase, it would suffice to derive the conservation laws for $c(\boldsymbol{x}, t)$ and $\boldsymbol{p}(\boldsymbol{x}, t)$, as variations in the scalar order parameter $S(\boldsymbol{x}, t)$ and tensorial order parameter $\boldsymbol{Q}(\boldsymbol{x}, t)$ are small when conducting a stability analysis around the ordered state. We are interested in regimes of self-propelled microorganisms which contribute polar and motile stresses that break the symmetry $\boldsymbol{p} = -\boldsymbol{p}$, however these terms act at higher order gradients than the activity stress tensor, which drives the system out of equilibrium, and consequently in favour of simplifying the stability analysis we choose to neglect these stresses to focus on the role of boundary conditions in strong confinement. The regimes where our analysis can be broadly applied and where further special consideration is required is discussed in the concluding remarks in Section 6.2.

1.2.2.1 Concentration and Director Field Conservation Laws

Having established that the concentration $c(\boldsymbol{x}, t)$ and director (average orientation) $\boldsymbol{p}(\boldsymbol{x}, t)$ fields can indeed be connected to well defined microscopic states described by a probability distribution function, we will proceed to lightly sketch the derivation of their conservation equations. In Section 2.2, we will make the simplifying assumption of constant concentration, but for completeness sake its governing equation is also included here. The mass conservation equation was already derived in equation (1.3), the swimmer concentration follows a similar conservation process, so we skip its derivation and state the result which reads,

$$\frac{\partial c}{\partial t} + \nabla \cdot (c\boldsymbol{u} + cv_P\boldsymbol{p}) = 0. \tag{1.20}$$

Here, the second term in the divergence expression describes swimmers with self-propulsion velocity $v_p\boldsymbol{p}$. The effects of diffusion and Brownian motion in equation (1.20) have been neglected. Next, we turn our attention to the equation of motion for the director, which is evaluated by a torque balance argument applied to a local swimmer at point $\boldsymbol{x}$, whose orientation is described by the unit vector $\boldsymbol{\nu}(\boldsymbol{x}, t)$. By the definition of the rate-of-change of orientation we have,

$$\dot{\boldsymbol{\nu}} = \boldsymbol{w} \times \boldsymbol{\nu}, \tag{1.21}$$

where $\dot{\boldsymbol{\nu}}$ denotes the material derivative and $\boldsymbol{w}$ the swimmer angular velocity. In seeking an expression for $\boldsymbol{w}$, we recall that a microswimmer satisfies the no-torque condition, such that the torque exerted on the swimmer due to rotational drag $\boldsymbol{T}_{\text{drag}}$ and the torque imposed by external forces $\boldsymbol{T}_{\text{ext}}$ balance one another, which yields

$$\boldsymbol{T}_{\text{drag}} + \boldsymbol{T}_{\text{ext}} = 0. \tag{1.22}$$

To find an expression for the rotational drag $\boldsymbol{T}_{\text{drag}}$, we follow a similar narrative to Michael D. Graham.[59] Note that the expressions for translational and rotational drag on a particle in a Stokes flow are proportional to the particles velocity $\boldsymbol{v}$ and angular velocity $\boldsymbol{w}$,

$$\boldsymbol{F}_{\text{drag}} = \zeta_h \boldsymbol{v}_p, \tag{1.23}$$

$$\boldsymbol{T}_{\text{drag}} = \zeta_r \boldsymbol{w}. \tag{1.24}$$

Here, ζ_h, ζ_r are the translational and rotational drag coefficients on the swimmer. For a sphere of radius a, the drag coefficients are known to be $\zeta_h^{sph} = 6\pi\mu a$, $\zeta_r^{sph} = 8\pi\mu a^3$, which can be shown by a straight-forward surface integral over the sphere. The generalisation to nonspherical particles describes the relationship between the translational drag $\boldsymbol{F}_{drag}$, rotational drag $\boldsymbol{T}_{drag}$, and stresslet $\boldsymbol{S}$ tensor, to the translational, rotational and shear flow experienced by the particle. For sufficiently small particles, the background flow $\boldsymbol{u}^{\infty}$ experienced can be approximated as a linear flow,

$$\boldsymbol{u}^{\infty} = \boldsymbol{\Omega} \cdot \boldsymbol{x} + \boldsymbol{E} \cdot \boldsymbol{x}, \tag{1.25}$$

where $\boldsymbol{\Omega}$ is the antisymmetric part of the velocity gradient tensor $\nabla \boldsymbol{u}$ and $\boldsymbol{E}$ its symmetric part. Then, by the linearity of the Stokes equation, (1.14) this allows us to write a general expression between the forces and velocities experienced by a particle,

$$\begin{bmatrix} \boldsymbol{F}_{\text{drag}} \\ \boldsymbol{T}_{\text{drag}} \\ \boldsymbol{S} \end{bmatrix} = \boldsymbol{\mathcal{R}} \cdot \begin{bmatrix} \boldsymbol{u} - \boldsymbol{v} \\ \boldsymbol{\omega} - \boldsymbol{w} \\ \boldsymbol{E} \end{bmatrix}$$

where $\boldsymbol{\omega}$ describes the local fluid vorticity. The second-rank tensor $\boldsymbol{\mathcal{R}}$ is known as the 'grand resistance tensor' and constitutes second, third and fourth-rank tensors which detail the resistance of a particle to translation, rotation, and strain; its elements are abbreviated $\boldsymbol{R}^{ij}$. For a full technical discussion, see Kim & Karrila[58] or Graham.[59] For our purpose, it suffices to write the relationship for the drag torque,

$$\boldsymbol{T}_{\text{drag}} = \boldsymbol{R}^{\text{T}\Omega} \cdot (\boldsymbol{\omega} - \boldsymbol{w}) + \boldsymbol{R}^{\text{TE}} \cdot \boldsymbol{E}, \tag{1.26}$$

The astute reader may observe the absence of a $\boldsymbol{R}^{\text{TU}}$ like term, the torque experienced due to pure translation, which would appear for particles with a chiral contribution to their shape, such as a corkscrew-like particle, or a swimmer with helical flagellum. Chiral contributions can result in translation of the particle due to shear-imposed, and would require a self-propulsion correction to the linear-flow profile (1.26) experienced by a particle. As chirality is a next-to-leading order effect for swimming microorganisms, whose dominant re-orientation mechanism is determined by vorticity and alignment to shear, we omit $\boldsymbol{R}^{\mathrm{TU}}$ and proceed with our derivation for an axisymmetric, fore-aft particle, but re-introduce chirality in Chapter 3 where we consider a chiral correction to the Jeffrey orbit equations from Ishimoto.[60] Substituting (1.26) into (1.22) and rearranging for $\boldsymbol{w}$ results in,

$$\boldsymbol{w} = \boldsymbol{\omega} + (\boldsymbol{R}^{\mathrm{T}\Omega})^{-1} \cdot \boldsymbol{R}^{\mathrm{TE}} \cdot \boldsymbol{E} + (\boldsymbol{R}^{\mathrm{T}\Omega})^{-1} \cdot \boldsymbol{T}_{\mathrm{ext}}. \tag{1.27}$$

Taking the cross product with $\boldsymbol{p}$ and substituting (1.21) gives,

$$\dot{\boldsymbol{\nu}} = \boldsymbol{\omega} \times \boldsymbol{\nu} + (\boldsymbol{R}^{\mathrm{T}\Omega})^{-1} \cdot \boldsymbol{R}^{\mathrm{TE}} \cdot \boldsymbol{E} \times \boldsymbol{\nu} + (\boldsymbol{R}^{\mathrm{T}\Omega})^{-1} \cdot \boldsymbol{T}_{\mathrm{ext}} \times \boldsymbol{\nu}. \tag{1.28}$$

The torque-vorticity tensor $\boldsymbol{R}^{\mathrm{T}\Omega}$ expresses the relationship between torque and angular velocity. For an axisymmetric fore-aft particle, $\boldsymbol{R}^{\mathrm{T}\Omega}$ is a rotational friction tensor, whose components comprise of $\zeta_r^{\parallel}$, friction due to rotations around the $\boldsymbol{\nu}$ vector, and $\zeta_r^{\perp}$, friction due to rotations perpendicular to the $\boldsymbol{\nu}$ vector,

$$\boldsymbol{R}^{\mathrm{T}\Omega} = \zeta_r^{\parallel} \boldsymbol{\nu}\boldsymbol{\nu} + \zeta_r^{\perp} (\boldsymbol{\delta} - \boldsymbol{\nu}\boldsymbol{\nu}), \tag{1.29a}$$

$$(\boldsymbol{R}^{\mathrm{T}\Omega})^{-1} = \frac{1}{\zeta_r^{\parallel}} \boldsymbol{\nu}\boldsymbol{\nu} + \frac{1}{\zeta_r^{\perp}} (\boldsymbol{\delta} - \boldsymbol{\nu}\boldsymbol{\nu}). \tag{1.29b}$$

Since rotations about the $\boldsymbol{p}$ axis don't change the suspension dynamics, we are free to discard the $\frac{1}{\zeta_r^{\parallel}}$ term and unambiguously write $\zeta_{\mathrm{r}} = \zeta_{\mathrm{r}}^{\perp}$. The torque-strain tensor $\boldsymbol{R}^{\mathrm{TE}}$ can be expressed as,[58]

$$R_{kij}^{\mathrm{TE}} = \zeta_{\mathrm{E}} (\epsilon_{ikl} \nu_j + \epsilon_{jkl} \nu_i) \nu_l \tag{1.30}$$

Here, ζ_{E} is the particle resistance to strain and ϵ_{ijk} is the *Levi-Civita* symbol. Substituting (1.29b) and (1.30) into (1.28) and applying identities for the equivalence of vorticity and angular velocity we get,

$$\dot{\boldsymbol{\nu}} = \lambda_1(\boldsymbol{\delta} - \boldsymbol{\nu}\boldsymbol{\nu}) \cdot \boldsymbol{E} \cdot \boldsymbol{\nu} - \boldsymbol{\Omega} \cdot \boldsymbol{\nu} + \frac{1}{\zeta_r}\boldsymbol{T}_{\mathrm{ext}} \times \boldsymbol{\nu}. \tag{1.31}$$

Here, the constant $\lambda_1 = \frac{\zeta_{\mathrm{E}}}{\zeta_{\mathrm{r}}}$ known as the *Bretherton constant*, describes the tendancy of a particle to align to local shear gradients. The Bretherton constant is a function of the swimmer geometry only: spherical particles which do not align to shear have a Bretherton number of 0, whereas rod-like particles which are strongly effected by extensile flows have a Bretherton number close to 1. In classical swimmer problems, the case of $\lambda_1 = 1$ corresponds to infinitely long rods, but certain liquid-crystal regimes (which we do not consider) can have an effective value of $|\lambda_1| > 1$. Alignment to shear plays an important role in the stability of an active matter suspension as it sets a preferential alignment direction for the director and will often be referred to during analysis throughout this work.

1.2.2.2 Determining Externally-Imposed Torque in a Suspension

Equation (1.31) can be coarse-grained to the suspension by substituting $\boldsymbol{\nu}$ for the director $\boldsymbol{p}$, and exchanging the externally-imposed torque $\boldsymbol{T}_{ext}$ acting on an individual swimmer for a volume-averaged torque $\boldsymbol{T}^V_{ext}$. Externally-imposed torques can arise from gravitational, magnetic or chemical forces, but in this work, we are interested in externally imposed ‘elastic-like’ torques occurring due to swimmer-swimmer alignment effects. We are interested in densely-populated suspensions close to their packing fraction, for which we can adopt a free-energy for the suspension to determine $\boldsymbol{T}^V_{ext}$, which is commonly used in liquid-crystal literature.

Rotational deformations of the director have a free-energy cost associated with the increase of rotational entropy of the suspension. By minimising this distortion energy, we will find the conditions for static equilibrium in the bulk and use this expression to detail the imposed torque on the swimmer. The most general treatment of the entropy production of an ordered anisotropic fluid lies within the field of liquid-crystals and is beyond the scope of this work. A general treatise can found in De Gennes & Prost[48] who provide a comprehensive overview of the physics of liquid crystals. The derivation of the imposed torque in this section closely follows the work of De Gennes & Prost, amongst others. To maintain the narrative and purpose of this work, we sketch the details in the main text here, but fully detail the calculations in Appendix A, with references made to the appendix through.

The simplest deformations the director field can undergo are splay, bend and twist (Figure 1.8): Splay deformations are represented by the local divergence of the director, directed along the director; rotational deformations in the director are calculated by director curl, and twist (bend) deformations are the component of director parallel (perpendicular) to curl, such that

$$\begin{aligned}\text{Splay} &= (\nabla\cdot\boldsymbol{p})\boldsymbol{p},\\ \text{Twist} &= \boldsymbol{p}\cdot(\nabla\times\boldsymbol{p}),\\ \text{Bend} &= \boldsymbol{p}\times(\nabla\times\boldsymbol{p}).\end{aligned}$$

The free-energy change associated with these elastic deformations, known as the Frank free-energy, is taken as a volume integral over a sample volume of the director[48] (Appendix A.2, equation (A.7)),

$$\mathcal{F}_T = \int_V \frac{1}{2}K_1(\nabla\cdot\mathbf{p})^2 + \frac{1}{2}K_2(\mathbf{p}\cdot\nabla\times\mathbf{p})^2 + \frac{1}{2}K_3||\mathbf{p}\times\nabla\times\mathbf{p}||^2 \ \mathrm{d}V. \tag{1.32}$$

From left to right, the three terms represent the elastic-energy contributions of the splay, twist and bend deformations seen in FIGURE 1.8, where the coefficients K_i are known as the Frank free-energy constants. The distortion constants K_i are typically the same order of magnitude, $K_i \approx 10^{-6}$dyn, so we adopt the common one-constant approximation such that $K_i = K$. The Frank free-energy integrand can be split-up into bulk energy terms and a saddle-splay term which acts on the surface. When these surface-energy contributions are significant, they will impose constraints on $\boldsymbol{p}$ at the boundaries; a regime called strong-anchoring. These terms can be neglected in our search for the external torque acting on a swimmer in the bulk and reconsidered by way of boundary conditions in Section 4.2. Under these assumptions, the integrand in (1.32) can be written (appendix equation (A.11)),

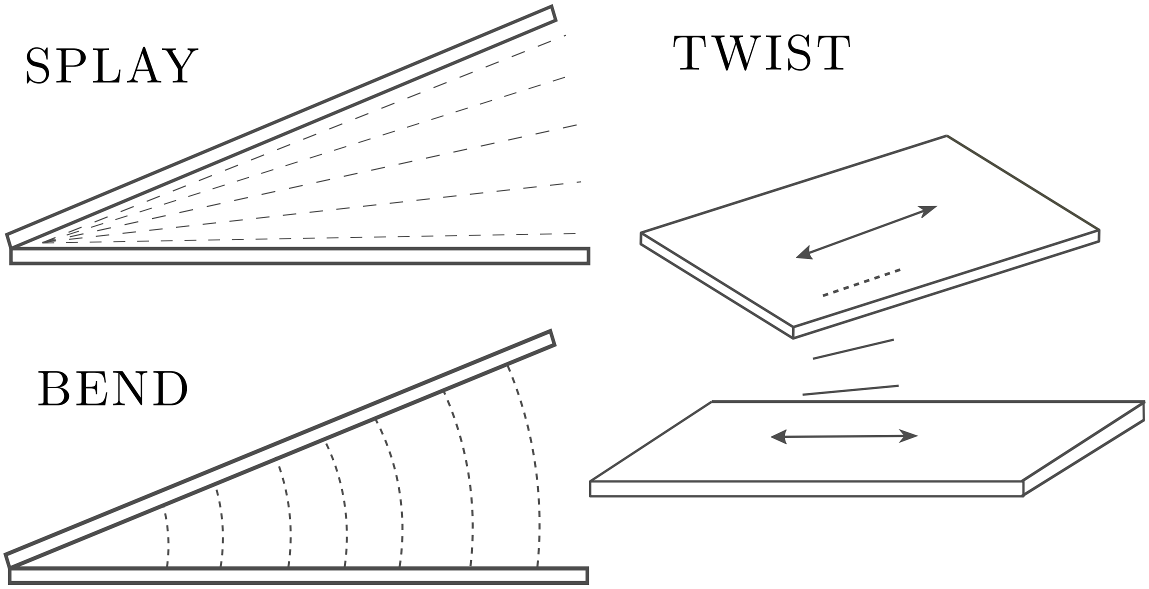

FIGURE 1.8: TOP LEFT TO RIGHT: Deformations in the director can be visualised by their alignment to glass plates. The local director orientation is indicated by the dashed lines in each diagram. When the director is aligned parallel to glass plates and the glass plates are 'opened', a splay deformation is formed. If instead the director is aligned perpendicular to the glass, a bend deformation is formed as the plates are separated. If instead the glass plates are held parallel to one another and twisted rotated relative to one another, a twist deformation is formed.

$$f_d = \frac{1}{2} K ||\nabla \boldsymbol{p}||^2. \tag{1.33}$$

To find the imposed torque, first the condition for static equilibrium in the director must be found (full derivation detailed in Appendix A, only the outline sketched here). Minimising the functional $\mathcal{F}_T$ with respect to variations in $\boldsymbol{p}$,

$$\begin{aligned}
\delta \mathcal{F}_T[\boldsymbol{p}] &= \mathcal{F}_T[\boldsymbol{p} + \delta \boldsymbol{p}] - \mathcal{F}_T[\boldsymbol{p}], \\
&= \int_V \Big[f_d\Big(\boldsymbol{x}, \boldsymbol{p} + \delta \boldsymbol{p}, \nabla \boldsymbol{p} + \delta \nabla \boldsymbol{p}\Big) - f_d\Big(\boldsymbol{x}, \boldsymbol{p}, \nabla \boldsymbol{p}\Big)\Big] \, \mathrm{d}V, \\
&= \int_V \delta \boldsymbol{p} \cdot \nabla_p f_d(\boldsymbol{p}, \nabla \boldsymbol{p}) + \delta \nabla \boldsymbol{p} \cdot \nabla_{p'} f_d(\boldsymbol{p}, \nabla \boldsymbol{p}) + \mathcal{O}\Big(\nabla_p^2, \nabla_{p'}^2\Big) \, \mathrm{d}V.
\end{aligned}$$

In the final line, we have expanded f_d by Taylors theorem where ∇_p indicates gradients with respect to p and similarly $\nabla_{p'}$ indicates gradients with respect to $\nabla \boldsymbol{p}$. Keeping only linear terms and minimising $\delta \mathcal{F}_T = 0$ to all variations in $\delta \boldsymbol{p}$ such that $|\boldsymbol{p}| = 1$, we obtain the suspension static equilibrium condition which we recognise as the standard Euler-Lagrange minimisation equation[61] (appendix equation (A.12)),

$$\frac{\partial f_d}{\partial p_i} - \frac{\partial}{\partial x_j} \frac{\partial f_d}{\partial (\partial_j p_i)} = \mathsf{h}_i, \tag{1.34}$$

where $\mathbf{h}$ is known as the *molecular field*. Equation (1.34) is known as the 'static equilibrium' condition for the director, *i.e.,* when the director is parallel to $\mathbf{h}$, the externally-imposed torque $\boldsymbol{T}^V_{ext}$ contribution to the generalised Jeffrey orbit equation vanishes. In the case of f_d as given by (1.33), the molecular field reads (appendix equation (A.13)),

$$\mathsf{h} = K\nabla^2 \boldsymbol{p}. \tag{1.35}$$

Leslie's 1992[62] rate of work hypothesis stipulates that the rate at which forces and moments do work in the system is absorbed by the distortion free-energy f_d, kinetic energy and lost through viscous dissipation. A rigorous application of this argument (Appendix A.3, A.4) finds that the imposed torque can be written (appendix equation (A.29)),

$$\boldsymbol{T}_{\text{ext}} = \boldsymbol{p} \times \mathsf{h}. \tag{1.36}$$

Substitution of (1.36) with the molecular field (1.35) into the coarse-grained version of (1.31) results in the equation of motion for the director,

$$\frac{\partial \boldsymbol{p}}{\partial t} + (\boldsymbol{u} + v_p \boldsymbol{p}) \cdot \nabla \boldsymbol{p} = \lambda_1 (\boldsymbol{\delta} - \boldsymbol{pp}) \cdot \boldsymbol{E} \cdot \boldsymbol{p} - \boldsymbol{\Omega} \cdot \boldsymbol{p} + D\Big(\nabla^2 \boldsymbol{p} - (\boldsymbol{p} \cdot \nabla^2 \boldsymbol{p})\boldsymbol{p}\Big) \tag{1.37}$$

where $D = \frac{K}{\zeta_r}$ and the identity for the triple cross product has been applied. In summary, from left-to-right the director is coupled to fluid flow by shear gradients: alignment to shear is governed by the rate-of-strain tensor $\boldsymbol{E}$ and shear alignment parameter λ_1 (also known as the Bretherton constant); rotation due to local fluid vorticity is represented by $\boldsymbol{\Omega}$ and the final term is director elasticity governed by D, which describes diffusion of rotational gradients in the suspension. We will refer to (1.37) as the *generalised Jeffrey orbit* equation, where the details encapsulated by the Smoluchowski capable of describing phase transitions, population dynamics, and phenomena such as particle dispersion, have been omitted in favour of studying densely populated, highly-ordered suspensions, where (1.37) is well-equipped to capture long-wavelength, and long-time phenomena.

2 | Bulk Hydrodynamic Instability of a 2D Suspension

In Section 1.2.1, we derived the hydrodynamic governing equations for a coarse-grained active matter system (equations (1.18a, b)) and showed they include a forcing term proportional to active particle activity, which was of the form $\nabla \cdot \boldsymbol{pp}$ (equation (1.17)). The active stress tensor, which was derived for a suspension of force dipoles, is independent of the microscopic detail of the swimmers propulsion mechanism, and reflects the highly non-equilibrium nature of active matter, which locally disperses energy everywhere throughout the suspension leading to active flow wherever there is a gradient in the director $\boldsymbol{p}(\boldsymbol{x}, t)$, where $\boldsymbol{p}$ describes the averaged local particle orientation in an anisotropic phase of active matter. In Section 1.2.2, we discussed the coupling between the orientation and local flow gradients, which yielded equation (1.37), detailing particle alignment to shear, rotation due to vorticity, and director elasticity, which penalises gradients in the director.

In an early result in the field of active matter, Simha & Ramaswamy[31] showed that the forcing arising from the active stress tensor will destabilise an ordered nematic active matter suspension for long-wavelength perturbations when coupling orientation, flow and concentration. In this Chapter, we will reproduce some of the main results from this paper to prepare for a comprehensive extension to the instability analysis. We begin in Section 2.1 by qualitatively describing the mechanism that causes hydrodynamic pumping due to bend and splay deformations in the director, before detailing linear instability analysis calculations in Section 2.3. By linearising around a steady state, we mathematically reduce the analysis to an eigenvalue problem, where we are interested in the growth rate, phase, and solution type of the corresponding eigenmodes. Throughout this chapter, our main goal is to build a strong intuition for the mechanical mechanism which drives the suspension out of equilibrium to prepare ourselves for the extension to the 3D regime in Chapter 3 and regimes of confinement in Chapter 4 and Chapter 5.

2.1 Qualitative Description

A bulk active matter suspension, free from the effects of shear, confinement or external alignment forces on the director, admits a steady, constant solution (denoted by overbars) for the velocity, pressure and director fields, such that,

$$\bar{\boldsymbol{u}} = \boldsymbol{0}, \qquad \bar{c} = c_0, \qquad \bar{\boldsymbol{p}} = \text{const.}, \qquad \bar{P} = P_A, \tag{2.1}$$

where P_A is set as atmopsheric pressure, and we set $\bar{\boldsymbol{p}} = \hat{\boldsymbol{x}}$ without loss of generality which is the general convention used throughout this work, except where explicitly mentioned. The constant solution can be visualised by imagining a suspension of idealised rods, whose contractile or extensile dipole moments act from the ends of each rod (FIGURE 1.7). By aligning the rods end-to-end and side-by-side, the physical interpretation of the constant solution is realised by analogy to a square lattice of aligned common bar-magnets, whose forces would cancel one another out when perfectly aligned — clearly, by that same analogy, any disturbance of said bar-magnets would result in net force local to the disturbance whose magnitude is proportional to the size of the disturbance. In a similar way to the bar magnets, a lattice of swimmers idealised as rods exerting force-dipole moments will admit a steady solution when all the rods are aligned (visualised in FIGURE 2.1A).

To understand the behaviour of a suspension of force-dipoles when spatial gradients in the director are present, recall that the director can undergo three types of rotational deformation: bend, twist and splay (Section 1.2.2, FIGURE 1.8). The hydrodynamic force associated with the bend and splay deformations emerge from the active stress tensor by rewriting it as,

$$\nabla \cdot \boldsymbol{p}\boldsymbol{p} = (\nabla \cdot \boldsymbol{p})\boldsymbol{p} + (\nabla \times \boldsymbol{p}) \times \boldsymbol{p}, \tag{2.2}$$

with the use of $(\boldsymbol{p} \cdot \nabla)\boldsymbol{p} = (\nabla \times \boldsymbol{p}) \times \boldsymbol{p} + \frac{1}{2}\nabla(\boldsymbol{p} \cdot \boldsymbol{p})^2$, where $\boldsymbol{p}$ is a unit vector. The first term represents splay as the divergence $\nabla \cdot \boldsymbol{p}$, whose hydrodynamic forcing is directed along $\boldsymbol{p}$; the second term represents bend $\boldsymbol{\nabla} \times \boldsymbol{p}$, whose hydrodynamic forcing is orthogonal to $\boldsymbol{p}$, *i.e.*, when the director is locally aligned, bend (splay) deformation occurs for director gradients parallel (perpendicular) to the alignment direction.

Both deformations have an associated elastic energy cost, which appears in the Frank free-energy equation (1.8) — note that there is no hydrodynamic force associated with a twist deformation. Active forcing is strictly at 2D phenomenon, in the sense that active flow occurs in the same plane as the deformation that caused it, and the lack of hydrodynamic forcing associated with a twist deformation we will reveal has importance consequences for the modes we can expect to observe in a 3D suspension (Chapter 3).

The active stress tensor is a coarse-grained approximation, a far-field flow approximation to the exact details near the swimmers. However, for the purposes of building intuition for the resultant flow fields when local orientational order is disturbed, we can decompose the force acting on an infinitesimal element of fluid between idealised rods to visualise the resultant net flow when orientational order is disturbed (FIGURE 2.1B). The direction of flow is proportional to the sign of activity α, and for an extensile (contractile) suspension, fluid is pumped toward (away from) the closed end of a splay deformation, and along (away from) the outward-normal of a bend deformation.

In general, gradients in the director are non-uniform, and the resultant flow hereafter referred to as *activity-driven flow*, or simply *active flow*, has an associated shear gradient, which we will refer to as *active shear*. In Section 1.2.2, we saw that the director is sensitive to shear gradients which imposed a *shear-induced torque* on the director. As seen in (2.4d), vorticity is the term driving shear-induced rotation and is directly proportional to the strength of shear. In FIGURE 2.2, we've illustrated the active flow from a bend and splay deformation, where the flow for bend (splay) is pointed along the outward-normal (closed end) of the deformation. The active units which propagate the deformation will also experience the shear-induced torque from the resulting active shear. In the case of bend in an extensile suspension, this shear-induced torque will *enhance* the original bend deformation, whereas for a splay deformation active shear will *suppress* the original splay deformation. The roles are reversed when considering a contractile suspension. Activity driven, shear-induced rotation is the primary mechanism for stability/instability in the ordered suspension and we'll see exactly how stabilising-splay and destabilising-bend fall out of the instability analysis for an extensile suspension in Section 2.3.2.

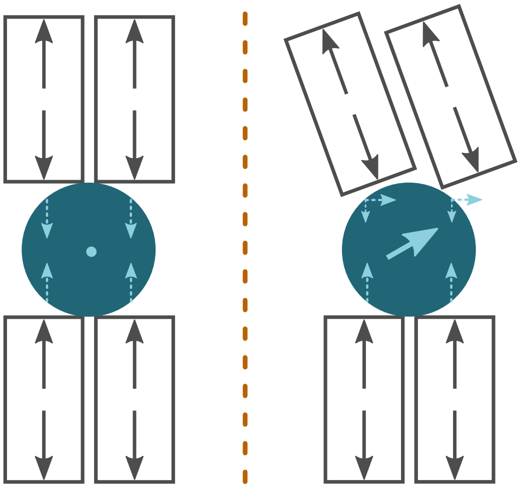

FIGURE 2.1: LEFT: A depiction of the constant equilibrium solution for a suspension of idealised rods exerting extensile forces (grey arrows) on a fluid element (dark blue circles) adjacent to rod ends. RIGHT: The net force acting on a fluid element between rows of idealised extensile dipole rods. Active forces are in grey and act on local fluid elements (blue circles). Breaking down the resulting forces on the fluid element (dashed light-blue) illustrates a net force (solid light-blue) acting along the outward-normal of director bend.

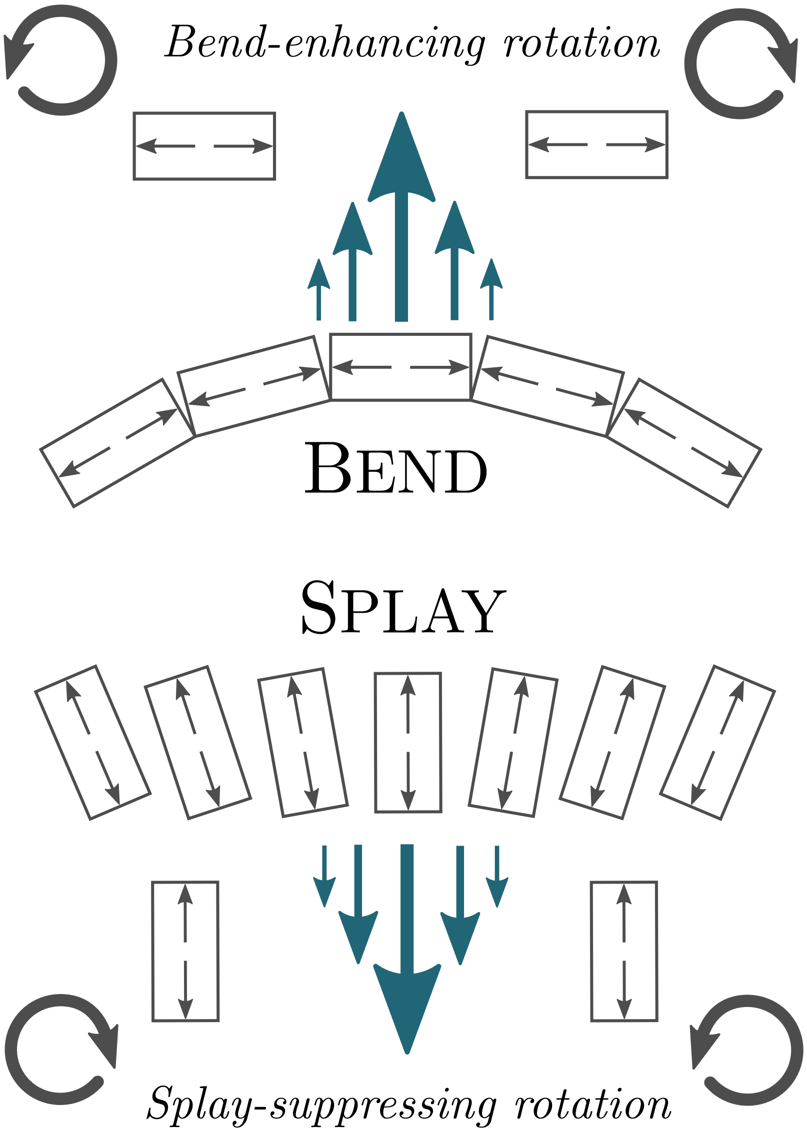

Figure 2.2: Top: Activity-induced flow enhances bend in an extensile suspension. Bottom: Activity-induced flow suppresses splay in an extensile suspension. For an extensile suspension, fluid is pumped toward the closed end of a splay deformation (outward normal of a bend deformation, respectively). The resulting activity-inducd flow has an associated shear, which induces a torque on the active units and suppresses (enhances, respectively) the original rotation. For a contractile suspension, fluid is pumped in the opposite direction for both bend and splay, and the situation is reversed (bend suppresses the deformation and splay enhances it).

2.2 Non-dimensionalisation of the Governing Equations

To quantitatively describe the instability mechanism, we will utilise a linear stability analysis on a simplified set of the governing equations derived in Section 1.2, where initially we will linearise around the constant, ordered steady-state described by equations (2.1), and in Chapter 5, we will linearise around non-constant steady-states. Summarising from Section 1.2, the full set of governing equations for an ordered suspension of active swimmers in an incompressible fluid comprises of the incompressibility condition (1.3), modified Navier-Stokes equation (1.18b), swimmer number-density evolution (1.20) and torque balance for the director (1.37), which together read,

$$\nabla \cdot \boldsymbol{u} = 0, \tag{2.3a}$$

$$\rho\Big(\frac{\partial \boldsymbol{u}}{\partial t} + (\boldsymbol{u}\cdot\nabla)\boldsymbol{u}\Big) = -\nabla P + \mu\nabla^2\boldsymbol{u} + \rho\boldsymbol{g} + \alpha\nabla\cdot\boldsymbol{pp}, \tag{2.3b}$$

$$\frac{\partial c}{\partial t} + \nabla\cdot\Big(c\boldsymbol{u} + cv_p\boldsymbol{p}\Big) = 0, \tag{2.3c}$$

$$\begin{aligned}\frac{\partial \boldsymbol{p}}{\partial t} + (\boldsymbol{u} + v_p\boldsymbol{p})\cdot\nabla\boldsymbol{p} &= \lambda_1(\boldsymbol{\delta} - \boldsymbol{pp})\cdot\boldsymbol{E}\cdot\boldsymbol{p} + \lambda_2\boldsymbol{p}\times[(\boldsymbol{\delta} - \boldsymbol{pp})\cdot\boldsymbol{E}\cdot\boldsymbol{p}] \\ &\quad - \boldsymbol{\Omega}\cdot\boldsymbol{p} + D\Big(\nabla^2\boldsymbol{p} - (\boldsymbol{p}\cdot\nabla^2\boldsymbol{p})\boldsymbol{p}\Big).\end{aligned} \tag{2.3d}$$

Equations (2.3a, 2.3b) govern the fluid flow (Section 1.2.1), where $\boldsymbol{u}$ is the fluid velocity, P the fluid pressure, α activity strength, μ is fluid viscosity, and ρ fluid density. Equations (2.3c, 2.3d) govern the swimmer suspension (Section 1.2.2) where $\boldsymbol{p}$ is a unit vector representing the average local orientation of swimmers, $\boldsymbol{E}$ the rate-of-strain tensor, $\boldsymbol{\Omega}$ the vorticity tensor and the final term is director diffusivity; alignment-to-shear is governed by λ_1, chirality (which has not yet been discussed, but is included here for completeness sake and is detailed in Chapter 3) is governed by λ_2, and D governs director elasticity, which diffuses gradients in the director throughout the suspension.

This work concerns active matter systems driven out of equilibrium by the active stress tensor, $\alpha\boldsymbol{pp}$; as such, time is scaled to balance active forcing and viscous dissipation, such that $T = \frac{\mu}{|\alpha|}$, which determines an active shear rate. Then, scaling variables as $\boldsymbol{x} = L\tilde{\boldsymbol{x}}$, $t = \frac{\mu}{|\alpha|}\tilde{t}$, $P = |\alpha|\tilde{P}$ returns the nondimensionalised equations (2.3a—2.3d) as,

$$\begin{aligned}
\tilde{\nabla} \cdot \tilde{\boldsymbol{u}} &= 0, && (2.4a)\\
\xi\Big(\frac{\partial \tilde{\boldsymbol{u}}}{\partial \tilde{t}} + (\tilde{\boldsymbol{u}} \cdot \tilde{\nabla})\tilde{\boldsymbol{u}}\Big) &= -\tilde{\nabla} P + \tilde{\nabla}^2 \tilde{\boldsymbol{u}} + \gamma \tilde{\boldsymbol{g}} + s^{\alpha} \tilde{\nabla} \cdot \boldsymbol{pp}, && (2.4b)\\
\frac{\partial \tilde{c}}{\partial \tilde{t}} + \tilde{\nabla} \cdot \Big(\tilde{c}\tilde{\boldsymbol{u}} + \vartheta \tilde{c}\boldsymbol{p}\Big) &= 0, && (2.4c)\\
\frac{\partial \boldsymbol{p}}{\partial \tilde{t}} + (\tilde{\boldsymbol{u}} + \vartheta \boldsymbol{p}) \cdot \tilde{\nabla} \boldsymbol{p} &= \lambda_1 (\boldsymbol{\delta} - \boldsymbol{pp}) \cdot \tilde{\boldsymbol{E}} \cdot \boldsymbol{p} + \lambda_2 \boldsymbol{p} \times [(\boldsymbol{\delta} - \boldsymbol{pp}) \cdot \tilde{\boldsymbol{E}} \cdot \boldsymbol{p}] && (2.4d)\\
&\quad - \tilde{\boldsymbol{\Omega}} \cdot \boldsymbol{p} + \eta^{-1}\Big(\tilde{\nabla}^2 \boldsymbol{p} - (\boldsymbol{p} \cdot \tilde{\nabla}^2 \boldsymbol{p})\boldsymbol{p}\Big),
\end{aligned}$$

where $s^{\alpha} = \operatorname{sgn}(\alpha)$, $\xi = \frac{\rho|\alpha|L^2}{\mu^2}$, $\gamma = \frac{\rho g L}{|\alpha|}$, $\eta^{-1} = \frac{D\mu}{L^2|\alpha|}$ and $\vartheta = \frac{v_p \mu}{|\alpha| L}$ are dimensionless parameters, and $\tilde{\boldsymbol{g}}$ is a unit vector describing the direction of gravitational forces. The tildes, which designate dimensionless variables, are dropped for convenience hereafter.

The characteristic length scale for the active matter instability is governed by activity which drives the system out of equilibrium, and controlled by elasticity and viscosity, which together dampen the resulting active flow. Rotational damping is governed by η^{-1}, where elasticity and swimmer drag contributions are contained in $D = \frac{K}{\zeta_r}$, where K is the one-constant Frank free-energy constant, and ζ_r is the rotational drag coefficient for the swimmer. As η governs rotational diffusivity, decreasing η corresponds to small activity, strong damping, and will stabilise the system and increasing η corresponds to strong swimmers, weak damping and will destabilise the system. Normalising η sets the length scale to $L^2 = \frac{D\mu}{|\alpha|}$, which allows us to explore length-scales where director elasticity balances activity driven shear gradients.

Parameter		**Size**
ρ,	kg/m^3	10^3
μ,	kg/ms	10^{-3}
$\lvert\alpha\rvert$,	N/m^2	10^{-2}
D,	m^2/s	10^{-10}
g,	m/s^2	10
v_p,	m/s	10^{-5}
T	s	10^{-1}
L,	m	$10^{-\frac{11}{2}}$

Term	**Size**
ξ	10^{-4}
γ	$10^{-\frac{1}{2}}$
η	1
ϑ	$10^{\frac{1}{2}}$

FIGURE 2.3: Size estimates for parameters and dimensionless numbers, summarised from Section 2.2.1.

Having set the length scale, we next consider the dimensionless parameter ξ, which now takes the form $\xi = \frac{D}{\mu_k}$, measuring the elastic damping rate to kinematic viscosity, $\mu_k = \frac{\mu}{\rho}$. By increasing the suspension elasticity D, we increase the Frank free-energy cost of maintaining a deformation in the director and decrease the deformation relaxation time which corresponds to larger instability growth rates as a deformation will disperse into the neighbouring region faster. Conversely, increasing kinematic viscosity damping will dampen active flow rates and corresponds to smaller instability growth. Confinement introduces a competing length scale on the instability, which we will consider full detail in Chapter 4, but does not introduce a competing time scale in this system. Consequently, the role of ξ is reduced to a time-scaling parameter and does not effect the instability criteria. Finally, ϑ measures the swim rate per-unit-length to active shear rate, which describes the relative strength of swimmer motility to activity-driven flows.

With the full set of dimensionless governing equations, the length and time scales set, and estimations of the parameter ranges, we can now set out the assumptions we use throughout the rest of this work. In the low-Reynolds linear limit, fluid inertia ($\boldsymbol{u} \cdot \nabla \boldsymbol{u}$) and director advection and motility ($(\boldsymbol{u} + \vartheta \boldsymbol{p}) \cdot \nabla \boldsymbol{p}$) are absent when linearising around a constant, steady-state; consequently, these terms are absent in the analytical and numerical analysis conducted in this work. Unlike the fluid velocity $\boldsymbol{u}$ and pressure P, the director takes on a non-zero value for the constant steady-state – consequently, the active stress tensor $\boldsymbol{pp}$ maintains a non-zero contribution to the governing equations and appears in the following analysis. In Chapter 5, we linearise around a non-constant steady-state, but as our interest lies in the dynamics of the instability mechanism and the role of boundary conditions, we choose to omit these terms here too. Finally, active matter instability mechanisms for varying swimmer number density is already a well-developed field, so we choose to employ a constant-concentration assumption throughout this work, but note that concentration appears heavily in the estimation of the activity parameter α.

2.2.1 Parameter Estimations

To provide a framework for discussion and understand likely regimes where we could experimentally witness the instability discussed in this work, we will need to have an order-of-magnitude estimation for the size of our terms. Since we are most interested in the dynamics of suspensions of microorganisms, in this section we will detail the calculations for four different microswimmers, *Bacillus subtilis*, *Bull sperm*, *Escherichia coli*, and *Chlamydomonas reinhardtii*, which lead to our default parameter values used throughout this work.

Recall that the activity parameter is defined by $\alpha = -f\hat{d}\Phi/V_c$ for force dipole strength f, where $f > 0$ ($f < 0$) indicates a pusher (puller) swimmer, average dipole length is given by $\hat{d}$, Φ is the particle volume fraction and V_c the cell volume; note that concentration has been substituted for $c = \Phi/V_c$. We consider microswimmers to be force-free, such that they obey,

$$F_{thrust} + F_{drag} = 0. \tag{2.5}$$

The drag acting on a swimmer is proportional to its self-propulsion velocity v_p, and the translational drag coefficient ζ_h, such that $F_{drag} = v_p\zeta_h$. The drag coefficient for a sphere is the well known 'Stokes drag', $\zeta_h = 6\pi\mu r$ for a sphere of radius r. However, we prefer to use a more refined drag coefficient suitable for rods and elongated ellipsoids translating along their orientation axis $\boldsymbol{\nu}$,[41]

Organism	**Radius,** μm	**Length,** μm	**Flagella,** μm	**Vol.,** fL	**Speed,** μm/s	**Ref.***
B. subtilis *Pusher,* *rod-like*	0.35 - 0.7	4 - 10	7.5 - 12	0.9 - 4.6	15 - 25	B-100211 B-100212 B-114921 B-114922 [41,63–67]
Bull sperm *pusher,* *disk-like*	2 - 2.7 0.4**	8.2 - 10.2	61.6	10.5 - 12	110 - 200	B-106855 [68–71]
C. reinhardtii *puller,* *ellipsoidal*	1.5 - 2	5 - 10	9.2 - 12.8	95 - 270	80 - 110	B-110530 [72–76]
E. coli *pusher,* *rod-like*	0.25 - 0.5	1.9 - 2.7	5 - 10	0.9 - 1.1	15 - 25	B-100095 B-101788 B-114924 [65]

Table 2.1: A range of parameter estimations for various swimmer microorganisms, where the data range represents typical values found in literature. *References beginning with B- refer to Bionumbers entries.[77] **Thickness of Bull sperm.

$$\zeta_h = \frac{2\pi\mu l_b}{\log\left(\frac{l_b}{2r_b}\right) + c_h}, \tag{2.6}$$

where l is the body length, r the body radius and c_h is a constant of order 1. Meaningful order-of-magnitude estimations for microswimmer parameters were obtained through existing literature on experiments of prolate, ellipsoidal swimming microorganisms which can all be categorised as either pusher or puller swimmers: this data is collated in Table 2.1, giving an appropriate range of values for swimmer dimensions.

The data was selected by considering a range of reported experiments and omitting outlier results. By taking an appropriate median of these values (Table 2.2) the force dipole strength and volume-fraction independent activity are calculated, using an estimation for the dipole length. Theoretically, the volume-fraction of swimmers in a suspension is itself a function of swimmer geometry, nutrient availability or swimmer motility,[78] amongst many other factors. For an order-of-magnitude estimation, we drew swimmer number density values from experiments corresponding to our exemplar microswimmers and made estimations for the activity parameter at $\Phi = 0.01$ and $\Phi = 0.2$ (TABLE 2.3). This gives a range the activity parameter as $\alpha \in [0.0011, 0.43]$.

The lower bound agrees well with literature estimations on the activity parameter, which suggest a range of $\alpha \in [0.002, 0.036]$.[79–81] However, the upper bound for our activity parameter is likely inflated due to the way we have estimated the dipole length. The dipole length is estimated as half the distance between the centre of drag and centre of thrust - these are the cell body midpoint and flagellum midpoint respectively. The actual centre of drag will be shifted toward the flagellum due to its drag contribution. For swimmers with short flagellum, this correction will be negligible; however, bull sperm flagella length are six-fold their body length, so this contribution is likely no longer negligible. Furthermore, the flagella length given is the total length, whereas the displacement between the centre of thrust and cell body will be significantly smaller due to the sinusoidal and helical motion which the flagellum undergoes. With these considerations in mind, we state an order of magnitude range for activity as $\alpha \in [0.001, 0.1]\mathrm{N/m}^2$.

Similarly, we wish to provide an order of magnitude estimation for $D = K/\zeta_r$, where $\zeta_r = \mu l_b^2 \Phi / 8 r_b^2$ is the rotational drag coefficient for a microswimmer generalised to the suspension (1.24). The Frank free energy constant K has the dimensions of $[\textit{energy density}] \cdot l_b^2$, for a swimmer length scale l_b. For active swimmers, an appropriate energy scale can be derived from $\epsilon \sim \zeta_h M_d$,[41] where M_d is the diffusion constant for swimming bacteria, which takes a value of approximately $10^{-11}\mathrm{m}^2/\mathrm{s}$ (B-100295,[15]), and is an appropriate order-of-magnitude estimation for all example microswimmers. Then, $K = \epsilon l_b^2 \zeta_r$ can be evaluated as,

$$K = c_p \epsilon \Phi^2 l_b^2 r_b^{-3}, \tag{2.7}$$

where c_p is a constant of proportionality of order-of-magnitude $\sim \mathcal{O}(10^{-2})$. The parameter estimations for our chosen exemplar microswimmers are recorded in TABLE 2.4. Note the strong volume-fraction dependence, which is a consequence of Φ^2 appearing in K. TABLE 2.4 gives an order-of-magnitude range for the suspension rotation parameter as $D \in [10 - 10^3]\mu\text{m}^2/\text{s}$. The Bretherton constant λ_1 depends only on the shape of the particle. For an ellipsoid with ratio e, it can be approximated as $\lambda_1 \approx = \frac{e^2-1}{e^2+1}$, which for our exemplar swimmers yields $\lambda_1 \in [0.60, 0.93]$ for elongated particles with an aspect ratio of $e \in [2, 5]$. The calculation for the chirality constant λ_2 is more involved, and is discussed further in Chapter 3. These values inform the parameters quoted in FIGURE 2.3 and our default value parameter set of $\eta^{-1} = 1.2$, $\xi = 1.1$, $\lambda_1 = 0.7$, $\lambda_2 = 0.1$ (Chapter 3 onwards), $\gamma = 1$ (Chapter 5 onwards).

Organism	r_b, μm	l_b, μm	l_f, μm	V_b*, fL	v_p, μm/s
B. subtilis	0.4	7	10	3.5	20
Bull sperm	2 (0.4**)	8	60	27	150
C. reinhardtii	1.8	9	10	110	100
E. coli	0.4	2	8	1	20

TABLE 2.2: Values for swimmer dimensions chosen on basis of data weighting in TABLE 2.1. *Calculated. **Thickness of Bull sperm head.

Organism	f_d, pN	l_d, μm	α/Φ, N/m^2	$\alpha_{0.01}$ N/m^2	$\alpha_{0.2}$ N/m^2
B. subtilis	0.34	3	-0.29	-0.0029	-0.059
Bull sperm	6.1	9.5	-2.2	-0.022	-0.43
C. reinhardtii	4	3.5	0.11	0.0011	0.023
E. coli	0.17	1.5	-2.7	-0.0023	-0.053

TABLE 2.3: Swimmer dipole strength, dipole length and activity calculations based on swimmer dimensions given in TABLE 2.2

Organism	$K\|_{\Phi=0.01}$ pN	$K\|_{\Phi=0.2}$ pN	$K/\zeta_{sr}\|_{\Phi=0.01}$ μm^2/s	$K/\zeta_{sr}\|_{\Phi=0.2}$ μm^2/s
B. subtilis	1.8e-2	7.4	41	810
Bull sperm	2.3e-4	9.2e-2	9.8	190
C. reinhardtii	4.5e-4	1.8e-2	12	240
E. coli	4.5e-4	1.8e-2	12	240

TABLE 2.4: The Frank elasticity and suspension rotational terms for swimmers. NB: The elasticity is a function of the ratio l_b/r_b, for which *C. reinhardtii* and *E. coli* have the same ratio, and hence identical values.

2.3 Quantitative Description

2.3.1 Calculations for the 2D Bulk Analysis

In this work, we are interested in understanding the way activity-driven mechanical stresses in an active matter suspension drive the ordered state out of equilibrium. From the set of governing equations given by (2.4), we choose to explore densely-populated suspensions with small variations in swimmer number-density (such that (2.4c) = 0), and assume that motility effects, governed by ϑ, are negligible compared to activity-driven flows. By linearisation about a constant, steady-state both $\boldsymbol{u}\cdot\nabla\boldsymbol{u}$, $(\boldsymbol{u}+\vartheta\boldsymbol{p})\cdot\nabla\boldsymbol{p}$ and $(\boldsymbol{p}\cdot\nabla^2\boldsymbol{p})\boldsymbol{p}$ from equations (2.4b) and (2.4d) vanish. Finally, until Chapter 3 where we extend our analysis into the 3D regime, we must also set $\lambda_2 = 0$. This returns the simplified governing equations, consisting of modified Stokes equation, generalised Jeffrey orbit equation, incompressibility, and the unit vector constraint on the director $\boldsymbol{p}$, such that:

$$\xi\partial_t\boldsymbol{u} = -\nabla P + \nabla^2\boldsymbol{u} + s^\alpha\nabla\cdot\boldsymbol{pp}, \tag{2.8a}$$

$$\partial_t\boldsymbol{p} = \lambda_1(\boldsymbol{\delta}-\boldsymbol{pp})\cdot\boldsymbol{E}\cdot\boldsymbol{p} - \boldsymbol{\Omega}\cdot\boldsymbol{p} + \eta^{-1}\nabla^2\boldsymbol{p}, \tag{2.8b}$$

$$\nabla\cdot\boldsymbol{u} = 0, \tag{2.8c}$$

$$|\boldsymbol{p}| = 1. \tag{2.8d}$$

Here, the director is expressed as $\boldsymbol{p} = (\cos\phi,\ 0,\ \sin\phi)$, where ϕ is the azimuthal angle in the x-z plane, measured anti-clockwise from the positive x-axis and which causes $\boldsymbol{p}$ to satisfy the normalisation criteria $|\boldsymbol{p}| = 1$. The coordinate system for the 2D regime is the same as the 3D regime, with rotation into the y-axis suppressed.(FIGURE 2.4, with $\theta = 0$). The coordinate system is chosen to emphasis that $\boldsymbol{p}$ can vary from alignment along the x-axis in either the y- or z-axis, which will prove the natural choice when considering the 3D regime and confinement in Chapters 3 and 4. Equations (2.8a—2.8d) satisfy the steady state,

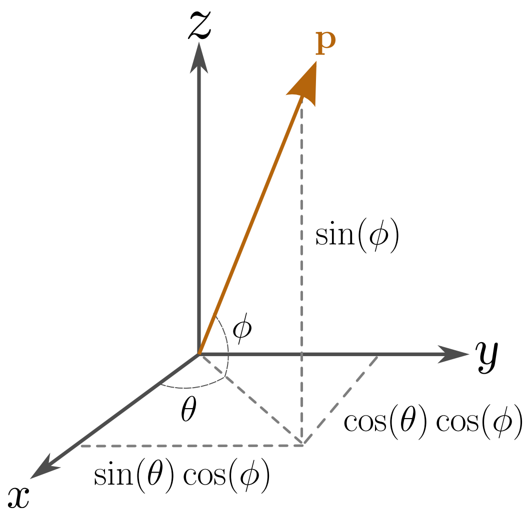

FIGURE 2.4: Coordinate system for the director $\boldsymbol{p} = (\cos\theta\cos\phi,\ \sin\theta\cos\phi,\ \sin\phi)$ as a 3D unit vector.

$$\bar{\boldsymbol{u}} = \boldsymbol{0}, \qquad \bar{P} = P_A, \qquad \bar{\phi} = 0, \qquad \bar{\boldsymbol{p}} = \hat{\boldsymbol{x}}.$$

Here, pressure is defined up to a constant P_A. Since the hydrodynamic force associated with splay and bend deformations propagates in-plane to the director, an initial analysis in the x-z plane suffices to capture the fundamental dynamics. The base state is perturbed as,

$$\boldsymbol{u} = \bar{\boldsymbol{u}} + \varepsilon(\partial_z\psi\hat{\boldsymbol{x}} - \partial_x\psi\hat{\boldsymbol{z}}), \qquad P = \bar{P} + \varepsilon P, \qquad \boldsymbol{p} = \bar{\boldsymbol{p}} + \varepsilon\phi\hat{\boldsymbol{z}}.$$

Here, ψ is the 2D stream function satisfying incompressibility such that $u_x = \partial_z\psi$, $u_z = -\partial_x\psi$ and $\varepsilon \ll 1$ is the perturbation parameter. Then, the active stress tensor and its divergence read,

$$
\boldsymbol{pp} = \begin{pmatrix} 1 & 0 & \varepsilon\phi \\ 0 & 0 & 0 \\ \varepsilon\phi & 0 & 0 \end{pmatrix}, \qquad \nabla \cdot \boldsymbol{pp} = \varepsilon \begin{pmatrix} \partial_z\phi \\ 0 \\ \partial_x\phi \end{pmatrix},
$$

where only terms to order ε have been retained. Comparison to the splay $(\nabla \cdot \boldsymbol{p})\boldsymbol{p}$ and bend $(\nabla \times \boldsymbol{p}) \times \boldsymbol{p}$ terms, reveals $\alpha\partial_z\phi\hat{\boldsymbol{x}}$ as the splay perturbation force parallel to the director, and $\alpha\partial_x\phi\hat{\boldsymbol{z}}$ as the bend perturbation force which is orthogonal to the director. Substitution into (2.8a) gives in first order ε,

$$
\xi\partial_t\partial_z\psi = -\partial_x P + [\partial_x^2 + \partial_z^2]\partial_z\psi + s^\alpha\partial_z\phi, \tag{2.9a}
$$

$$
-\xi\partial_t\partial_x\psi = -\partial_z P - [\partial_x^2 + \partial_z^2]\partial_x\psi + s^\alpha\partial_x\phi. \tag{2.9b}
$$

Square brackets designate a differential operator, acting on terms to its right. Cross-differentiating and equating (2.9a) and (2.9b) gives

$$
\xi[\partial_x^2 + \partial_z^2]\partial_t\psi - [\partial_x^2 + \partial_z^2]^2\psi + s^\alpha[\partial_x^2 - \partial_z^2]\phi = 0. \tag{2.10}
$$

For the director equation, the tensor $\boldsymbol{\delta} - \boldsymbol{pp}$ takes the form,

$$
\boldsymbol{\delta} - \boldsymbol{pp} = \begin{pmatrix} 0 & 0 & -\varepsilon\phi \\ 0 & 1 & 0 \\ -\varepsilon\phi & 0 & 1 \end{pmatrix},
$$

and the rate-of-strain and vorticity tensors take the form,

$$\boldsymbol{E}\cdot\boldsymbol{p} = \begin{pmatrix} E_{xx} \\ E_{yx} \\ E_{zx} \end{pmatrix}, \qquad \boldsymbol{\Omega}\cdot\boldsymbol{p} = \begin{pmatrix} 0 \\ \Omega_{yx} \\ \Omega_{zx} \end{pmatrix}$$

Note that here the rate-of-strain and vorticity tensor are of order ε. Then in the z-axis and for order ε only, the director equation reads

$$\begin{aligned} \partial_t \phi &= \lambda_1 E_{zx} - \Omega_{zx} + \eta^{-1}\nabla^2\phi, \\ &= [\lambda_1^{-}\partial_z^2 - \lambda_1^{+}\partial_x^2]\psi + \eta^{-1}[\partial_x^2 + \partial_z^2]\phi, \end{aligned} \tag{2.11}$$

where $\lambda_1^{\pm} = \frac{1}{2}(\lambda_1 \pm 1)$. Equations (2.10) and (2.11) describe the spatial-temporal evolution of a perturbation to the steady state and we choose to seek solutions as Fourier modes of the form,

$$\psi = \psi_k \exp(i\boldsymbol{k}\cdot\boldsymbol{x} - i\omega t), \qquad \phi = \phi_k \exp(i\boldsymbol{k}\cdot\boldsymbol{x} - i\omega t),$$

where ψ_k, ϕ_k are constants describing the perturbation amplitude, $\boldsymbol{k}$ is the 2D wave-vector describing perturbation orientation in space and $\omega(k)$ as a function of k is the wave-frequency. Following substitution of Fourier modes into (2.10) and (2.11) gives,

$$0 = \xi\omega|\boldsymbol{k}|^2\psi_k i - |\boldsymbol{k}|^4\psi_k + s^{\alpha}(k_z^2 - k_x^2)\phi_k, \tag{2.12}$$

$$i\omega\phi_k = \psi_k(\lambda_1^{+}k_x^2 - \lambda_1^{-}k_z^2) + \eta^{-1}|\boldsymbol{k}|^2\phi_k, \tag{2.13}$$

substitution of (2.13) into (2.12) returns a quadratic equation in ω,

$$\xi\omega^2|\boldsymbol{k}|^2 + i\omega|\boldsymbol{k}|^4(1+\xi\eta^{-1}) - \eta^{-1}|\boldsymbol{k}|^6 - s^\alpha(k_x^2 - k_z^2)(\lambda_1^+ k_x^2 - \lambda_1^- k_z^2) = 0. \tag{2.14}$$

Finally, solving equation (2.14) for the wave frequency ω yields the equation,

$$\omega^\pm = -\frac{i|\boldsymbol{k}|^2(1+\xi\eta^{-1})}{2\xi} \pm \frac{i|\boldsymbol{k}|^2}{2\xi}\sqrt{(1-\xi\eta^{-1})^2 - 4|\boldsymbol{k}|^{-6}\xi s^\alpha(k_x^2-k_z^2)(\lambda_1^+ k_x^2 - \lambda_1^- k_z^2)},$$

and rewriting the wave-number as $\boldsymbol{k} = k(\cos q,\ 0,\ \sin q)$ simplifies the equation to,

$$\omega^\pm = \frac{ik^2}{2\xi}\Big(-(1+\xi\eta^{-1}) \pm \sqrt{(1-\xi\eta^{-1})^2 - 2k^{-2}\xi s^\alpha \cos 2q(1+\lambda_1\cos 2q)}\,\Big) \tag{2.15}$$

2.3.2 Stability of Bend and Splay Modes

Equation (2.15) is known as a ‘dispersion relation’ and determines the wave-frequency from a given wave-number. The solutions $\omega^\pm$ are eigenvalues of the system and their associated eigenvectors describe the possible modes of propagation a perturbation can take. Expressing the complex wave frequency as $\omega = \omega_r + i\omega_i$ allows us to rewrite a Fourier mode as,

$$f_k \exp(\omega_i t)\exp(i\boldsymbol{k}\cdot\boldsymbol{x} - i\omega_r t),$$

which yields a time-dependent perturbation amplitude as $f_k\exp(i\omega_i t)$. From henceforth, any discussion related to the growth of the perturbed nodes directly corresponds to the magnitude and sign of $\omega_i^\pm$, and the stability of the perturbation reduces to the sign of $\omega_i^\pm$, where $\omega_i^\pm < 0$ ($\omega_i^\pm > 0$) yields stable (unstable) modes. In Figure 2.5, we plot the growth rate $\omega_i^\pm$ and wave speed $\omega_r^\pm$ for both roots against the non-dimensional wavenumber $k \in [0,1]$ and $q = 0$, which shows that (2.15) yields a stable (ω^-) and unstable (ω^+) mode. The system length scale is set to balance activity driven shear to rotational torque, and so both modes increase in stability as $k \to 1$, as rotational damping which acts at $\mathcal{O}(k^2)$ will suppresses any growth of the modes, driven by activity of order $\mathcal{O}(k)$. Investigating the unstable mode ω^+, note that the first term of (2.15) can be written,

$$-i\frac{k^2}{2}(\xi^{-1} + \eta^{-1}). \tag{2.16}$$

Both terms are stabilising, damping terms, arising from viscosity dampening (equation (2.8a)) and elastic dampening (equation (2.8b)) as the ratio of the terms,

$$\xi^{-1}\frac{\nabla^2 \boldsymbol{u}}{\partial_t \boldsymbol{u}} = \frac{\textit{Viscous dissipation}}{\textit{Linear inertia}}, \qquad \eta^{-1}\frac{\nabla^2 \boldsymbol{p}}{\partial_t \boldsymbol{p}} = \frac{\textit{Director elasticity}}{\textit{Rotational inertia}}.$$

Expression (2.16) tells us that viscosity and elasticity damping act independently from each other, and from activity, to stabilise a perturbation. Activity driving terms are restricted to the discriminant, which reads

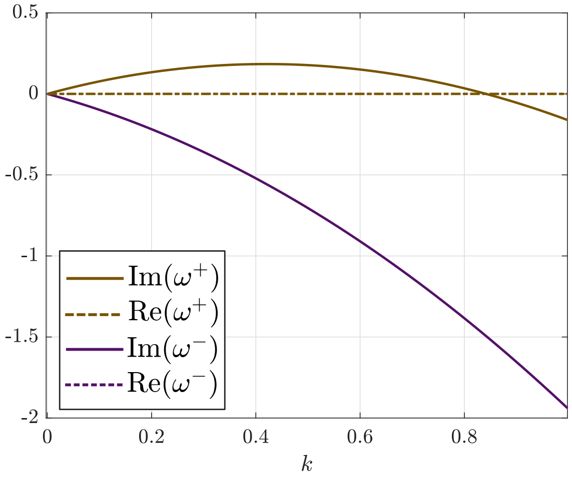

FIGURE 2.5: The dispersion relation of the fundamental active matter instability for an extensile suspension given by equation (2.15), and the default parameter set $\xi = 1.2$, $\eta^{-1} = 1.1$, $\lambda_1 = 0.7$, $s^\alpha = -1$. The imaginary part of ω is solid and the real imaginary part is dashed; the positive, unstable root is yellow, the negative, stable root is purple. Note that real part of both roots is identically zero.

$$\frac{ik^2}{2}\sqrt{(\xi^{-1}-\eta^{-1})^2 - 2k^{-2}\xi^{-1}s^{\alpha}\cos 2q(1+\lambda_1\cos 2q)} \tag{2.17}$$

The first term in the square root is of the same form as the damping terms in (2.16) and determines a minimum level of active forcing required for the instability to propagate. The second term is a product of the active stress and flow alignment terms—it is this term which drives an active matter system out of equilibrium. In the limiting case of $\eta^{-1} \to 0$, the instability associated with eigenvalue ω^{+} becomes instability condition reads,

$$-s^{\alpha}\xi\cos 2q(1+\lambda_1\cos 2q) > 0. \tag{2.18}$$

The instability condition for the dispersion relation (2.15) reveals how active shear gradients, determined by fluid vorticity and rate-of-strain, govern the instability growth rate. The vorticity term $\boldsymbol{\Omega}\cdot\boldsymbol{p}$ in the governing equations yields a $-s^{\alpha}\xi\cos 2q$ contribution to the instability condition, and acts independently of the swimmer geometry, where the parameter governing the perturbation growth/decay rate is determined by $\xi = \frac{D}{\mu_k}$ and the sign of activity s^{α}. Swimmer alignment to shear, governed

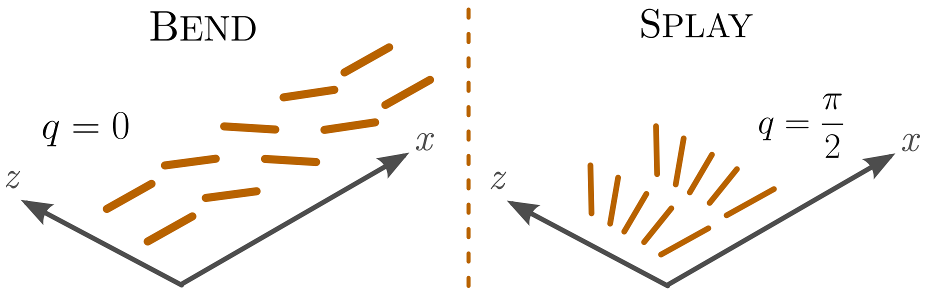

FIGURE 2.6: The direction of gradients in the director (orange rods) correspond to the wavevector angle q. Consequently, a pure bend perturbation (left) is associated with wavevector angle $q = 0$, whereas a pure splay perturbation (right) is associated with wavector angle $q = \pi/2$.

by $(\boldsymbol{\delta} - \boldsymbol{pp}) \cdot \boldsymbol{E} \cdot \boldsymbol{p}$, yields a $-s^\alpha \xi \lambda_1 \cos^2 2q$ contribution to the instability condition. Note that without the presence of background shear, rotational effects governed by vorticity and alignment-to-shear mutually enhance/suppress a perturbation.

Both terms are independent from the wavevector amplitude k, and (2.15) predicts that the stability of a disturbance depends solely on relative of the perturbation to the local ordering direction. For a perturbation angle $q \in [0, \pi/2]$, note that $\cos 2q(1 + \lambda_1 \cos 2q)$ has only one root at $q = \pi/4$. As we've not included any polar or motile stresses, we do not need to include wavevector angles of $q > \pi/2$. Since $\lambda_1 > 0$ and $\xi > 0$, only s^α can also contribute a sign change and the inequality is satisfied for a pusher (puller) with $q \in [0, \pi/4)$ ($q \in (\pi/4, \pi/2]$, respectively). As we've sought planar-wave solutions to the perturbed equations, spatial gradients in the director are entirely determined by our choice of the wavevector $\boldsymbol{k} = (\cos q,\ 0,\ \sin q)$. Equation (2.15) then reveals that extensile suspensions are unstable to bend-dominated perturbations ($q \in [0, \pi/4)$, FIGURE 2.6A), whereas contractile suspensions are unstable to splay-dominated perturbations ($q \in [\pi/4, \pi/2]$, FIGURE 2.6B).

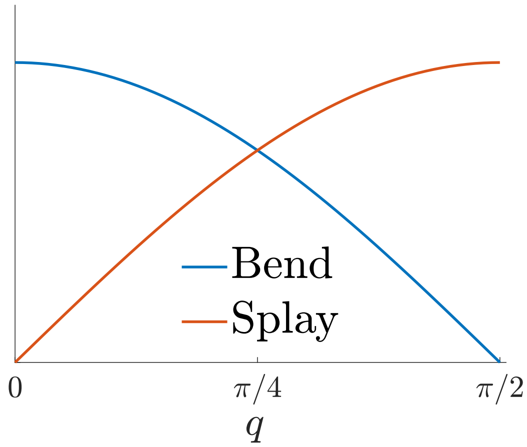

FIGURE 2.7: The hydrodynamic forcing due to activity as a function of q for an extensile suspension. For $q < \frac{\pi}{4}$, bend is the dominant mode of hydrodynamic forcing in the system. At $q = \frac{\pi}{4}$, the splay becomes the dominant hydrodynamic forcing, indicative of a possible bifurcation.

2.3.2.1 Hydrodynamic Forcing due to Activity

When seeking planar-wave solutions to the linear stability problem, gradients in the director correspond to the disturbance wavevector angle q. Bend is introduced into the system when a component of the director gradients are parallel to the ordered axis, and a pure bend mode corresponds to $q = 0$. Conversely, splay is introduced when a component of the director gradients are perpendicular to the ordered axis and a pure splay mode corresponds to $q = \pi/2$, illustrated in FIGURE 2.6. In the governing equation for the fluid, activity forcing is proportional to the divergence of the stress tensor, $\nabla \cdot \boldsymbol{pp}$. When seeking planar-wave solutions, these gradients are prescribed by the wavevector amplitude k and the waveangle q such that activity induced hydrodynamic pumping due to bend and splay deformations are $ik\cos q$ and $ik\sin q$ respectively. Increasing q from 0 to $\pi/2$ corresponds to decreasing bend and increasing splay forcing in the fluid (FIGURE 2.7).

At $q = \pi/4$, we see a switch from bend being the dominant hydrodynamic forcing to splay being dominant. Mechanically, the criterion for instability (equation (2.18)) on q corresponds to extensile suspensions being unstable to bend perturbations and contractile suspensions being unstable to splay perturbations, which corresponds to our quantitative analysis (Section 2.1, FIGURE 2.2) and is known in literature. Without elasticity or viscous damping, (2.18) tells us that an extensile active matter suspension is unconditionally unstable for $q < \pi/4$ — *i.e.*, the system will admit an unstable solution for any value of k. The dependence on the wavevector angle, as opposed to its amplitude, will have interesting consequences when we consider the 3D regime in Chapter 3 and when confinement is introduced in Chapter 4. Including elasticity back into ω yields,

$$k^2 < -s^\alpha \frac{\cos 2q(1 + \lambda_1 \cos 2q)}{2\eta}. \tag{2.19}$$

The instability condition (2.19) determines an upper bound on k for which we have instability. For an extensile suspension, $s^\alpha = -1$, and the maximal growth rate is associated with a pure bend deformation $q = 0$. In this limiting case, the instability condition reduces to,

$$k^2 < \frac{1 + \lambda_1}{2\eta}. \tag{2.20}$$

Equation (2.20) tells us a swimmer suspension is always unstable to long-wavelength perturbations, provided k meets an upper boundary set by rotational damping, η^{-1}. The dimensionless parameter $\xi = \frac{\rho D}{\mu}$ does not contain an activity term and is absent from the instability condition as it only controls the rate-of-propagation; ξ is effectively a time-scaling parameter in the problem. Physically, this corresponds to the fact that viscous damping only acts on fluid elements that are moving — a fluid by definition cannot sustain any deformation, but the rate-of-strain is controlled by the fluid viscosity parameter μ. Conversely, director elasticity acts *at all times*, irrespective of the motility of its elements, and determines a length scale for which orientational gradients (and thereby active shear) is governed. However, the role of ξ should be reconsidered in any environment where competing time scales are present.

Shear gradients are the primary coupling mechanism between the hydrodynamics and director dynamics, and the instability condition (2.20) represents a torque balance between flow alignment terms and elastic damping, which can be seen directly from (2.13) with $k_z = 0$. Vorticity and alignment-to-shear enter the instability condition as $1/2$ and $\lambda_1/2$ respectively, where explicit dependence on the magnitude of local shear vanishes by consequence of setting our length scale to balance activity-driven shear and viscous damping. The vorticity term in (2.3d) has no parameter acting on it, so can be said to act numerically at order $\mathcal{O}(1)$ to destabilize the suspension, whereas the parameter governing alignment to shear can take values in the range $\lambda_1 \in [0, 1)$, meaning shear alignment effects are always smaller than vorticity effects. For a bend deformation, active flow pumps fluid perpendicular to bend deformation, and consequently alignment to shear effects will rotate the director away from the the ordered axis. In the instability criteria, this dictates that for close-to-spherical swimmers alignment to shear will have a minimal effect on the growth rate of a disturbance, for elongated rods, shear alignment effects initially act at the same strength as vorticity, but outside a linear instability analysis will have diminishing returns as the director becomes aligned with local shear.

2.3.3 Eigenmodes for Unstable Eigenvalue ω^+

To further understand the bend-splay instability mechanism for an extensile suspension, we consider the eigenvectors associated to the unstable eigenvalue ω^+. FIGURE 2.8 plots u_k, w_k, and ϕ_k over $q \in [0, \pi/2]$ for k^m, the maximum wavevector amplitude for each $q \in [0, \pi/2]$, and normalised to $\phi_k = 1$. A bend (splay) deformation is associated with hydrodynamic pumping perpendicular (parallel) to the alignment direction, which is quantified by $u_k = 0$ and nonzero w_k at $q = 0$. At $q = \pi/4$, the eigenmodes undergo a bifurcation, indicated by the change in phase between the director and the fluid.

In FIGURE 2.9, we fully detail the relationship between the director phase, active flow, active shear, and rotation due to shear. In brief, when $q = 0$, the system admits a pure bend deformation in the director and when seeking planar-wave solutions to

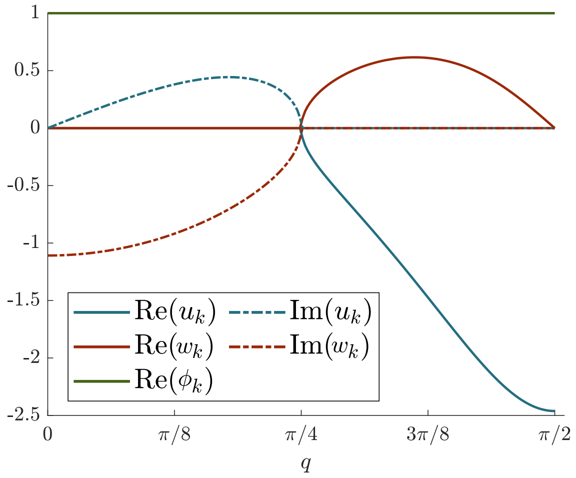

FIGURE 2.8: The eigenvectors associated with ω^+ from (2.15) over $q \in [0, \pi/2]$, normalised to $\phi_k = 1$ and evaluated at the wavevector $k = k^m$, where k^m is the wavevector associated with $\max(\omega_i^+(\boldsymbol{k}))$.

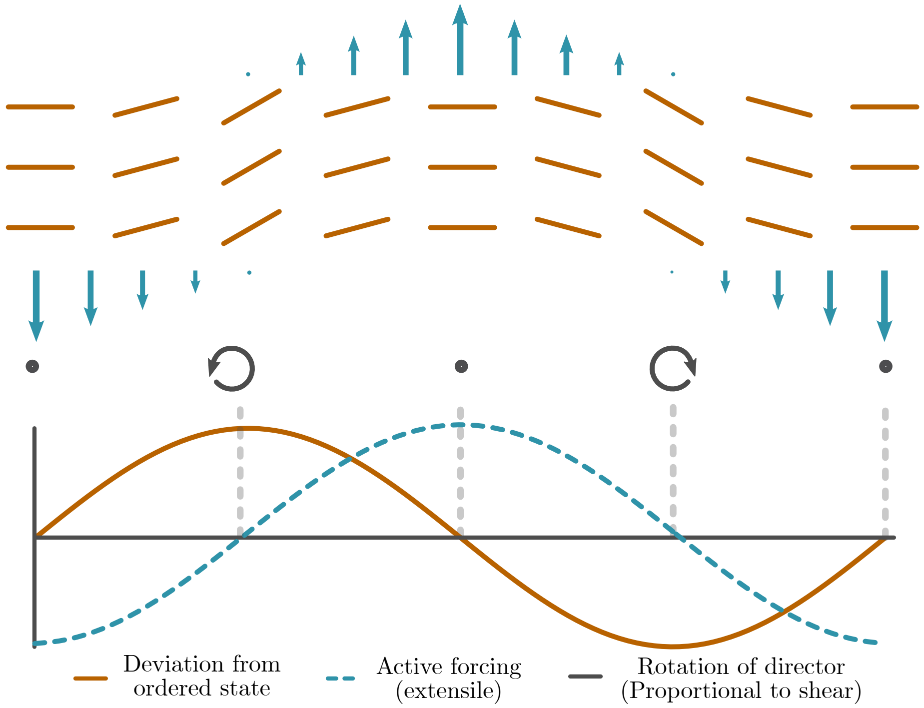

FIGURE 2.9: When seeking planar-wave solutions to perturbations of the ordered state (*orange rods, illustration*), the maximum deviation of the director (measured in the main text by ϕ) from the ordered state (*orange line, graph*) occurs at the peaks and troughs of the planar-wave solution. However, bend is proportional to the gradient of the director, at a maximum at the nodes of the planar-wave. Since activity is proportional to gradients in the director, active forcing (*light blue arrows, illustration*) has its maximum at the nodes of the planar-wave solution to the director, and so has a $\pi/2$ phase difference with the maximum deviation of the director (*light blue dashed, graph).* Note that the direction of forcing shown here is for an extensile suspension; a contractile suspension will cause an active forcing on the fluid in the other direction. The corresponding active flow, which is proportional to forcing and which is perpendicular to the ordered direction creates shear gradients which are at a maximum in-phase with the phase of ϕ. Since shear rotational effects on the director are proportional to shear gradients in the fluid, the maximum rotation of the director (*grey arrows, illustration*) occurs at the peaks and troughs of the planar-wave solution and for an extensile suspension enhance deviation from the ordered state, creating an instability.

the active matter suspension, bend — which is proportional to director gradients — is at a maximum at the nodes of a sinusoidal wave, not at its peaks and troughs. Consequently, activity driven flow will be $\pm\pi/2$ out-of-phase with the director, depending on the sign of activity. However, rotational effects are proportional to the active shear gradient, which is itself $\pi/2$ out-of-phase with active flow. For a bend deformation and an extensile suspension, shear rotation is in-phase with the original director deformation, meaning a perturbation to the director field will be enhanced by its own active flow. For a splay deformation and an extensile suspension, shear rotation is out-of-phase with the original deformation, meaning a perturbation to the director field will be suppressed by its own active flow.

The eigenvalues ω^{+} and ω^{-} correspond to regimes of phase: for ω^{+}, the director and fluid velocity modes have a phase difference of $\pi/2$, hydrodynamic pumping and rotation due to shear complement one another, causing an instability in the active matter suspension, as long as director elasticity is sufficiently small; for ω^{-}, the director and fluid velocity modes have a phase difference of $-\pi/2$ and active flow will suppress the fluid velocity perturbation, stabilising the perturbation. The eigenmodes corresponding to ω^{+} are graphed in Figure 2.10 where the vectorfield over the perturbation wavelength *i.*, select vectorfield over $\boldsymbol{k}\cdot\boldsymbol{x}$ *ii.*, and the phase relationship between the fluid and the director *iii.* are plotted for the unstable eigenvalue ω^{+} and wavevector angles (a) $q = 0$, (b) $q < \pi/4$ and (c) $q > \pi/4$. In Figure 2.10a the vectorfields corresponding to the unstable eigenvalue ω^{+} are plotted where the out-of-phase relationship between the director and the velocity field can more clearly be seen. As the perturbation angle q is increased from zero, splay increases in the system, inducing hydrodynamic pumping toward the closed end of the splay. Bend remains the dominant deformation but evidence of increasing splay can be seen in the flow fields (Figure 2.10b *i.*). As q increases further it crosses the critical value $q^{c} = \pi/4$ for which bend and splay pump the fluid in equal amounts. Above $\pi/4$, (Figure 2.10c) splay becomes the dominant mechanism for fluid forcing and the system undergoes a bifurcation as fluid is now pumped along $\boldsymbol{p}$ as opposed to perpendicular to it. When splay is dominant, the eigenmode $\boldsymbol{u}_k$ is in-phase with

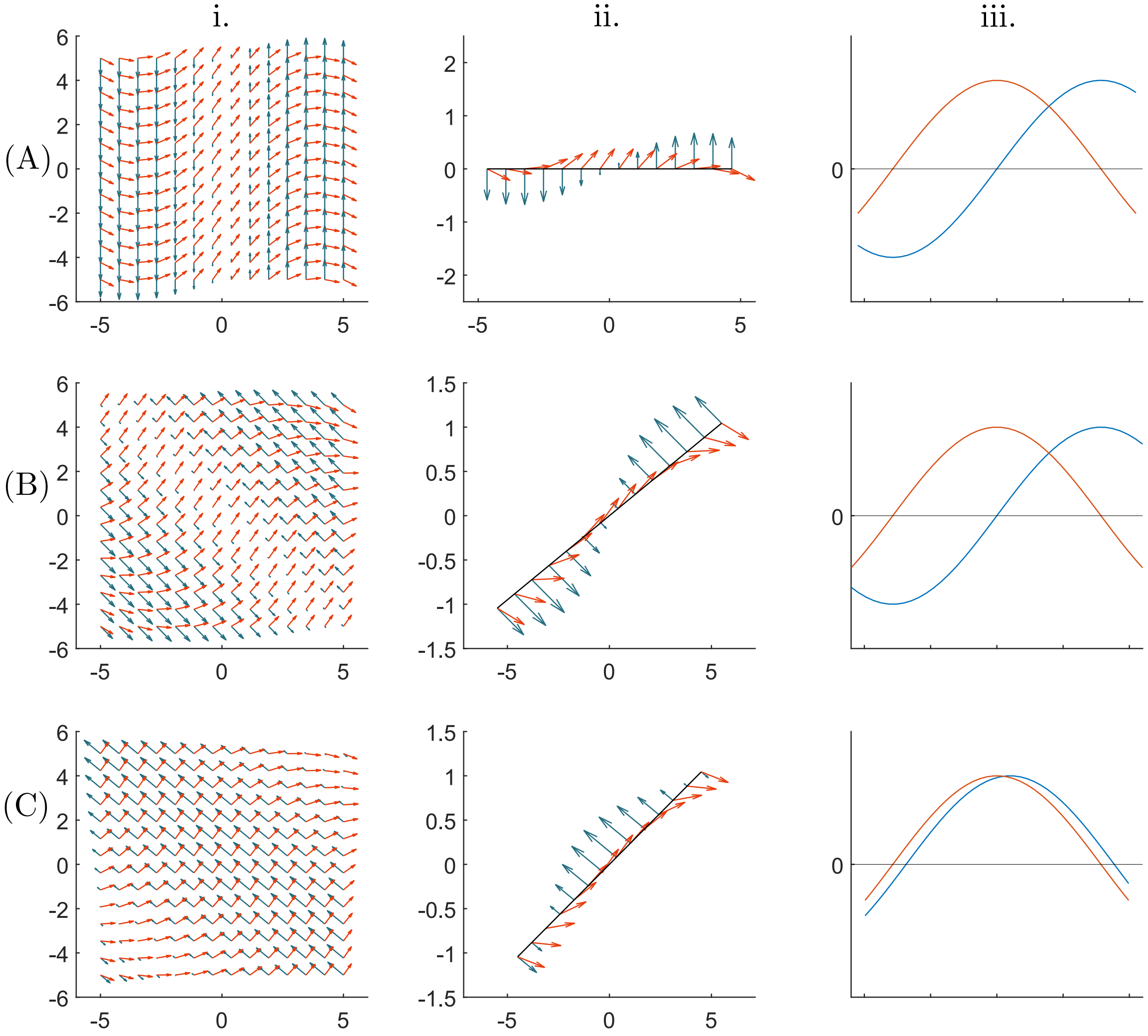

FIGURE 2.10: Snapshot of the flow field (blue) and director field (red) for modes associated with ω^+ in a 2D system, cases correspond to: (A) $q = 0$, (B) q just below $\pi/4$, (C) just above $\pi/4$. *i.* Vector field plot of instantaneous fluid flow and director field, *ii.* vector field plot over one wavelength of $\boldsymbol{k} \cdot \boldsymbol{x}$, *iii.* magnitude of θ and $\boldsymbol{u}$ over $\boldsymbol{k} \cdot \boldsymbol{x}$ to illustrate phase difference.

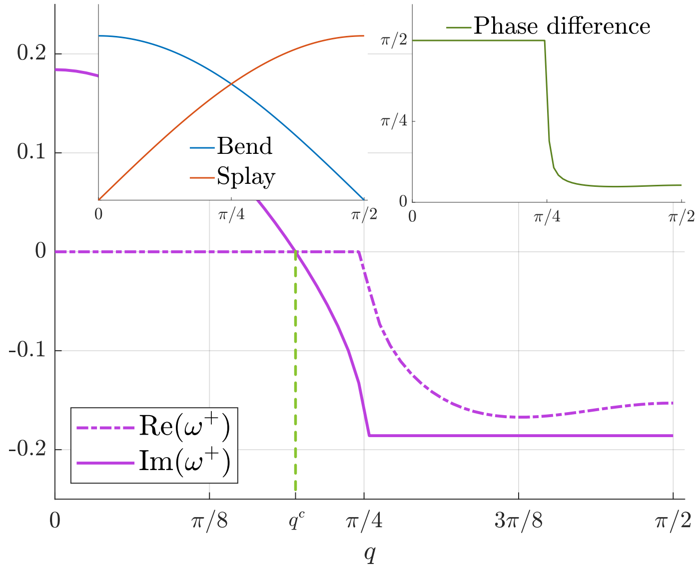

Figure 2.11: *Main plot:* Real and imaginary parts of ω^+ evaluated at $k^m|_{q=0}$, plotted over $q \in [0, \pi/2]$. *Sub-plot i:* Bend and splay components of eigenvectors over q. Bend is dominant for $q < \pi/4$ and splay is dominant for $q > \pi/4$. *Sub-plot ii:* Phase difference between eigenvectors over q. The director and fluid are stationary, out-of-phase for $q < \pi/4$ and travelling, in-phase waves for $q > \pi/4$ as seen in the associated eigenvector plots (Figure 2.8, Figure 2.10).

the director, meaning shear gradients are out-of-phase; alignment to shear no longer positively reinforces the perturbation and the system becomes unconditionally stable for a pusher.

The dependence of the disturbance growth rate ω^+ over q is summed up in Figure 2.11 for which the growth rate ω_i^+, wave speed ω_r^+, bend and splay, and the phase difference between $\boldsymbol{p}$ and $\boldsymbol{u}$, are plotted over $q \in [0, \pi/2]$ for $k^m|_{q=0}$, the wavevector for which $\omega_i^+(q = 0)$ is a maximum. The growth rate starts at a maximum for $q = 0$, diminishing as q increases as the total bend decreases. For critical $q = q^c < \pi/4$, elasticity dampens the bend modes (and therefore activity driven shear) sufficiently to stabilise the suspension. At $q = \pi/4$, a bifurcation occurs as splay becomes the dominant hydrodynamic forcing mode. Contrary to a bend deformation, for planar-wave solutions splay is at a maximum at the peaks and troughs of its phase, and so maximal hydrodynamic pumping is maximally pumped in-phase with the director. In an extensile suspension, splay-driven shear produces a counter-rotation of active units ahead of the closed end of the splay, causing a travelling wave which disperses the splay into the neighbouring region. In a polar motile suspension where concentration is allowed to vary, we would also expect to see splay-concentration modes as motility enhances an 'inward' pointing splay deformation. This particular mode of instability is well documented in literature and discussed in the original paper by Ramaswamy & Simha.[31]

Finally, we quantify the maximal growth rate k^m, which is obtained from differentiating (2.15), giving

$$\frac{\mathrm{d}\omega}{\mathrm{d}k} = \frac{ik}{\xi}\left(- D_+ \pm \frac{D_-^2 - k^{-2}\xi s^\alpha g(q)}{\sqrt{D_-^2 - 2k^{-2}\xi s^\alpha g(q)}} \right), \tag{2.21}$$

where $D_\pm = (1 \pm \xi\eta^{-1})$ and $g(q) = \cos 2q(1 + \lambda_1 \cos 2q)$. Solving for the least stable wavelength k_m gives,

$$k_m = \sqrt{\frac{1}{2a}\Big(- b - \sqrt{b^2 - 4ac}\Big)}, \tag{2.22}$$

where $a = D_-^2(D_-^2 - D_+^2)$, $b = 2\xi s^\alpha g(q)(D_+^2 - D_-^2)$ and $c = \xi^2 g(q)^2$. The wavelength observed in experiments will be determined by k^m, which is strongly dependent on the viscosity and elasticity parameters.

2.4 Remarks: Phase Determines Eigenmode Stability

The dispersion relation in equation (2.15) describes the stability for a coarse-grained suspension of active swimmers modelled as force-dipoles where momentum between the active units and their medium is conserved. The dispersion relation was derived from a simplified version of the governing equations (2.4) and is a minimalist description capturing the driving force (activity) and damping (viscosity, elasticity) which destabilise and restore orientational order in the system respectively.

In our initial analysis in Section 2.3.2, we found agreement with early active matter field literature (Simha & Ramaswamy[31]) and recovered that the dispersion relation has a stability criterion strongly dependent on the wavevector angle, q and that an extensile suspension is unstable to bend deformations and that a contractile suspension is unstable to splay perturbations. This was because when seeking planar-wave solutions to perturbations of the ordered state, bend and splay deformations in the director are directly proportional to the wavevector angle q which controls the orientation of the planar-wave solution and therefore the direction of gradients in the director. By examining where in the phase of a planar-wave solution maximal activity driven hydrodynamic pumping occurs, and where in the phase of a planar-wave maximal shear gradients occur, we revealed that a perturbation is unstable when the director and fluid velocity have a $\pi/2$ phase difference. The dispersion relation yielded two eigenvalues: eigenvectors corresponding to eigenvalue ω^+ share this $\pi/2$ phase difference, whereas the eigenvectors corresponding to ω^- yield the director and velocity profile to be in-phase with one another. Consequently, ω^+ is the eigenvalue for which the system admits stationary, unstable planar-wave solutions. This phase relationship between the director and fluid flow is illustrated in Figure 2.12.

Finally, we quantified the long-wavelength instability criteria, which propagates due to activity acting at order $\mathcal{O}(k)$ and damping acting at order $\mathcal{O}(k^2)$ for distur-

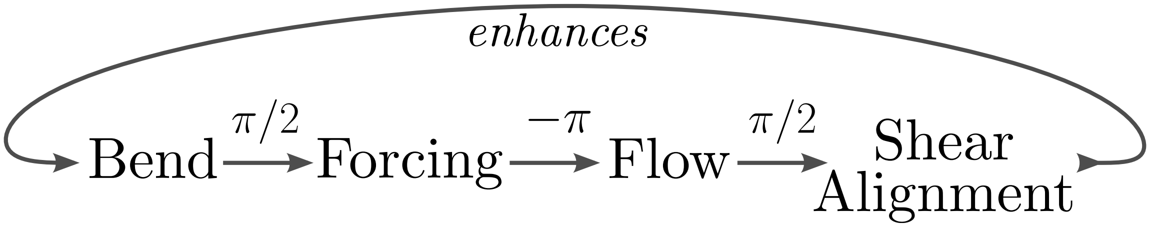

FIGURE 2.12: When prescribing planar-wave solutions, a bend deformation has a $\pi/2$ phase difference with hydrodynamic forcing, which in turn has a $-\pi$ phase difference with flow. In turn, shear gradients have a $\pi/2$ phase difference with activity induced flow. Consequently, alignment to shear shares the same phase as the original bend deformation, enhancing the bend. For an extensile suspension and a splay deformation, active forcing has a $-\pi/2$ phase difference with the director, and shear rotational effects dampen the original perturbation.

bance amplitude k, meaning that in the unbounded regime a suspension will *always* be unstable to wavelengths smaller than a critical value set by elasticity damping $\eta^{-1} = \frac{D\mu}{L^2|\alpha|}$, where L is the characteristic length scale balancing elastic restoration forces and active shear. This chapter establishes a framework from which we will extend the analysis into the unbounded 3D regime in Chapter 3 and the mechanisms, equations and diagrams act as a reference for discussion throughout the rest of this work.

3 | Bulk Hydrodynamic Instability of a 3D suspension

In this Chapter, I extend the 2D bulk analysis of the Stokesian instability established in Chapter 2 and whose growth is described by equation (2.15) to an unbounded 3D regime. In the previous chapter, we revealed that a coupling between active flow, driven by deformations in the director, and shear-induced torque, will lead to the growth of planar-wave perturbations to the constant, ordered state. The director deformations, active flow and re-orientation of the director field all occur within the same plane: in the 3D regime, the system gains a spatial degree of freedom, and we reveal a new eigenvalues and eigenmodes that result from a de-coupling of the governing equations in Section 3.2.

Following our analysis in Section 3.3.1, we introduce a new component to the governing equation for the director by means of a chirality term (Section 3.3.2). Chirality is unique to the 3D regime as it introduces an 'out-of-plane' rotational effect on an individual swimmer — here, the term 'out-of-plane' quantifies a rotational effect on the director that is orthogonal to the plane of imposed shear. This is contrary to the 'in-plane' torque that alignment-to-shear and vorticity induce. In a linear stability analysis of the ordered steady state, we show that the role of chirality is to induce travelling twist-bend modes with qualitatively similar growth rates to the 2D regime.

Finally, the effects of imposed shear in the 3D regime with chirality are discussed in Section 3.4, which reveals a unique interplay between alignment-to-shear and chiral effects. When both terms terms are present, imposed shear induces oscillatory solutions which can enhance the growth rate of the instability by up to 10% compared to particles without chirality.

3.1 Chiral Contribution to the Jeffrey Orbit Equation

The extension of the linear instability analysis to the 3D regime follows the same simplifications to the governing equations established in Section 2.2, namely: non-linear fields in $\boldsymbol{u}$ and $\boldsymbol{p}$ vanish when linearising around $\boldsymbol{u} = \boldsymbol{0}$, $\boldsymbol{p} = \hat{\boldsymbol{x}}$, swimmer number density c is held constant, and we consider a non-motile particle regime. Then, we recover the linearised equations (2.8a-2.8d), with the inclusion of a chirality term in the director equation governed by λ_2,

$$\xi \partial_t \boldsymbol{u} = -\nabla P + \nabla^2 \boldsymbol{u} + s^\alpha \nabla \cdot \boldsymbol{pp}, \tag{3.1a}$$

$$\partial_t \boldsymbol{p} = \lambda_1 (\boldsymbol{\delta} - \boldsymbol{pp}) \cdot \boldsymbol{E} \cdot \boldsymbol{p} + \lambda_2 [(\boldsymbol{\delta} - \boldsymbol{pp}) \cdot \boldsymbol{E} \cdot \boldsymbol{p}] \times \boldsymbol{p} - \boldsymbol{\Omega} \cdot \boldsymbol{p} + \eta^{-1} \nabla^2 \boldsymbol{p}, \tag{3.1b}$$

$$\nabla \cdot \boldsymbol{u} = 0, \tag{3.1c}$$

$$|\boldsymbol{p}| = 1. \tag{3.1d}$$

When $\lambda_2 = 0$, equation (3.1b) is a generalisation of the Jeffrey equation for elliptic particles in a Stokes flow to elliptical particle suspensions. The Jeffrey orbit equation is derived by considering a body-of-revolution in a Stokes flow, however, the many microorganisms don't fall into an axisymmetric, body-of-revolution categorisation, but instead have a degree of chirality by virtue of body-shape or appendage. Bacterium such as *Arthrospira* can utilise their helix-shaped body to deter grazing by ciliate,[82,83] the chiral morphotype of *Paenibacillus dendritiformis* exhibit beautiful left-handedness in bacterial colonies,[84] and many swimming microorganisms utilise helical flagellum to propel themselves which play an important next-to-leading order effect on swimmer dynamics.

In a recent paper by Ishimoto,[52] the dynamics of particle in Stokes flow with n-fold symmetry ($n \geq 3$) were examined; when $n \geq 4$, the dynamics were shown to be identical to those of a helicoidal object described by two parameters: the Bretherton constant and a chirality parameter λ_2 whose contribution in (3.1) appears as the additional term $[(\boldsymbol{\delta} - \boldsymbol{pp}) \cdot \boldsymbol{E} \cdot \boldsymbol{p}] \times \boldsymbol{p}$. In his work, Ishimoto demonstrates that the inclusion of chirality can lead to chaotic angular dynamics and unique Jeffery orbits for a particle suspended in simple shear. When the director is coupled to fluid flow, chirality induces an *out-of-plane* rotation when a background shear is impose, the direction of which depends on the left/right-handedness of the helix (FIGURE 3.1b). This rotation is in contrast to the *in-plane* rotation associated with vorticity and shear alignment (FIGURE 3.1a).

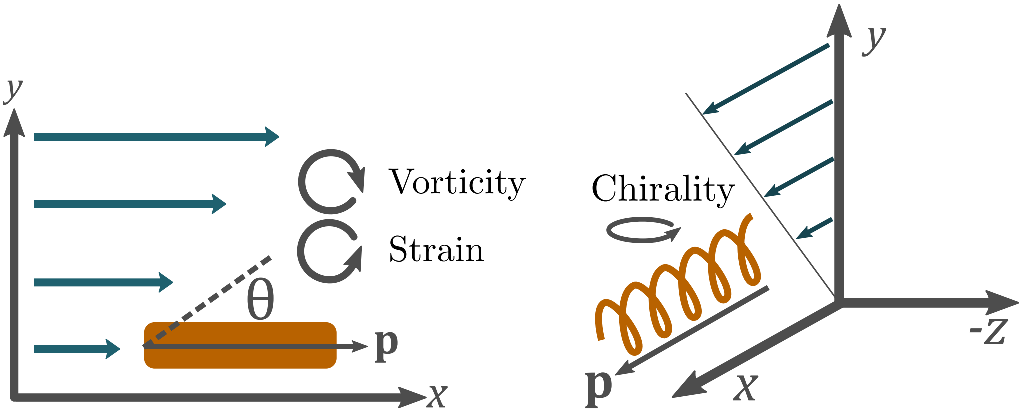

(A) (B)

FIGURE 3.1: (A) A rod in a shear flow experiences in-plane (x-y) rotation due to vorticity and extensile fluidic stress. (B) Any microswimmer with a degree of chirality will experience out-of-plane (x-z) rotation, whose direction depends on the left/right-handedness of the chirality.

The natural question arises: how does the inclusion of chirality into the Jeffrey equations affect the stability of an ordered suspension of active matter? Marcos *et al.*[85] subjected a suspension of *B. subtilis* to an imposed shear gradient along their long-axis. The bacteria comprise of a rod-like head which induces a large hydrodynamic drag penality on the swimmer move, and several left-handed helical flagella. The bacterium head acts as an anchor to the helical flagella which are subject to a lift force due to the imposed shear. The resulting mechanical torque reorientates the bacteria across the fluid streamlines, and the authors showed that chirality contributes a drift velocity to a suspension of *B. subtilis* which amounts to a 'considerable fraction' of the total swim speed with $V/U = 6.5\% \pm 2.4\%$ where V is the chiral induced drift velocity and U the bacterial swim speed. In a high-concentration limit for non-motile particles, we will show in the linear limit that the reorientation phenomenon manifests itself as a twist deformation throughout the director, resulting in new solutions for a suspension of swimmers.

3.2 Calculations for the 3D Bulk Analysis

The following calculations can be skipped over in favour of the resulting analysis in Section 3.3. The 3D governing equations satisfy the constant base state, $\boldsymbol{u}_0 = 0$, $P = P_A$, $\boldsymbol{p}_0 = \hat{\boldsymbol{x}}$. Writing the director in parametised cartesian coordinates as $\boldsymbol{p} = (\cos\theta\cos\phi,\ \sin\theta\cos\phi,\ \sin\phi)$ (Figure 2.4) and perturbing around the base state with $\boldsymbol{u} = \varepsilon\boldsymbol{u}_1$, $P = P_A + \varepsilon P_1$, $\theta = \varepsilon\theta_1$ and $\phi = \varepsilon\phi_1$ returns the system of equations at order $\mathcal{O}(\varepsilon)$ as,

$$= -\xi \partial_t u_1 - \partial_x P_1 + \nabla^2 u_1 + s^\alpha (\partial_y \theta_1 + \partial_z \phi_1), \tag{3.2a}$$

$$0 = -\xi \partial_t v_1 - \partial_y P_1 + \nabla^2 v_1 + s^\alpha \partial_x \theta_1, \tag{3.2b}$$

$$0 = -\xi \partial_t w_1 - \partial_z P_1 + \nabla^2 w_1 + s^\alpha \partial_x \phi_1, \tag{3.2c}$$

$$0 = -\partial_t \theta_1 + \lambda_1 E_{yx} + \lambda_2 E_{zx} - \Omega_{yx} + \eta^{-1} \nabla^2 \theta_1, \tag{3.2d}$$

$$0 = -\partial_t \phi_1 + \lambda_1 E_{zx} - \lambda_2 E_{yx} - \Omega_{zx} + \eta^{-1} \nabla^2 \phi_1. \tag{3.2e}$$

$$= \partial_x u_1 + \partial_y v_1 + \partial_z w_1. \tag{3.2f}$$

Introducing Fourier nodes of the form $f = f_k e^{\omega_i t} e^{i\boldsymbol{k}\cdot\boldsymbol{x} - i\omega_r t}$ returns a linear system of equation at order $\mathcal{O}(\varepsilon)$,

$$0 = \kappa_1 u_k - ik_x P_k + is^\alpha (k_y \theta_k + k_z \phi_k) \tag{3.3a}$$

$$0 = \kappa_1 v_k - ik_y P_k + is^\alpha k_x \theta_k \tag{3.3b}$$

$$0 = \kappa_1 w_k - ik_z P_k + is^\alpha k_x \phi_k \tag{3.3c}$$

$$0 = \kappa_2 \theta_k + \lambda_1^- k_y u_k + \lambda_1^+ k_x v_k + {}^{\lambda_2}\!/_{2} (k_z u_k + k_x w_k) \tag{3.3d}$$

$$0 = \kappa_2 \phi_k + \lambda_1^- k_z u_k + \lambda_1^+ k_x w_k - {}^{\lambda_2}\!/_{2} (k_y u_k + k_x v_k) \tag{3.3e}$$

$$0 = k_x u_k + k_y v_k + k_z w_k ., \tag{3.3f}$$

where $\kappa_1 = i\xi\omega - k^2$ and $\kappa_2 = \omega + i\eta^{-1} k^2$. I eliminate pressure by a linear combination of (3.3a, 3.3b, 3.3c) giving

$$0 = (k_x v_k - k_y u_k)\kappa_1 + is^\alpha \Big(\theta_k (k_x^2 - k_y^2) - k_y k_z \phi_k \Big), \tag{3.4a}$$

$$0 = (k_x w_k - k_z u_k)\kappa_1 + is^\alpha \Big(\phi_k (k_x^2 - k_z^2) - k_y k_z \theta_k \Big). \tag{3.4b}$$

Rearranging (3.3d) and (3.3e) for θ_k, ϕ_k gives,

$$\theta_k = -\kappa_2^{-1}\Big(\lambda_1^{-}k_y u_k + \lambda_1^{+}k_x v_k + {}^{\lambda_2}\!/_2(k_z u_k + k_x v_k)\Big), \tag{3.5a}$$
$$\phi_k = -\kappa_2^{-1}\Big(\lambda_1^{-}k_z u_k + \lambda_1^{+}k_x w_k - {}^{\lambda_2}\!/_2(k_y u_k + k_x w_k)\Big). \tag{3.5b}$$

and substitution into (3.4a) and (3.4b) results in,

$$\begin{aligned} 0 = -k_y u_k\Big[\tilde{\omega}^2 + is^\alpha\lambda_1^{-}(k_x^2 - k_\perp^2)\Big] + k_x v_k\Big[\tilde{\omega}^2 - is^\alpha\lambda_1^{+}(k_x^2 - k_y^2)\Big] + is^\alpha k_x k_y k_z \lambda_1^{+} w_k \\ - is^\alpha\tilde{\lambda}_2\Big[k_z k_x^2 u_k + k_x(k_x^2 - k_y^2)v_k + k_x k_y k_z w_k\Big], \end{aligned} \tag{3.6a}$$

$$\begin{aligned} 0 = -k_z u_k\Big[\tilde{\omega}^2 + is^\alpha\lambda_1^{-}(k_x^2 - k_\perp^2)\Big] + is^\alpha k_x k_y k_z \lambda_1^{+} v_k + k_x v_k\Big[\tilde{\omega}^2 - is^\alpha\lambda_1^{+}(k_x^2 - k_z^2)\Big] \\ + is^\alpha\tilde{\lambda}_2\Big[k_y k_x^2 u_k + k_x k_y k_z v_k + k_x(k_x^2 - k_z^2)w_k\Big]. \end{aligned} \tag{3.6b}$$

Here, $\tilde{\omega}^2 = \kappa_1\kappa_2$, $k_\perp^2 = k_y^2 + k_z^2$ and $\tilde{\lambda}_2 = {}^{\lambda_2}\!/_2$. Substituting in (3.3f) as $u_k = -k_x^{-1}(k_y v_k + k_z w_k)$ gives,

$$0 = f_{-}(k_y)v_k + g_{-}(k_z)w_k, \tag{3.7a}$$
$$0 = g_{+}(k_y)v_k + f_{+}(k_z)w_k, \tag{3.7b}$$

where,

$$\begin{aligned} f_\pm(k_i) &= \tilde{\omega}^2(k_x^2 + k_i^2) + \frac{is^\alpha}{2}\Big(\lambda_1(2k_x^2k_i^2 - k_i^2k_\perp^2 - k_x^4) + k_i^2k_\perp^2 - k_x^4 \pm \tilde{\lambda}_2 k_x^2(k_x^2 - k_i(k_y + k_z)\Big) \\ g_\pm(k_i) &= k_y k_z\Big(\tilde{\omega}^2 + \frac{is^\alpha}{2}\Big(\lambda_1(2k_x^2 - k_\perp^2) - k_\perp^2 \pm \tilde{\lambda}_2 k_x^2(k_y k_z + k_\perp^2 - k_i^2)\Big)\Big). \end{aligned}$$

Then, eigenvalues are given by $f_{+}(k_z)f_{-}(k_y) - g_{+}(k_y)g_{-}(k_z) = 0$, which yields

$$\begin{aligned}\tilde{\omega}^4(k_x^4 + k_x^2k_\perp^2) + \tilde{\omega}^2k_x^2\frac{is^\alpha}{2}\big[\lambda_1(k_x^2k_\perp^4 - k_\perp^4 - 2k_x^4) + k_\perp^4 - 2k_x^4 - k_x^2k_\perp^2\big] \\ - \frac{k_x^4}{4}\big[\lambda_1^2(k_x^4 - k_\perp^2(2k_x^2 - k_\perp^2)) + 2\lambda_1k_x^2(k_x^2 - k_\perp^2) + k_x^4 - k_\perp^4 \\ - \tilde{\lambda}_2(k_x^4 - k_x^2k_\perp^2 + k_yk_z(k_\perp^2 - 2k_yk_z)\big] = 0. \quad (3.8)\end{aligned}$$

Dependence on k_y and k_z reduces to a symmetric contribution in the form of $k_\perp$, reflecting the rotational invariance around the x-axis. To illustrate the dependence on the angle from the x-axis and provide meaningful comparison to the 2D results, I write $\boldsymbol{k} = k(\cos q,\ \sin q\cos q',\ \sin q\sin q')$. Then (3.8) can be written,

$$\tilde{\omega}^4 - \tilde{\omega}k^2\frac{is^\alpha}{2}\tilde{b} - \frac{k^4}{4}(\tilde{c} + \tilde{d}) = 0, \quad (3.9)$$

where,

$$\begin{aligned}\tilde{b} &= \lambda_1(1 - 3\cos^2 q + 4\cos^4 q) + 3\cos^2 q - 1, \\ \tilde{c} &= \frac{1}{2}\cos 2q(1 + \cos 2q)(1 + \lambda_1)(1 + \lambda_1\cos 2q), \\ \tilde{d} &= \lambda_2^2\cos^2 q\cos^2 2q.\end{aligned}$$

and $\tilde{\omega}^2 = (\omega + i\eta^{-1}k^2)(i\xi\omega - k^2)$. Solving for ω gives,

$$\omega = \frac{ik^2}{2\xi}\left(- D_{+} \pm \sqrt{D_{-}^2 - k^{-2}s^\alpha\xi(\tilde{b} \pm \sqrt{L_0 + \lambda_1L_1 + \lambda_1^2\hat{L}_1 - \lambda_2^2\hat{L}_2}}\right), \quad (3.10)$$

for $D_\pm = (1 \pm \xi\eta^{-1})$, $\boldsymbol{k} = k(\cos q, \sin q\cos q', \sin q\sin q')$ and

$$\begin{aligned} L_0 &= \sin^4 q, \\ L_1 &= 2\sin^4 q(4\cos^2 q - 1), \\ \hat{L}_1 &= (4\cos^4 q - 5\cos^2 q + 1)^2, \\ \hat{L}_2 &= 4\cos^2 q\cos^2 2q. \end{aligned}$$

In the limiting case of $\lambda_1 \neq 0, \lambda_2 = 0$ the dispersion simplifies to the four roots,

$$\omega_1^{\pm} = \frac{ik^2}{2\xi}\Big(- D_{+} \pm \sqrt{D_{-}^2 - 2k^{-2}s^{\alpha}\xi\cos 2q(1+\lambda_1\cos 2q)}\Big), \tag{3.11a}$$

$$\omega_2^{\pm} = \frac{ik^2}{2\xi}\Big(- D_{+} \pm \sqrt{D_{-}^2 - k^{-2}s^{\alpha}\xi(1+\cos 2q)(1+\lambda_1)}\Big), \tag{3.11b}$$

and in the limiting case of $\lambda_1 = 0, \lambda_2 \neq 0$ we find the roots,

$$\omega_3^{\pm} = \frac{ik^2}{2\xi}\Big(- D_{+} \pm \sqrt{D_{-}^2 - k^{-2}s^{\alpha}\xi\Big(3\cos^2 q - 1 + i\sqrt{4\lambda_2^2\cos^2 q\cos^2 2q - \sin^4 q}\Big)}\Big), \tag{3.12a}$$

$$\omega_4^{\pm} = \frac{ik^2}{2\xi}\Big(- D_{+} \pm \sqrt{D_{-}^2 - k^{-2}s^{\alpha}\xi\Big(3\cos^2 q - 1 - i\sqrt{4\lambda_2^2\cos^2 q\cos^2 2q - \sin^4 q}\Big)}\Big). \tag{3.12b}$$

3.3 Dominance of Bend Modes for an Extensile Suspension

Completing a linear instability analysis for the 3D regime yielded four eigenvalues: $\omega_1^\pm$, $\omega_2^\pm$ which occur in the limit $\lambda_2 = 0$ and $\omega_3^\pm$, $\omega_4^\pm$ which occur in the limit $\lambda_1 = 0$. In the following analysis, we explore the limiting case of $\lambda_2 = 0$ before exploring the limiting case of $\lambda_1 = 0$ in Section 3.3.2.

3.3.1 Non-chiral Particles: De-coupling of Governing Equations

From (3.11a), (3.11b) we can extract the instability condition, which corresponds to $\omega_i > 0$,

$$\text{Imag}(\omega_1^+) > 0 \implies -s^\alpha \cos 2q(1 + \lambda_1 \cos 2q) > 2\eta^{-1}k^2, \tag{3.13a}$$

$$\text{Imag}(\omega_2^+) > 0 \implies -s^\alpha(1 + \cos 2q)(1 + \lambda_1) > 4\eta^{-1}k^2. \tag{3.13b}$$

Immediately, we notice that the instability condition given by ω_1^+ is identical to the instability condition for the 2D case, discussed by Simha & Ramaswamy[31] and discussed in Section 2.3.2, equation (2.15). Since $\cos 2q(1 + \lambda_1 \cos 2q)$ is positive for $q \in [0, \pi/4)$ and negative for $q \in (\pi/4, \pi/2)$, we recover that ω_1^+ is an unstable node for pushers (pullers) for wave-vectors below (above) 45°, for sufficiently small k. As shown in Section 2.3.2, the modes associated to ω_1^+ are bend-splay modes, where fluid is perpendicular (parallel) to a bend (splay) deformation. The second root ω_2^+ is unique to the 3D regime. Firstly, we observe that both roots obey the same limit as $q \to 0$, which we will denote with the notation,

$$\lim_{q\to 0} \omega_1^+ = \lim_{q\to 0} \omega_2^+ = \omega_{1,2}^+.$$

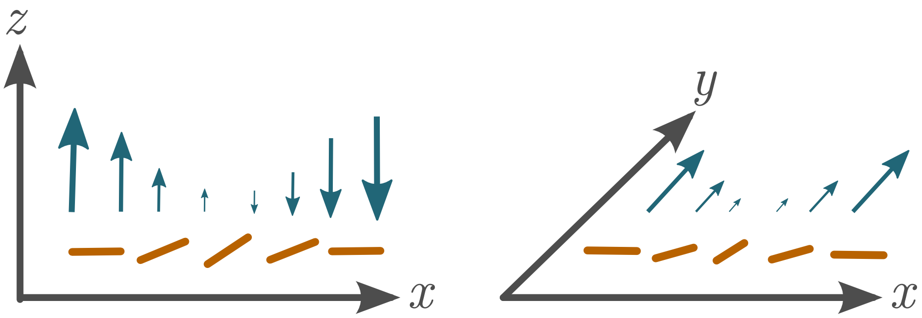

Figure 3.2: By the choice of parametrisation of $\boldsymbol{p}$, in the limiting case of $q = 0$, a planar bend wave (and consequential flow) can extend into the x-y plane or x-z plane with equal probability.

The convergence to $\omega^{+}_{1,2}$ becomes intuitive when considering the choice of parametrisation for the director $\boldsymbol{p}$ and the wavevector $\boldsymbol{k} = k(\cos q, \sin q \cos q', \sin q \sin q')$. When $q = 0$, the perturbed system is invariant to rotations around the x-axis, it is only when we imposed a wavevector with orientation of some non-zero q that we break rotational symmetry about the x-axis. A pure bend deformation is strictly a 2D phenomena — it is contained entirely in a 2D plane, and consequently a bend deformation will break rotational symmetry in the suspension. By our choice of parametrisation for $\boldsymbol{p}$, which parametrises rotations of the director into the y- and z-axis by θ and ϕ respectively, we can without loss of generality observe the effects of breaking symmetry by application of a non-zero q. With these considerations, we see that our choice of parametrisation causes the modes associated with $\omega^{+}_{1,2}$ to cause the bend perturbation to propagate either in the x-y plane, the x-z plane, or a linear combination of the two. See Figure 3.2 for further illustration.

Having understood the convergence of the $\omega^{+}_{1,2}$ in the limiting case of $q = 0$, we return to the instability conditions (3.13a, 3.13b) to compare the stability of the modes associated with ω^{+}_{1} and ω^{+}_{2}. The second root ω^{+}_{2} is unique to the 3D regime and plotting ω^{+}_{1}, ω^{+}_{2} over $k \in [0, 1]$ for varying q, we observe that this new eigenvalue yields unstable (stable) nodes for a pusher (puller) *for all* q and sufficiently small k (Figure 3.3, *main plot*) which boasts larger perturbation growth rates than the

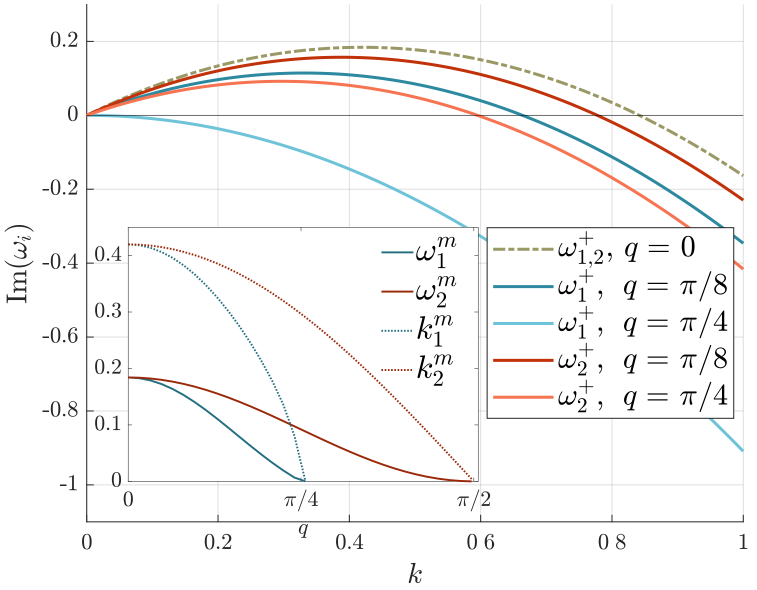

FIGURE 3.3: *Main plot:* Growth rate of the dispersion relation given by ω_1^{+} and ω_2^{+} for varying q. Instability exists for $\mathrm{Im}(\omega)$ greater than zero. Roots converge for the case $q = 0$. *Sub-plot:* Maximum of $\mathrm{Im}(\omega_1^{+})$ and $\mathrm{Im}(\omega_2^{+})$ and corresponding k^m for increasing q. The instability mode associated with ω_2^{+} (red) is the dominate mode in a 3D system.

eigenvalue ω_1^{+} for all values of q (FIGURE 3.3, *sub plot*).

To understand why ω_2^{+} yields faster growing modes than ω_1^{+}, we return to the calculations for the linear stability analysis and note that the governing equations with $\lambda_2 = 0$ for θ and ϕ are coupled to one another at order $\mathcal{O}(\varepsilon)$ only by shear gradients (equations 3.3a, 3.3b),

$$\partial_t \theta = \lambda_1 E_{yx} - \Omega_{yx} + \eta^{-1} \nabla^2 \theta,$$
$$\partial_t \phi = \lambda_1 E_{zx} - \Omega_{zx} + \eta^{-1} \nabla^2 \phi.$$

When seeking Fourier mode solutions, the velocity and director gradients are determined by our choice of wavevector $\boldsymbol{k}$. Since our model swimmers are axisymmetric around their principle axis of orientation, we can restrict (without loss of generality) the wavevector $\boldsymbol{k}$ to the x-y plane, *i.e.* $q' = 0$. Then, the eigenvalues ω_1^{+} and ω_2^{+} fall out of the linearised equation (equations (3.3a—3.3f) with $\lambda_2 = 0$) as a decoupling of u_k, v_k and θ_k from w_k and ϕ_k,

$$
\begin{aligned}
0 &= (\omega + i\eta^{-1}k^2)(k_x v_k - k_y u_k) + is^{\alpha}(k_x^2 - k_y^2)\theta_k, & 0 &= (\omega + i\eta^{-1}k^2)k_x w_k + is^{\alpha}k_x^2\phi_k,\\
0 &= (i\xi\omega - k^2)\theta_k + \lambda_1^{-}k_y u_k + \lambda_1^{+}k_x v_k, & 0 &= (i\xi\omega - k^2)\phi_k + \lambda_1^{+}k_x w_k,\\
0 &= k_x u_k + k_y v_k,
\end{aligned}
$$

where $\omega_1^{\pm}$ is associated to u_k, v_k, θ_k and $\omega_2^{\pm}$ is associated to w_k and ϕ_k. By restricting the orientation of $\boldsymbol{k}$ to the x-y plane, the governing equations decouple into a perturbation propagating in the x-y plane and a perturbation propagating in the x-z plane. Due to this decoupling, the eigenmodes u_k, v_k and θ_k associated with ω_1^{+} are disturbed by the wavevector $\boldsymbol{k}^{xy} = k(\cos q,\ \sin q,\ 0)$. Since k_y is non-zero, this mode experiences both a bend and splay deformation, and as splay is stabilising in an extensile suspension, the mode experiences a reduced growth rate. Conversely, in the decoupled equations for w_k and ϕ_k, k_y does not appear. Consequently, the eigenmodes propagating into the x-z plane are disturbed by the wavevector $\boldsymbol{k}^{xz} = k(\cos q,\ 0,\ 0)$, which corresponds to a pure bend mode, propagating into the x-z plane. The instability conditions in (3.13) tell us that the growth rate associated with a pure bend mode of reduced amplitude $|\boldsymbol{k}^{xz}| = k\cos q$ will always trump the growth rate associated with a bend-splay perturbation, whose amplitude is $|\boldsymbol{k}^{xy}| = k$.

3.3.2 Chiral particles: Re-coupling of Governing Equations

We have established that in the bulk 3D regime, an extensile suspension is unstable to bend deformations where the least-stable mode is associated with a perturbation wavevector parallel to the ordered axis. In the 2D regime as the perturbation wavevector angle q increases from zero, we observe a decrease in hydrodynamic pumping due to bend and an increase in hydrodynamic pumping due to splay. At a wavevector angle $q = \pi/4$ the dominant pumping switches from bend, which pumps fluid perpendicular to the ordered axis, to splay, which pumps fluid parallel to the ordered axis. In the 3D regime, we uncovered two unstable modes: ω_1^+ and ω_2^+. The modes associated to ω_1^+ demonstrate the same instability mechanism as the 2D regime, where the perturbation kinematics are restricted to x-y plane only. We then established that the modes associated with ω_2^+ *when the wavevector* $\boldsymbol{k}$ *is restricted to the* x-y *plane* propagates instead into the x-z plane with a bend deformation *only*, due to a decoupling between θ_k and ϕ_k. This decoupling only occurs at order $\mathcal{O}(\varepsilon)$, at higher orders the modes would be re-coupled. Having established the de-coupling of θ_k and ϕ_k in the bulk 3D case, we will model the effects of chirality, which causes active units to rotate out-of-plane to an imposed shear. We will show that this *re-couples* θ_k and ϕ_k at order $\mathcal{O}(\varepsilon)$. We will initially explore the limiting case of $\lambda_1 = 0$ to better isolate chiral effects on the director.

The effects of chirality on the evolution of the director are small compared to alignment to shear and vorticity. This is because the governing parameter λ_2 is an order of magnitude smaller than λ_1, with a range of $\lambda_2 \in [-0.1, 0.1]^{60}$ compared to $\lambda_1 \in [0, 1]$ and vorticity, which has no parameter acting on it. Numerically, we should expect any phenomena arising due to chiral effects to act on much longer time scales than alignment to shear and vorticity effects. In Chapter 2, we established that the instability criteria is solely dependent on the balance of activity-driving and elasticity-restoring length scales, where the instability growth/decay rate is determined by the active shear rate. As chirality acts on longer time scales than vorticity and alignment-to-shear, the eigenvalues ω_3^+ and ω_4^+ (3.12a, 3.12b) for $\lambda_1 = 0$, $\lambda_2 = 0.1$ share the maximum growth rate as their ω_1^+, ω_2^+ counter-parts. Consequently, plotting the growth rates of ω_3^+, ω_4^+ against k is yields an almost identical profile to the plot for ω_1^+ and ω_2^+ in FIGURE 3.3 with negligible numerical differences.

However, instead of comparing the k-dependent dispersion relation, when plotting the q-dependent dispersion profile for ω_3^+, ω_4^+, we find the eigenmodes exhibit markedly different behaviour with respect to changes in the perturbation angle q than their non-chiral counter-parts. Vorticity is the driving instability mechanism and alignment-to-shear is a numerically next-to-leading order effect, consequently to isolate the effects of chirality we choose to compare the chiral eigenmodes to ω_0^+ for which $\lambda_1 = 0$ and $\lambda_2 = 0$. Figure 3.4 plots three important quantities over $q \in [0, \pi/2]$ for ω_0^+, ω_3^+, ω_4^+ evaluated at their maximum wavevector amplitude k^m: the solid lines indicate the growth rate $\mathrm{Im}(\omega)$ of the eigenmodes, the dashed lines illustrate the perturbation wave speed $\mathrm{Re}(\omega)$, and the dotted lines plot the corresponding maximum wavevector k^m.

The maximum growth rate when $q = 0$ corresponds to Figure 3.3, and we find strong agreement between the growth rates of ω_0^+, ω_3^+ and ω_4^+, where the differences between the growth rates with and without chirality are less than a percentile (Figure 3.5, Top). As q increases from zero in the non-chiral case, we observed two distinct modes corresponding to perturbations in the x-direction and perturbations in the x-y plane; in the chiral case, we find these two modes have the same growth rate for small q, but observe the eigenmodes obtained a non-zero wavespeed ($\mathrm{Re}(\omega) \neq 0$), which in 3.3.2.1 we will see correspond to twist-bend waves propagating into the x-z and x-y plane. The growth rates of ω_3^+ and ω_4^+ diverge at a critical wavevector q^c, which is determined from equations (3.12a) and (3.12b),

$$4\lambda_2^2 \cos^2 q^c \cos^2 2q^c - \sin^4 q^c = 0. \tag{3.14}$$

When $q < q^c$ the dispersion roots can be written,

$$\omega_{3,4}^+ = \frac{ik^2}{2\xi}\Big(- D_+ + \sqrt{a \pm ib}, \Big) \tag{3.15}$$

where $a = D_-^2 - k^{-2} s^\alpha \xi (3\cos^2 q - 1)$ and $b = k^{-2} s^\alpha \xi \sqrt{4\lambda_2^2 \cos^2 q \cos^2 2q - \sin^4 q}$. In this regime the imaginary components of ω_3^+, ω_4^+ converge and the instability condition

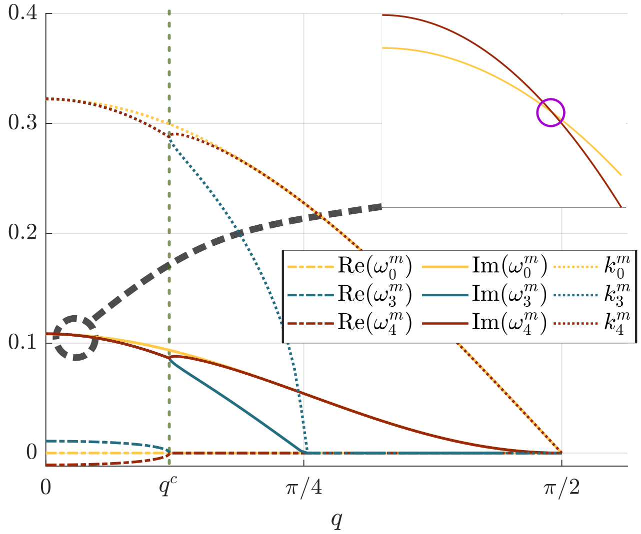

FIGURE 3.4: *Main plot:* Real and imaginary parts of ω_0^+, ω_3^+, ω_4^+ evaluated at their maximum with wave vector amplitude k^m over $q \in [0, \pi/2]$. Bifurcation occurs at $q = q^c$; proximity to $q = \pi/8$ is coincidental to parameter values chosen. *Sub plot:* Highlight of cross-over between ω_0^+ and ω_4^+ (purple circle).

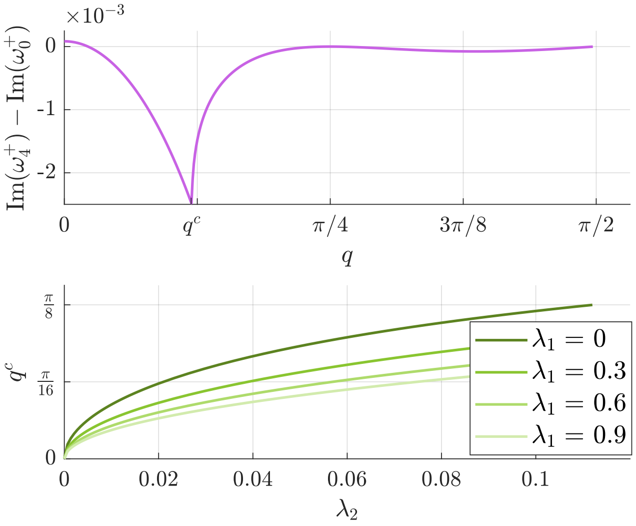

FIGURE 3.5: (TOP) Difference between ω_4^+ and ω_0^+ (where $\lambda_1 = 0$, $\lambda_2 = 0$). For all ranges of meaningful parameters, ω_4^+ is larger than ω_0^+ only for very small q. (BOTTOM) The critical q^c for which the system undergoes a bifurcation; q^c is dependent on λ_1 and λ_2 only and increases from zero as λ_2 increases.

becomes,

$$\mathrm{Imag}(\omega^{+}_{3,4}) > 0 \implies -D_{+} + \nu^{\frac{1}{2}} \cos\left(\frac{\chi}{2}\right) > 0, \tag{3.16}$$

where $\nu = \sqrt{a^2 + b^2}$ and $\chi = \tan^{-1}(\frac{b}{a})$. For $q > q^c$, instability is determined by

$$\begin{aligned}
\mathrm{Imag}(\omega^{+}_{3}) = 0 &\implies k < \sqrt{\frac{\eta}{4}\Big(3\cos^2 q - 1 - \sqrt{\sin^4 q - 4\lambda_2^2 \cos^2 q \cos^2 2q}\Big)}, \\
\mathrm{Imag}(\omega^{+}_{4}) = 0 &\implies k < \sqrt{\frac{\eta}{4}\Big(3\cos^2 q - 1 + \sqrt{\sin^4 q - 4\lambda_2^2 \cos^2 q \cos^2 2q}\Big)}.
\end{aligned}$$

The full system with non-zero λ_1 has a bifurcation angle q^c dependent on λ_1 and λ_2 (Figure 3.5b); for $q < q^c$ the roots $\omega^{+}_{3,4}$ yield a real part implying two possible solutions of a travelling wave (Figure 3.5c), propagating either forwards or backwards. For $q > q^c$ the wave does not propagate with time and $\omega^{+}_{3,4}$ yields two roots of different stability where ω^{+}_{4} yields the least stable modes.

3.3.2.1 Eigenvectors for $q = 0$

To understand how chirality changes the bend-splay modes, we investigate the eigenvectors for ω^{+}_{4}, which are captured in the eigenvector plot in Figure 3.6, *main*, where the eigenvectors for ω^{+}_{4} are plotted over $q \in [0, \pi/2)$, evaluated at k^m for which the growth rate of ω^{+}_{4} is at a maximum.[*] From the analysis in Section 3.3.1 where $\lambda_2 = 0$, we know that when the perturbation wavevector $\boldsymbol{k}$ is restricted to the x-y plane, the least stable mode is associated with ω^{+}_{2}, where a pure bend deformation propagates into the x-z plane; expecting likewise, we normalise the eigenvectors to $\phi_k = 1$. At $q = 0$, we observe the phase difference between ϕ_k (purple) and w_k (yellow) is slightly

---

[*] The eigenmodes for ω^{+}_{3} and $q < q^c$ share the same growth rate and general characteristics, except that θ_k and ϕ_k have a different phase and wave direction, which will be described throughout this section.

shifted from $\pi/2$ (FIGURE 3.6, *sub*), where an exact phase difference of $\pi/2$ between the waves is characteristic of a bend deformation (Section 2.3.3, FIGURE 2.9). However, we also observe that the phase relationship between θ_k (green) and v_k (red) is *also* slightly shifted from $\pi/2$, indicating another bend deformation, propagating into the x-y plane.

Recall that when the ordered state is perturbed with wavevector angle $q = 0$, a bend perturbation can either propagate into the y-axis or the z-axis by virtue of θ_k or ϕ_k respectively. When λ_2 is non-zero, θ_k and ϕ_k are coupled together and the bend deformations (one in the y-axis and one in the z-axis) co-exist as one mode where θ_k and ϕ_k have a phase difference of $\pm\pi/2$ ($+\pi/2$ for ω_4^+, $-\pi/2$ for ω_3^+)[†]. The resulting mode resembles two spirals of outward pointing arrows with a phase difference of

---

[†] For θ_k, ϕ_k the modes associated with ω_3^-, ω_4^- have a phase difference of $\pm\pi$, but these modes are stable.

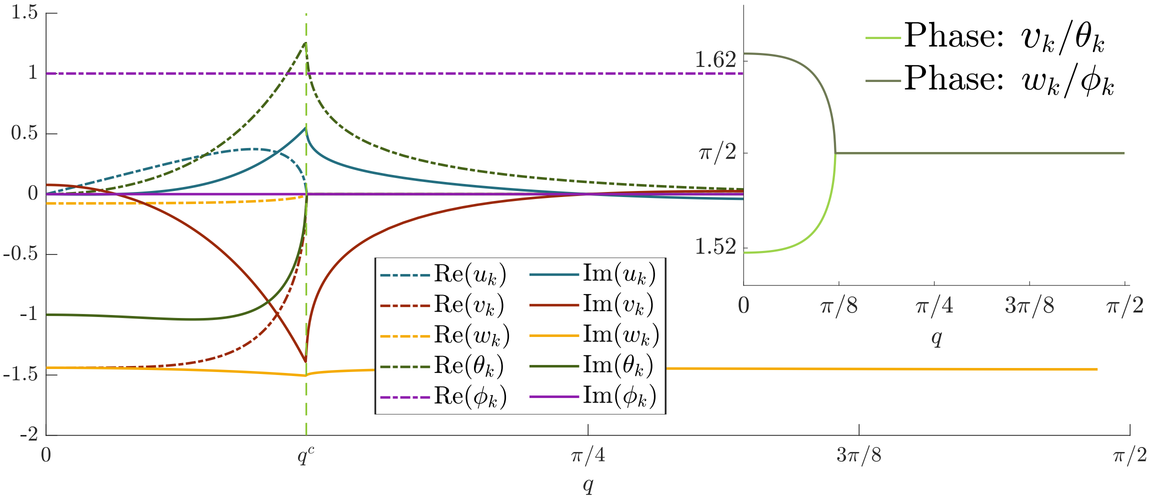

FIGURE 3.6: *Main:* Eigenvectors corresponding to ω_4^+, evaluated at k^m for which ω_4^+ is at a maximum over $q \in [0, \pi/2)$. Eigenvectors are normalised to $\phi_k = 1$ and the q-dependent bifurcation of ω_4^+ occurs at q^c. Here, ϕ_k and w_k display the dominant bend-splay mode discussed in the ω_2^+ case. *Sub:* Phase difference between v_k, θ_k and w_k, ϕ_k. The phase difference converges to $\pi/2$ for stationary waves when $q > q^c$.

$\pi/2$, which is illustrated in Figure 3.7 where the director (orange) and fluid flow (blue) are plotted along the x-axis for $x \in [0, 2\pi/k]$. This spiral is clockwise for ω_4^+ and anticlockwise for ω_3^+.

To understand why the phase difference between θ_k and v_k (ϕ_k and w_k respectively) is shifted slightly from $\pi/2$ for $q = 0$, recall that a bend deformation is a 2D phenomena — the deformation creates a hydrodynamic forcing into the same plane that the bend propagates into, furthermore, alignment to shear and the vorticity term $\boldsymbol{\Omega} \cdot \boldsymbol{p}$ cause a rotation in the director in the same plane that the shear gradients occur in. However, when the chirality term is present and a bend deformation occurs, the director is rotated *out of the plane* that the bend deformation occurs in, *i.e.* a change in θ_k (or ϕ_k respectively) due to chiral effects is determined by shear gradients *orthogonal* to y (or z respectively), which is quantified in the components of the director equation (equations 3.3a, 3.3b),

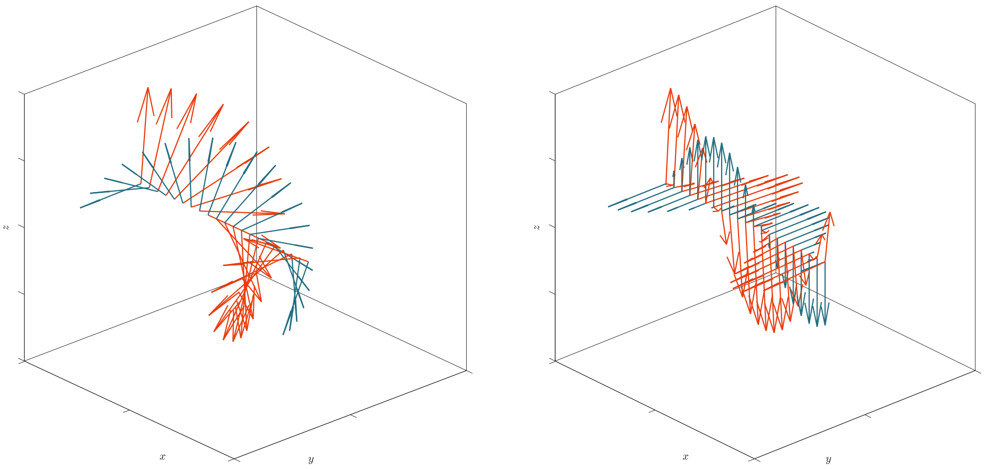

Figure 3.7: Vector field plots of the modes associated with ω_4^+ plotted along the x-axis for $x \in [0, 2\pi/k]$ and $q = 0$. The director is plotted in orange and the flow is plotted in blue. Left: The full vector field plot. Right: The same vectors, but with the director and fluid flow split to illustrate two simultaneous bend modes.

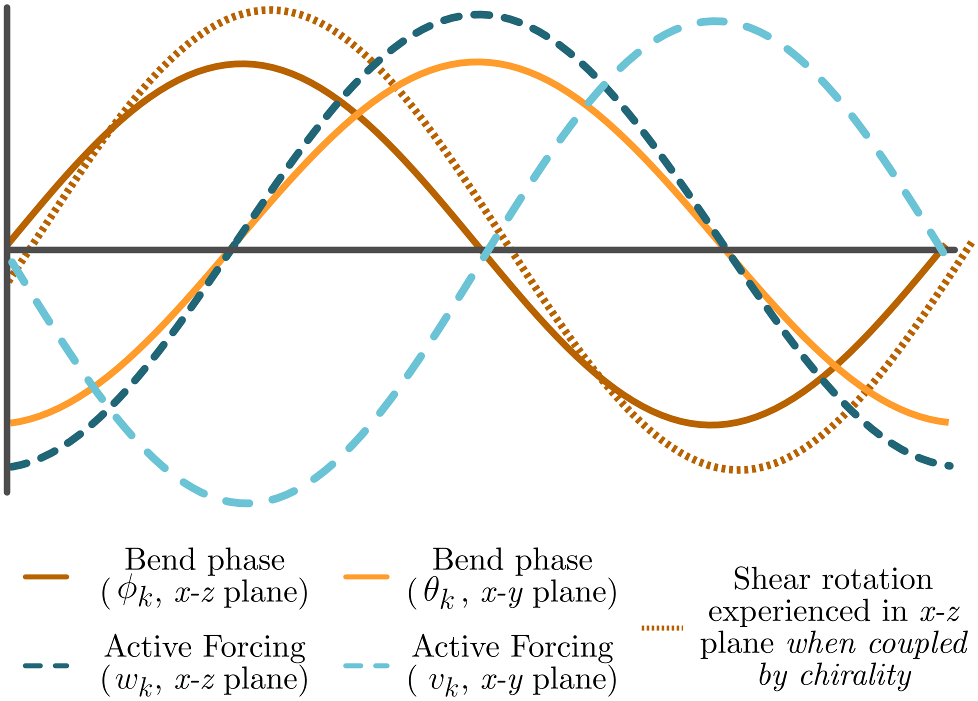

Figure 3.8: Graph of two uncoupled ($\lambda_2 = 0$) bend modes with a $\pi/2$ phase difference in the x-z plane (ϕ_k, orange) and in the x-y plane (θ_k, light orange). Each deformation causes an active forcing in the fluid, which is proportional to the gradient in the director and propagates into the same plane as its corresponding deformation (w_k, dashed blue and v_k dashed light blue). Rotation due to shear is proportional to the gradient of flow, which is itself proportional to active forcing. To this point, this illustration is the same as Figure 2.9, but extended to 3D with a second bend mode. When chirality is introduced, rotational effects in the x-z plane are coupled to shear in the x-y plane. Since the flow in the x-y plane has a $\pi/2$ phase difference to the flow in the x-z plane, chirality causes a shift in the location of maximum rotation experienced in the x-z plane. Numerically, chirality effects are much smaller than vorticity, so this phase shift is correspondingly small (orange, dotted).

$$\partial_t \theta_k = \lambda_1 E_{yx} - \Omega_{yx} + \lambda_2 E_{zx} + \nabla^2 \theta_k,$$
$$\partial_t \phi_k = \lambda_1 E_{zx} - \Omega_{zx} - \lambda_2 E_{yx} + \nabla^2 \phi_k.$$

As the two bend perturbations in θ_k and ϕ_k have a phase difference of $\pi/2$, so does the associated hydrodynamic forcing and the consequential flow. Consequently, shear gradients in the z-axis (y-axis) have a π phase difference to θ_k (ϕ_k), and rotational effects due to chirality occur with a phase difference of $\pm\pi/2$ in comparison to alignment to shear and vorticity effects. However, since chirality is governed by $\lambda_2 \in [-0.1, 0.1]$, rotation due to chiral effects is small compared to shear alignment and vorticity, and the phase shift in the director compared to the $\lambda_2 = 0$ modes is relatively small. The difference between the phases of a bend deformation in the x-y and x-z plane, the corresponding flow and phase shift are graphed in FIGURE 3.8. The two modes ω_3^+, ω_4^+ correspond to a wave travelling forwards, or backwards, depending on whether the phase difference between θ_k and ϕ_k is $\pm\pi/2$.

3.3.2.2 Eigenvectors for $q \neq 0$

As the perturbation wave angle increases from 0, three changes occur. Firstly, splay is introduced into the system: splay is a restoring force in an extensile suspension (see Section 2.3.3) and the growth of ω_4^+ decrease correspondingly. Secondly, twist is introduced into the system: when $k_z = 0$, twist is determined by $k_y \phi_k$, and the twist deformation corresponds to a rotation of the director about the y-axis (FIGURE 3.9). A twist deformation does not induce fluid forcing, but it does change the direction that bend and splay deformations force fluid. Thirdly, increasing the magnitude of twist in the suspension causes a shift in the phase difference between θ_k and ϕ_k until the critical value $q = q^c$, where the relative phases of θ_k, v_k and ϕ_k, w_k converge to $\pi/2$ and θ_k and ϕ_k become in-phase with one another.

When the phase differences between θ_k and ϕ_k becomes 0 at $q = q^c$, the system

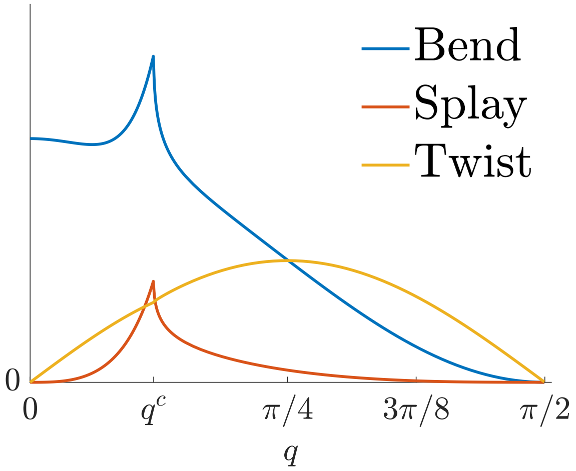

FIGURE 3.9: The bend, splay and twist free-energy in the perturbed suspension corresponding to the components of the Frank free -energy integrand (1.32). Hydrodynamic forcing is proportional to the bend and splay, but a twist deformation does not induce a hydrodynamic forcing. The deformation energies correspond to the modes plotted in FIGURE 3.6. Note: the spike at $q = q^c$ corresponds to the choice of normalising the eigenvectors to ϕ_k.

undergoes a bifurcation and ω_3^+ and ω_4^+ obtain different growth rates. In the same way as in Section 3.3.1, when the wavevector $\boldsymbol{k}$ is restricted without loss of generality to the x-y plane, the least stable mode ω_4^+ corresponds to a bend deformation in the x-z plane (where as ω_3^+ corresponds to a bend-splay deformation in the x-y plane). Unlike the bulk case however, chirality couples the bend mode in the x-y axis and the bend mode in the x-z axis together. In FIGURE 3.10A for which the wavevector angle q is just above q^c, the vector plots of the modes of ω_4^+ are plotted, and the decomposition of the θ_k and ϕ_k in FIGURE 3.10B indicates that the in the least stable configuration, the suspension tends towards a pure bend deformation as opposed to a superposition of a bend and splay.

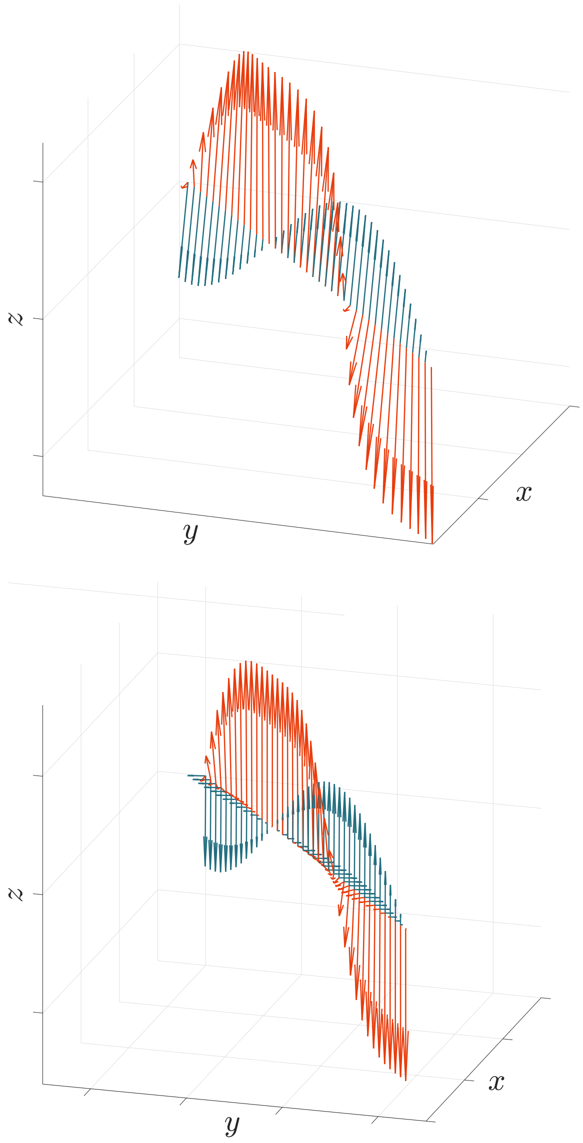

Figure 3.10: Vector field plots of the modes associated with ω_4^+ plotted along the x-axis for $x \in [0, 2\pi/k]$ and $q > q^c$. The director is plotted in orange and the flow is plotted in blue. Top: The full vector field plot. Bottom: The same vectors, but with the director and fluid flow split to illustrate two simultaneous bend modes. The phases of θ_k and ϕ_k coincide when $q > q^c$.

3.4 Imposed Shear in a Bulk Fluid

Following the analysis established in Section 2.3.3 and Section 3.3, we wish to understand how the underlying instability mechanism of the ordered steady state interacts with an imposed background shear. We will see in Chapter 5 that an active suspension in the 2D regime confined to a channel or film can admit a non-trivial steady solution with a non-zero flow and director field as a static torque balance between shear-induced torque and elastic torque. However, in the 2D regime with $\boldsymbol{p} = \text{const.}$, attempting to solve for a steady state with an imposed shear yields,

$$0 = \lambda_1 E_{yx} - \Omega_{yx}.$$

This represents a torque balance between alignment to shear and rotation due to vorticity, which can be resolved only when $\lambda_1 = 1$: note that chirality is absent as it is strictly a 3D phenomena. As alluded to in the introductory Chapter, certain liquid-crystal regimes do allow the shear alignment parameter to obtain values larger than 1, however, our interest lies in suspensions of swimming microorganisms where $\lambda_1 \in [0, 1)$, so we omit this possibility. In the unbounded 3D regime (with or without chirality), with the same set of governing equations as Section 3.3 (equations (3.1)), the director admits only one constant, steady solution in an linear background shear regime, where the director is *orthogonal* to the plane of imposed shear (see FIGURE 3.11 for illustration). Following our convention of $\bar{\boldsymbol{p}} = \hat{\boldsymbol{x}}$, this corresponds to a steady state solution of,

$$\bar{\boldsymbol{u}} = \tilde{A} y \hat{\boldsymbol{z}} \qquad \bar{P} = P_A, \qquad \bar{\phi} = 0, \qquad \bar{\boldsymbol{p}} = \hat{\boldsymbol{x}}, \tag{3.17}$$

where $\tilde{A} = \frac{A\mu}{|\alpha|}$ determines shear strength dimensionless shear strength; $\tilde{A} \ll 1$ ($\tilde{A} \gg 1$) implies background shear is much less than (much greater than) active shear. As per the convention adopted in Chapter 2, we drop the tilde denoting a dimensionless quantity, and refer to dimensionless shear as A for the rest of the corresponding analysis. In Fourier space, the linearised governing equations at order $\mathcal{O}(\varepsilon)$ (adapted from Section 3.2, equations (3.3a-f)) become,

$$0 = \kappa_1 u_k - ik_x P_k + is^{\alpha}(k_y\theta_k + k_z\phi_k), \tag{3.18a}$$
$$0 = \kappa_1 v_k - ik_y P_k + is^{\alpha}k_x\theta_k, \tag{3.18b}$$
$$0 = \kappa_1 w_k - ik_z P_k + is^{\alpha}k_x\phi_k, \tag{3.18c}$$
$$0 = \kappa_2\theta_k + \lambda_1^{-}k_y u_k + \lambda_1^{+}k_x v_k + {}^{\lambda_2}\!/_{2}(k_z u_k + k_x w_k) - iA\lambda_1^{-}\phi_k - iA^{\lambda_2}\!/_{2}\theta_k, \tag{3.18d}$$
$$0 = \kappa_2\phi_k + \lambda_1^{-}k_z u_k + \lambda_1^{+}k_x w_k - {}^{\lambda_2}\!/_{2}(k_y u_k + k_x v_k) - iA\lambda_1^{+}\theta_k + iA^{\lambda_2}\!/_{2}\phi_k, \tag{3.18e}$$
$$0 = k_x u_k + k_y v_k + k_z w_k. \tag{3.18f}$$

It is known in literature that a background shear flow can stabilize a suspension of swimming microorganisms by breaking spatial symmetry and giving particles a preferred direction to align to:[86,87] for sufficiently large shear, we find agreement with this and show that introducing background shear dampens long-wavelength perturbations in the system. Shear contributes a coupling between θ_k and ϕ_k due to shear alignment and rotation due to vorticity, which acts independent of the perturbation

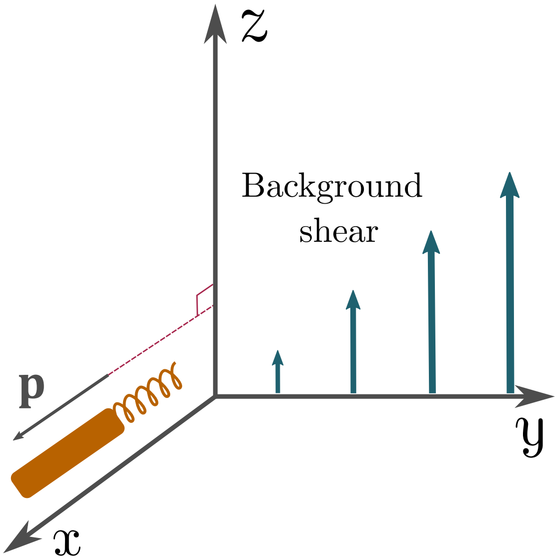

FIGURE 3.11: A rod-like particle with chiral contributions in an imposed shear flow has one constant, steady-state configuration, where its principle axis is orthogonal to a background shear flow.

wavevector as $-iA\lambda_1^-\phi_k$ in equation (3.18d) and $-iA\lambda_1^+\theta_k$ in equation (3.18e). Long-wavelength perturbations of the director in θ_k and ϕ_k experience a restorative torque due to background shear, which stabilises the suspension by suppressing the bend instability which acts at $\mathcal{O}(k)$. In the dispersion relation, plotted in Figure 3.12a, we see that the characteristic long-wavelength perturbation associated with unstable bend modes, is dampened for increasing shear, until A surpasses a critical value A^c for which the system is completely stabilised by imposed shear. This critical value A^c is a function of λ_1, λ_2 only, and A^c asymptotically approaches infinity for $\lambda_1 \to 1$ (Figure 3.12a, *Sub*).

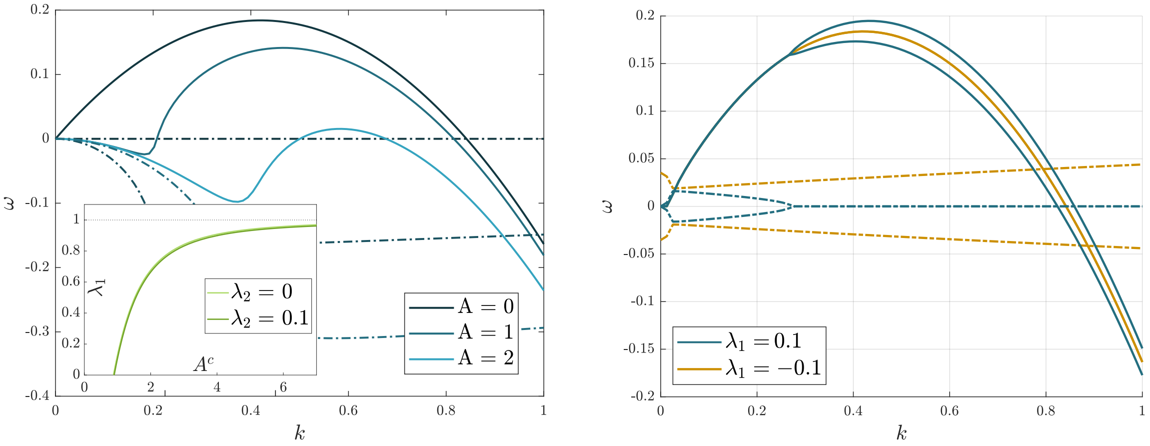

(A)

(B)

Figure 3.12: (A) *Main:* Dispersion relation with background shear A for $k \in [0, 1]$. Imaginary part of ω is solid, real part of ω is dashed. Data is plotted for $\lambda_1 = 0.7$, $\lambda_2 = 0$, $q = 0$. *Sub:* The critical value A^c for which $A > A^c$ the system is unconditionally stable. A^c is strongly a function of λ_1, but λ_2 has a negligent contribution. A^c asymptotically approaches infinity as $\lambda_1 \to 1$. (B) Introducing chirality can destabilize the system for small background shear. When A and λ_2 are the same sign (blue) ω undergoes a bifurcation which can destabilize the system. If A and λ_2 differ in sign (yellow) no bifurcation occurs. Data plotted for $\lambda_1 = 0.7$, $\lambda_2 = -0.1, 0.1$, $A = 0.1$, $q = 0$.

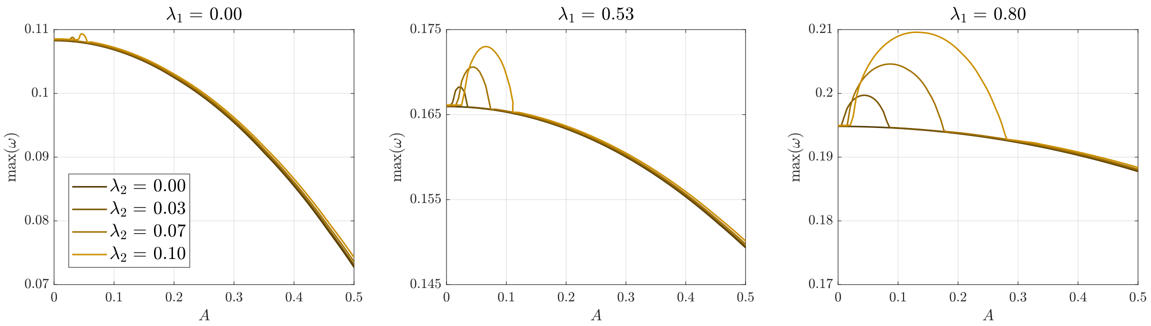

FIGURE 3.13: The maximum of $\mathrm{Imag}(\omega)$ can increase for small values of A and is dependent on both λ_1 and λ_2.

Background shear changes the wave type from stationary to travelling — the driving instability mechanism occurs due to the out-of-phase nature between the fluid pumping, which is proportional to deformation curvature, and alignment to active shear, which is proportional to shear strength. The presence of a background shear enhances active shear gradients and shifts the location of maximal shear from the centre of the bend curvature to just ahead, or just behind it (dependent on the shear direction and phase of the director). The change in location of maximal shear drives a travelling wave, as the director experiences its maximum rotation due to shear slightly ahead (slightly behind) its maximum deformation, causing a forward (backward) travelling wave.

For small background shear, we uncover a new regime where chirality plays an important role in destabilizing the system. When background shear rate A is an order of magnitude less than the active shear rate $\frac{|\alpha|}{\mu}$, chirality and shear alignment can work together to destabilise the suspension beyond the growth rates seen in absence of background shear. The director is orthogonal to plane of imposed shear with the projection of $\boldsymbol{p}$ on to the y-z plane given by $\varepsilon(0\ \theta_k,\ \phi_k)$. Vorticity uniformly rotates the director about the x-axis, vanishing when θ and ϕ are zero. Introducing alignment-to-shear and chirality will deform this orbit, as alignment-to-shear wants to enhance the projection of $\boldsymbol{p}$ into the x-y plane to become aligned to background shear, and chirality rotates the director away from the alignment axis. This breaking of invariance from deviations away from the x-axis appears due to the λ_1^+ and λ_1^- terms in governing equations (3.18e, f).

When A and λ_2 share the same sign, shear alignment alignment and chirality both rotate swimmers out of the ordered direction, and the combination can be strong enough to promote instability beyond the stabilising effect of vorticity term. The phenomena occurs as a bifurcation in ω, seen in the dispersion relation (Figure 3.12b). The location of the bifurcation is critical as to whether the effect enhances instability and is dependent on both λ_1 and λ_2 — if the bifurcation occurs at a wavelength greater than the wavelength of maximum active shear, the effect will still be destabilising, but will not enhance the maximum growth rate. The role of λ_1 in initially promoting the instability is crucial — Figure 3.13 plots the maximum growth rate of ω for varying λ_1 and λ_2, and Figure 3.14 shows the range of values for which λ_1 and λ_2 enhance the instability.

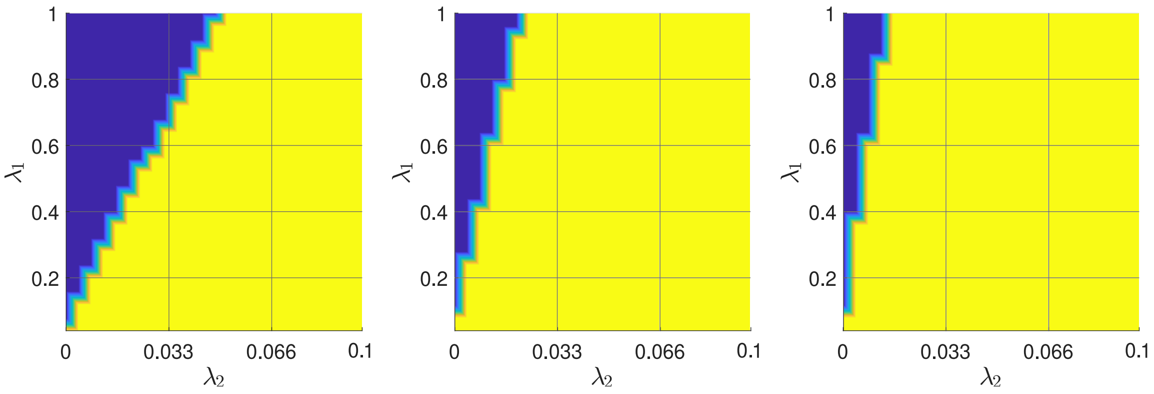

Figure 3.14: The bifurcation of ω depends on λ_1 and λ_2. This parameter space plot categorises where we find different solutions—for blue, chirality is enhancing and we have stationary solutions, in yellow, chirality is not enhancing and we have oscillatory solutions. The plots are plotted left-to-right for $A = [0.1, 0.23, 0.37]$.

Unlike the case of $A = 0$, where the effect of chirality destabilising the system was marginal, here the combined effect of chirality and alignment to shear can meaningfully promote the instability growth rate by up to 10%. Neutralising background shear in experiments *in vivo* is very difficult and the range of background shear for which the phenomena would be seen could be reproduced *in vitro*. This regime remains an area of active interest for future work.

3.5 Remarks: Bend is Dominant for an Extensile Suspension

In Chapter 3 we began to extend the analysis established in Chapter 2 for the Stokesian instability into the 3D regime. In Section 3.3, we established that the growth rates of pure bend deformations in an 3D extensile ordered suspension will always boast faster growth rates than modes comprised of bend and splay deformations put together. This was quantified in Section 3.3.1 when comparing the growth rate of the two unstable eigenvalues for the 3D regime, ω_2^+ and ω_1^+ where we discovered that the modes associated with ω_2^+, which consist of a pure bend deformation, had larger growths rates than the modes of the eigenvalue ω_1^+, which consisted of both bend and splay deformations. When prescribing planar-wave solutions as in a linear stability analysis, bend and splay deformations are a purely 2D phenomena in the sense that the deformations occurs in a 2D plane and causes hydrodynamic forcing into that same plane. A perturbation defined by the wavevector $\boldsymbol{k}$ will have a vectorial component pointing along the x-axis, and the least stable mode associated with ω_2^+ propagates with respect to this component only.

When chiral terms are present (Section 3.3.2) in the governing equation for the director, we saw that the governing equations are re-coupled as chiral particles are rotated orthogonal to active shear induced by bend and splay deformations. Bend remains the fastest growing deformation, and the least stable chiral eigenvalue ω_4^+ describes two coupled bend modes: one propagating in the x-y plane, and one propagating in the x-z plane, with a phase difference of $\pm\pi/2$. The superposition of the two bend modes results in a 'spiralling' mode, whose left/right-handedness depends on whether θ_k and ϕ_k share a positive or negative phase difference.

When the two bend modes exist with a $\pm\pi/2$ phase difference, their corresponding hydrodynamic forcing has a $\pi/2$ phase difference from the respective mode. Alignment-to-shear and rotation due to vorticity are proportional to the derivative of the flow, which brings shear rotational effects in phase with the director deformation, which was illustrated in Chapter 2. However, chiral rotation is governed by active shear *orthogonal* to the director, which due to the phase difference between the bend modes propagating in the x-y and x-z plane, is $\pi/2$ out-of-phase with the director.

Numerically, the effects of chirality are small compared to shear alignment terms, so the net shift in shear-induced rotation due to chirality is small, on the order of $\pi/64$ for $|\lambda_2| = 0.1$. The effect of this phase shift is to create a travelling wave in the director, as maximal shear gradients (and therefore, maximal director rotation) is always slightly ahead (or slightly behind, depending on if θ_k, ϕ_k have a positive or negative $\pi/2$ phase difference) of the maximum deviation of the director from the ordered state.

In the final section of Chapter 3, we imposed a background shear flow orthogonal to the alignment direction (y-z plane). When the director is orthogonal to the alignment direction, vorticity rotates the director about its long axis $\boldsymbol{p}$ and contributes a stabilising effect on the active particles. However, shear alignment seeks enhance the projection of the director in the y-z plane due to the extensile component of the imposed shear, the by-product of which is to enhance chiral effects. When the background shear A is sufficiently small ($A \in [0.1, 0.5]$, where unit is normalised to elasticity balancing active shear flows), we observed an increase in the growth rate of the bend instability when both alignment-to-shear and chiral terms are strong enough to overcome stabilising vorticity. The increase in growth rate as compared to the no-shear regime can be as much as 10%, depending on the values of λ_1 and λ_2.

Chapter 2 and Chapter 3 comprise the first half of this work where we have invested our effort into discussing the instability mechanism for the Stokesian instability, in particular: 1) The mechanical origin of hydrodynamic forcing due to bend and splay deformations in Section 2.1, 2) The role of phase between the fluid and the director summarised by FIGURE 2.9 and FIGURE 2.12, 3) The consequence of bend and splay being a 2D phenomena and the emergence of dominant bend modes in 3D, discussed in Section 3.3.1, 4) The re-coupling of the governing equations for chirality in Section 3.3.2, and, 5) A new regime of instability with imposed shear, which can enhance growth rates beyond that of the unbounded regime in Section 3.4. In the second half of this work, we will explore the consequences of confinement, connecting bulk instability growth rates to regimes of weak, intermediate and strong confinement; we will discuss the role of boundary conditions on the types of modes we can expect to observe experimentally, and, we will investigate non-constant, steady director and steady flow fields.

4 | Confinement due to a Channel and Film

4.1 Literature Examples of Confinement

Academic literature contains many examples of analytical, numerical and experimental extensions to the active matter Stokesian instability: in a paper published by Sumesh Thampi,[40] the bend instability for an extensile suspension was explored by numerical simulation to understand the effects of topological defects in the director. Thampi demonstrated that the bend instability develops into mesoscale turbulence with two distinct phases: firstly, the suspension undergoes the Stokesian instability to develop walls of strong bend deformations; secondly, the walls relax by forming oppositely charged pairs of $\pm\frac{1}{2}$ defects. The $\pm\frac{1}{2}$ defects are associated with high positive and negative vorticity and a state of mesoturbulence emerges as the defects disperse throughout the neighbouring region, where spontaneous annihilation and creation events continually occur. Doostmohammadi & Yeomans,[7] and Chandragiri[88] similarly study the effects of topological defects in the suspension by utilising active matter simulations for active particles in a channel under imposed flow conditions, where they reveal regimes for 'active turbulence' as a function of activity and channel width (Figure 4.1b).

In an early result, Sankararaman & Ramaswamy[51] analytically extended the instability to a thin-film regime of confinement. In a regime of strong confinement, the destabilizing role of the active stress tensor is suppressed by the boundary conditions of alignment on the director which suppresses the propagation of bend and splay deformations. To investigate possible mechanisms for instability, Sankararaman & Ramaswamy incorporate a boundary condition at the free-surface which couples polar active units to the local free-surface tilt, which takes the form $-C\int \boldsymbol{p}_\perp \cdot \nabla_\perp h \, \mathrm{d}^2x$, where x is a spatial coordinate along the free-surface profile described by h and determined by the kinematic boundary condition (Section 4.2), $\perp$ indicates gradients perpendicular to the unperturbed free-surface and C is a phenomenological constant. By directly coupling director deformations to a free-surface tilt, the resulting instability mechanism is entirely determined by boundary effects, and their analysis reveals an instability with a growth rate on the order of $|\alpha| C k^2$, to leading order of wavefrequency k, which vanishes for $C \to 0$. Notable from this work is the direct dependence of the instability mechanism to the choice of boundary conditions; in particular, careful consideration must be taken to choose boundary conditions reflective of observed behaviours.

The majority of numerical and experimental results have thus-far been restricted to two dimensions,[13] but recent results have unveiled unique dynamics in the 3D regime: Chatterjee *et al.* include inertia in a theoretical analysis where the instability is stabilised to a statistically steady isotropic hedgehog-defect turbulent state;[53] Strubing *et al.*[90] conduct experiments on microtubule and kinesin-1 motors, revealing a unique 'wrinkling' instability for which the known bend-instability contracts a microtubule ribbon into the z-axis. In a particularly relevant recent publication, Chandrakar *et al.*[6] (FIGURE 4.1A) explore regimes of intermediate confinement by experimentally investigating the instability in the 3D regime for active liquid crystals composed of extensile microtubule bundles and kinesin molecular motors. The microtubule bundles were placed in long channel of height 100μm and width 3mm. The dominant instability plane for the microtubule bundles is set by the confining boundaries and

---

[*] Reprinted figure with permission.[6] DOI, `http://dx.doi.org/10.1103/PhysRevLett.125.257801`

[†] Reprinted figure with permission, under Open Access.[89] DOI, `https://doi.org/10.1140/epjst/e2019-700109-x`

the authors revealed that the Stokesian instability survives when confinement length scale is larger than the length scale set by the balance of activity driven flow and elastic restoration, which we find agreement with in Section 4.4.1. The experiments validate the value of a linear instability analysis, as the authors reveal a linear growth regime in the initial phase of the instability before being proceeded by exponential growth. The choice of boundary conditions is strongly influential on the types of phenomena we might expect to observe, as the dominance of boundary conditions *"demonstrate[s] the inherent challenge of using boundary-free calculations to explain experiments"*. The experiments are exemplar for demonstrating the existence of the bend-instability in bacterial active matter and the results are qualitatively similar to the theoretical analysis we will perform in this chapter. In the second half of this work, we wish to add our analysis to this mature field by capturing a question common to all regimes of confinement: *How does confinement affect the stability of a momentum-conserving suspension of active particles?*

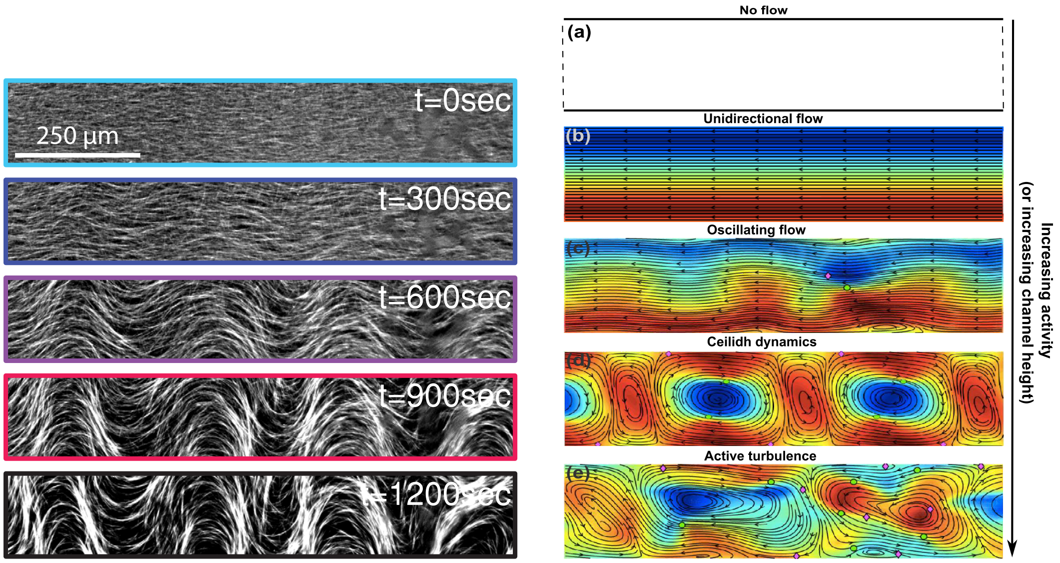

FIGURE 4.1: (A) An exemplar demonstration of the bend instability in confined microtubule-based active nematics. Reproduced from Chandrakar **et al.* 2020.[6] (B) Simulations reveal the underlying flow states of active nematics confined in a channel. Reproduced from Doostmohammadi & Yeomans, 2019[†][7]

4.2 Common Active Matter Boundary Conditions

Active matter suspensions typically exist in regimes of strong confinement: sperm navigating the female reproductive tract, white blood cells in veins, cancerous cells in tumours, rods in granular active matter. Confinement is characterised by two factors: geometry and boundary effects. Typical geometries of interest include channels with rigid boundaries such as arteries, films with deformable interfaces such a mucus membranes, junctions between channels such as veins and lattice structures like the extracellular matrix. Each geometry can have many different boundary effects: rigid boundaries can be elastic,[91] films can be permeable,[92] swimmers can display unique mechanical phenomena such as 'slipping' at a boundary,[49] and navigating through a lattice presents complex path-finding problems for a microswimmer, which qualitatively change observed behaviour.[93]

For this work, we wish to address appropriate boundary conditions for coarse-grained active matter. Specifically, we wish to explore how the choice of boundary conditions in the coarse-grained limit can reflect observed behavioural mechanisms in the microscopic limit. We will interpret our results in the framework of the instability analysis discussed in Chapter 2 and Chapter 3, seeking to understand how commonly used boundary conditions affect the Stokesian instability and introducing confinement as an infinitely long film and channel in both 2D and 3D regimes. To facilitate this analysis, we will begin by introducing the geometries of interest and discussing general forms of common boundary conditions on the fluid and the director before making the appropriate simplifications for a linear instability analysis in both 2D and 3D regimes.

In this work, we characterise a channel by two rigid walls placed orthogonal to the z-axis at $z = 0$ and $z = h$, where the distance between the two walls is measured by a constant parameter h. In the 2D regime, this leaves the x-axis unbounded, and in the 3D regime this leaves the x-y plane unbounded. We will also discuss the dynamics of a film, which is similarly defined, but with a free-surface at $z = h$ instead of a rigid wall. In principle, we could allow h to vary in the film regime (corresponding to a deforming free-surface), but to isolate the affect of boundary conditions on the instability mechanism, we will leave h as a constant.

Experimental observations of fluid kinematics at boundaries reveal that the fluid velocity at a boundary must equal the velocity of the boundary itself. This velocity continuity condition imposes constraints on both the tangential components and normal components of the fluid. The first constraint, which is imposed on the tangential components, is known as the 'no-slip' boundary condition, and when the rigid wall is stationary this boundary condition becomes,

$$\boldsymbol{u} \cdot \boldsymbol{t} = 0, \tag{4.1}$$

where $\boldsymbol{t}$ is a tangential vector to the boundary. The second constraint, which is imposed on the normal components, is known as 'impermeability', and reflects the fact that fluid particles cannot pass through a rigid wall, nor leave its surface. Again, for a stationary rigid wall, this yields the boundary condition,

$$\boldsymbol{u} \cdot \boldsymbol{n} = 0, \tag{4.2}$$

where $\boldsymbol{n}$ is the vector orthogonal to the boundary. For a 2D or 3D channel, matching the velocity of the fluid and boundary through the no-slip and impermeability conditions is sufficient to describe the fluid dynamics, but to describe the free-surface at a film we additionally need to resolve the total stress acting across the boundary. This is known as the 'stress continuity' condition and reads,

$$(\boldsymbol{\sigma}^{f_1} - \boldsymbol{\sigma}^{f_2}) \cdot \boldsymbol{n} = 0. \tag{4.3}$$

Here, $\boldsymbol{\sigma}^{f_1}$ and $\boldsymbol{\sigma}^{f_2}$ denote the stress tensors for each fluid (or gas) either side of the boundary. In principle, the right-hand side of (4.3) should be proportional to the product of the curvature of the free-surface and surface tension, but as we are only considering a constant free-surface in this work, we can unequivocally set it to zero. In this work, the total (dimensionless) stress is comprised of the viscous stress tensor (1.10) and the active stress tensor (1.17), which together read

$$\boldsymbol{\sigma}^{f_1} = -P\boldsymbol{\delta} + 2\boldsymbol{E} + s^{\alpha}\boldsymbol{pp}. \tag{4.4}$$

Similarly to velocity continuity, the stress continuity condition (4.3) imposes a normal and tangential condition on the fluids either side of the boundary. Often, we might have a gas or a liquid with a small viscosity compared to the fluid in the film, and in these regimes the second stress tensor reduces to a pressure constraint which we can approximate as a constant P_A such that, $\boldsymbol{\sigma}^{f_2} = -P_A\boldsymbol{\delta}$. Then the normal and tangential condition on the fluid read,

$$-P + 2\boldsymbol{n}\cdot\boldsymbol{E}\cdot\boldsymbol{n} + 2s^{\alpha}(\boldsymbol{p}\cdot\boldsymbol{n}) = -P_A, \tag{4.5}$$

$$\boldsymbol{t}\cdot\boldsymbol{E}\cdot\boldsymbol{n} + s^{\alpha}(\boldsymbol{p}\cdot\boldsymbol{t})(\boldsymbol{p}\cdot\boldsymbol{n}) = 0. \tag{4.6}$$

To complete (4.5) and (4.6) requires a description of the director at the free-surface and the fluid velocity at the free-surface. Application of the velocity continuity boundary condition at the free-surface determines the ‘kinematic’ boundary condition, which again tells us that fluid particles at the interface must remain at the interface,

$$\partial_t h + \boldsymbol{u}\cdot\nabla h = \boldsymbol{u}\cdot\boldsymbol{n}. \tag{4.7}$$

Since we have determined that h remains constant for this work, this reduces to

$\boldsymbol{u} \cdot \boldsymbol{n} = 0$ at the free-surface. Finally it remains to determine the constraints on the director, both at the rigid boundary and free-surface. In the introductory chapter describing the governing equations for suspension (Section 1.2.2), we introduced the Frank free-energy which describes a free-energy arising from elastic deformations. The integrand of the Frank free-energy (equation (1.32)) was split into a bulk and surface energy contribution, where the surface contributions are omitted in the calculation of the static equilibrium condition. Surface energy contributions are re-introduced phenomenologically by considering a strong anchoring regime at a rigid wall, which determines a regime where the substrate can impose strong torques on the director. In its simplest form, this corresponds to,

$$\boldsymbol{p} \cdot \boldsymbol{n} = \sin(\beta_j), \tag{4.8}$$

where $\beta_j = 0$ corresponds to swimmers parallel to the substrate and $\beta_j = \frac{\pi}{2}$ corresponds to swimmers orthogonal to the substrate. Throughout this Chapter, we will consider $\beta_j = 0$, with a non-zero β_j considered in Chapter 5. In the 2D regime, as the director is subjected to a unit vector constraint, (4.8) is sufficient to completely determine the director at a rigid substrate. In the 3D regime, we must also consider the tangential component of the director. Fine tuning the mechanical and chemical properties of a substrate would theoretically allow for any alignment condition at the rigid boundary, including those where active shear is produced due to the local director profile. However, since we're conducting a linearised instability analysis around a constant steady-state, imposing a non-zero tangential alignment condition (with respect to the ordering direction) on the director would impose twist across the suspension. This is discussed further in Section 4.9, but for the majority of this work we will a no-twist condition at the substrate, such that we are aligned to the bulk,

$$\boldsymbol{p} \cdot \boldsymbol{t} = \hat{\boldsymbol{x}}. \tag{4.9}$$

The free-surface constitutes a weak-anchoring regime where we cannot impose strong torques on the director, consequently, by the above reasoning, the tangential component of the director must also satisfy $\boldsymbol{p} \cdot \boldsymbol{t} = 0$. In Section 1.2.1, we discovered that splay gradients in the director yield active flows directed parallel to the local ordering direction as, $(\nabla \cdot \boldsymbol{p})\boldsymbol{p}$: to maintain consistency with the kinematic boundary condition (4.7) and a constant free-surface, it follows that the normal component of the director at the free-surface must also be zero, which yields an 'impermeability-like' condition such that,

$$\boldsymbol{p} \cdot \boldsymbol{n} = 0. \tag{4.10}$$

With (4.8) and (4.10) determined by the director boundary conditions, we can summarise the full set of boundary conditions for our active matter suspension. At a rigid wall, the no-slip (4.1), fluid impermeability (4.2), aligned director (4.8), and in 3D, no-twist condition (4.9), together read,

$$\boldsymbol{u} \cdot \boldsymbol{t} = 0, \tag{4.11a}$$

$$\boldsymbol{u} \cdot \boldsymbol{n} = 0, \tag{4.11b}$$

$$\boldsymbol{p} \cdot \boldsymbol{n} = 0, \tag{4.11c}$$

$$\boldsymbol{p} \cdot \boldsymbol{t} = \hat{\boldsymbol{x}}. \tag{4.11d}$$

The boundary conditions at the free-surface comprise of the kinematic boundary condition (4.7), which with a constant free-surface profile h reduces to an impermeability condition, the tangential stress condition (4.6), which with $\boldsymbol{p} \cdot \boldsymbol{n} = 0$ reduces to a no-shear condition, aligned director (4.8), and in 3D, no-twist condition (4.9), which together read,

$$\boldsymbol{u} \cdot \boldsymbol{n} = 0, \tag{4.12a}$$

$$\boldsymbol{t} \cdot \boldsymbol{E} \cdot \boldsymbol{n} = 0, \tag{4.12b}$$

$$\boldsymbol{p} \cdot \boldsymbol{n} = 0, \tag{4.12c}$$

$$\boldsymbol{p} \cdot \boldsymbol{t} = \hat{\boldsymbol{x}}. \tag{4.12d}$$

Equations (4.11) and (4.12) form a minimalistic set of boundary conditions for the fluid and director in either a film or channel and either a 2D or 3D regime. The boundary conditions form a reference point from which we will establish a link between the instability mechanism in the bounded and unbounded regime and are the default set of boundary conditions discussed in this work. Where other boundary conditions are used, such as in Section 4.9 and Chapter 5, it will be stated which boundary conditions have been replaced.

4.3 Numerical Methods in Matlab

Up until this point, we have utilised an analytic analysis to find the dispersion relation for perturbations of the linearised governing equations (2.8). We have sought Fourier-mode solutions of the form $f = f_k \exp(i\boldsymbol{k}\cdot\boldsymbol{x} - i\omega t)$, where f_k is held constant. Introducing confinement into the system necessitates allowing f_k to vary across the channel/film height, which yields a z-dependence as,

$$f = f_k(z) \exp(i\boldsymbol{k}_{\parallel} \cdot \boldsymbol{x} - i\omega t), \tag{4.13}$$

where $\boldsymbol{k}_{\parallel}$ denotes components of $\boldsymbol{k}$ orthogonal to the axis of confinement, such that $\boldsymbol{k}_{\parallel} = (k_x,\ k_y,\ 0)$ in the 3D regime and $k_y = 0$ in the 2D regime. Initially, we will continue to use the set of linearised governing equations about the ordered, constant steady-state, $\bar{\boldsymbol{u}} = \boldsymbol{0}$, $\bar{\boldsymbol{p}} = \hat{\boldsymbol{x}}$, discussed in Chapter 3 (3.1a—3.1d) which in component form read,

$$
\begin{aligned}
0 &= -\xi\partial_t u_1 - \partial_x P_1 + \nabla^2 u_1 + s^\alpha(\partial_y\theta_1 + \partial_z\phi_1), && \text{(4.14a)}\\
0 &= -\xi\partial_t v_1 - \partial_y P_1 + \nabla^2 v_1 + s^\alpha\partial_x\theta_1, && \text{(4.14b)}\\
0 &= -\xi\partial_t w_1 - \partial_z P_1 + \nabla^2 w_1 + s^\alpha\partial_x\phi_1, && \text{(4.14c)}\\
0 &= -\partial_t\theta_1 + \lambda_1 E_{yx} + \lambda_2 E_{zx} - \Omega_{yx} + \eta^{-1}\nabla^2\theta_1, && \text{(4.14d)}\\
0 &= -\partial_t\phi_1 + \lambda_1 E_{zx} - \lambda_2 E_{yx} - \Omega_{zx} + \eta^{-1}\nabla^2\phi_1. && \text{(4.14e)}\\
0 &= \partial_x u_1 + \partial_y v_1 + \partial_z w_1. && \text{(4.14f)}
\end{aligned}
$$

Substitution of the z-dependent Fourier modes (4.13) into the linearised governing equations (4.14) returns a linear system of ODEs,

$$
\begin{aligned}
0 &= \kappa_1 u_k + u_k'' - ik_x P_k + s^\alpha(ik_y\theta_k + \phi_k') && \text{(4.15a)}\\
0 &= \kappa_1 v_k + v_k'' - ik_y P_k + is^\alpha k_x\theta_k && \text{(4.15b)}\\
0 &= \kappa_1 w_k + w_k'' - P_k' + is^\alpha k_x\phi_k && \text{(4.15c)}\\
0 &= \kappa_2\theta_k + \lambda_1^- k_y u_k + \lambda_1^+ k_x v_k + {}^{\lambda_2}\!/_2(k_x w_k - iu_k') + i(k^2\theta_k - \theta_k'') && \text{(4.15d)}\\
0 &= \kappa_2\phi_k - i\lambda_1^- u_k' + \lambda_1^+ k_x w_k - {}^{\lambda_2}\!/_2(k_y u_k + k_x v_k) + i(k^2\phi_k - \phi_k'') && \text{(4.15e)}\\
0 &= ik_x u_k + ik_y v_k + w_k', && \text{(4.15f)}
\end{aligned}
$$

where, $\kappa_1 = i\xi\omega - k^2$ and $\kappa_2 = \omega + i\eta^{-1}k^2$ and $k^2 = |\boldsymbol{k}|$. Note that differentiation of the Fourier modes (4.13) with respect to x and y brings down from the exponent k_x and k_y respectively, but differentiation with respect to z yields $\frac{\partial f}{\partial z} = f_k'$. Then, application of the boundary conditions discussed in Section 4.2 yields a 10th-order boundary-value problem (BVP).

As more terms are included in the governing equations for the active matter system, analytic solutions become increasingly difficult to attain, and a numerical approach can be preferable to analytically solving the BVP. We choose to conduct our numerical analysis on MATLAB 2021A, utilising the in-built numerical BVP solvers bvp4c, or bvp5c which implement the three-stage Lobatto IIIa formula.[94] The Lobatto IIIa formula utilises approximations to the solution of a BVP problem taken at the end-points z_i and z_{i+1} from the subinterval $\{z_i, z_{i+1}\}$. Consequently, solving BVP problems using in-built MATLAB solvers requires intelligent guesses at possible solutions to the BVP, and an inaccurate initial approximations will result in a divergence between the approximation and the solution. If this divergence grows too large, the numerical algorithms will fail and no solution will be returned.

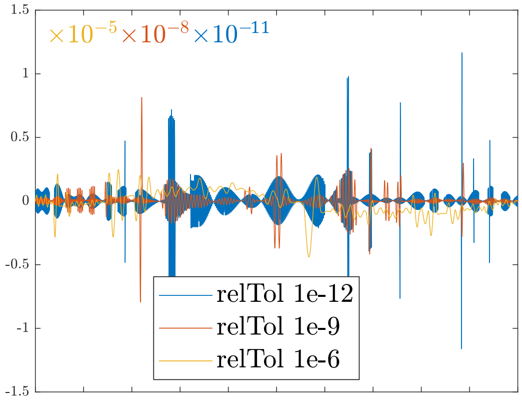

FIGURE 4.2: Differences between solutions for the eigenvectors of the 2D channel. Solutions vary in accuracy and are measured against a reference solution at accuracy *relTol* 1e-15. Differences are scaled according to axis labeling.

The in-built MATLAB BVP solvers allow the user to determine this divergence threshold by controlling the maximum size of the error estimate by means of two optional arguments: *relTol*, which determines the relative difference between two successive points along the BVP, and *absTol*, which determines the absolute difference between successive points (FIGURE 4.2). As the solver progresses over the solution domain, it can utilise an adaptive mesh size to ensure the solver always maintains the required accuracy between successive points in the solution space. Increasing the accuracy beyond a minimum threshold is necessary to ensure the solver is converging to a correct solution, but beyond this threshold decreasing error tolerances provide no meaningful benefit. To solve the coupled system of ODEs in (4.14), MATLAB's numerical solvers require the 10th–order system to be broken down into a system of coupled first–order differential equations, which can be written as,

$$
\begin{aligned}
f_1 &= u_k, & f_2 &= v_k, & f_3 &= w_k,\\
f_4 &= u_k', & f_5 &= v_k', & f_6 &= P_k,\\
f_7 &= \theta_k & f_8 &= \phi_k, & &\\
f_9 &= \theta_k' & f_{10} &= \phi_k'. & &
\end{aligned}
$$

Then, taking $\frac{\partial f_i}{\partial z}$ and substituting (4.15a–4.15f) yields the coupled-equations,

$$
\begin{pmatrix} f_1' \\ f_2' \\ f_3' \\ f_4' \\ f_5' \\ f_6' \\ f_7' \\ f_8' \\ f_9' \\ f_{10}' \end{pmatrix}
=
\begin{pmatrix}
u_k' \\
v_k' \\
-ik_x u_k - ik_y v_k \\
-\kappa_1 u_k + ik_x P_k - s^\alpha(ik_y\theta_k + \phi_k') \\
-\kappa_1 v_k + ik_y P_k - is^\alpha k_x \theta_k \\
\kappa_1 w_k - ik_x u_k - ik_y v_k + is^\alpha k_x \phi_k \\
\theta_k' \\
\phi_k' \\
-\kappa_2\theta_k - \eta\Big(\lambda_1^- k_y u_k + i\lambda_1^+ k_x v_k + {}^{\lambda_2}\!/_2\Big(u_k' + ik_x w_k)\Big) \\
-\kappa_2\phi_k - \eta\Big(\lambda_1^- u_k' + \lambda_1^+ ik_x w_k - {}^{\lambda_2}\!/_2\Big(ik_y u_k + ik_x v_k\Big)\Big)
\end{pmatrix}
\tag{4.16}
$$

where all quantities can be re-expressed in terms of f_i. The parameters $\boldsymbol{k}$, ξ, s^α, η, λ_1 and λ_2 can all explicitly be provided to the numerical solvers as values, but the complex wave-frequency ω (also contained in κ_i) is an unknown parameter and a function of $\boldsymbol{k}$, as seen in (2.15) and (3.11a–3.12b). The existence of the unknown parameter ω turns equations (4.16) into an eigenvalue for eigenvalue ω and eigenmodes f_k, and solving for ω requires an additional boundary condition to (4.12) and (4.11) to satisfy the extra degree of freedom. Since we are solving a perturbation analysis, the magnitude of the Fourier modes f_k is arbitrary, and we can choose any f_k which is non-zero at the boundary. We choose to set the velocity gradient $v_k' = 1$ at $z = 0$, as this is modelled as a rigid substrate for both the channel and film regimes in both 2D and 3D, which has the effect of scaling all the Fourier modes relative to velocity gradients near the substrate, which will almost always be non-zero due to the no-slip condition.

Boundary-value problems can have one, many, or even infinitely many solutions, and the convergence of the numerical BVP solvers to a solution is heavily dependent on providing meaningful initial guesses which fulfil the provided boundary conditions. Two major considerations must be made when conducting a numerical instability analysis: First, a substantial search must be conducted to identify which solutions are the most dominant and likely to appear experimentally for a given wavelength. Second, since we are interested in constructing the numerical equivalent of the dispersion relation as in (2.15) and (3.11a–3.12b), we need to be able to establish if any two solutions produced by the numerical BVP solvers are the same type of solution, or exist on a different branch entirely.

In order to satisfy these considerations, I developed a custom interface to MATLAB's BVP solvers which establishes the authenticity of a solution returned from the `bvp4c` or `bvp5c` solvers, for which the numerical algorithm is summarised graphically in FIGURE 4.3. After using guesses to find an initial likely solution $F^1_{\chi_1}$ for a given set of parameters χ_1 to the BVP problem for a given wavevector k_1, this initial solution is converted into a format which can be used as an approximation for the next desired solution $F^2_{\chi_1}$ for wavevector k_2. This process can be repeated iteratively until a target wavevector k_n is reached, at which point the entire array of solutions $F^1_{\chi_1} \dots F^n_{\chi_1}$ is algorithmically scanned to verify its continuity. The continuity of this solution space is established by inspecting the $F^i_{\chi_1}$ solutions eigenmodes and dispersion relation for discontinuities with respect to changes in the wavevector k_i. Where problematic solutions are discovered, they can be resolved by increasing the number of solution points between $F^{i-1}_{\chi_1}$ and $F^i_{\chi_1}$, or traversing the solution space backwards to use $F^{i+1}_{\chi_1}$ as an approximation to $F^i_{\chi_1}$. After establishing the continuity of solutions $F^1_{\chi_1} \dots F^n_{\chi_1}$, the entire solution space can be solved in parallel utilising MATLAB's in-built parallelisation-functionality for a new set of parameters χ_2, re-checked for discontinuity errors, and iteratively re-solved until a desired target parameter set χ_m is reached.

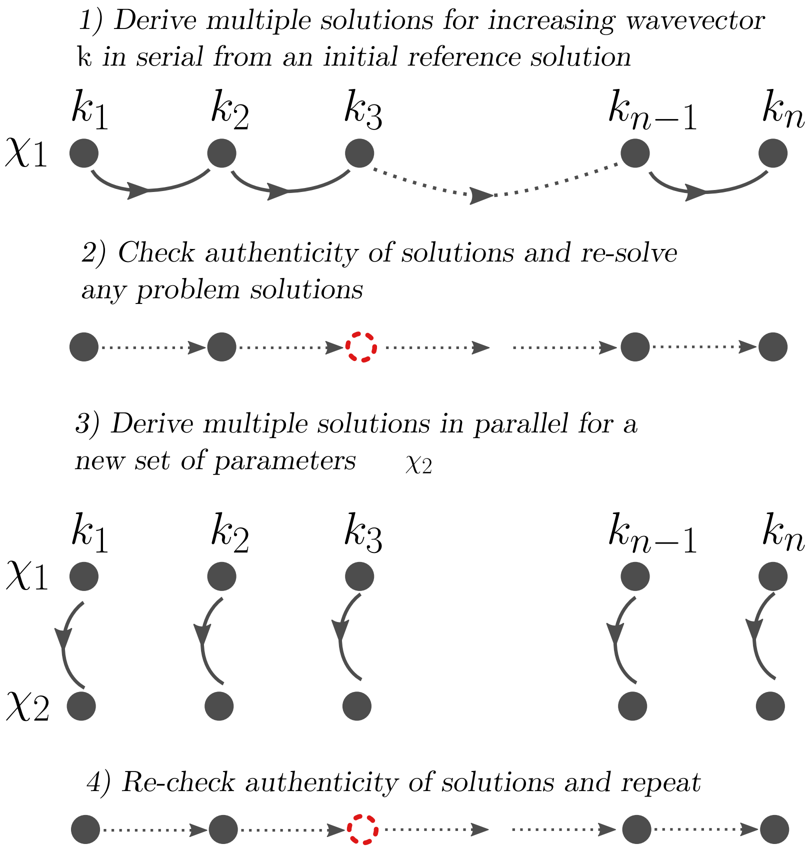

FIGURE 4.3: Numerical algorithm for establishing the continuity of solutions over wavevector.

By this methodology, we are able to track the evolution of a particular branch of solution over large changes in parameter space, identify competing stabilising and destabilising mechanisms, and confidently connect the growth rates in unbounded and strongly-bounded regimes. All graphs and figures hereafter are plotted using data produced from this custom interface, where the eigenvalues plotted are those whose eigenmodes have the fastest growth rates. The code will be published at a later date for public use, and the code and solutions are available on request.

4.4 2D Channel: Emergence of the Vortex Lattice

The 2D channel represents an experimentally realisable regime for which orientational symmetry is broken in a controlled manner. Whilst minimalistic, it provides an excellent stepping stone to understanding the behaviour of the disturbed state in more complex confinements and regimes. Our analysis in the 2D regime revealed that an extensile suspension is most unstable to perturbation wavevectors which are parallel to the ordered axis, but that the corresponding fluid flow is perpendicular to the ordered axis. *A priori* we might hypothesise that when the ordered axis is along the length of an infinite channel, that confinement will suppress the columns of fluid perpendicular to the ordered axis by virtue of impermeability, and further, that the bend deformation will be suppressed near the boundaries due to alignment. In the following analysis, we reveal how both boundary conditions actually affect the modes and which boundary condition can be considered 'stronger', in the sense of suppressing instability growth.

We model the infinitely long channel, extending along the x-axis, with the steady ordered state also aligned along the x-axis, corresponding to the configuration used throughout the rest of this work. Confinement is modelled at $z = 0$ and $z = \tilde{h}$ by two rigid walls which impose the set of boundary conditions given by (4.11) consisting of

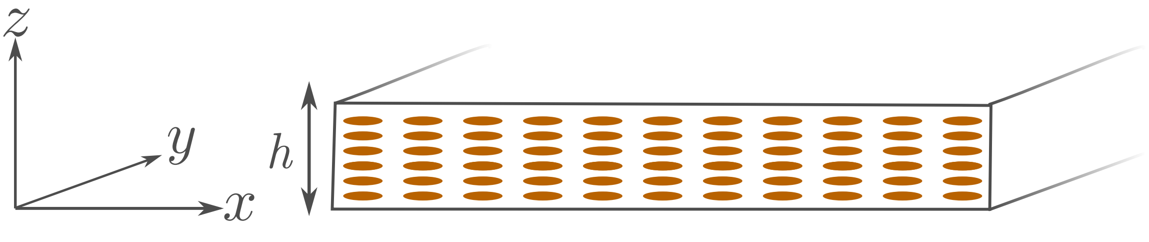

FIGURE 4.4: Orientation of axes for the 2D and 3D channel and film. The channel/film width is given by h and confinement is modelled at $z = 0$ and $z = h$ by the appropriate boundary conditions. The director is aligned along the x-axis in the ordered state. In the 2D regime, dynamics in the y-axis are suppressed.

no-slip (4.11a) and impermeability (4.11b) on the fluid, and strong anchoring (4.11c) and no-twist on the director (4.11d). Here, the channel width is described by $\tilde{h} = \frac{h}{L}$, (tilde droped hereafter) where L is the characteristic length scale balancing activity driven shear and elasticity.

In Section 4.4.1 we begin exploring confinement for the 2D channel (FIGURE 4.4) in the limit of $h \gg 1$, corresponding to the modes of instability comparable to the unbounded regime. Our goal is to compare the instability growth rate in regimes of weak confinement to the analysis conducted in Chapter 2 and Chapter 3, and in particular, to understand the quantitative differences between observed modes. In Section 4.6 we reduce h to find the critical length h^c for which confinement suppresses the instability. We use this critical width as a control parameter to provide a framework for understanding the effect of different boundary conditions, which we later explore in Section 4.9 after discussing the 3D regime in Section 4.7.

All analysis is conducted for an extensile suspension with the parameter set $\eta^{-1} = 1.2$, $\xi = 1.1$, $\lambda_1 = 0.7$, except where indicated (see Section 2.2.1 for parameter estimates). In Chapter 2, we discovered that there are broadly two types of eigenmode with associated eigenvalues $\omega^{\pm}$ where we discovered that for an extensile suspension, ω^{+} yielded unstable modes and ω^{-} yielded stable modes. The two types of eigenmode emerge due to the possibility of the director and fluid being $\pm\frac{\pi}{2}$ out-of-phase with one another when subject to a pure bend deformation. In the numerical analysis for the bounded regime, there are a multitude of eigenvalues corresponding to different ordered modes, but they can still be characterised by their phase difference between the director and fluid. Consequently, hereafter we will use ω^{+} to denote the eigenvalue with the fastest growing eigenmodes and a $\frac{\pi}{2}$ phase difference between the director and fluid (which is generally unstable), and ω^{-} to denote the eigenvalue with the fastest growing eigenmodes with a $-\frac{\pi}{2}$ phase difference between the director and fluid (which is generally stable). We will see that the fastest growing eigenmodes are associated with order 1 modes (Section 4.4.1.1) which will be denoted $\omega^{\pm}_{n=1}$, where the subscript is dropped hereafter for the $n = 1$ case.

4.4.1 Recovering Bulk Stability Growth Rates

When the channel width is large, the effects of confinement are only felt close to the channel wall which imposes constraints on fluid propagation due to the no-slip and impermeability conditions (4.11a, 4.11b) and can impose surface torques on the director due to director alignment (4.11c, 4.11d), where the rigid boundary conditions (4.11) on the director $\boldsymbol{p}$ in the 2D regime correspond to the conditions $\theta_k = 0$ and $\phi_k = 0$ on the Fourier modes. Consequently, when solving the eigenvalue problem set by equations (4.15) for eigenvalue ω, we expect to retrieve the instability growth rates $\mathrm{Im}(\omega)$ discussed in Chapter 2 as confinement length $h \to \infty$. In the analytical analysis conducted in the first half of this work, eigenvalues which led to unstable eigenmodes with a phase difference of $\frac{\pi}{2}$ between the director and fluid were referred to as ω^{+}_{j}, and eigenvalues which led to stable eigenmodes with a phase difference of $-\frac{\pi}{2}$ between the director and fluid were referred to as ω^{-}_{j} where j refers to an eigenvalue discussed in a specific regime. We keep this notation for the second half of this work and always plot the least stable modes for both ω^{+} and ω^{-}, except where explicitly mentioned.

In FIGURE 4.5, we graph the numerically determined dispersion relation for unstable and stable eigenvalues ω^{+} and ω^{-} in the 2D channel alongside the dispersion relation described in Chapter 2 for ω^{+}_{1} and ω^{-}_{1} (determined by equation (2.15)). The numerical results strongly agree with the 2D bulk analysis for short-wavelength perturbations at $h = 100$ and indicate unstable, stationary waves for $\omega^{+}_{k=k^m}$ where k^m is the least-stable wavenumber (FIGURE 4.5, LEFT, *main*). Confinement introduces a new phenomena for long-wavelength perturbations; FIGURE 4.5, (*Sub*) indicates the system undergoes a bifurcation at $k = k^c$ for which the growth rate of eigenvalues ω^{+} and ω^{-} converge, and both modes collapse into a stable mode with travelling wave solutions for $k < k^c$. The phenomena occurs when the perturbation wavelength crosses a threshold on the order of $k^c \approx \pi/h$, *i.e.* when the disturbance wavelength exceeds the channel width.

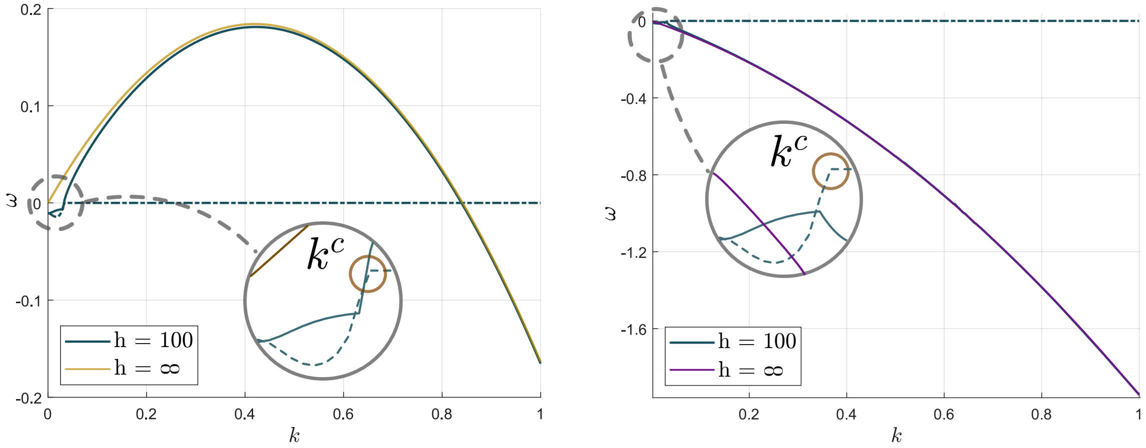

Figure 4.5: Dispersion relation for a 2D channel with rigid wall boundary conditions (4.11) applied at both $z = 0$ and $z = h$ for width $h = 100$. Numerical data is in blue, where the growth rate $\mathrm{Im}(\omega)$ is solid, and wave speed $\mathrm{Re}(\omega)$ is dashed. Left, *Main:* The numerical dispersion relation for ω^+ has excellent agreement with analytic results, where ω_1^+ is in yellow. *Sub:* ω^+ undergoes a bifurcation for $k < k^c$. Right, *Main:* The numerical dispersion relation for ω^- also has excellent agreement with analytical results, where ω_1^- is in purple. *Sub:* ω^- undergoes the same bifurcation for $k < k^c$.

To investigate this phenomena further, we plot the eigenvector, quiver and streamline plots for $\omega^{\pm}$ at $k = 0$, $k < k^c$, and ω^+, ω^- at $k > k^c$ in Figure 4.6. Referencing the analysis in Chapter 2, note that when the complex argument of $\boldsymbol{u}$ and $\boldsymbol{p}$ is an integer multiple of $\pi/2$, this is indicative of stationary wave solutions for the bend deformation. In the unbounded case, the vectorfield plots (Figure 2.10) illustrated a bend perturbation in director with well-defined columns of fluid, alternating in direction depending on the phase of $\boldsymbol{p}$ and Figure 4.6c, d for $k > k^c$ indicates that the finite channel yields the same instability mechanism as the unbounded regime. Confinement, by virtue of the impermeability boundary condition, forces these fluid columns to 'collapse' at the boundaries, causing oscillatory modes and creating a vortex lattice along the channel.

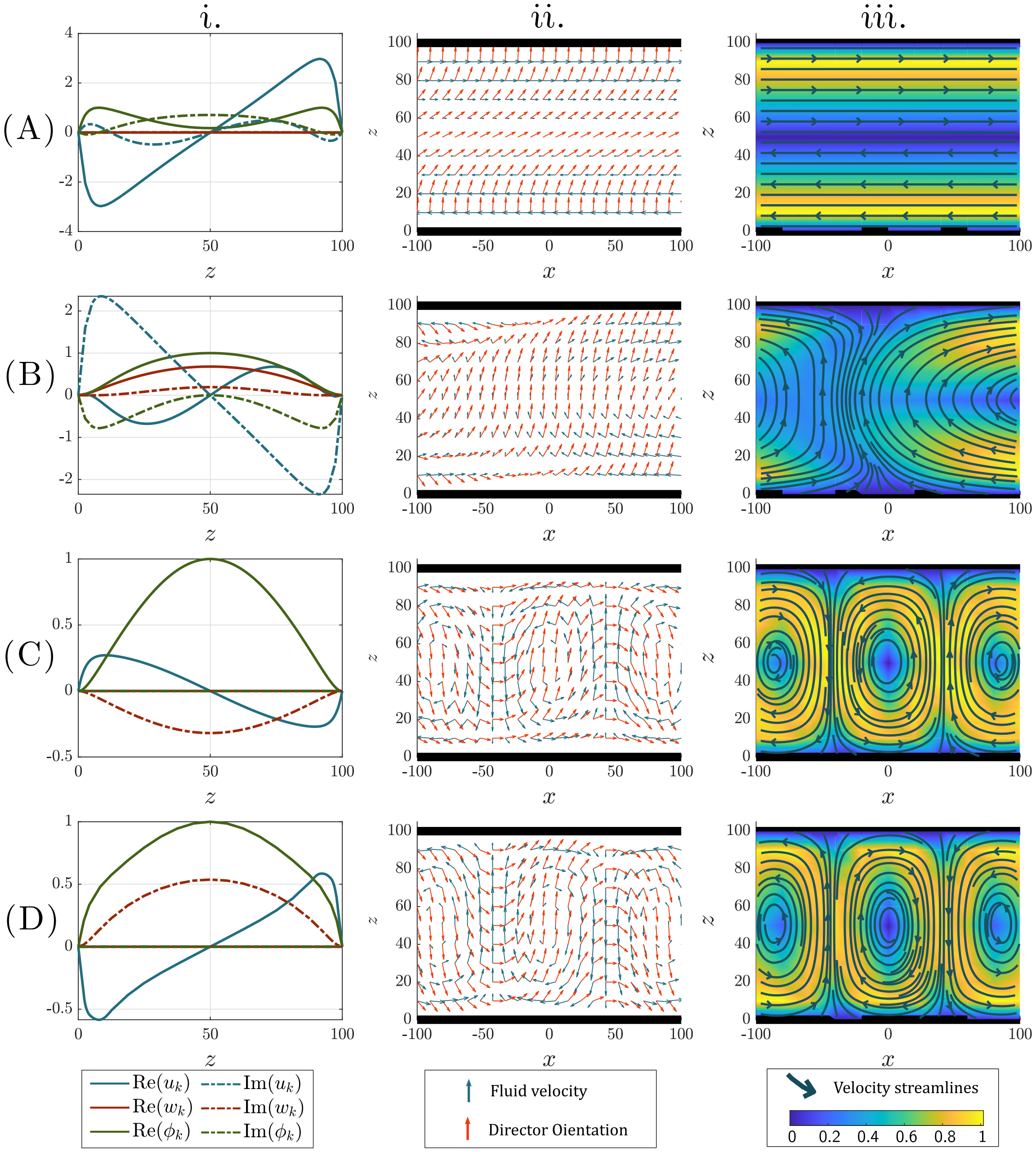

FIGURE 4.6: (*i*) Eigenvector, (*ii*) quiver, (*iii*) and streamline plots for a 2D channel of width $h = 100$, corresponding to specific values of $\boldsymbol{k}$ in FIGURE 4.5 as (*A*) ω^{+} for $k \approx 0$. (*B*) ω^{+} for k just below k^c. (*C*) ω^{+} for k just above k^c, the critical value for bifurcation (*D*) ω^{-} for k just above k^c. Eigenvector plots are normalised to $\phi_k = 1$.

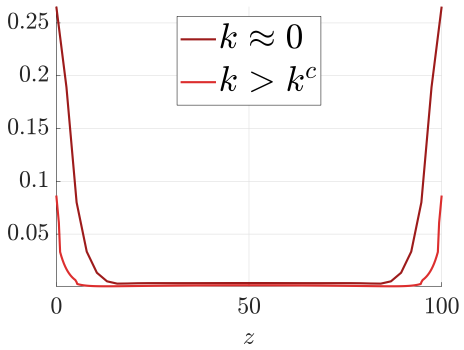

FIGURE 4.7: Elastic torque across a channel of width $h = 100$, evaluated at $k \approx 0$ and k just above the critical value k^c. Elastic torque is determined by the final term in (1.37).

For long-wavelength disturbances ($k < k^c$, FIGURE 4.6A, B), these columns cannot fit length-ways into the channel and are forced width-ways instead — the critical wavenumber k^c represents the switch for when length-way oscillatory modes are preferable over width-way oscillatory modes. Here, parallel alignment at the boundaries reveals itself to be a dominating boundary condition as the eigenvectors gradients (FIGURE 4.6A *i.*) indicate a sharp change in the director profile as proximity to the boundary increases and the director is forced to align to the boundary. Elasticity is proportional to second-order director gradients (1.32) and elastic torque acting on the director can be calculated by the $\nabla^2 \boldsymbol{p} - (\boldsymbol{p} \cdot \nabla^2 \boldsymbol{p})\boldsymbol{p}$ term in the director (1.37). In FIGURE 4.7, the elastic torque across the channel is plotted and indicates that applying director alignment causes the $k \approx 0$ modes to have large values of imposed elastic torque near the boundaries. The large values of imposed torque near the surface indicate that the alignment boundary condition imposes strong torques on the director, and experimentally these modes could only be realised if a source of strong surface torque was present.

4.4.1.1 Higher Order Modes

In the confinement regime, the eigenmodes $f_k(z)$ are allowed to vary with the channel width. This allows for the possibility of higher order modes in the channel, where the vortex lattice admits multiple cells of vortices across the channel width. Here, an n^{th} mode refers to a solution with n rows of vorticies across the channel, where the solution plotted in FIGURE 4.6 is an $n = 1$ mode, with associated eigenvalue $\omega^*_{n=1}$.

FIGURE 4.8 plots the eigenvectors and streamlines associated to the eigenvalue ω^{+} for the second, third and fifth order modes in a channel of width $h = 100$. Mathematically, there is no upper limit to the number of rows of vorticies across the channel width, as the boundary conditions in a channel only impose that u_k, w_k and ϕ_k are zero at the boundary.

However, increasing the number of rows of vorticies across the channel width induces stronger gradients over $w_k(z)$ and $\phi_k(z)$. Since viscosity and elasticity damping are proportional to these gradients, increasing the mode number comes with a penalising energy cost due to damping. Damping is proportional to the second order gradients in the fluid and director, whereas active forcing is proportional to the first order gradient in the director only. Consequently, increasing the mode number will always correspond to increases stability in the system due to viscosity and elasticity. This is quantified in FIGURE 4.9 where the dispersion relation is plotted for the second, third and fifth modes.

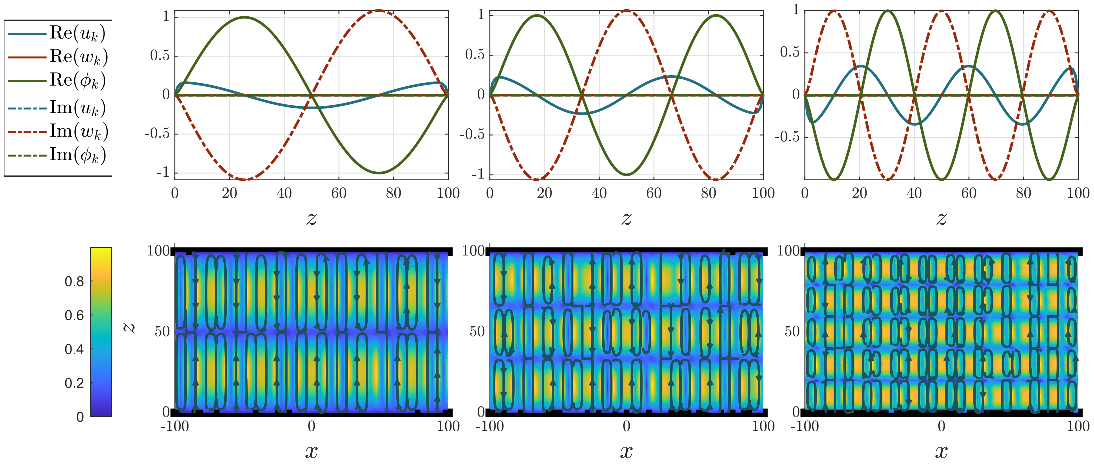

FIGURE 4.8: The eigenvector and streamline plots for the 2nd, 3rd and 5th modes associated to unstable eigenvalues $\omega^{+}_{n=2}$, $\omega^{+}_{n=3}$, and $\omega^{+}_{n=5}$

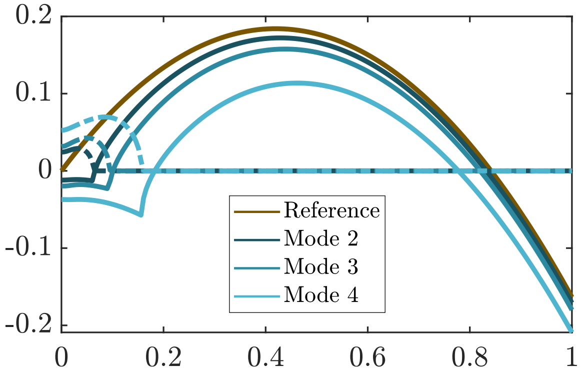

FIGURE 4.9: The dispersion relation for ω^+ corresponding to the 2nd, 3rd and 5th modes. Increasing the number of modes across the channel width increases the system stability. The associated eigenvector plot is found in FIGURE 4.8.

4.5 2D Film: Application of the Free-Surface BC

The 2D film is defined similarly to the 2D channel, where confinement is modelled as a rigid wall at $z = 0$ and a free-surface at $z = h$ for constant film-height h with the x-axis left unbounded. The boundary conditions on the rigid wall again consist of no-slip (4.11a) and impermeability (4.11b) for the fluid, and strong-anchoring (4.11c) on the director. At the free -surface, the kinematic boundary condition (4.12a) places restrictions on the normal components of the fluid velocity, and resolving fluidic stresses at the free-surface results in a no-shear condition (4.12b) and an ‘impermeability-like’ condition is placed on the director (4.12c) to prevent swimmers escaping the surface.

It may come as a surprise that an active thick film ($h \gg 1$) shares the same dispersion relation as a wide 2D channel (FIGURE 4.5) — typically, the no-slip condition heavily suppresses fluidic instabilities and a no-shear condition is generally considered a weaker boundary condition. However, the instability associated with ω^+ is driven by the divergence of the active stress tensor, $\boldsymbol{\sigma}^\alpha = \boldsymbol{pp}$, and as described in Section 4.4, imposing alignment on a constant free-surface is a stronger constraint than either no-slip, or no-shear. This will be quantified in Section 4.9 when we consider the no-torque boundary condition for the director at the free-surface.

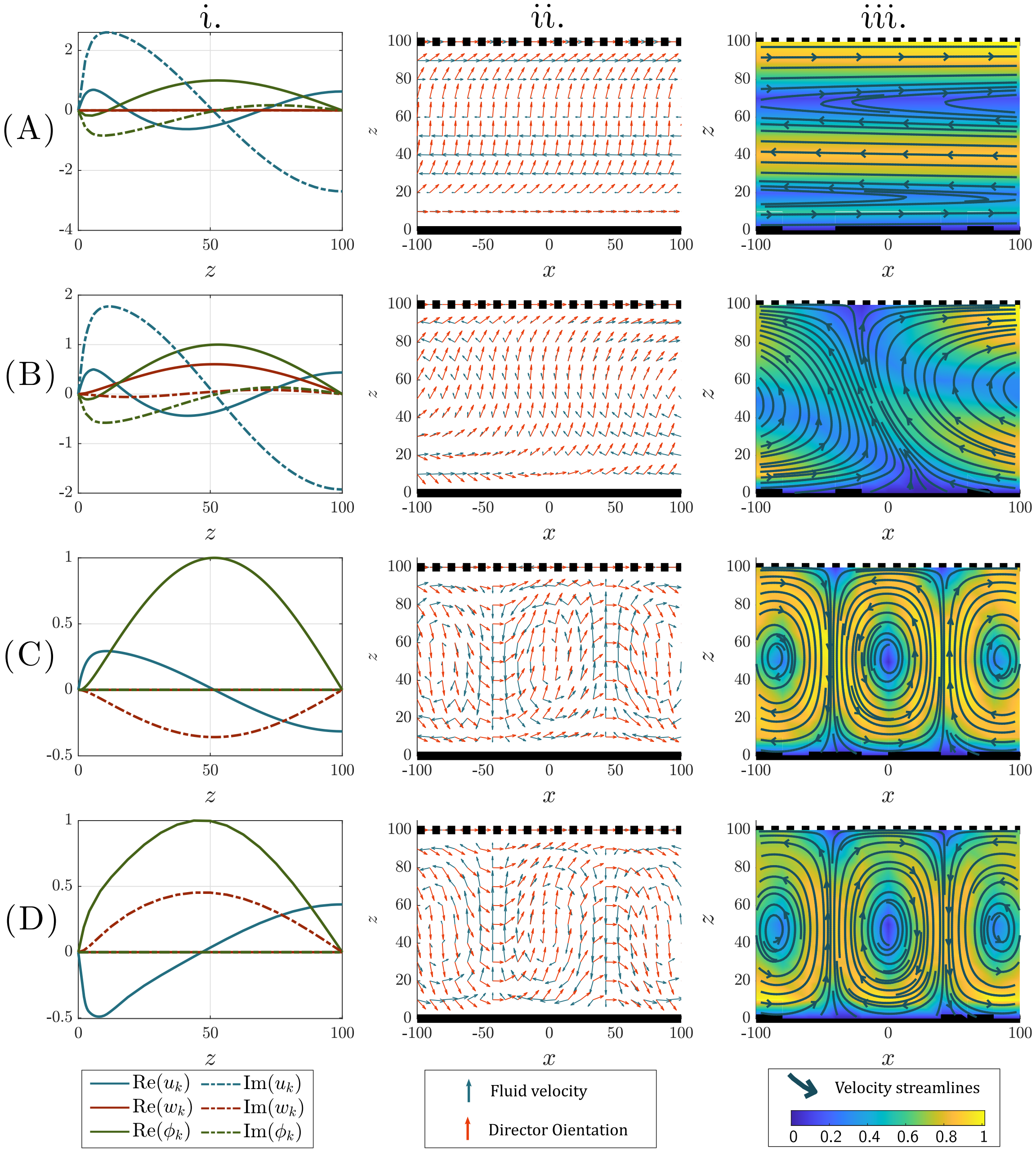

FIGURE 4.10: (*i*) Eigenvector, (*ii*) quiver, (*iii*) and streamline plots for a 2D film of width $h = 100$ evaluated for wavevector $\boldsymbol{k}$ as (*A*) ω^+ for $k \approx 0$. (*B*) ω^+ for k just below k^c. (*C*) ω^+ for k just above k^c. (*D*) ω^- for k just above k^c. Eigenvector plots are normalised to $\phi_k = 1$ and the corresponding dispersion relation for the film is identical to the channel 4.5.

Figure 4.10 is a sibling figure to Figure 4.6 for the 2D film, plotting the eigenmodes for the first-mode and least-stable mode $\omega^{\pm}$ at $k = 0$, $k < k^c$ and ω^{+}, ω^{-} for $k > k^c$, where k^c is the critical wavenumber for which the vortex lattice can no longer fit length-ways in the film. When $k > k^c$ (Figure 4.6C, D), the perturbation wavelength is smaller than the film height and the vortex lattice fits into the film. The modes are qualitatively and qualitatively similar to the modes discussed in the 2D channel case; this should come without surprise, as for such weak regimes of confinement the effects of the boundaries is negligible.

For $k < k^c$, the vortex lattice no longer fits in the film height and the modes instead propagate length-ways down the film. Here, we find a discernible difference in the propagation of the eigenmodes: the symmetry in boundary conditions for the 2D channel placed these columns of fluid at equal distance from $z = 0$ and $z = h$, but allowing the fluid to have a non-zero velocity at the free-surface effectively skews the oscillatory modes by only suppressing tangential fluid flow close to $z = 0$. This can be seen in Figure 4.10A, B*iii.*, as the regimes of high-flow (bright-yellow) are skewed relative to the boundaries, in direct comparison to the channel regime Figure 4.6A, B*iii.* where the streamlines indicate the resultant vortex lattice has simply been ‘squashed’.

The skewing of the oscillatory modes is a characteristic trait seen in other experiments, in particular a recent series of papers by Doostmohammadi & Yeomans.[7,8,13] Here, symmetry is broken by the presence of permanent $\pm 1/2$ topological defect pairs. Half the defect pairs travel in one direction along the vortex lattice and the other half travel in the opposite direction. The defect pairs do not annihilate one another, instead they dance around one another skewing the flow vortices, which eventually causes a transition into a state of active turbulence.

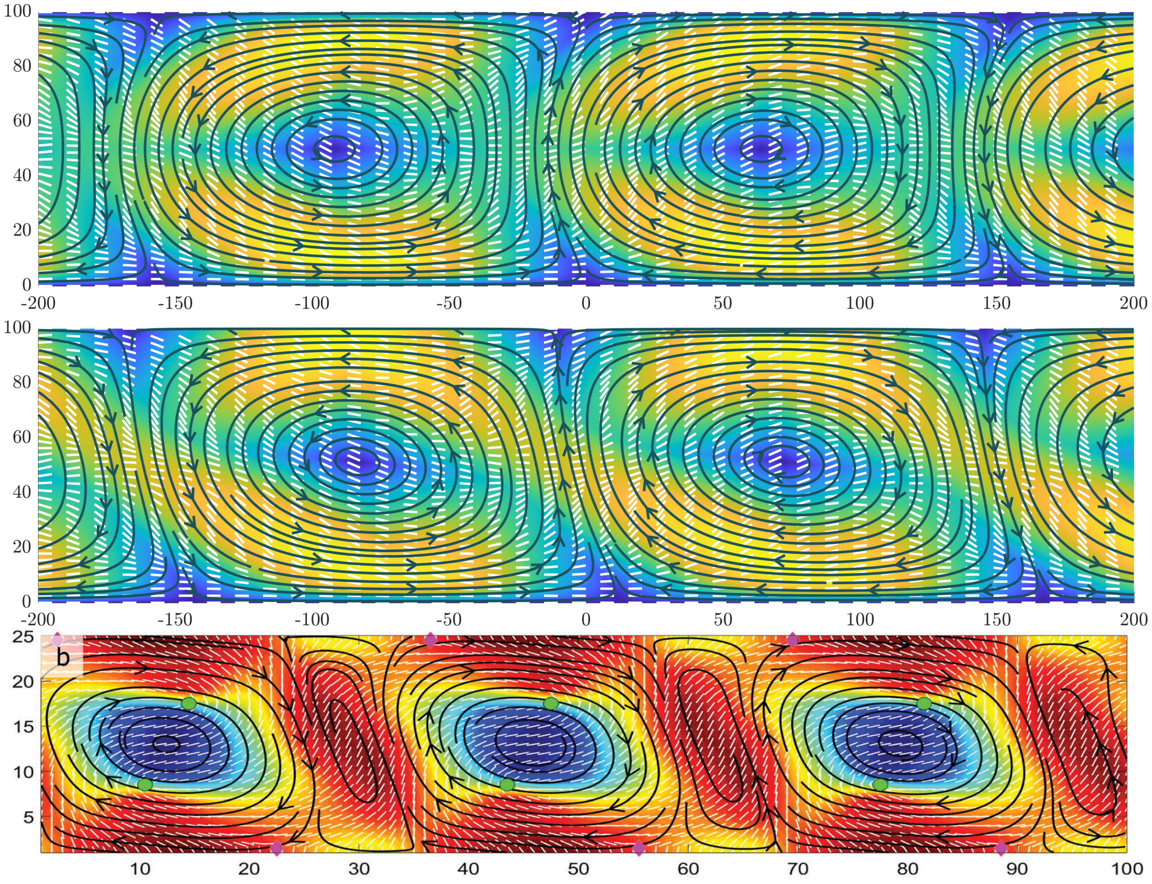

FIGURE 4.11: The vortex lattice for the 2D channel (*top*), the skewed vortex lattice for the 2D film (*mid*) and comparison to a vortex lattice skewed by topological defect pairs (*bottom*, Doostmohammadi & Yeomans[8]).

We make a direct comparison between the experimental results of Doostmohammadi & Yeomans and our own instability analysis in FIGURE 4.11 where the vortices skewed by asymmetric boundary-conditions and dancing ±1/2 defect pairs is illustrated. Of immediate comparison is the existence of smaller, secondary vortices between the larger primary vortices. In future work, we wish to investigate these secondary vortices by a stability analysis of a non-steady solution to the director consisting of a vortex lattice across the film width.

4.6 Critical Confinement for Suppressing Growth Rate

As the dimensionless channel width h is measured relative to $L = \sqrt{D\mu/\alpha}$, for which elasticity and active shear balance, we define 'intermediate' length scales for which h is above some critical length scale h^c, where $h = h^c$ is defined as the critical confinement length to completely suppress the instability growth rate for the eigenvalue $\omega^+_{n=1}$ with the least-stable eigenmodes (which always corresponds to the first-mode). To seek this length scale numerically, we evaluate $\omega^+_{k=k^m}$, where k^m is the wavevector associated with the maximum growth rate of ω^+ for a given channel height, evaluated at decreasing channel widths from $h = 100$ until the instability is suppressed.

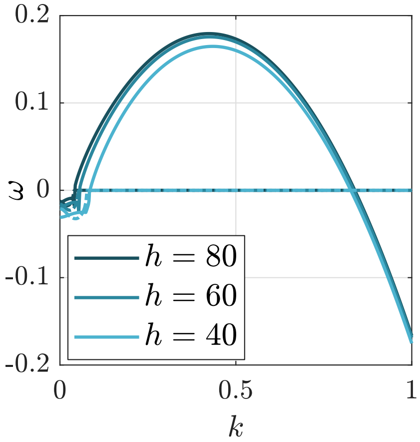

FIGURE 4.12: Dispersion relation for a 2D channel of width $h = 80$, 60, 40, evaluated for the eigenvalue ω^+ with the least-stable eigenmodes. Confinement drives vortex flows in the suspension, but has a limited effect on growth rate for $h \gg h^c$.

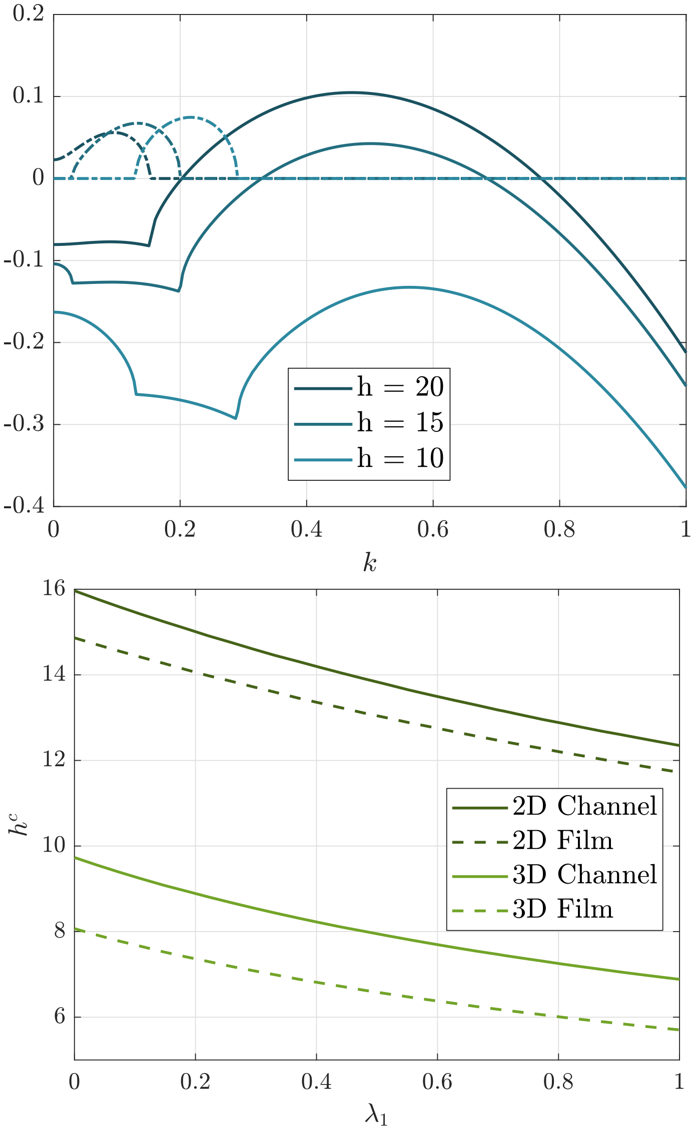

FIGURE 4.13: (A) Dispersion relation for a 2D channel at intermediate channel widths $h = 20$, 15, 10 for eigenvalue $\omega^{+}_{n=1}$, where solid lines denote growth-rate and dashed lines denote wave-speed. Confinement plays a strong role on suppressing the active matter instability for $h < h^c$. (B) Critical h^c against the shear alignment parameter λ_1: the default parameter for $\lambda_1 = 0.7$. Since the no-slip condition drives strong shear gradients at the substrate, alignment-to-shear plays an important role in the critical value h^c.

As confinement restricts the maximum size of an activity driven vortex, we can *apriori* estimate this critical length scale by comparison of the channel width to the wavevector associated with maximum growth in the bulk: $h^c \approx 2\pi/k_1^m$, where k_1^m is the wavenumber of the least stable bulk perturbation. Since the wavevector k corresponds to gradients in the director, the wavenumber k_1^m corresponds to length scale for which activity – which drives the system out of equilibrium at order $\mathcal{O}(k)$ – is balanced with elasticity, which acts at order $\mathcal{O}(k^2)$ and restores the system. For our default parameter set, this yields $h^c \approx 13$, so intermediate channel widths are here defined for h between 10 and 20.

The dispersion relation for eigenvalue $\omega^{+}_{n=1}$ at $h = 80$, 60 and 40 is plotted in FIGURE 4.12, which indicates that for length-scales where $h \gg h^c$, confinement continues to have a minimum impact on the suspension instability. The critical wavenumber k^c discussed in Section 4.4.1, for which the vortex length exceeds the channel width, decreases with h as should be expected.

The dispersion relation for eigenvalue $\omega^{+}_{n=1}$ at $h = 20$, 15 and 10 is plotted in FIGURE 4.13A. Confinement imposes a maximum vortex length due to the channel width, and so as soon as confinement crosses below the critical length $h = h^c \approx 13$, the growth rate rapidly decreases as elasticity and viscosity damping, which acts at long wavelengths, are dominant over activity driving the system out of equilibrium. The wavevector amplitude k_1^m for the maximum growth in the bulk is dependent on λ_1 (equation (2.22)), and increases as λ_1 increases: correspondingly, in FIGURE 4.13B we plot the critical confinement length h^c against λ_1, where increasing λ_1 corresponds to a decrease in the critical length-scale h^c as expected. Plotted also are the 2D film, 3D channel and 3D film regimes, which are discussed in Section 4.7 onwards.

4.7 3D Channel: Maximising the Instability Growth Rate

The 3D channel is an extension of the 2D channel, such that we are unbounded in the x-y plane with rigid walls at $z = 0$ and $z = h$. The boundary conditions on $\boldsymbol{u}$ are generalised to the 3D versions of the no-slip and impermeability boundary conditions, as discussed in Section 4.2 (4.11a–4.11d), but swimmer impermeability only imposes a boundary condition on ϕ_k and the director is 'free' to take any angle of θ_k on the top and bottom walls without violating alignment. Twist deformations do not induce fluid pumping, and allowing such a deformation will not violate the steady fluid state — it will however attract a penalising energy contribution due to director elasticity. The natural boundary condition to impose on the director is a zero-twist regime (4.11d), which corresponds to $\theta(z = 0) = 0$ and $\theta(z = h) = 0$ to avoid imposing arbitrary torques on the suspension. However, it does raise an interesting question — particularly when chirality is introduced which causes twist deformations — what would be a natural boundary condition to reflect the invariance of θ at the boundaries? This regime remains an area of active interest and will be investigating in future works. In this work, we will restrict ourselves to the zero-twist regime.

In the unbounded regime, we observed that when seeking perturbations of the form $\boldsymbol{k}_\perp$, where $\perp$ indicates components of $\boldsymbol{k}$ in the x-y plane, the governing equations *de-coupled* into two systems with eigenvalues ω_1^* and ω_2^*. The eigenmodes connected with ω_2^* was the least stable system, and exhibited a pure bend deformation. The de-coupling occurs as we broke symmetry by introducing $\boldsymbol{k}_\perp$ with some non-zero wavevector angle q, and reflects the suspensions propensity to allow bend modes to propagate through the fluid instead of the bend-splay modes associated with ω_1^*, which were less stable. By introducing confinement in the z-axis at $z = 0$ and $z = h$, we break rotational symmetry in the system by confinement instead of imposing a non-zero wavevector angle, and *a priori*, we can make a prediction on the types of modes we expect to see based on our analysis in Chapter 3: 1) the least stable modes will propagate as pure bend modes, pumping fluid into the x-y plane, 2) the

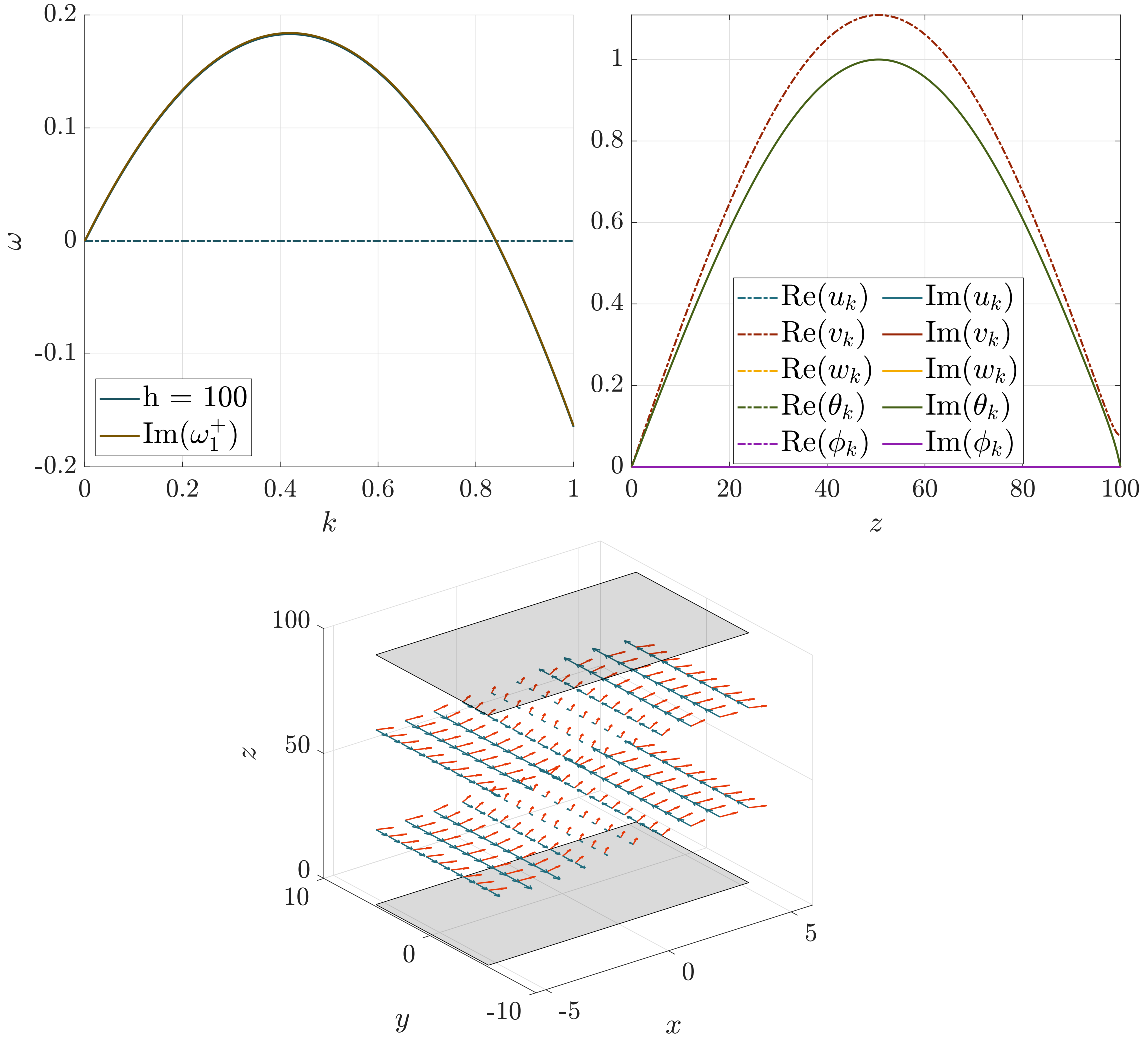

Figure 4.14: (a, Top Left) Dispersion relation for ω^+ in the 3D channel. Numerical results for ω^+ (blue) are displayed alongside the analytical dispersion relation for ω_1^+ (yellow). Note that the analytical result is difficult to distinguish as ω^+ and ω_1^+ are almost identical. (b, Top Right) Corresponding eigenvector plot, (c, Bottom) corresponding quiver plot.

instability growth rates should be comparable to the unbounded regime for large h, 3) there should be no critical k^c as described in Section 4.4, as this occurred when the wavelength exceeded the channel width, but in the 3D regime we have no such bounds in the x-y plane, 4) confinement effects should occur for smaller values of h than the 2D regime.

Firstly, we investigate the eigenmodes for large h, which are plotted in FIGURE 4.14B, normalised to $\theta_k = 1$. The Fourier modes θ_k and v_k display a $\pi/2$ out-of-phase relationship typical of a bend mode (as described in Chapter 2), whilst all other modes are completely suppressed. This indicates that all dynamics are occurring entirely in the x-y plane, with no deformations of the director propagating into the x-z plane. Consulting the 3D vectorfield plot in FIGURE 4.14C over the channel height confirms exactly this: the director field extending into the unbounded x-axis is pumping fluid into the unbounded y-axis.

Director alignment forces the magnitude of the bend perturbation to decrease with increasing proximity to the boundaries. Since elastic torque is proportional to second-order gradients in the director (1.32), to minimise elasticity-cost, gradients in the

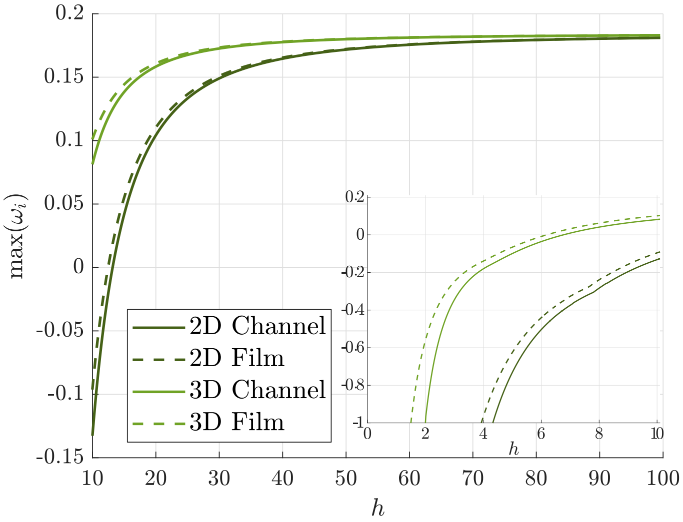

FIGURE 4.15: Maximum instability growth rate $\omega^{+}_{n=1}$ over h for the 2D channel, film and 3D channel, film.

director are close to constant, except in the middle of the channel where director gradients necessarily switch sign. The suspension dynamics in the limit of large h are straightforward, but we would expect to see more niche boundary-layer phenomena in the full, non-linear system.

Our second and third hypotheses are answered in FIGURE 4.14A for which the dispersion relation is plotted over $k \in [0, 1]$ alongside ω_1^+, the bulk instability growth rate described in Chapter 2 — since we are investigating a pure bend mode, ω_1^+ is equivalent to ω_2^+, the least stable growth mode described in Section 3.3.1. The agreement of the confinement dispersion relation to the unbounded regime is uncanny; the maximum difference in growth rate between the two regimes is less than a percentile, neither does the dispersion exhibit the bifurcation as described in the 2D regime.

Finally, we investigate the change in growth rate as confinement decreases. By consequences of 1) through 3), the instability growth rate in the 3D regime isn't damped with decreasing channel width to the same extent as the 2D regime — FIGURE 4.15 plots the maximum growth rate over h (see also FIGURE 4.13). The critical h^c for the 3D channel is approximate $h^c \approx 7.52$, compared to $h^c \approx 13.5$ for the 2D channel and at its critical value, the modes remain qualitatively similar to the bulk case.

4.8 3D Film & Chirality: Chirality Mixes the Vortex Lattice

Next, we investigate the 3D film, which shares the same configuration as the 3D channel, but with substitution of the no-shear condition for no-slip at $z = h$ (Section 4.2, (4.12)). For $h \gg 1$, the narrative of the 3D film is similar to the 3D channel, with the exception that the fluid is free to flow at the free-surface. In FIGURE 4.16B, C the eigenmode and vector field plots for the 3D film at critical film height $h = h^c$ are plotted, where we observe the characteristic phase relationship between the di-

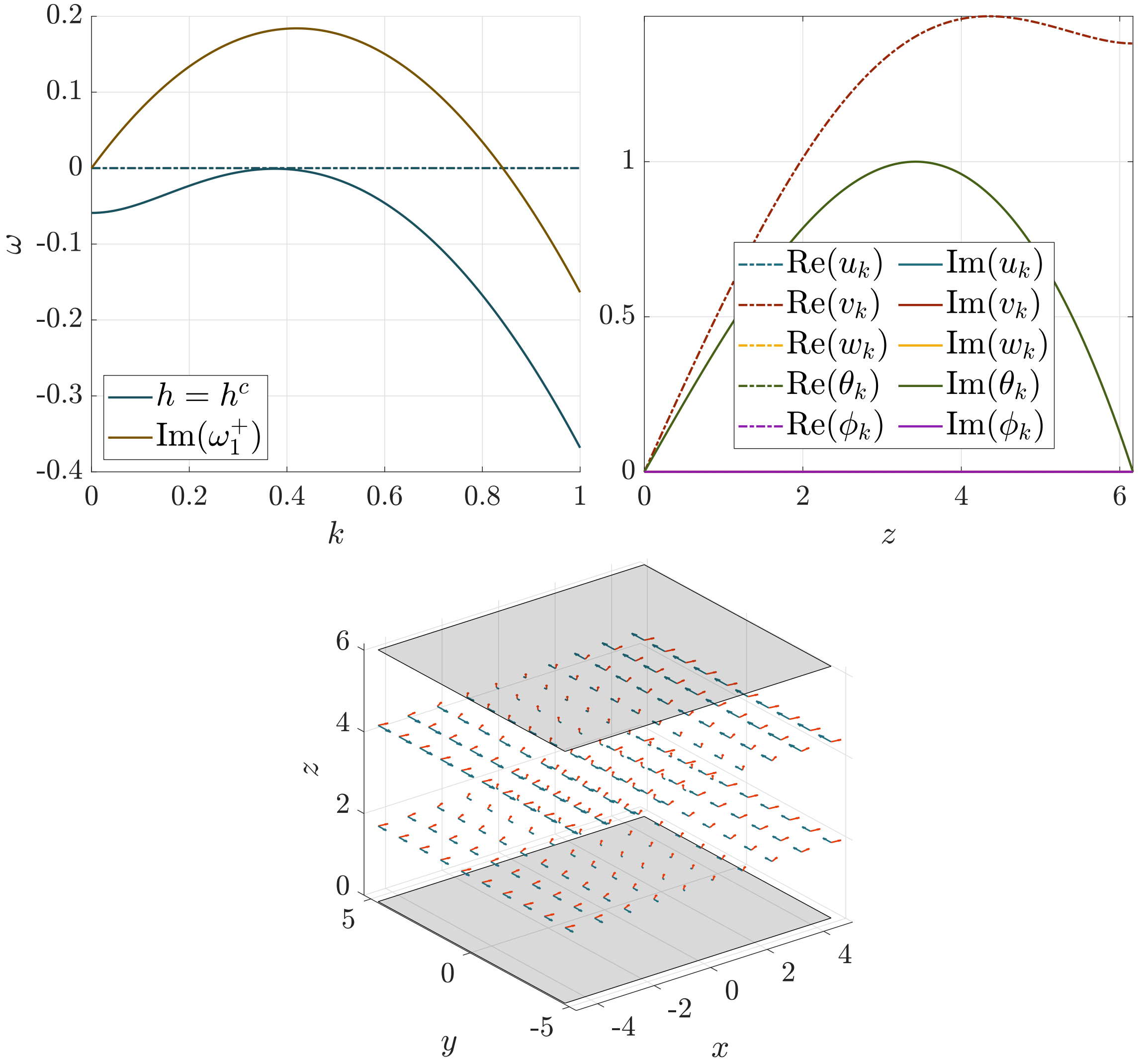

Figure 4.16: (a, Top Left) Dispersion relation for ω^+ in the 3d film at $h = h^c \approx 6.16$. Numerical results for ω^+ (blue) are displayed alongside ω_1^+ (yellow) (b, Top Right) Corresponding eigenvector plot, (c, Bottom) Corresponding quiver plot.

rector and the fluid. As $z \to 0$, the eigenmodes decay due to director alignment and no-slip at the substrate, and we note an interesting peak in the eigenmode plot for v_k around $z \approx 4.5$: this peak occurs as imposing no-shear at the free-surface dampens activity-driven flow, but there are no restrictions imposed on θ'_k close to the boundary, meaning activity-driven flow must decay at the free-surface. We will explore this idea further in Section 4.9. In Section 4.5, we described director alignment as the 'dominant' boundary condition, where 'dominant' indicates that alignment on the director suppresses perturbation growth stronger than no-slip or no-shear do, by consequence, the critical film height h^c for the 3D film is similar to the channel, where $h^c \approx 6.16$.

In Chapter 3, we saw that introducing chirality *re-couples* the active matter governing equations, as chiral particles rotate orthogonal to the plane of imposed shear. We observed in Section 3.3.2 that for wavevector angle $q = 0$, the resultant modes could be visualised as two bend modes with a $\pi/2 \pm \varepsilon$ phase relationship, where the magnitude of ε was dependent on the amount of twist introduced into the system. Now, we will continue this story by investigating a channel with chiral particles, evaluated at $h = h^c$. In FIGURE 4.17B, C we once again plot the eigenmodes and eigenvector plots. The eigenmodes illustrate the characteristic bend mode propagating in the x-y plane, but we can now see a second bend mode associated with ϕ_k in the x-z plane which is π *out-of-phase* with θ_k. This second bend mode arises due to rotational coupling to v_k, however, the corresponding active flow (yellow, w_k) is strongly suppressed by confinement[*], as the critical film height for modes propagating in the x-z plane is significantly larger than modes propagating in the x-y plane.

---

[*] The eigenmode w_k appears to be zero in FIGURE 4.17B, but further investigation reveals it is an order of magnitude smaller than ϕ_k.

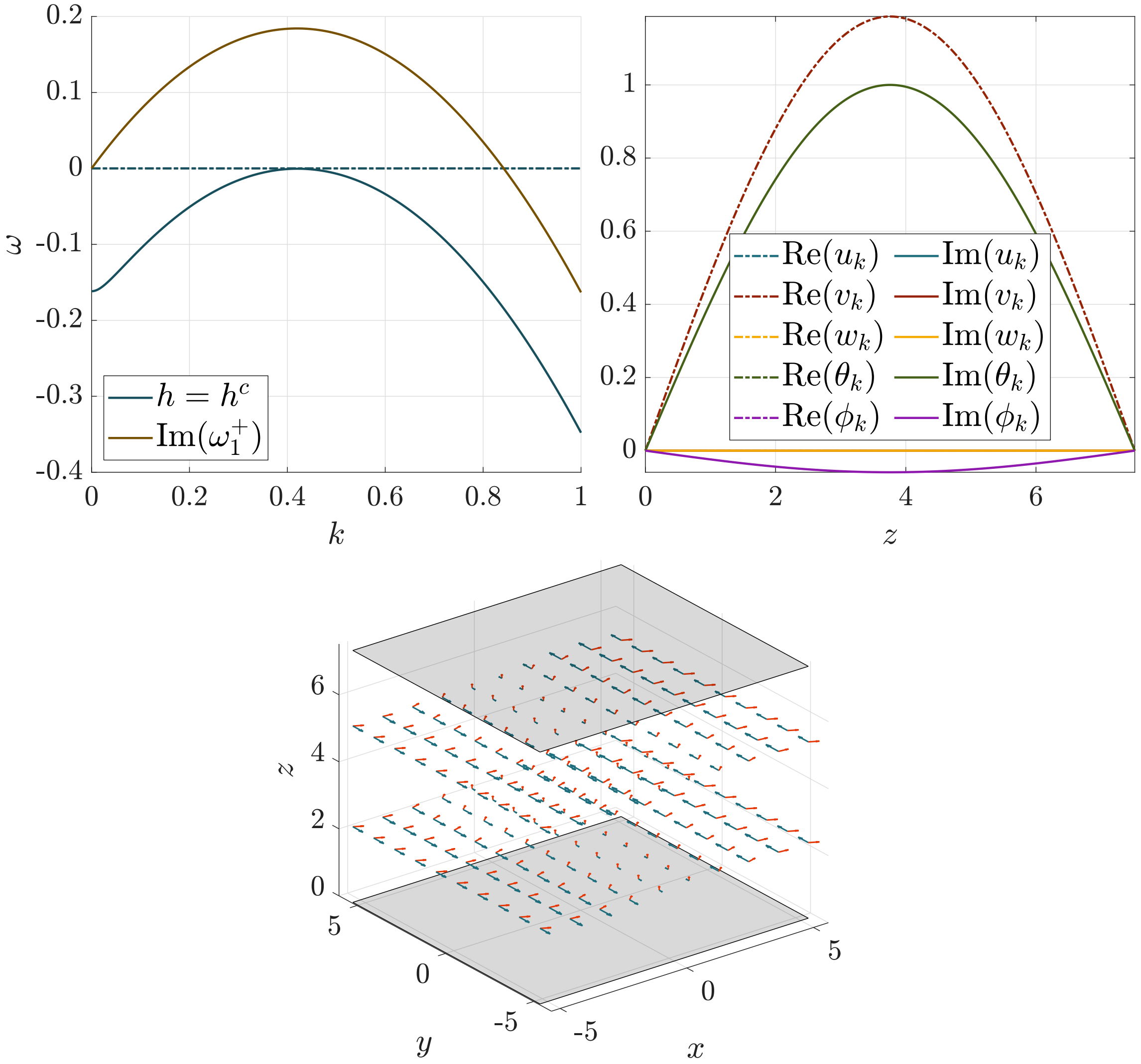

Figure 4.17: (a, Top Left) Dispersion relation for ω^+ in the 3D channel with chiral particles at $h = h^c \approx 7.52$. Numerical results for ω^+ (blue) are displayed alongside analytical ω_1^+ (yellow) (b, Top Right) Corresponding eigenvector plot, (c, Bottom) Corresponding quiver plot.

4.9 Torque-free Free-surface Boundary Condition

Up until this point, we have rigorously applied alignment at the boundary for the director and demonstrated its importance in suppressing the instability. At a rigid substrate, alignment remains a strong candidate as an appropriate boundary condition due the strong surface-torques a rigid substrate could induce. However, at a free-surface, this argument becomes weaker — the surface-torques imposed at a free-surface due to surface-tension are weaker than an inelastic substrate.

In seeking a new boundary condition for the director, one might consider a tangential stress balance of the form $\boldsymbol{n} \cdot \boldsymbol{\sigma} \cdot \boldsymbol{t}$ for surface normal n and any tangential vector $\boldsymbol{t}$. But, as in Section 4.2, applying this to the total stress (viscous plus active) in a linear instability analysis with a constant free-surface only reveals that $\phi(h) = 0$ without imposing any constraints on $\theta(h)$. We can, however, consider a new argument by considering activity-driven shear and director gradients at the free-surface: activity-driven flows are proportional to director gradients on the free-surface, given by $\nabla_\perp = (\partial_x, \partial_y, 0)$, such that $\boldsymbol{u}_\perp \propto \nabla_\perp \boldsymbol{pp}$. Taking gradients in the z-direction, which is perpendicular to the free-surface, yields $\partial_z \boldsymbol{u}_\perp \propto \partial_z \nabla_\perp \boldsymbol{pp}$. However, as we have resolved tangential stress at the free-surface, $\partial_z \boldsymbol{u}_\perp$ must vanish at the free-surface, and consequently so must $\partial_z \nabla_\perp \boldsymbol{pp}$.

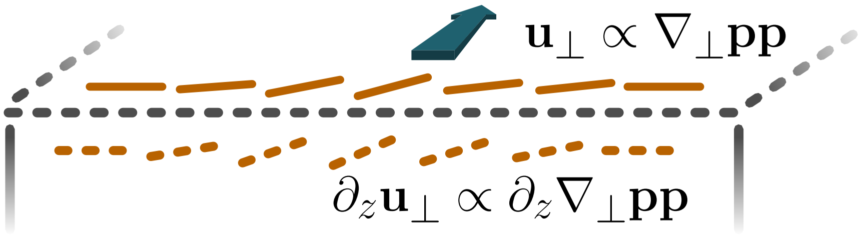

FIGURE 4.18: Activity-driven fluid flows are proportional to gradients in the director. When activity-driven flows occur in the x-y plane, z-gradients in the director are proportional to shear, which must be zero at the free-surface.

This can be visualised by imagining a bend deformation just below the free-surface whose bend magnitude is greater than that of the bend at the free-surface; the difference in the activity-driven flow just below the free-surface and at the free-surface generates shear gradients orthogonal to the free-surface, which conflicts the no-shear condition, and a schematic illustrating the boundary condition is drawn in FIGURE 4.18. When considering the boundary conditions on the Fourier modes, this corresponds to substituting $\theta_k(h) = 0$ with $\theta_k'(h) = 0$, *i.e.* substituting no-imposed torque over the bulk with a torque-free swimmer at the surface, and the boundary condition is hereafter affectionately referred to as the 'Gecko' boundary condition.

Application of the Gecko boundary condition to a 3D film at $h = 20$ yields strong perturbation growth rates for the swimmer suspension when comparing to alignment (FIGURE 4.19A). When h is only an order of magnitude about the characteristic elasticity length scale, the instability growth rate is only 4% smaller than that of the bulk case, compared to a 15% reduction in growth rate for the 3D channel. The eigenvector plot in FIGURE 4.19B makes the story clear: the fundamental bend instability propagates into the x-y plane, as is characteristic of the confined 3D regime, and the director, being free to rotate (but not tilt) at the free-surface, propagates this bend-instability even at the free-surface.

Chirality couples the bend mode in the x-y plane to a second bend mode in the x-z plane. Each bend mode generates a vortex lattice in their respective plane, and the superposition of each mode onto one another yields a tilted vortex lattice, where the tilt angle is a function of the relative strength of each bend mode. At the substrate, no-slip and alignment suppress active flow, but allows for shear and director gradients, which causes a net upwelling of the fluid; conversely, at the free-surface, no-shear and alignment allow flow to propagate along the free-surface, but the Gecko boundary condition ensures that this flow is contained within the x-y plane. The resultant modes exhibit a tilted vortex lattice in the fluid, where the vortex cells are tilted upward near the substrate where the tilt tends to zero as $z \to 0$. Two streamline plots in FIGURE 4.19C illustrate this mode: the first streamline plot is orientated

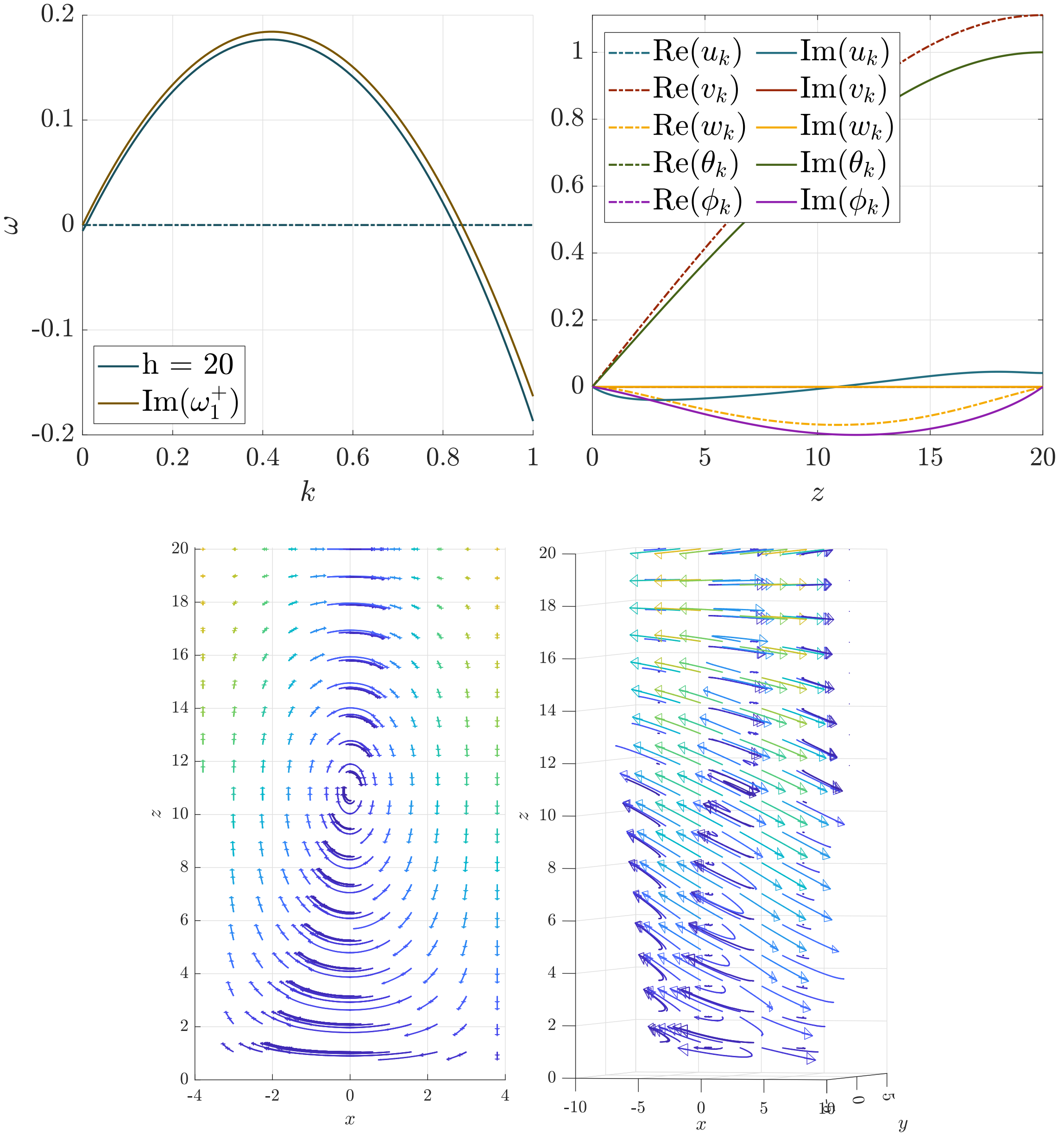

FIGURE 4.19: (A, TOP LEFT) The dispersion relation for ω^{+} at $h = 20$, (B, TOP RIGHT) and associated eigenmode plots, for the 3D film with the ‘Gecko’ condition applied. Numerical results for ω^{+} (blue) are displayed alongside ω_1^{+} (yellow). (C, BOTTOM) Two streamline plots for the chiral suspension: both plots correspond to the dispersion and eigenmode plots above. The first plot isolates flow in the x-z plane, whereas the second is rotated slightly to illustrate the tilting of the vortex lattice.

perpendicular to the y-axis and isolates the second bend instability propagating in the x-z plane, the second streamline plot is the same system, but rotated slightly to demonstrate the tilted vortex lattice.

4.10 Remarks: 3D Regimes Boast Larger Growth Rates

In this chapter, we have sought to explore how the instability mechanism described in Chapter 2 works in regimes of weak, intermediate and strong confinement. We applied traditional boundary conditions on the fluid for the 2D channel (4.11) and film (4.12) regimes, and initially applied a strong anchoring on the substrate and swimmer impermeability on the free-surface, before considering a torque-free boundary condition for a swimmer at the free-surface, which we affectionately refer to as the Gecko boundary condition.

In the 2D analysis, we observed a collapse of the columns of fluid seen in the unbounded regime, to a lattice of vortex nodes propagating length-ways, or width-ways in the film and channel, where the collapse of fluid columns occurs due to impermeability at the substrate and free-surface. A critical wavenumber k^c determined if the vortex lattice fit length-ways or width-ways: when $k > k^c$, the vortex cells could fit length-ways into confinement, when $k < k^c$, the vortex cells exceeded the confinement length and were forced down the unbounded channel length. A striking takeaway from the 2D analysis was the dependence of the critical confinement length h^c, for which confinement suppresses the instability, to the wavevector k_1^m associated with the maximum growth rate of the instability in the bulk. The wavevector k_1^m is strongly dependent on the viscosity and elasticity of the suspension; in particular, the elasticity of the suspension can be tuned by modifying the number density of the swimmers, and in regimes of intermediate confinement, experimental control of the instability growth rate could be realised by changing the density of swimmers.

In a natural continuation to the results of Chapter 3, we revealed that the 3D regime exhibits a smaller critical confinement length h^c. Spatial symmetry is broken by introducing confinement into the z-axis, and we showed that this causes bend modes to propagate into the unbounded x-y plane. Alignment and no-slip dampen the modes close to substrate in the 3D channel, but as the flow is parallel to the boundaries, we did not see the emergence of the vortex lattice in either the film or channel. This result has important consequences for the growth rates we might expect to see in experiments: the growth rate was close to the unbounded regime when confinement was only a little larger that the critical confinement length h^c, which was around an order of magnitude larger than the length scale set by elasticity balancing activity, and we would expect to see growth rate comparable to the unbounded analysis for large, thick films..

Finally, in Section 4.8 we continued the narrative on chirality by considering a chiral suspension in a 3D channel and film. Similar to the bulk analysis, we observed a second bend mode appearing due to the coupling of active flow in the x-y plane to director rotations in the x-z plane. This second bend mode was bounded by the film height and causes a vortex lattice to emerge, similar to the 2D regime. Impermeability at the free-surface only places a restriction on the azimuthal angle ϕ, so in Section 4.9 we explored the Gecko boundary condition, a torque-free argument on θ' which allows bend modes to propagate at the free-surface. The resultant modes illustrated a tilted vortex lattice, where the no-slip and alignment condition tilt the vortex cells close to the substrate when chirality is present. Allowing the director the freedom to rotate reduced the critical confinement length $h^c \approx 3.73$ — an order of magnitude less than the 2D regime.

5 | Non-constant Steady States in Confinement

Chapter 4 investigated the effects of confinement in the 2D and 3D regimes for a channel and for a film, where we determined that director alignment can strongly suppress the bend instability mechanism growth rates for sufficiently strong confinement. We observed that 3D regimes are less stable than their 2D counter parts, and in the final section, we observed that careful application of boundary conditions can yield regimes with growth rates comparable to the bulk, and that boundary phenomena quantitatively and qualitatively affect observed modes.

In this Chapter, we wish to explore alternative boundary conditions on the director to model some of the niche behaviours that microswimmers exhibit at the boundaries. Boundaries can be a source of strong surface energy, exerting a preferential alignment orientation on the suspension[48] and swimmers can 'slip' along a boundary, where orientation assumes a different direction to their trajectory[49] (FIGURE 1.4). Both boundary conditions can be modelled by changing the boundary condition on ϕ at the substrate. In Section 5.1 we explore the effects of rotating the constant steady state in a channel, such that the director is aligned into and away from the bounding walls at some angle β_j. In section Section 5.3, we consider the scenario where the suspension is aligned in the bulk along the $\hat{\boldsymbol{x}}$, but allowed to 'slip' at, *i.e.* allowed to rotate into, the substrate, and in the final section, we consider the effects of inclining a film of active matter in Section 5.4.3.

5.1 Rotated Constant State in a 2D Channel

Alignment of the director is applied at a solid substrate with the understanding that surface torques are strong enough to impose a preferential direction on the director — a condition referred to as strong anchoring. At a free-surface, alignment is applied by the logic that motile swimmers cannot 'swim through' a free-surface. Certainly, in liquid crystal literature, imposed alignment at a boundary is a reasonable boundary condition. However, the dynamics of suspensions of swimming microorganisms whilst analogous to their liquid crystal counter parts, are not identical. Pusher swimmers can 'slip' along a boundary with their head pointing toward the boundary and flagellum bundles pointing away from the substrate.

Inspired by this, we investigate the constant steady state in the 2D channel where the director is rotated by an angle β_j from the bottom substrate, such that $\beta_j = 0$ corresponds to swimmers pointing down the infinite channel (FIGURE 5.1). We note that for motile particles, conclusions drawn from this exercise should be carefully interpreted, as without concentration or scalar order variations, such a rotation only makes sense for non-motile, or nematic particles, as motile swimmers would swim away from the boundary at the bottom, and would exert motility-induced stresses on the boundary at the top which would have to be considered. Regardless, the exercise is a useful stepping stone to understanding non-constant steady states with slip, as explored in Section 5.2 onwards.

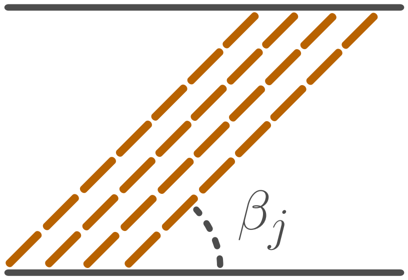

FIGURE 5.1: An alternative configuration for a nematic director for which $\boldsymbol{\nu} \cdot \boldsymbol{p} = \beta_j$, where $\boldsymbol{\nu}$ is the unit normal to the boundaries.

5.1.1 Shear Alignment Significantly Enhances Growth

In Chapter 4, Section 4.4 we saw that confinement suppresses the bend instability when particles are aligned along the channel due to alignment and no-slip at the boundaries. Ahead of any quantitative analysis, we can presuppose that the rotation of the constant steady state will enhance the instability growth rate for the bend instability, as bend-driven flow will be pumped down the unbounded length of the channel, instead of being pumped toward confining walls.

A numerical analysis of the rotated constant state reveals some surprising conclusions. Increasing β_j from zero to $\pi/2$, we hypothesised that we would obtain a maximum growth rate for $\beta_j = \pi/2$ when alignment no longer hindered the prop-

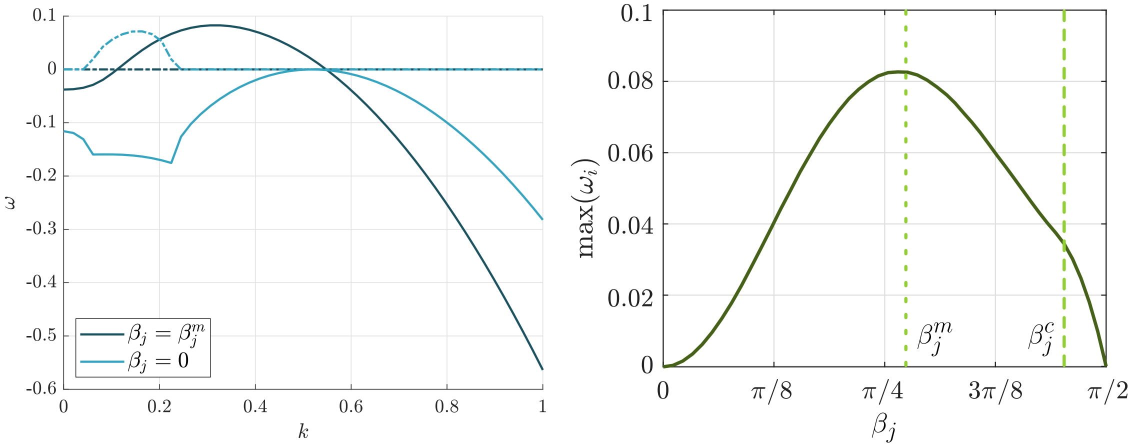

Figure 5.2: (a) Dispersion relation for ω^+ in the constant steady state, rotated such that $\boldsymbol{\nu} \cdot \boldsymbol{p} = \beta_j^m$ with a reference solution for $\beta_j = 0$, where solid lines indicate growth rate and dashed lines indicate wave-speed. (b) The maximum growth rate of ω_i over $\beta_j \in [0, \pi/2]$. The angle β_j^m for which ω_i obtains its maximum is slightly above $\pi/4$ (light green, dotted). The angle β_j^c for which we switch from oscillatory modes to channel modes occurs at the light green dashed line. In both plots, $h = h^c|_{\beta_j=0}$, the critical confinement length in the limit $\beta_j = 0$.

agation of the bend modes. Instead, the maximum growth rate was achieved for $\beta_j \approx \pi/4$ (FIGURE 5.2B, light green dotted line). Comparing the dispersion relation for the maximum growth rate case $\beta_j = \beta_j^m$ and a reference solution $\beta_j = 0$, FIGURE 5.2A reveals a shift in the wavevector associated with the maximum growth rate of the instability from $k^m \approx \frac{2\pi}{h}$ to $k^m \approx \sin\beta_j \frac{2\pi}{h}$. The wavenumber shift reflects the elongation of the vortex cells as the vortex lattice is skewed by β_j, and the location of k^m against β_j for $\lambda_1 = 0.7$ is plotted in FIGURE 5.3A. The narrative appears to continue as the maximum wavenumber also obeys the limit $k^m \to 0$ as $\beta_j \to \pi/2$; however, in FIGURE 5.2B, we plot the maximum growth rate of the instability against the β_j to discover the maximum growth rate occurs at $\beta_j \approx \pi/4$, not at $\beta_j = \pi/2$, which initially seems to violate our original hypothesis.

The proximity of β_j^m to $\pi/4$ is reminiscent of the analysis performed in Chapter 2, where the bulk suspension was perturbed with wavevector $\boldsymbol{k} = (\cos q,\ 0,\ \sin q)$. In Section 2.3.2, we uncovered that an extensile suspension is unstable to a wavevector

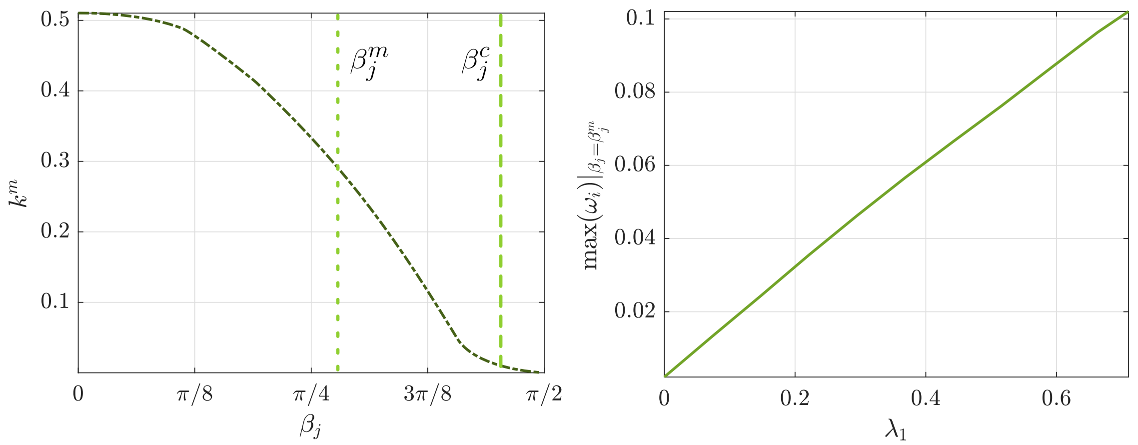

FIGURE 5.3: (A) The wavevector associated to the maximum, $\max(\omega_i)$ plotted against the rotation angle of the director. Data corresponds to FIGURE 5.5 (B) The maximum growth rate of the director over $\beta_j \in [0, \pi/2]$ such that $\omega_i(k^m)|_{\beta_j=\beta_j^m}$ plotted against λ_1. For each value of λ_1, the channel width is set at the critical width $h = h^c$ corresponding to FIGURE 4.13

angle $q < \pi/4$, so long as elasticity is small enough. At $q = \pi/4$, splay becomes the dominant mode of director deformation in the suspension, and the system undergoes a bifurcation into a stable regime as q increases further (FIGURE 2.7). In the 2D channel, the perturbation is propagated along $\hat{\boldsymbol{x}}$ with wavenumber k, such that a perturbed mode is written, $f_1(x,z) = f(z)\exp(i\boldsymbol{k}\cdot\boldsymbol{x} - i\omega t)$. However, when we rotate the ordered axis of the director by β_j, but keep the system of coordinates and Fourier modes the same, we effectively change the perturbation angle q by rotating the director with respect to the disturbance. When $\beta_j = \pi/2$, perturbing along the channel length is equivalent to imposing gradients perpendicular to the director, which corresponds to a *splay* deformation, not a pure *bend* deformation. Consequently, as β_j increases, splay increases and the system stabilises beyond $\beta_j = \pi/4$.

To investigate the relationship of the maximum growth rate to the rotation angle β_j^m, we explored the effect of the alignment-to-shear parameter λ_1 on the maximum growth rate for ω_i over $\beta_j \in [0, \pi/2]$. To obtain FIGURE 5.3B, first we set the channel width to h^c, where h^c corresponds to the critical width where the instability is suppressed. Since this value is proportional to λ_1 (FIGURE 4.13), each data point corresponds to a different critical channel width. Then, the maximum of $\omega_i(k^m)|_{\beta_j=\beta_j^m}$ is plotted against λ_1.

Unexpectedly, as $\lambda_1 \to 0$, the maximum growth rate tends to zero. This is quite a contrast to the bulk analysis, where the maximum growth rate of the instability is proportional to, but not critically dependent on λ_1 (FIGURE 5.4). We suggest the following line of thought: in the 2D regime, shear rotational effects consist of rotation due to vorticity and shear alignment, governed by λ_1. As the vortex lattice skews due to the rotation of the director, so does the orientation of active shear: when $\beta_j = 0$, flow is pumped perpendicular to the boundaries, and shear is at a maximum along the channel length; increasing β_j re-orientates active shear. As spatial symmetry is broken by the presence of boundaries, when the vortex lattice is skewed the relative angle between the orientation and shear changes also. This only effects the shear alignment term, as rotation due to vorticity is independent of the particle orienta-

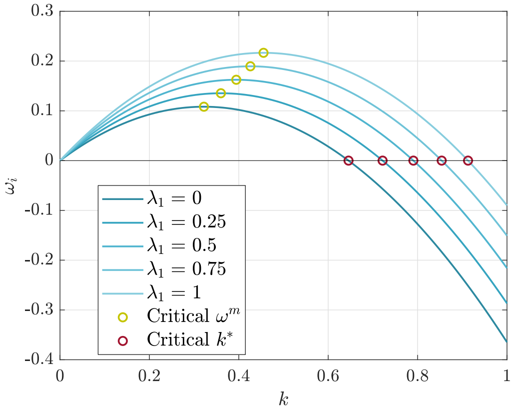

Figure 5.4: The dispersion relation for ω^+ in the 2D bulk regime for varying values of λ_1, where solid lines indicate growth rate and dashed lines indicate wave-speed. The maximum growth rate is proportional, but not critically dependent on the value of λ_1.

tion, whereas the magnitude of shear alignment effects are dependent on whether the particle is not aligned to the direction of shear.

The skewing of the vortex lattice is clearly seen in Figure 5.5 for which the eigenmodes, eigenvector field and streamlines are plotted for $\beta_j = 0$, $\pi/4$, β_j^m, $\pi/2$. In the reference solution $\beta_j = 0$, the vortex lattice (*iii.*) for maximum wavevector k^m are elongated vortex modes stretching across the channel height with a width determined by the perturbation wavelength k^m. As the director is rotated anti-clockwise by β_k, the vortex modes are correspondingly skewed to left. The eigenvector plots over $\beta_j \in (0, \pi/2)$ appear to produce a complex phase relationship between $\boldsymbol{p}_k$ and $\boldsymbol{u}_k$, which in previous analysis has been indicative of a travelling wave instability. However, investigating the phase between the director and velocity fields reveals the same out-of-phase relationship they shared in the bulk; the skewed vortex lattice remains a stationary phenomenon, regardless of the orientation of bounding walls.

Returning to the graph for the maximum growth rate over β_j (Figure 5.2b), we can observe a subtle bifurcation around $\beta_j = 11\pi/24$ (light-green dashed line) where the maximum growth rate wavevector k^m tends to zero and the optimum configuration is a single vortex stretching along the infinite length of the channel (Figure 5.5d *iii*). In this configuration, the no-slip condition replaces alignment as the dominant boundary condition, suppressing the instability mechanism near the boundaries.

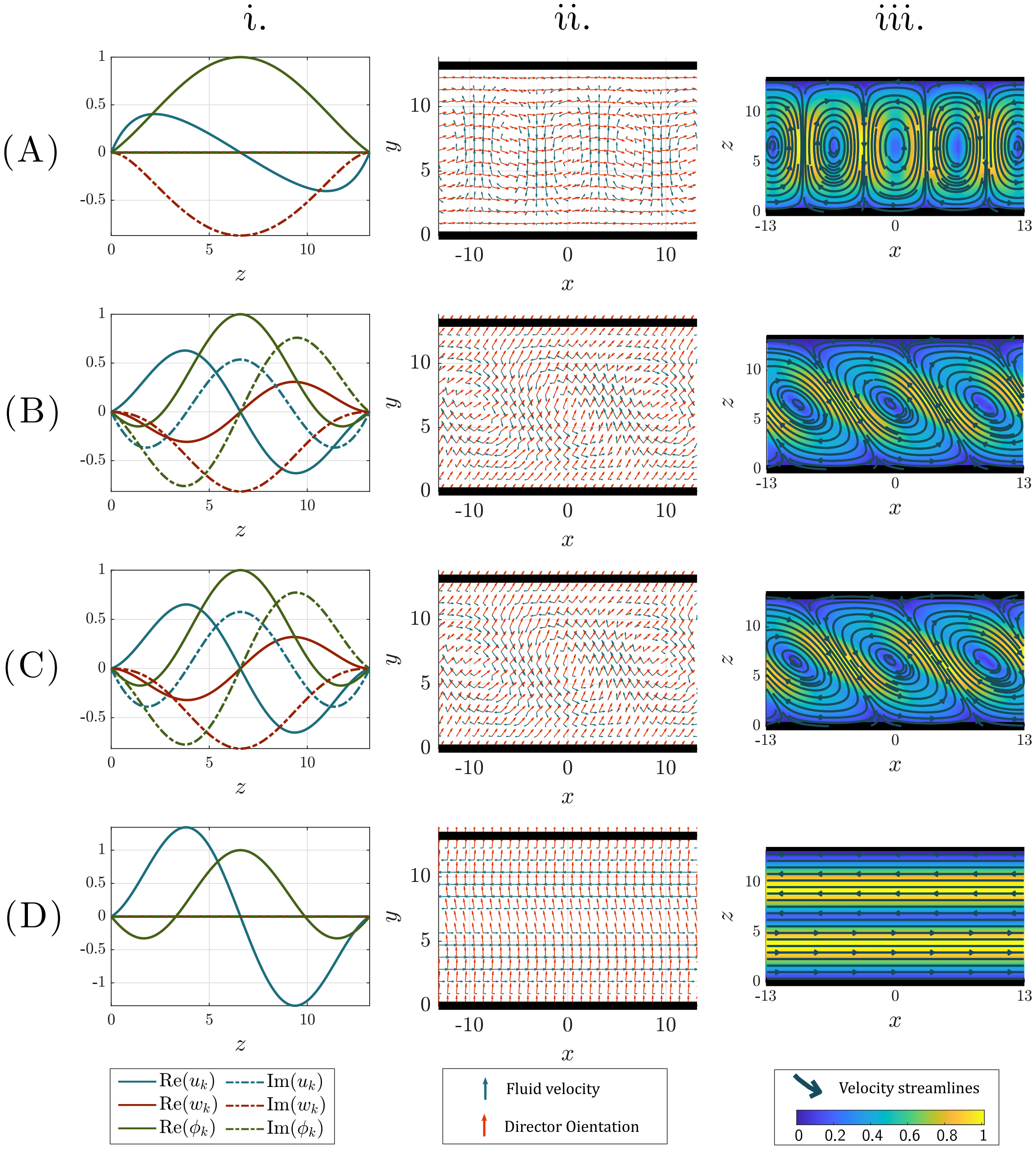

Figure 5.5: *i.* Eigenmodes plots, *ii.* eigenmode vector fields, *iii.* streamlines (full solutions, steady & perturbed state) for the rotated constant state, corresponding to the dispersion relation plotted in Figure 5.3 and evaluated at $k = k^m$ and $h = h^c$ (for $\beta_j = 0$ case), where (a) $\beta_j = 0$, (b) $\beta_j = \pi/4$, (c) $\beta_j = \beta_j^m$, (d), $\beta_j = \pi/2$.

5.2 Investigating Non-constant Steady States

Externally imposed flows are unavoidable in biological and mechanical systems: in the blood stream, systolic and diastolic pressure generates Poiseuille flow through veins; Marangoni surface stresses in active droplets generate internal microflows; and gravity drives parabolic flows in inclined films. Gradients in imposed flow are typically strongest near the boundaries due to the no-slip condition applied at a rigid substrate: this can cause a swimmers to rotate into (or away from) the boundary, depending on orientation, and can drive niche boundary phenomena, such as swimmer slip,[49] trapping,[47] or tumbling.[95]

To investigate the stability of these states requires investigation into possible non-constant steady states of the director and corresponding active flow. Up until this point, we have explored the stability of a constant steady state where the director is initially everywhere aligned. In the unbounded regime, this is the only possible configuration of the director as any gradient in the director results in a net flow, creating a local deformation in the director, and any gradient in imposed flow will induce rotation of the director. Without externally imposed constraints, such deformations will necessarily lead to non-steady regimes, typically described as Jeffrey orbits.

When in a confined geometry, we introduce additional constraints on the director and fluid by the way of boundary conditions at the walls of the channel, or free-surface of the film. These constraints impose additional torques on the director and allow for a static torque balance across the channel between shear-driven torque and restoring elasticity.

In Section 5.3, we will investigate an 'imposed slip' regime by *imposing* a slip angle on the director of $\pm\beta_j$ at the top and bottom boundaries. *A priori*, we know that the resultant director gradient will induce active flow, and for an extensile suspension we can expect it to flow into the negative x-axis. We would expect the resultant deformation to primarily be composed of splay, with small corrections to the director due to the active flow FIGURE 5.6.

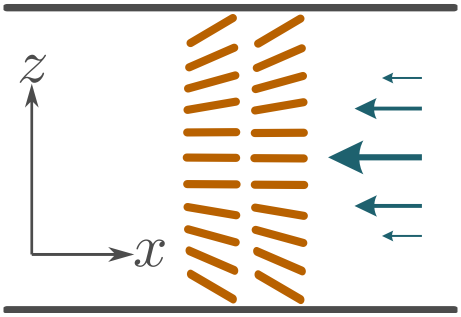

FIGURE 5.6: Imposing a slip angle at the top and bottom of a 2D film creates a splay deformation and a Poiseuille-like flow over a channel of width h, with rigid walls at $z = 0$, $z = h$, and unbounded in the x-axis.

A film of fluid on an inclined plane will experience a parabolic flow due to gravity, dictated by the boundary conditions of no-slip at the rigid boundary and no-shear at the free-surface. The corresponding gravitationally-driven shear gradients in the fluid causes rotation in the director field, which in turn generate activity-driven shear. Unless the film is *very* thin, gravitationally-driven flow induced by the plane inclination will be of an order-of-magnitude stronger than activity-driven flow, and active shear will be a next-to-leading order effect on the steady, parabolic fluid velocity profile, illustrated in FIGURE 5.7. In Section 5.4, we investigate this regime by introducing gravitational effects on the fluid, where the plane is inclined by an angle β.

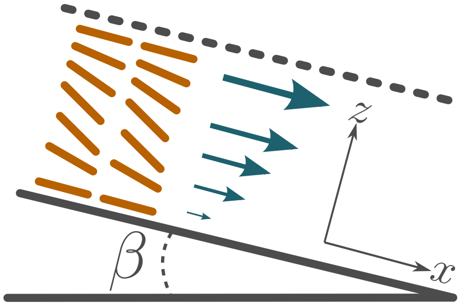

FIGURE 5.7: An inclined 2D film with a rigid wall at $z = 0$ and free-surface at $z = h$, and unbounded in the x-axis, has a parabolic flow-profile due to gravitational effects whose flow speeds act at an order-of-magnitude above active shear gradients. Inclination is measured by β. The director profile is determined by gravitational shear.

5.2.1 Derivation of the Steady State

The derivation of the steady state for the 2D channel bend deformation and 2D inclined film follow the same derivation, with the exception of the boundary condition applied at $z = h$ and the exclusion of the gravitational term. The simplifications to the dimensionless governing equations (2.4), follow from the previous chapters, where fluid inertia and swimmer motility is neglected, but with the inclusion of the gravitational term for the inclined film regime as $\gamma \boldsymbol{g}$, where $\gamma = \frac{\rho g L}{|\alpha|}$ controls the relative strength between gravitational effects and activity. Repeated here, the simplified governing equations read,

$$\xi \partial_t \boldsymbol{u} = -\nabla P + \nabla^2 \boldsymbol{u} + \gamma \boldsymbol{g} + s^{\alpha} \nabla \cdot \boldsymbol{pp}, \tag{5.1a}$$

$$\partial_t \boldsymbol{p} = \lambda_1 (\boldsymbol{\delta} - \boldsymbol{pp}) \cdot \boldsymbol{E} \cdot \boldsymbol{p} - \boldsymbol{\Omega} \cdot \boldsymbol{p} + \eta^{-1} \Big(\nabla^2 \boldsymbol{p} - \big(\boldsymbol{p} \cdot \nabla^2 \boldsymbol{p} \big) \boldsymbol{p} \Big), \tag{5.1b}$$

$$\nabla \cdot \boldsymbol{u} = 0. \tag{5.1c}$$

We seek a steady-state solution to (5.1) of the form,

$$P = P_0(z), \qquad \boldsymbol{u} = u_0(z) \hat{\boldsymbol{x}}, \qquad \phi = \phi_0(z),$$

where ϕ is an azimuthal angle measured from the x-axis such that the director can be written as

$$\boldsymbol{p} = \Big(\cos \phi_0, \ 0, \ \sin \phi_0 \Big)$$

and the constraint $|\boldsymbol{p}| = 1$ is satisfied automatically. The active stress tensor $\boldsymbol{pp}$ becomes,

$$\boldsymbol{pp} = \begin{pmatrix} \cos^2\phi_0 & 0 & \sin\phi_0\cos\phi_0 \\ 0 & 0 & 0 \\ \sin\phi_0\cos\phi_0 & 0 & \sin^2\phi_0 \end{pmatrix}. \tag{5.2}$$

In the film case, we can resolving (5.1a) in the z-axis gives an integrable equation in $P_0(z)$,

$$\partial_z P_0 = -\gamma\cos\beta + s^\alpha \partial_z[\sin^2\phi_0]. \tag{5.3}$$

Integrating with boundary conditions at the (constant) free surface of $P_0(h) = P_{\text{atm}}$ and $\phi_0(h) = 0,\ \pm\pi$ gives us an expression for P_0,

$$P_0 = P_{\text{atm}} + s^\alpha \sin^2\phi_0 + \gamma(h-z)\cos\beta, \tag{5.4}$$

where P_{atm} is a reference pressure. For the channel regime, pressure is simply defined up to a constant value. Resolving (5.1a) in the x-axis gives a z-integrable expression,

$$\partial_z^2 u_0 + s^\alpha \partial_z[\sin\phi_0\cos\phi_0] + \gamma\sin\beta = 0,$$

Integrating with respect to z with the boundary conditions of alignment ($\phi(h_0) = 0,\ \pm\pi$), and no-shear for the film regime, gives us an expression for the gradient of u_0,

$$\textbf{Film} \qquad \partial_z u_0 = \gamma\sin\beta(h-z) - \frac{1}{2}s^\alpha \sin 2\phi_0, \tag{5.5a}$$

$$\textbf{Channel} \qquad \partial_z u_0 = c_1 - \frac{1}{2}s^\alpha \sin 2\phi_0, \tag{5.5b}$$

where c_1 is a constant of integration, determined by $u_0(h) = 0$. For the steady solution, (5.1b) the rate-of-strain and vorticity tensors take the form,

$$\lambda_1\Big(\boldsymbol{\delta} - \boldsymbol{pp}\Big)\cdot \boldsymbol{E}\cdot\boldsymbol{p} - \boldsymbol{\Omega}\cdot\boldsymbol{p} + \eta^{-1}\Big(\nabla^2\boldsymbol{p} - \Big(\boldsymbol{p}\cdot\nabla^2\boldsymbol{p}\Big)\boldsymbol{p}\Big) = 0. \tag{5.6}$$

The rate-of-strain tensor $\boldsymbol{E}$ and vorticity tensor $\boldsymbol{\Omega}$ are reduced to,

$$\boldsymbol{E} = \begin{pmatrix} 0 & 0 & E_{zx} \\ 0 & 0 & 0 \\ E_{zx} & 0 & 0 \end{pmatrix}, \qquad \boldsymbol{\Omega} = \begin{pmatrix} 0 & 0 & -E_{zx} \\ 0 & 0 & 0 \\ E_{zx} & 0 & 0 \end{pmatrix},$$

where $E_{zx} = \frac{1}{2}\partial_z u_0$. Then with $\boldsymbol{pp}$ given by equation (5.2), the flow-alignment terms read in the z-axis,

$$\begin{aligned}\Big[\lambda_1\Big(\boldsymbol{\delta} - \boldsymbol{pp}\Big)\cdot\boldsymbol{E}\cdot\boldsymbol{p} - \boldsymbol{\Omega}\cdot\boldsymbol{p}\Big]_z &= \lambda_1 E_{zx}\Big(\cos^3\phi_0 - \sin^2\phi_0\cos\phi_0\Big) - E_{zx}\cos\phi_0, \\ &= E_{zx}\cos\phi_0\Big(\lambda_1\cos 2\phi_0 - 1\Big). \end{aligned} \tag{5.7}$$

The elasticity terms read,

$$\begin{aligned}\Big[\nabla^2\boldsymbol{p} - \Big(\boldsymbol{p}\cdot\nabla^2\boldsymbol{p}\Big)\boldsymbol{p}\Big]_z &= \partial_z^2\sin\phi_0 - \Big(\cos\phi_0\partial_z^2\cos\phi_0 + \sin\phi_0\partial_z^2\sin\phi_0\Big)\sin\phi_0, \\ &= \phi_0''\cos\phi_0, \end{aligned} \tag{5.8}$$

Collecting these contributions gives an expression for the spatial evolution of the director,

$$\cos\phi_0\Big(\eta^{-1}\phi_0'' + \frac{1}{2}\partial_z u_0\Big(\lambda_1\cos 2\phi_0 - 1\Big)\Big) = 0. \tag{5.9}$$

Noting that the trivial solution $\phi_0(z) = \pi/2$ violates previously imposed boundary conditions, the equation reduces to the second-order non-linear differential equation in z as

$$\phi_0'' = \frac{\eta}{2}\partial_z u_0\Big(1 - \lambda_1 \cos 2\phi_0\Big). \tag{5.10}$$

Equation (5.10) describes a balance between the elastic torque $\eta^{-1}\phi_0''$ and shear alignment effects. The balance is sensitive to boundary conditions, and external shear effects contained in the $\partial_z u_0$ term are also dependent on the boundary conditions applied. Applying the film and channel boundary conditions gives,

$$\textbf{Film} \qquad \phi_0'' = \frac{\eta}{2}\Big(\gamma \sin\beta(h - z) - \frac{s^\alpha}{2}\sin 2\phi_0\Big)\Big(1 - \lambda_1 \cos 2\phi_0\Big), \tag{5.11a}$$

$$\textbf{Channel} \qquad \phi_0'' = \frac{\eta}{2}\Big(c_1 - \frac{s^\alpha}{2}\sin 2\phi_0\Big)\Big(1 - \lambda_1 \cos 2\phi_0\Big). \tag{5.11b}$$

5.2.2 Derivation of the Perturbed State

Having solved the steady state, we consider perturbations in the x-z plane, such that

$$P = P_0(z) + \varepsilon P_1(t, x, z), \qquad \boldsymbol{u} = u_0(z)\hat{\boldsymbol{x}} + \varepsilon \boldsymbol{u}_1(t, x, z), \qquad \phi = \phi_0(z) + \varepsilon\phi_1(t, x, z),$$

where $\boldsymbol{u_1} = (u_1,\ 0,\ w_1)$ and $\varepsilon \ll 1$. To $\mathcal{O}(\varepsilon^2)$, the director $\boldsymbol{p}$ becomes

$$\boldsymbol{p} \approx (\cos\phi_0 - \varepsilon\phi_1 \sin\phi_0,\ 0,\ \sin\phi_0 + \varepsilon\phi_1\cos\phi_0), \tag{5.12}$$

and the tensor $\boldsymbol{pp}$ reads,

$$\boldsymbol{pp} = \begin{pmatrix} \cos^2\phi_0 - \varepsilon\phi_1 \sin 2\phi_0 & 0 & \cos\phi_0 \sin\phi_0 + \varepsilon\phi_1 \cos 2\phi_0 \\ 0 & 0 & 0 \\ \cos\phi_0 \sin\phi_0 + \varepsilon\phi_1 \cos 2\phi_0 & 0 & \sin^2\phi_0 + \varepsilon\phi_1 \sin 2\phi_0 \end{pmatrix}. \tag{5.13}$$

Taking the divergence of the active stress gives,

$$\nabla \cdot \boldsymbol{pp} = \begin{pmatrix} \partial_x[\cos^2\phi_0 - \varepsilon\phi_1 \sin 2\phi_0] + \partial_z[\cos\phi_0 \sin\phi_0 + \varepsilon\phi_1 \cos 2\phi_0] \\ 0 \\ \partial_x[\cos\phi_0 \sin\phi_0 + \varepsilon\phi_1 \cos 2\phi_0] + \partial_z[\sin^2\phi_0 + \varepsilon\phi_1 \sin 2\phi_0] \end{pmatrix}.$$

Resolving equation (5.1a) into its $\hat{\boldsymbol{x}}$ and $\hat{\boldsymbol{z}}$ components and equating first order ε coefficients yields,

$$-\partial_x P_1 + (\partial_x^2 + \partial_z^2)u_1 + s^\alpha\Big(\partial_z[\phi_1 \cos 2\phi_0] - \partial_x[\phi_1 \sin 2\phi_0]\Big) = \xi \partial_t u_1, \tag{5.14}$$

$$-\partial_z P_1 + (\partial_x^2 + \partial_z^2)w_1 + s^\alpha\Big(\partial_x[\phi_1 \cos 2\phi_0] + \partial_z[\phi_1 \sin 2\phi_0]\Big) = \xi \partial_t w_1. \tag{5.15}$$

Eliminating pressure by a cross-differentiation gives a third-order expression for the fluid velocity,

$$\partial_z^3 u_1 + 2\partial_x \partial_z^2 u_1 - \partial_x^3 w_1 + s^\alpha\Big((\partial_z^2 - \partial_x^2)\big[\phi_1 \cos 2\phi_0\big] - 2\partial_{xz}^2\big[\phi_1 \sin 2\phi_0\big]\Big) = \xi \partial_t(\partial_z u_1 - \partial_x w_1).$$

Expanding derivatives results in the expression,

$$
\begin{aligned}
\xi\partial_t(\partial_x w_1 - \partial_z u_1) + \partial_z^3 u_1 + 2\partial_x\partial_z^2 u_1 - \partial_x^3 w_1 + s^\alpha\alpha\Big(\cos 2\phi_0\Big(\partial_z^2 - \partial_x^2)\phi_1 - \\
2\sin 2\phi_0 \partial_{xz}^2\phi_1 \ - 4\phi_0'\Big(\sin 2\phi_0\partial_z\phi_1 + \cos 2\phi_0\partial_x\phi_1\Big) + \phi_1\Big(\cos 2\phi_0\Big)''\Big) = 0. \quad (5.16)
\end{aligned}
$$

We now turn our attention to the equation of motion for the director $\boldsymbol{p}$,

$$
\partial_t\boldsymbol{p} = \lambda_1\Big(\boldsymbol{\delta} - \boldsymbol{pp}\Big)\cdot\boldsymbol{E}\cdot\boldsymbol{p} - \boldsymbol{\Omega}\cdot\boldsymbol{p} + \eta^{-1}\Big(\nabla^2\boldsymbol{p} - \Big(\boldsymbol{p}\cdot\nabla^2\boldsymbol{p}\Big)\boldsymbol{p}\Big) \qquad (5.17)
$$

observing that the perturbed director is time dependent. The rate-of-strain and vorticity matrices are reduced to the form,

$$
\boldsymbol{E} = \begin{pmatrix} E_{xx} & 0 & E_{zx} \\ 0 & 0 & 0 \\ E_{zx} & 0 & -E_{xx} \end{pmatrix}, \qquad \boldsymbol{\Omega} = \begin{pmatrix} 0 & 0 & -E_{zx} \\ 0 & 0 & 0 \\ E_{zx} & 0 & 0 \end{pmatrix}.
$$

where $E_{xx} = \varepsilon\partial_x u_1$ and $E_{zx} = \frac{1}{2}\partial_z\Big(u_0 + \varepsilon u_1\Big)$. Following our previous approach and turning our attention to the flow-alignment terms yields,

$$
\boldsymbol{E}\cdot\boldsymbol{p} = \begin{pmatrix} E_{xx}\cos\phi_0 + E_{zx}(\sin\phi_0 + \varepsilon\phi_1\cos\phi_0) \\ 0 \\ -E_{xx}\sin\phi_0 + E_{zx}(\cos\phi_0 - \varepsilon\phi_1\sin\phi_0) \end{pmatrix},
$$

$$
\boldsymbol{\Omega}\cdot\boldsymbol{p} = \begin{pmatrix} -E_{zx}\Big(\sin\phi_0 + \varepsilon\phi_1\cos\phi_0\Big) \\ 0 \\ E_{zx}\Big(\cos\phi_0 - \varepsilon\phi_1\sin\phi_0\Big) \end{pmatrix}.
$$

Substituting first order velocity gradients from equation (5.5), the flow-alignment for first order ε in the z-axis only become,

$$\begin{aligned}\Big[\lambda_1\Big(\boldsymbol{\delta}-\boldsymbol{pp}\Big)\cdot\boldsymbol{E}\cdot\boldsymbol{p}-\boldsymbol{\omega}\cdot\boldsymbol{p}\Big]_z = &-2\lambda_1 E_{xx}\sin\phi_0\cos^2\phi_0 - E_{zx}\cos\phi_0\Big(1-\lambda_1\cos 2\phi_0\Big)\\ &+\varepsilon E_{zx}\phi_1\sin\phi_0\Big(1-\lambda_1\Big(3\cos 2\phi_0+2\Big)\Big).\end{aligned}$$

Substituting E_{xx}, E_{zx} and disregarding zero'th order ε terms (observing that E_{xx}, E_{zx} contain ε terms) gives the following expression for flow-alignment terms,

$$\begin{aligned}&\frac{1}{2}\partial_z u_0\phi_1\sin\phi_0\Big(1-\lambda_1\Big(3\cos 2\phi_0+2\Big)\Big)-\frac{1}{2}\partial_z u_1\cos\phi_0\Big(1-\lambda_1\cos 2\phi_0\Big)\\ &\qquad -4\lambda_1\partial_x u_1\sin\phi_0\cos^2\phi_0+\frac{1}{2}\partial_x w_1(1+\lambda_1\cos(2\phi_0)).\end{aligned}\tag{5.18}$$

Turning our attention to the elastic torque terms in equation (5.1b), the $\nabla^2\boldsymbol{p}$ term can be expanded as,

$$\nabla^2\boldsymbol{p}=\begin{pmatrix}\partial_z^2\cos\phi_0-\varepsilon\nabla^2[\phi_1\sin\phi_0]\\ 0\\ \partial_z^2\sin\phi_0+\varepsilon\nabla^2[\phi_1\cos\phi_0]\end{pmatrix}.\tag{5.19}$$

Similarly, the $\boldsymbol{p}\cdot\nabla^2\boldsymbol{p}$ term becomes,

$$\begin{aligned}\boldsymbol{p}\cdot\nabla^2\boldsymbol{p}&=\cos\phi_0\partial_z^2\cos\phi_0+\sin\phi_0\partial_z^2\sin\phi_0+\varepsilon\phi_1\Big(\cos\phi_0\partial_z^2\sin\phi_0-\sin\phi_0\partial_z^2\cos\phi_0\Big)\\ &\qquad-\varepsilon\Big(\cos\phi_0\nabla^2[\phi_1\sin\phi_0]-\sin\phi_0\nabla^2[\phi_1\cos\phi_0]\Big),\\ &=B_1(\phi_0)+\varepsilon\phi_1 B_2(\phi_0)-\varepsilon B_4(\phi_0).\end{aligned}$$

Here, $B_1(\phi_0)$, $B_2(\phi_0)$ and $B_4(\phi_0)$ are given by identities (B.1 – B.2, B.4). Applying these identities gives us the simplified expression,

$$\boldsymbol{p} \cdot \nabla^2 \boldsymbol{p} = -\phi_0'^2 - 2\varepsilon \phi_0' \partial_z \phi_1. \tag{5.20}$$

Writing down these contributions to the torque terms, we have in the z-axis,

$$\begin{aligned}
[\nabla^2 \boldsymbol{p} - \Big(\boldsymbol{p} \cdot \nabla^2 \boldsymbol{p}\Big)\boldsymbol{p}]_z &= \partial_z^2 \sin\phi_0 + \varepsilon \nabla^2[\phi_1 \cos\phi_0] + (\phi_0'^2 + 2\varepsilon\phi_0'\partial_z\phi_1)(\sin\phi_0 + \varepsilon\phi_1\cos\phi_0), \\
&= \phi_0'' + \varepsilon\Big(\phi_1 \nabla^2 \cos\phi_0 + 2(\nabla\phi_1)\cdot(\nabla\cos\phi_0) + \cos\phi_0 \nabla^2\phi_1 \\
&\qquad + \phi_0'^2 \phi_1 \cos\phi_0 + 2\phi_0' \sin\phi_0 \partial_z \phi_1\Big),
\end{aligned}$$

where we have disregarded terms of $\mathcal{O}(\varepsilon^2)$. Expanding the derivatives and simplifying gives,

$$[\nabla^2 \boldsymbol{p} - \Big(\boldsymbol{p} \cdot \nabla^2 \boldsymbol{p}\Big)\boldsymbol{p}]_z = \phi_0'' \cos\phi_0 + \varepsilon\Big(\cos\phi_0 \nabla^2 \phi_1 - \phi_1 \phi_0'' \sin\phi_0\Big) \tag{5.21}$$

Finally, putting together the first-order ε contributions of equations (5.11a), (5.18) and (5.21), we obtain an expression for the evolution of the perturbed director,

$$\begin{aligned}
\sec\phi_0 \partial_t \phi_1 = {} & -\phi_1 \partial_z u_0 G_1(\phi_0) - \partial_z u_1 G_2(\phi_0) \\
& - 2\partial_x u_1 G_3(\phi_0) + \partial_x w_1 G_4(\phi_0) + \eta^{-1}\nabla^2\phi_1.
\end{aligned} \tag{5.22}$$

Here $G_1(\phi_0), G_2(\phi_0)$ and $G_3(\phi_0)$ are functions related to the geometry of the swimming particles and steady-state solution,

$$
\begin{aligned}
G_1(\phi_0) &= \lambda_1 \tan\phi_0(1+\cos 2\phi_0)\\
G_2(\phi_0) &= \frac{1}{2}(1-\lambda_1\cos 2\phi_0),\\
G_3(\phi_0) &= \lambda_1 \sin 2\phi_0,\\
G_4(\phi_0) &= \frac{1}{2}(1+\lambda_1\cos(2\phi_0))
\end{aligned}
$$

Then, equations (5.11a, b) along with (5.22) describes the evolution of a perturbation to the generalised steady suspension. The equations are applicable to both the 2D channel and the 2D film by appropriate application of boundary conditions and form a numerically solvable eigenvalue problem when seeking planar-wave solutions of the form $f_1 = f_k(z)\exp(ikx - i\omega t)$.

5.3 Channel with Imposed Swimmer Slip

Numerically solving the steady channel equation, (5.11b), with the channel boundary conditions of $\phi_0(h) = \beta_j$, $\phi_0(0) = \beta_j$, $u_0(0) = 0$, $u_0(h) = 0$ yields a steady solution with a non-constant director field and non-zero velocity field, which is symmetrical over the channel width. In FIGURE 5.8, the steady solution is plotted for $\beta_j = \pi/4$ and $h = h^c$, where h^c is the critical channel height for suppressing the bend instability in the 2D channel regime (Section 4.4). Imposing a slip angle at the substrate is only possible in regimes of strong anchoring, where the substrate can impose torque on the suspension. FIGURE 5.8A reveals torque, proportional to second-order gradients in the director, is strongest in a small boundary layer close both the top and bottom substrate. The width of this boundary layer is determined by the director elasticity η^{-1}, which penalises second-order gradients in the director field and confines the regions of maximum elastic torque close to the substrate. Consequently in the centre of the channel, the deviation of the director from the x-axis is small.

Figure 5.8b reveals that imposing swimmer slip at the boundary leads to the emergence of a splay deformation across the channel height and yields a net-flow into the negative x-axis. The resultant active flow arises due to the non-constant director field and is proportional to the gradients in the director. Splitting up the divergence of the active stress tensor into forcing due to bend and splay (2.2) leads to,

$$(\nabla \times \boldsymbol{p}) \times \boldsymbol{p} = (\frac{\phi_0'}{2}\sin 2\phi_0,\ 0,\ -\phi_0' \cos^2 \phi_0), \tag{5.23a}$$

$$(\nabla \cdot \boldsymbol{p})\boldsymbol{p} = (\frac{\phi_0'}{2}\sin 2\phi_0,\ 0,\ \phi_0' \cos^2 \phi_0), \tag{5.23b}$$

where (5.23a) details the flow due to bend and (5.23b) the flow due to splay. Note that bend and splay both contribute a hydrodynamic forcing into the z-axis, but these flows are equal and opposite and cancel one another out. Conversely, the flows in the x-axis are cumulative, causing a net back flow for an extensile suspension. Increasing the imposed slip angle increases the amplitude of flow at the centre of the channel, but with very little qualitative change to the observed modes for $\beta_j < \pi/2$. Interestingly, the steady state equations are capable of finding steady states for im-

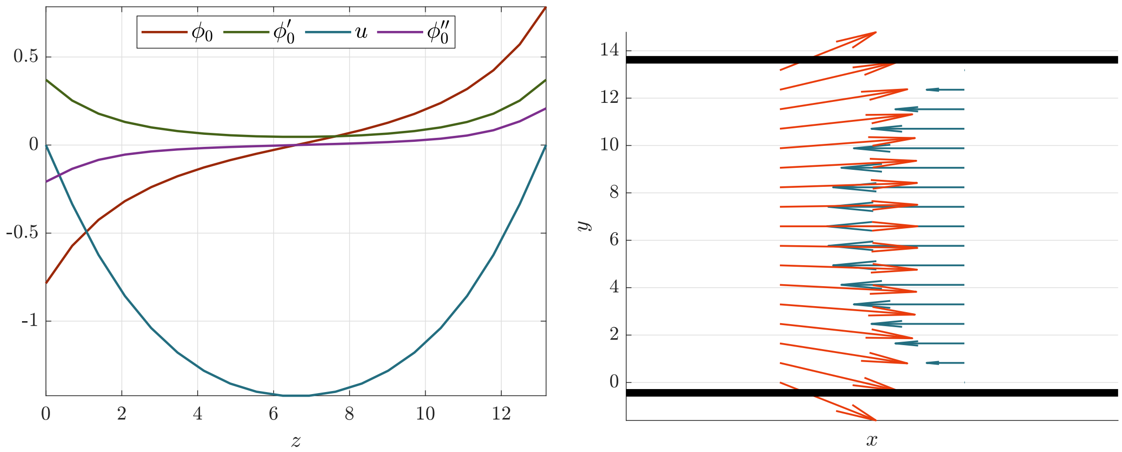

Figure 5.8: (a) Plot for the steady state of imposed swimmer slip over a channel where $\beta_j = \pi/4$. (b) Director field and velocity field over the 2d channel for the same regime.

posed slip for $\beta_j \in [0, 2\pi]$: in FIGURE 5.9, the steady state for $\beta_j = \pi$ is plotted, whilst local ordering in the center of the channel remains along the positive x-axis. However, such a regime could only be feasible with strong torques imposed across the whole channel, which could be achievable by using magnetic fields to force alignment, but lie out of the scope of this work.

5.3.1 Slip Enhances Growth Rate

Numerically solving the perturbed director (5.22) and perturbed fluid (5.16), along with the solved steady states for $\boldsymbol{u}_0$ and $\boldsymbol{p}_0$ as described above, reveals a transition from the vortex lattice to a net flow down the channel length. In FIGURE 5.10, we choose to plot the perturbed channel eigenmodes with their corresponding steady state and streamlines to illustrate the resultant dynamics for $\beta_j = 0$, $\beta_j > 0$, $\beta_j = \pi/4$, $\beta_j = \pi/2$; all states are evaluated for $h = h^c|_{\beta_j=0}$. The reference state FIGURE 5.10A illustrates the vortex lattice (*iii.*) across the film height. As β_j is increased from zero (B–D), the velocity component of the steady solution increases, causing a merging of the vortex lattice and a net-flow into the negative x-axis. The vortex lattice disappears when the net steady flow is larger than the maximum flow amplitude of the perturbed vortex cells. Note that the streamlines are plotted for

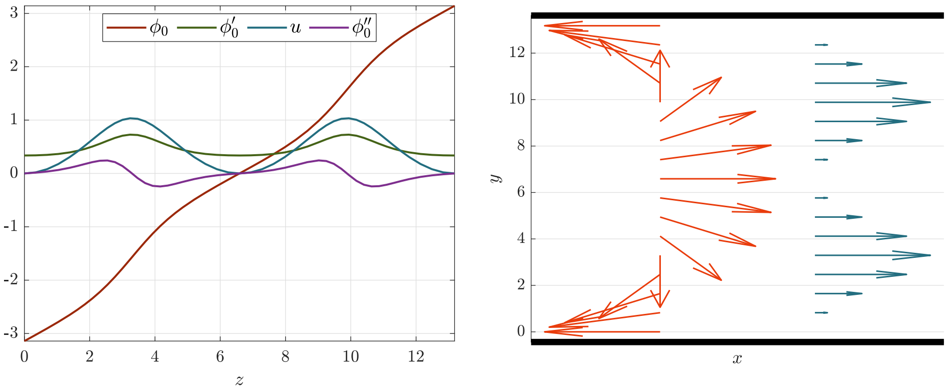

FIGURE 5.9: (A) Plot for the steady state of an imposed slip over a channel where $\beta_j = \pi$. (B) Director field and velocity field over the 2D channel for the same regime.

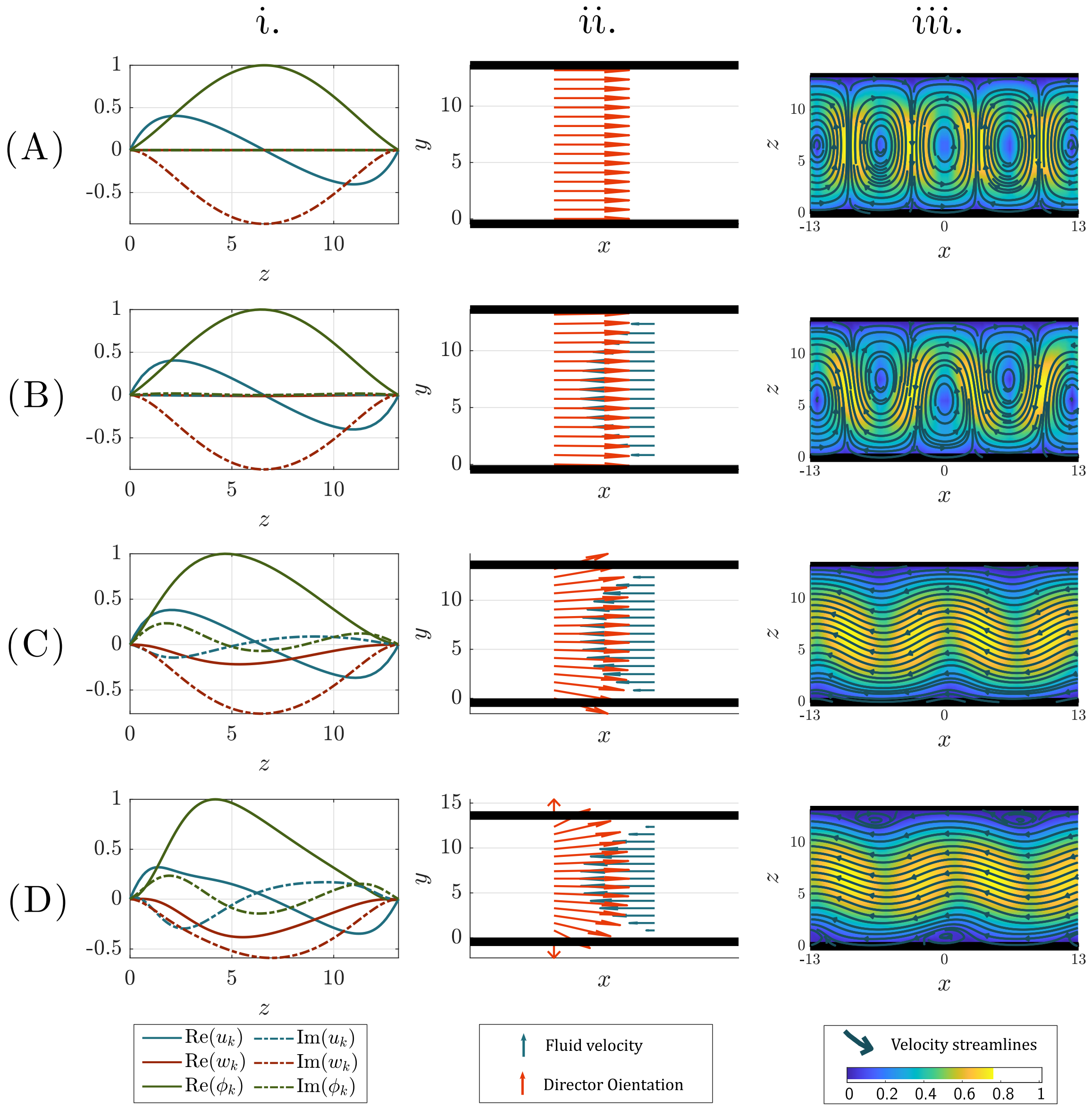

FIGURE 5.10: *i.* Eigenmodes plots, *ii.* steady state vectorfields, *iii.* streamlines (full solutions, steady & perturbed state) for the imposed slip constant state, evaluated at $k = k^m$ and $h = h^c$ (for $\beta_j = 0$ case), where (A) $\beta_j = 0$, (B) $\beta_j > 0$, (C) $\beta_j = \pi/4$, (D), $\beta_j = \pi/2$.

the full solution $\boldsymbol{u} = \boldsymbol{u}_0 + \varepsilon \boldsymbol{u}_1$, where ε is set to 0.2 and the value of β_j for which the vortex lattice disappears is arbitrarily dependent on the choice of ε.

The maximum growth rate of the director is plotted in FIGURE 5.11A, where the data corresponds to $\beta_j \in [0, \pi/2]$ and the modes plotted in FIGURE 5.10. Increasing β_j corresponds to an increased growth rate, obtaining a maximum at $\beta_j = \pi/2$. Investigating the dispersion relation for $\beta_j = \pi/4$ and $\beta_j = \pi/2$ reveals that imposing slip causes a transition for all wavelengths from stationary planar-waves to travelling planar-waves (FIGURE 5.11B). Since the director is non-constant, perturbing the director results in morphed vortex cells, as seen in the streamlines for the perturbed modes *only*, plotted in FIGURE 5.12. The perturbed director at the centre of the channel pumps fluid perpendicular to the channel walls, as described in Chapter 4, but near the substrate the director is tilted and a planar-wave perturbation down the channel length induces both bend and splay deformations near the substrate. The emergence of travelling waves arises from the splay contribution to director deformation, which pump fluid parallel to the local to director.

5.4 Inclined Film with Gravity-driven Flow

The inclined film regime is an extension to the 2D film regime discussed in Section 4.5 by the inclusion of a gravitational body force acting on the fluid *only* — no gravitational torque effects are modelled on the swimmer suspension; the suspension orientation is effected only by virtue of the resultant flow from tilting the film. Unlike Section 5.1 and Section 5.3, we do not impose an angle β_j on the director at the substrate, but use director alignment and no-slip on the substrate, and director alignment and no-shear on the free-surface, as described by Section 4.2, (4.11) and (4.12). Inclination is controlled by the parameter β, such that $\sin\beta = 0$ indicates a level film (FIGURE 5.7), which would correspond to the analysis of Chapter 4. We continue to neglect surface tension at the free-surface.

5.4.1 Tumbling Regime for Axisymmetric Swimmers

Axisymmetric swimmers can undergo ‘tumbling’ orbits in simple shear flow which are characterised by long periods with the swimmer aligned parallel to the flow direction, with periodic changes in orientation where the particle ‘flips’ by π such that it is pointing in the opposite direction. The onset of tumbling is sensitive to the vorticity component of shear, which acts on the swimmer irrespective of its orientation. The alignment to-shear term governed by λ_1 is comprised of the extensile component of simple shear, but its contribution to rotational torque is dependent on relative direction between the swimmer orientation and shear, and will vanish for $\phi_0 = \pi/4$. Without stabilising effects such as motility, inertia or suspension elasticity, the orientation of a lone swimmer is sensitive to shear flows. Consequently, the existence of a steady state for the director in the inclined regime is not guaranteed, but dependent on the elasticity term governed by $\eta^{-1}\nabla^2\boldsymbol{p}$ being strong enough to balance rotational effects due to gravity-induced shear and impose orientational order over the film height.

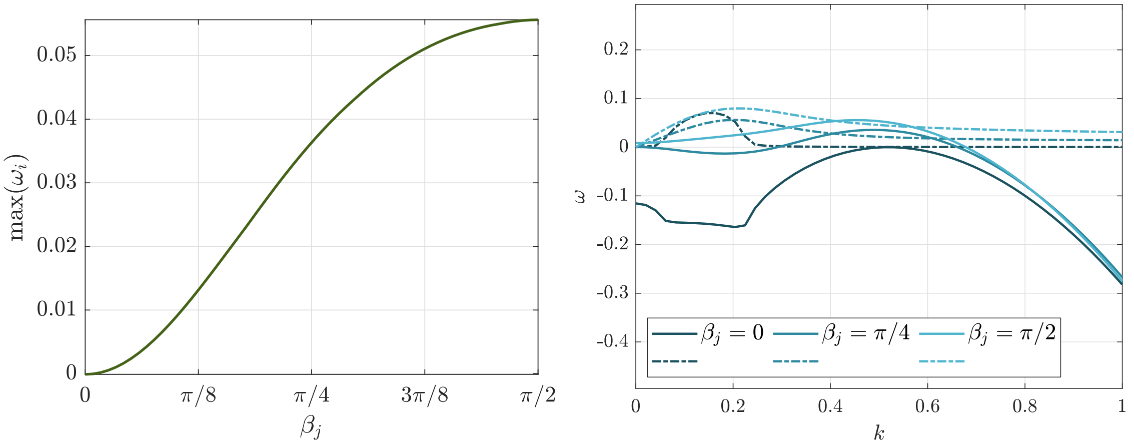

Figure 5.11: (a) The maximum growth rate of ω_i for the 2D channel with imposed slip β_j, evaluated at $h = h^c|_{\beta_j=0}$, where h^c is the critical channel width for which confinement suppresses the bulk instability with $\beta_j = 0$. (b) Dispersion relation for ω^+ for $\beta_j = 0$, $\pi/4$, $\pi/2$, where solid lines indicate growth rate and dashed lines indicate wavespeed.

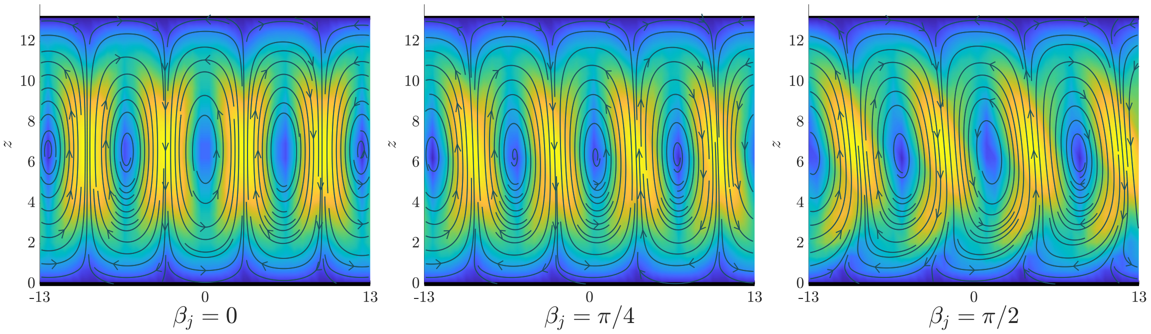

$\beta_j = 0$ $\beta_j = \pi/4$ $\beta_j = \pi/2$

FIGURE 5.12: Streamlines for the perturbed modes *only*, where $\beta_j = 0$, $\pi/4$, $\pi/2$, corresponding to the full solutions in FIGURE 5.10.

When elasticity is strong and inclination is sufficiently small, we solve the steady equations (5.11) for the profile of $\phi_0(z)$. In FIGURE 5.13, the steady state and corresponding vectorfield is plotted for $\beta = \pi/64$ at the critical film height $h = h^c$ for which the instability is suppressed by confinement in the limit of $\beta = 0$. By virtue of the no-slip and no-shear conditions, the gravitational-flow profile is parabolic over the film height and imposes shear gradients (leading to shear-induced torque) on the suspension, which rotates the director away from the ordered direction in the x-axis. Shear is at a maximum at the substrate $z = 0$ and decreases to zero at $z = h$; the corresponding rotation due to shear causes a downward tilting of the director close to the substrate. We've seen that a non-constant steady director profile — in Section 5.3 imposed by a 'slip' angle at the top and bottom of the substrate — can result in a net flow along the x-axis and that more generally, bend and splay contributions to flow in the z-axis cancel one another out. In the inclined regime, alignment to gravitational-shear causes splay over the film height. Consequently activity-driven flow, governed by $s^\alpha \phi_0' \cos(2\phi_0)$, contributes to the steady shear flow profile and can enhance or suppress the gravitational flow depending on the sign of activity: extensile (contractile) suspensions pump fluid toward the open (closed) end of a splay deformation, an extensile (contractile) suspension will suppress (enhance) the steady flow compared to a passive suspension (FIGURE 5.14, $h = 5$, $\beta = \pi/128$).

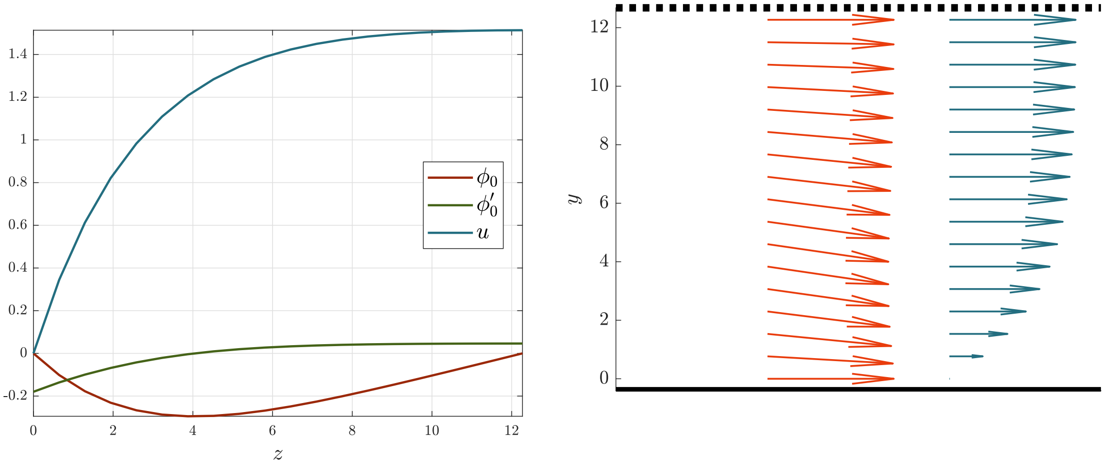

FIGURE 5.13: (A) Plot of the steady state for an inclined film. The film is inclined at an angle $\beta = \pi/64$ and the film height is $h = h^c$ for which h^c is the critical height for which confinement suppresses the active matter instability. (B) Director and velocity vector fields over the 2D film for the same regime.

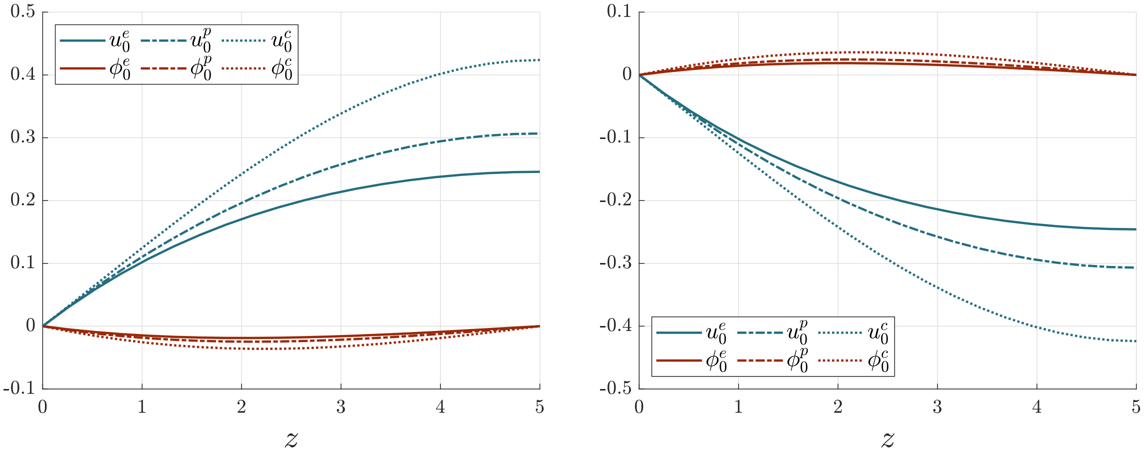

FIGURE 5.14: The steady flow and director profile for extensile (e), contractile (c), and passive (p) particle suspensions when the particles are pointed (A) downhill, and (B) uphill. Data is for $h = 5$, $\beta = \pi/128$. Extensile (contractile) active flow suppresses (enhances) background flow due to a splay deformation in the director inducing active shear.

5.4.2 Tumbled Regime for Active Suspensions

When elasticity is weak, or the film height is large compared to elasticity length scales, gravitational flows can be strong enough to cause tumbling, which by its nature, implies a non-steady director field. For small inclination angles, we've seen that director elasticity can be sufficiently strong to enforce a balance between shear-induced torque and elasticity-induced torque, but what happens as inclination increases? By using the numerical methodology discussed in Section 4.3, we can seek increasingly unstable solutions to the steady inclined state by slowly incrementing the inclination angle β. This could be experimentally imagined by fixing the orientation of a suspension of particles down an inclined plane using an external-alignment field, such as an imposed magnetic fix, gradually increasing the inclination of particles, and observing how the suspension behaves as the external-alignment field is switched off.

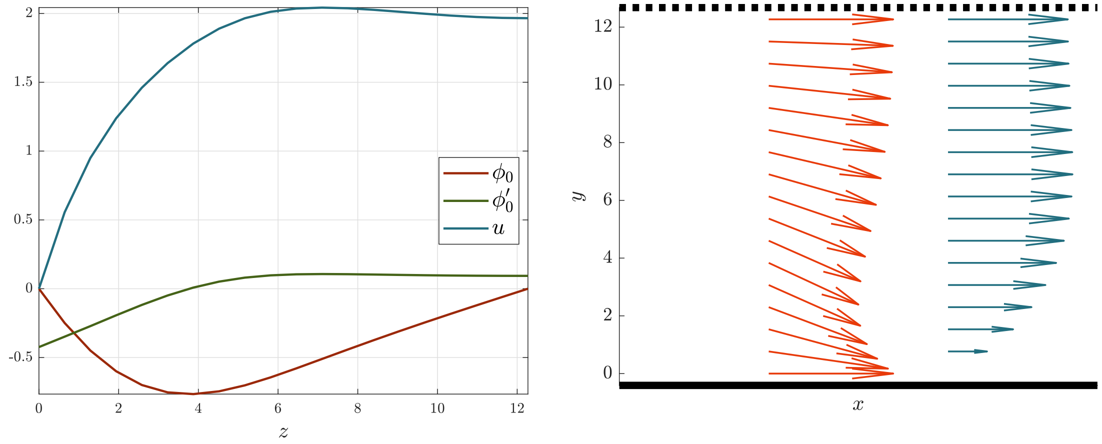

FIGURE 5.15: (A) Plot of the steady state for an inclined film. The film is inclined at an angle $\beta < \beta^c$, where β^c is the numerically-determined critical inclination for tumbling, evaluated at film height $h = h^c$ for which h^c is the critical height for which confinement suppresses the active matter instability in the limit $\beta = 0$. (B) Director and velocity vector fields over the 2D film for the same regime.

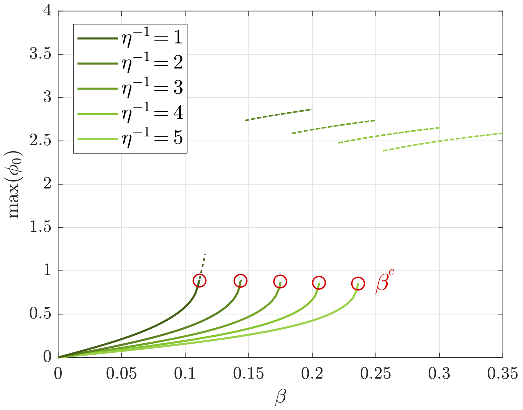

FIGURE 5.16: The maximum angle obtained in the steady director for an extensile suspension with varying elasticity, evaluated at $h < h^c$, where the critical confinement length is evaluated for the default parameter size $\eta^{-1} = 1.2$. Solid lines indicate a 'tilted' state (modes corresponding to FIGURES 5.13 and 5.15), dashed lines correspond to a 'tumbled' state (modes corresponding to FIGURE 5.17).

Since we are able to closely follow a particular type of steady solution for the suspension to an arbitrary level precision as inclination is increased, if the continuity algorithm described in Section 4.3 fails to converge to the same solution type, we can ascertain that that particular type of solution is no longer valid for that value of β. We determine 'tumbling' to occur at the onset of this failure, where if we were in an experimental regime and had continued to increase the film inclination, we would no longer be able to find a steady state for the director field without disinclinations and refer to the critical inclination angle for tumbling to occur as $\beta = \beta^c$.

In FIGURE 5.16, the maximum angle ϕ_0^m over the film height is plotted against the inclination angle β for various values of elasticity at $h \approx h^c|_{\eta^{-1}=1.2}$, where the inclination is gradually increased from 0. When $\beta < \beta^c$, we refer to the system as being in a 'tilting' regime (solid lines in FIGURE 5.16, with modes qualitatively corresponding to FIGURES 5.13 and 5.15), where director elasticity is strong enough to continuous local order over the film height. Experimentally, as long as inclination is gradually increased, we would expect to be able to find all the steady states between $\beta = 0$ and $\beta < \beta^c$. As inclination is increased further, the continuity algorithm fails, and although we are able to find steady state solutions (dashed lines), we would not expect to be able to find these states experimentally by gradually increasing inclination, as the stability of the suspension decreases as β approaches β^c from 0. Consequently,

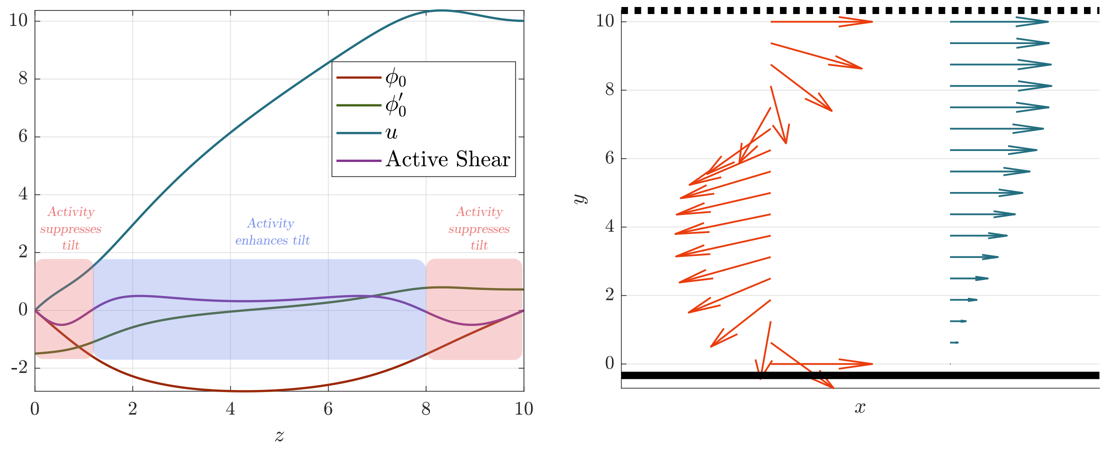

FIGURE 5.17: (A) Plot of the steady state for an inclined film. The film is inclined at an angle $\beta > \beta^c$ for an extensile suspension. Regions highlighted in blue (red) are where active-shear enhances (suppresses) local rotation. (B) Director and velocity vector fields over the 2D film for the same regime.

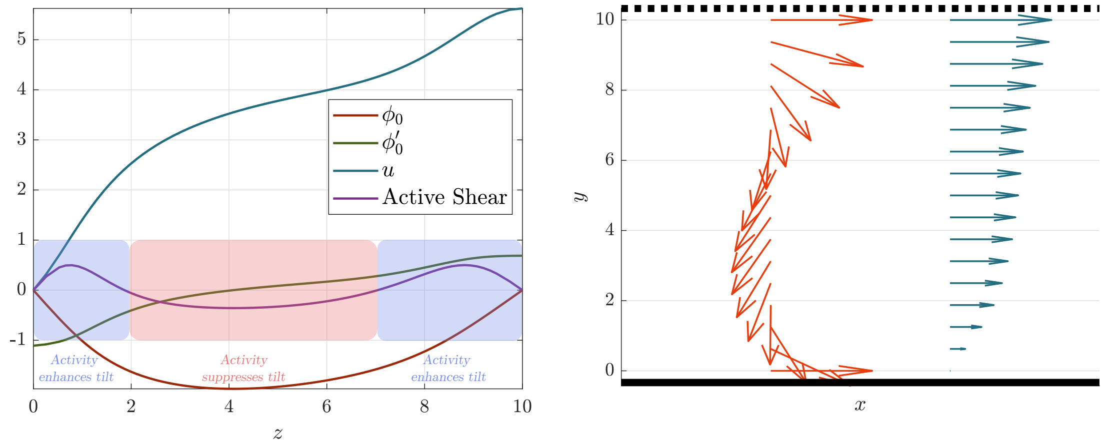

FIGURE 5.18: (A) Plot of the steady state for an inclined film. The film is inclined at an angle $\beta \approx \beta^c$ for a contractile suspension. Regions highlighted in blue (red) are where active-shear enhances (suppresses) local rotation. (B) Director and velocity vector fields over the 2D film for the same regime.

we refer to these theoretical states as ‘tumbled’ states, and suggest they could be found experimentally by using an external-alignment field.

Increasing η^{-1} corresponds to increasing elasticity in the suspension which will increases the stability of the suspension by penalising gradients in the director field and cause the critical film height h^c to also increase. Consequently, when the film height is held constant, the critical inclination angle β^c to induce tumbling will increase (β^c in red circles) as η^{-1} increases. The critical value β^c is dependent on several factors: the elasticity suspension, which penalises gradients in ϕ_0 and increases the inclination threshold for tumbling; the film height h, which confines the vortex modes as discussed in Chapter 4 and increases orientational stability by imposing order at the boundaries, changes in the swimmer geometry, which are reflected in the alignment-to-shear parameter λ_1, and, the sign of activity. For an extensile suspension, active shear which is proportional to $\sin 2\phi_0$ (equation (5.5a)) suppresses local shear when $\phi_0 > -\pi/4$ and enhances local shear when $\phi_0 < -\pi/4$. Figure 5.16 corresponds to an initially stable film which is slowly inclined by angle β, but as soon as $|\phi_0^m|$ exceeds $\pi/4$ the local shear-induced torque experienced by the suspension rapidly increases. Since this occurs in two locations, close to the bottom of the film near the substrate ($z = z_1$) and close to the free-surface ($z = z_2$), when $\beta > \beta^c$ we find that the director in the region of $z \in [z_1, z_2]$ flips into a ‘tumbled’ regime (dashed lines in Figure 5.16 with modes qualitatively corresponding to Figure 5.17). Conversely, when studying a contractile suspension, increasing β such that $|\phi_0^m|$ exceeds $\pi/4$ shows no corresponding jump to a ‘tumbled’ regime, as activity enhances local director rotation for $\phi_0 > -\pi/4$ and suppresses it for $\phi_0 < -\pi/4$. The dashed lines in Figure 5.16 and the associated modes plotted in Figure 5.17 could be realised experimentally by investigating a suspension initially stabilised by elasticity and gently tilted until a region flips into a tumbled state.

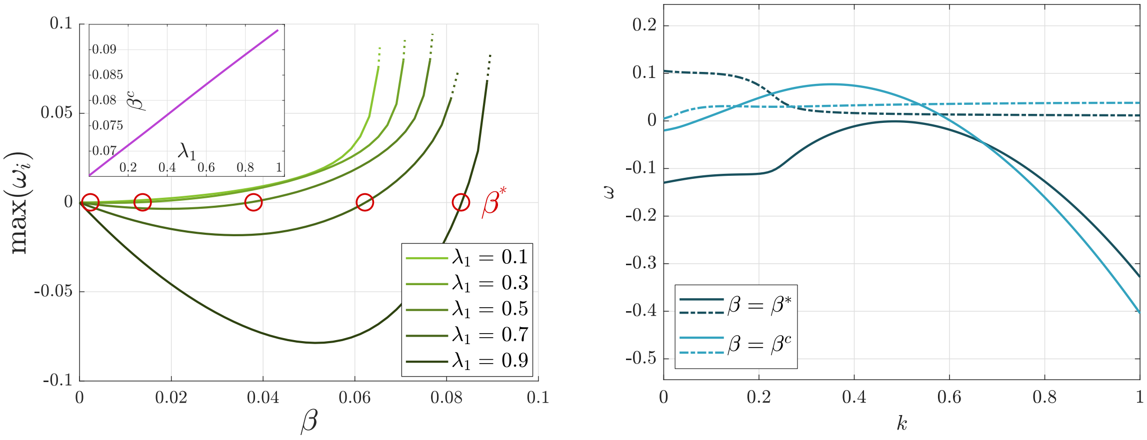

FIGURE 5.19: (A) *Main:* The maximum growth rate ω_i for $\lambda_1 = [0.1, 0.3, 0.5, 0.7, 0.9]$ over $\beta \in [0, \beta^c]$ for which β^c is the critical inclination to induce tumbling. The numerical solutions are solved for $h = h^c$, where h^c is the critical confinement height to suppress the bulk instability. As the director approaches the tumbled angle $\phi_0 \approx \pi/4$, we are no longer able to numerically solve the steady state (dotted lines). *Sub:* The tumbling angle β^c is linearly dependent on the alignment-to-shear parameter, λ_1. (B) Dispersion relation for ω^+ for $h = h^c|_{\beta=0}$ and inclination $\beta = \beta^*$, the inclination value for which the suspension becomes unstable and $\beta = \beta^c$ the critical inclination angle for the tumbled regime. The imaginary part of ω is plotted with a solid line and the real part is plotted with the dashed line.

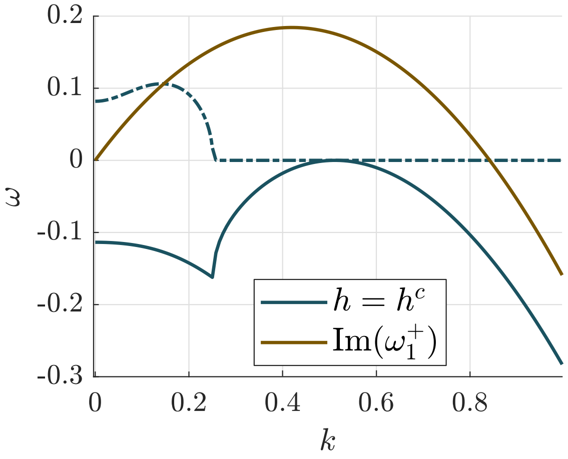

FIGURE 5.20: Dispersion relation for ω^+ in the 2D film, with $\beta = 0$ and comparison to the bulk growth rate ω_1^+. A bifurcation occurs at $k \approx 0.25$ where the system switches between stationary and travelling planar-waves.

5.4.3 Shear Alignment Significantly Dampens Growth

We investigate the effect of inclination on the stability of the active suspension at the critical film height $h = h^c$ for which confinement suppresses the bulk instability in the $\beta = 0$ case (FIGURE 4.13B). In FIGURE 5.19A *main*, the maximum growth rate of the perturbation is plotted for $\lambda_1 = 0.1$, 0.3, 0.5, 0.7 and 0.9. We uncover two regimes of stability as the inclination angle β is increased from zero, determined by the parameter β^*: when $\beta < \beta^*$, inclination is stabilising and when $\beta > \beta^*$, inclination is destabilising. Similarly to Section 3.4 (equations (3.18)), imposed shear acts at order $\mathcal{O}(1)$, and when $\lambda_1 = 0$ any inclination will destabilise the suspension, as the rotation-due-to-vorticity component of the imposed shear given by $\frac{1}{2}\partial_z u_0 \phi_1 \sin\phi_0$ is always destabilising, independent of the perturbation wavelength $\boldsymbol{k}$ (equation (5.18)). However, for non-zero λ_1, initially inclination provides a net *stabilising* effect by introducing a preferential alignment direction by virtue of gravitationally imposed shear gradients. As β increases beyond β^* (reference steady solution for $\beta^* < \beta < \beta^c$ in FIGURE 5.15), ϕ^m exceeds $\pi/4$ and alignment-to-shear becomes destabilising, as discussed in FIGURE 5.16, and both vorticity and alignment-to-shear work together to destabilise the suspension. Finally, as $\beta \to \beta^c$, the growth rate *appears* becomes exponentially proportional to β, as a perturbation will locally cause tumbling. However, as we approach β^c, the numerical solver fails to converge to a solution as the tumbling regime goes beyond what our linear stability analysis can model. Plotting the dispersion relation for $\beta = \beta^*$ and $\beta \approx \beta^c$ in FIGURE 5.19B reveals a transition for all $k \in [0, 1]$ from stationary planar-waves to travelling planar-waves and a smoothing of the growth rate near the bifurcation at $k \approx 0.25$ in the $\beta = 0$ case (FIGURE 5.20).

Plotting the eigenvectors, steady state and vectorfields for $\beta = 0$, 0.001, 0.005 and 0.02 in FIGURE 5.22 reveals a similar narrative to regime of imposed slip in Section 5.3.1, FIGURE 5.10: as β increases and the amplitude of imposed shear flow increases, we observe a transition from the vortex lattice characteristic of Chapter 4 to a 'wonky' flow regime with a net flow down the film length in the x-direction. Without an imposed flow, the director is aligned down the film along the x-axis.

Perturbing the suspension by a planar-wave creates regions (columns) of up- and down-flow, and the columns collapse at the boundaries due to the impermeability boundary condition, creating a vortex lattice which consists of alternating clockwise and anti-clockwise vortex cells, where the boundary between vortex cells corresponds to the regions of up- and down- flows. We label anti-clockwise vortex cells as 'odd' and clockwise vortex cells as 'even'. When a gravitational shear is imposed, the director tilts downwards towards the substrate, and when the suspension is perturbed by a planar-wave the vortex cells are tilted with respect to the long axis of the film. Since the background flow is non-uniform and fastest near the substrate, a net flow emerges as the odd (even) vortex cells *appear* to migrate toward the surface (substrate). However, the instability mechanism for the inclined film regime remains the same: in FIGURE 5.21 the streamlines for the perturbed modes corresponding to FIGURE 5.22 are plotted. Note that these streamlines are for the perturbed modes *only* (*i.e.* only ϕ_1, $\boldsymbol{u}_1$ are plotted, not $\phi = \phi_0 + \varepsilon\phi_1$, $\boldsymbol{u} = \boldsymbol{u}_0 + \varepsilon\boldsymbol{u}_1$ *etc.*). In FIGURE 5.22 the vortex lattice disappears completely when the net background flow $u_0(z)\hat{\boldsymbol{x}}$is larger than $\max(\boldsymbol{u}_k)$. Since the solutions are summed as $f = f_0 + \varepsilon f_1$, where $\varepsilon \ll 1$ is an undetermined small parameter, the value of β for which this occurs is dependent on our choice of ε. For FIGURE 5.22 and all other similar figures in this Chapter, $\varepsilon = 0.2$ for the purpose of illustrating net streamlines.

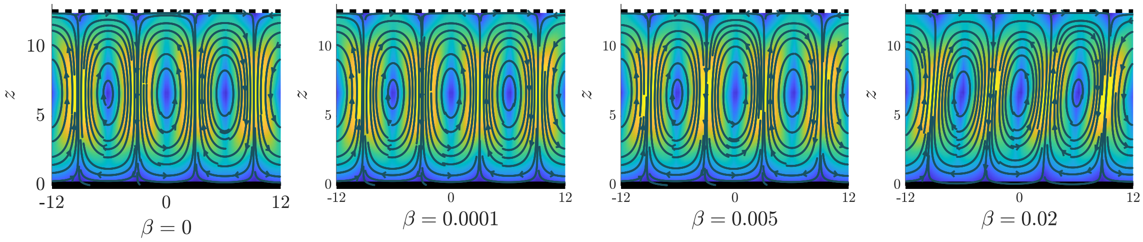

$\beta = 0$

$\beta = 0.0001$

$\beta = 0.005$

$\beta = 0.02$

FIGURE 5.21: Streamlines corresponding to the eigenmodes of the inclined film, evaluated at $k = k^m$ and $h = h^c|_{\beta=0}$. *Only* the perturbed modes are plotted, the full solutions are plotted in FIGURE 5.22.

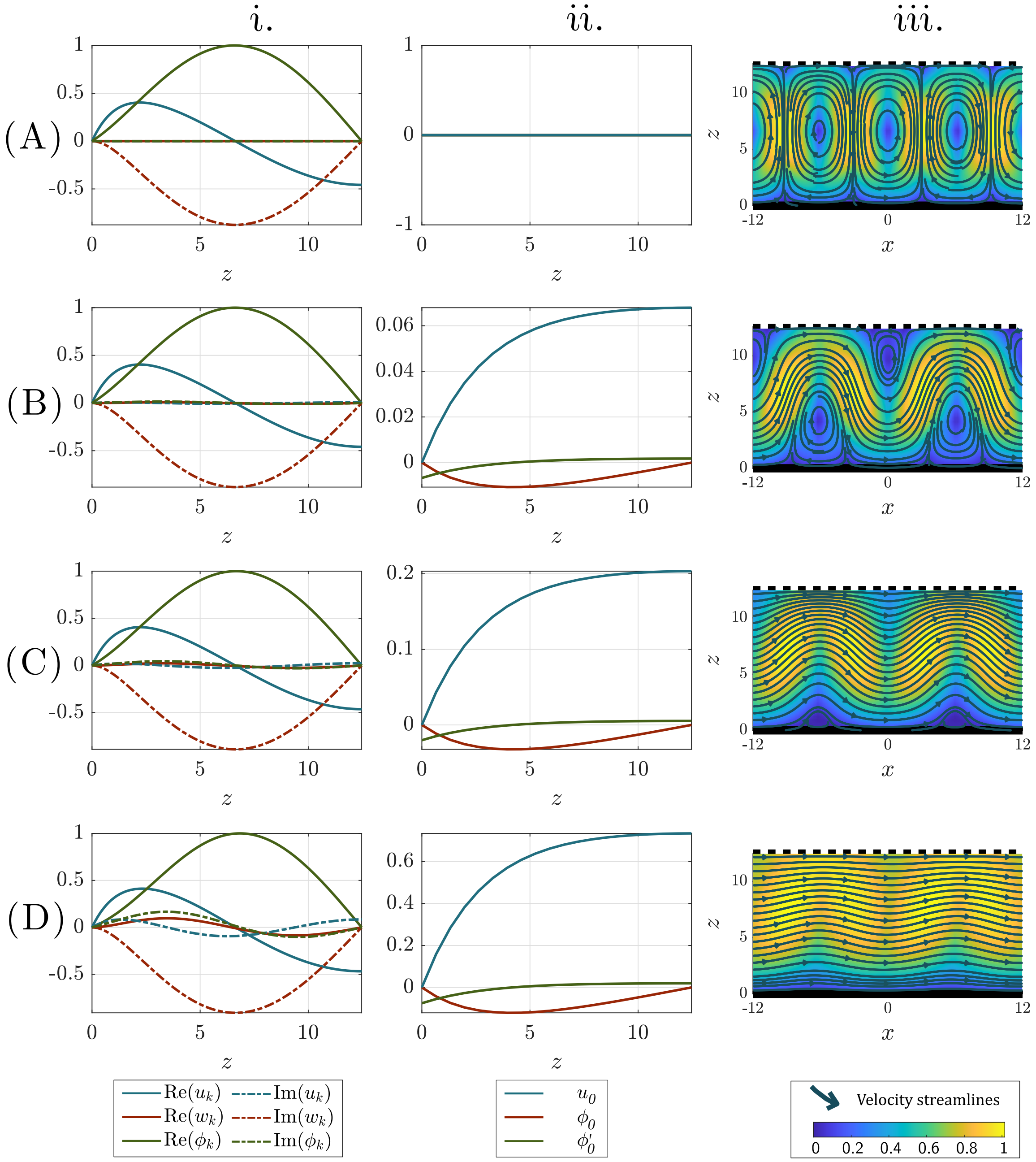

FIGURE 5.22: *i.* Eigenmodes plots, *ii.* steady state plots, *iii.* streamlines (full solutions, steady & perturbed state) for the inclined film, evaluated at $k = k^m$ and $h = h^c|_{\beta=0}$, where (A) $\beta = 0$, (B) $\beta = 0.001$, (C) $\beta = 0.005$, (D), $\beta = 0.02$.

5.5 Remarks: Boundary Phenomena Qualitatively Alter Modes

In this final chapter, we have matured the numerical work undertaken in Chapter 4 to regimes with alternative steady states. Initially, we explored the effect of rotating the director with respect to the channel in Section 5.1. In the analysis conducted in Chapter 2, we had uncovered that the least stable mode in the bulk suspension was concerned with a bend deformation which corresponded to gradients in the director along the ordered axis and fluid pumped perpendicular to the ordered axis. Consequently, our initial hypothesis for the rotated constant steady state was that the instability growth rate would reach a maximum when perpendicular to the boundaries, as this would allow activity-driven flow to orient down the infinite length of the channel. However, the unintended side effect of rotating the director by an angle β_j was that it effectively changed the perturbation wavevector angle, denoted by q in the bulk analysis, and introduced stabilising splay into the suspension. An increase in the growth rate was achieved by rotating the constant steady state for non-zero λ_1, but the maximum was obtained near to $\beta_j = \pi/4$.

In Section 5.2, we determined the static torque balance equation, describing the steady state of the director in background shear, or self-imposed active flow, which we used in Section 5.3, to impose a slip angle for the channel at the substrate. The resulting director profile resembled a splay deformation over the height of the film, and by consequence of activity, generated a steady Poiseullie-like flow field. Investigating the perturbed modes unveiled a ‘wonky’ net back flow orientated down the unbounded channel length, where oscillations in the flow occur due to the superposition of the background active flow with the regular vortex lattice, as described in Chapter 4.

The planar-waves were travelling, and boasted a growth rate that monotonically increases with imposed slip angle β_j, obtaining a maximum growth rate for $\beta_j = \pi/2$.

However, whilst there are regimes where such a slip angle might exist, the rigid application of an *imposed* slip angle at the substrate should be interpreted carefully as fixing the boundary condition has implications on the types of solutions we might find: phenomena in the bulk channel are determined *by* the conditions set at the boundary, and system is coerced into satisfying niche criteria which might not reflect reality. A suitable extension of this regime would be to include polarity and number density variations, which could reflect *E. Coli* experiments, which exhibit trapping at the substrate.[47] Swimmers approaching a substrate can get trapped at the substrate for significant periods of time due to a mixture of hydrodynamic and steric interactions.

Lastly, in Section 5.4 we explored the effects of inclining the 2D film. The inclined film imposes a gravitational shear, which tilts the director at a maximum closest to the substrate. The introduction of an imposed shear introduces the possibility of tumbling, and we found that the onset of the tumbling regime is influenced by the activity type: when pointing downhill, extensile suspensions are *less* prone to tumbling, as the active flow arising from the steady director deformation suppresses local shear. This effect occurs as long as the maximum angle of the director is less than $\pi/4$, when this angle is exceeded, activity *enhances* local shear and we saw a jump from a tilted regime to a 'tumbled' regime in which a small region of the director profile flips to pointing uphill.

Finally, investigating the stability of the inclined plane, we found that the stability of the perturbed modes was strongly dependent on the alignment-to-shear parameter λ_1, as the existence of an imposed shear creates a preferential alignment direction for the director which stabilises the suspension. However, for all values of $\lambda_1 < 1$, vorticity ensures that inclination is always destabilising for a sufficiently large inclination angle β.

6 | Conclusion

In this thesis, we have explored and extended a long-wavelength instability known to affect suspensions of ordered microswimmers in a momentum-conserving medium. Active flow develops as a result of bend and splay deformations in the director field, and the subsequent shear is contained in the same plane as the deformation. When a constant director field is perturbed, an instability develops when the active flow enhances the director deformation by shear-imposed torque. This work discussed this phenomena in a variety of regimes and confinements, and the chapters are briefly summarised as follows: Chapter 2 established the fundamental instability, detailing the instability mechanism for extensile and contractile suspensions, and in particular, the phase relationship between the fluid flow and director. Chapter 3 extended this 2D analysis into the 3D regime, where the 2D nature of the active flow leads to a de-coupling in the governing equations and the dominance of bend modes for extensile suspensions. In our main result, we included a chirality term in the Jeffrey orbit equations which re-couples the governing equations for the active matter suspension, and leads to an alternative instability regime whereby the bulk instability growth rate is enhanced for small imposed shear flow, so long as both chirality and alignment-to-shear terms are present. In Chapter 4, we studied the instability in films and channels, connecting instability growth rates from the bulk, to thick films and thin films, and discussed the critical film/channel height to suppress the instability. Here, we discovered that the de-coupled equations discussed in Chapter 3 cause the 3D regime to boast larger growth rates compared to the 2D regime for a given confinement length, and with careful application of boundary conditions the critical confinement length can be reduced by an order of magnitude. In Chapter 5, we rotate the director field from being orientated down the channel length to being perpendicular to it and surprisingly discover the optimum angle to enhance the instability growth rate is around $\pi/4$ when the alignment-to-shear term is non-zero. Finally, investigating regimes with a steady, non-constant director field we explored a regime of imposed slip which evolves the vortex lattice into a regime of net flow with decreased stability, and reveal a 'tumbled' regime for the inclined flow, showing that inclination will enhance the instability growth rate, as long as alignment-to-shear is sufficiently small.

6.1 Thesis Overview

A suspension of microswimmers exerts a hydrodynamic stress on their surrounding medium proportional to the activity level of the swimmers. The divergence of the active stress $\alpha\nabla \cdot \boldsymbol{pp}$, which was derived using a coarse-grained approximation for a suspension of force-dipoles, contributes a forcing term into the Stokes equations wherever there exists local deformations in the director, a unit vector describing the local averaged orientation of swimmers. The forcing changes sign depending on whether we're investigating an extensile ($\text{sgn}(\alpha) = -1$) or contractile suspension ($\text{sgn}(\alpha) = 1$).

Following the derivation of the active stress in Section 1.2.1, we discussed the governing equations for the director in Section 1.2.2. We utilised the Jeffrey orbit equations to describe the evolution for a swimmers orientation due to vorticity and shear alignment effects and generalised the Jeffrey orbit equations to a suspension with orientational order by inclusion of an elasticity term derived from liquid-crystal literature which restores local order on the suspension by penalising gradients in the director. Having established the active matter governing equations in Chapter 1, in Chapter 2 we sought to understand the mechanism for instability by performing a linear instability analysis about the constant ordered state $\boldsymbol{p} = \hat{\boldsymbol{x}}$, $\boldsymbol{u} = \boldsymbol{0}$.

The growth/decay of a perturbation of wavelength $2\pi/k$ to the steady state was quantified by the imaginary component of the eigenvalue $\omega(k)$ when seeking planar-wave solutions of the form $f = f_k \exp(i\boldsymbol{x}\cdot\boldsymbol{k} - i\omega t)$. In Section 2.3, we found (in agreement with pre-existing literature) that an extensile (contractile) suspension is unstable to long-wavelength bend (splay) perturbations, subject to an upper bound $k^2 < \frac{1+\lambda_1}{2\eta}$ ($k^2 < \frac{1-\lambda_1}{2\eta}$) due to elasticity, where λ_1 measures alignment-to-shear and elasticity damping is contained in the dimensionless parameter $\eta^{-1} = \frac{D\mu}{L^2|\alpha|}$, and L is a characteristic length scale, which we set as $L = \sqrt{\frac{D\mu}{|\alpha|}}$ to balance elastic restoration forces and active shear. The instability acts at long-wavelengths due to activity acting at order $\mathcal{O}(k)$ and elasticity damping acting at order $\mathcal{O}(k^2)$ for disturbance amplitude k.

In an extensile suspension, we recovered that bend (splay) deformations in the director pump fluid along the outward normal of a bend formation (out the closed end of a splay deformation, respectively). When seeking perturbations as planar-wave solutions of the ordered state, active pumping due to bend and splay is proportional to the gradients in the director, not the the maximum deviation from the ordered state. Consequently, active flow arising from planar-wave deformations is $\mp\pi/2$ out-of-phase with the director, with the sign dependent on the extensile/contractile nature of the suspension, and, whether we have a bend or splay deformation. Rotational effects on the director are governed by the magnitude of shear, which in turn has a $\pi/2$ out-of-phase relationship with active flow. Consequently in an extensile (contractile) suspension, rotation due to active shear gradients is shifted in-phase (π out-of-phase) to the bend deformation and bend modes are unstable (stable) for extensile (contractile, respectively) suspensions. In the 2D regime, gradients in the director were quantified by the wavevector angle q such that $\boldsymbol{k} = k(\cos q,\ 0,\ \sin q)$, and a pure bend (splay) deformation is quantified by $q = 0$ ($q = \pi/2$, respectively). Increasing the wavevector angle q from zero to $\pi/2$ corresponds to an increase of splay in the system and a decrease of bend. At $q = \pi/4$, we saw an important phase shift as splay becomes the dominant mode, stabilising (de-stabilising) an extensile (contractile, respectively) suspension. This phase relationship was illustrated by FIGURE 2.12.

Having established and understood the fundamental instability mechanism as described in Chapter 2, we proceeded to extend the instability analysis into the 3D regime in Chapter 3. Firstly, we observed that when applying a perturbation wavevector $\boldsymbol{k}$ restricted (without loss of generality) to the x-y plane, the corresponding Fourier modes de-coupled into two systems: the first systems components consisted of the Fourier modes associated with the x-y plane, and the second systems components consisted of the Fourier modes associated with the z-axis. The unstable eigenvalue associated with the first system experiences the full wavevector $\boldsymbol{k}$, and correspondingly exhibited both bend and splay deformations in the director field, and their associated active flow. Since the active flow and corresponding shear-induced rotation of a bend/splay deformation is contained within the same plane as the deformation itself, the instability mechanism and stability of this system was consistent with the 2D analysis discussed in Chapter 2, where increasing the wavevector angle q corresponds to an increase of stabilising splay in the system (for an extensile suspension). The second of the de-coupled systems, whose Fourier components are those pointing in the z-axis, only experiences the projection of the wavevector $\boldsymbol{k}$ onto the x-axis, such that the projection wavevector takes the form, $\tilde{\boldsymbol{k}} = k \cos q \hat{\boldsymbol{x}}$. The instability mechanism and stability of this system was consistent with a 2D system perturbed by a pure bend mode with $\tilde{q} = 0$ and $|\tilde{\boldsymbol{k}}| = k \cos q$. The eigenvalue analysis of the decoupled modes indicate that in the 3D regime, the second system associated with a pure bend mode will always grow faster than the first system, consisting of mixed bend/splay deformations.

In Section 3.3.2, we introduced swimmer chirality into the director equation by including the term $\lambda_2 \boldsymbol{p} \times [(\boldsymbol{\delta} - \boldsymbol{pp}) \cdot \boldsymbol{E} \cdot \boldsymbol{p}]$ into the Jeffrey orbit equation. Chirality induces out-of-plane rotation in the director, where out-of-plane is quantified by a rotation with a component in the orthogonal axis to the plane of shear. Consequently, chirality re-couples the de-coupled bend and bend/splay modes described for a wavevector restricted to the x-y plane. In the least stable configuration, the two components of the perturbed director orthogonal to the ordered axis are $\pi/2 \pm \epsilon$ out-of-phase, where the magnitude of ϵ depends on the strength of the chirality parameter λ_2 and each component can be thought of as bend mode of the director propagating into the y- and z-axis respectively. The shift in phase difference from exactly $\pi/2$ occurs due to a shift in the location of the maximum rotation due to shear: deviation from the ordered state is enhanced by the flows orthogonal to plane as well as flows in the plane when chirality is present, and the coupling between components causes the resultant mode to 'spirals' around the ordered axis due to the introduction a twist deformation. In the final section of Chapter 3, we investigated the change in growth rate to the fundamental instability when imposing a shear flow orthogonal to the ordered direction. We revealed an interesting relationship between the alignment-to-shear and chirality, where the growth rate was enhanced by up to 10% versus the bulk instability rate when both λ_1 and λ_2 were non-zero and dimensionless shear took the values $A \in [0.1, 0.5]$, where unity is normalised to the active shear rate.

Two results in Chapter 4 illustrate the importance of studying bulk systems without confinement: firstly, the critical film height h^c to suppress the instability in the 2D regime takes the value $h^c \approx \pi/k^m|_{h=\infty}$, where k^m is the wavenumber associated with the maximum growth rate in the bulk, and secondly, the 3D regime is less stable than the 2D regime in confinement as the 3D bulk analysis showed that the suspension is unstable for *all* $q \in [0, \pi]$, as opposed to $q \in [0, \pi/4]$. We demonstrated this by connecting the bulk instability analysis to two regimes of confinement (a channel and film) by numerically solving the linear instability analysis for Fourier modes $f = f_k(z)\exp(i\boldsymbol{k}_\perp \cdot \boldsymbol{x}_\perp - i\omega t)$, where $\perp$ indicates x-y components, and using alignment of the director at the substrate/free-surface and no-slip/no-shear on the fluid as our boundary conditions. In the limit of large $h \gg 1$, where the confinement length is normalised to the characteristic length scale L for which elasticity balances activity driven shear, we recovered the bulk instability growth rate for $k \approx k^m|_{h=\infty}$. This is because for large enough k, the infinitely long columns of fluid characteristic of the bulk analysis collapse into a lattice of elongated vortex modes due to the impermeability condition at the boundaries. However, for small k, we observed a bifurcation at $k^c \approx \pi/h$ when the vortex modes, whose length are dictated by the wavevector k, can no longer fit into the channel height and instead are forced along the unbounded channel length. In the final section of this Chapter, we discussed an alternative torque-free boundary condition on the free-surface for a 3D film, which we affectionately called the 'Gecko' boundary condition. The boundary condition enhances the instability growth rate by allowing the director to rotate in the x-y plane at the free-surface, which consequently allows bend modes to propagate and pump fluid on the boundary without being suppressed. When applying the Gecko boundary condition, we found an order of magnitude decrease in the critical confinement height required to completely suppress the instability.

In Chapter 5, we explored the effect of confinement on three alternative steady states: a constant director field, rotated with respect to the length of a channel; an 'imposed slip' regime, with a non-constant director across the channel width and a non-zero steady flow; and an inclined film, where alignment is imposed at the top and bottom, but gravitational forces give rise to a steady parabolic flow and impose a non-constant director over the film height. In the first regime, the rotation of the director field along the channel was quantified by the boundary condition $\boldsymbol{p} \cdot \boldsymbol{n} = \beta_j$; since active flow arising from a bend deformation is perpendicular to the director angle, increasing the rotation angle β_j increases the available space for the vortex lattice to fill and results in a tilting of the vortex lattice. Consequently, as $\beta_j \to \pi/2$, we observed a switch between a tilted vortex lattice to the vortex modes filling the infinitely long channel. In Chapter 4 we saw the instability growth rate was suppressed as the vortex lattice became increasingly confined as the confinement height decreased. However, in the limiting case of $\lambda_1 = 0$, rotating the director had no effect on the stability growth rate, as the increased vortex cell length is exactly balanced by the increase of splay in the system, which stabilises an extensile suspension. Unexpectedly, we found that for non-zero λ_1, the growth rate *increased* with β_j, with a maximum around $\beta_j = \pi/4$. We suggest that this occurs due to the skewing of the vortex lattice: as the vortex cells are tilted, the net flow is skewed from propagating perpendicular to the director, providing an preferential alignment direction down the channel length and enhancing director rotation.

In the second regime, we imposed a slip angle at the top and bottom of the substrate, which results in non-constant steady director, which exhibits a splay deformation over the height of the film. Since director gradients result in activity driven flow, we found the resultant flow was Poiseuille-like and expresses a static torque balance between shear-induced torque and elasticity. Perturbing this steady state resulted in a 'wonky' net flow along the channel length, where the oscillatory flow arises from the vortex lattice characteristic of the suspension in a channel, imposed on to the steady background flow. Increasing the imposed slip angle corresponded to an increased growth rate, as the vorticity term of the background shear destabilises the suspension. Experimentally, such a regime could only be realised if the substrate could impose strong torque on the director, or if the active particles themselves exhibit niche behavioural mechanisms near the boundary.

In the final regime, we explored the effects of inclining a 2D film. This regime was solved with the same static torque balance equation that the imposed slip regime was, but where gravitational shear causes a tilting on the director. Lone swimmers are subject to tumbling when shear is imposed, and we found that the onset of tumbling differed depending on the activity type: extensile suspensions enhance local shear when the director angle is greater than $|\pi/4|$ to the substrate, whereas contractile suspensions suppress local shear when the director angle is greater than $|\pi/4|$. Consequently, contractile suspensions have a higher tumbling threshold than extensile suspensions. Extensile suspensions instead display a jump to a tumbled regime, in which a small region of the director flips to pointing the opposite way. Lastly, we found that inclination was destabilising due to the vorticity component of the gravitational shear, but for sufficiently small inclination, alignment-to-shear is strongly stabilising as gravitational flow introduces a preferential alignment axis for the director.

6.2 Remarks and Future Works

The model employed throughout this work is a minimalist description to capture the choice of boundary conditions and to connect the dynamics of the bulk to regimes of confinement. The simplest extensions to the model studied would be to conduct a linear stability analysis on the full set of governing equations given by (2.4a–d), as our simplifications included constant concentration, zero-motility, and constant scalar order parameter. The publications discussed by Doostmohammadi & Yeomans[8] and Sumesh Thampi[40] indicate how topological defects can qualitatively effect observed modes, and we would like to further extend the model by implementing Q-tensor theory from liquid-crystal literature which would allow us to model topological defects in the director.

The majority of the analysis conducted has centred around an extensile suspension, which is susceptible to bend deformations. Since a bend deformation produces an active flow perpendicular to the ordered axis, we inevitably suppress the fundamental instability when restricting an extensile suspension to a 2D channel. We hypothesised that when the director was instead perpendicular to the boundaries, a bend deformation would be free to pump fluid down the infinite length of the channel. However, to our surprise, this regime had the same stability as the case when the steady director was parallel to the boundary. This raises the question: what would occur with a contractile suspension aligned down, or perpendicular to, the boundaries of a channel? We hypothesise that the critical confinement length h^c for suppressing a contractile suspension might be much smaller, as contractile suspensions are unstable to splay perturbations which would generate active flow down the unbounded length of the channel, instead of being directed towards boundaries.

Throughout this work, wherever a free-surface has been modelled we have imposed $\boldsymbol{p} \cdot \boldsymbol{n} = 0$, as swimmers cannot swim through the boundary. Secondly, we presume that the free-surface cannot impose a strong-anchoring regime like at the substrate, which led us to considering the Gecko boundary condition in Section 4.9. We would like to investigate when are these presumptions admissible, and in particular, are there regimes where a suspension of swimmers can deform the free-surface by swimming into it? This would require modelling surface tension in the boundary conditions for the film height h, and an analysis surrounding a new dimensionless parameter balancing surface tension to activity. Applying the Gecko boundary condition to allow the director to rotate at the free-surface would effectively couple activity to free-surface tilt, which could lead to growing capillary surface waves for sufficiently strong activity.

In the penultimate chapter, we discussed the existence of alternative steady states for the director as a static torque balance. As a possible research avenue, the steady state equations for the 3D regime were also evaluated and coded. Using this code, we would like to explore a regime of imposed twist, where the director is forced into alignment at the top and bottom of a channel with a twist deformation across the channel height; as twist alters the propagation direction for active flow, we would expect this regime to yield strong mixing in the vortex lattice. Introducing chirality negates the possibility of steady states with imposed shear, such as in the inclined film, but could yield unique modes for the imposed twist regime.

The code developed in the second half of this work is extendable to these regimes of interest, but any discussion will always suffer the same casualty: a numerical linear instability analysis is always hindered by the choice of boundary conditions, which may or may not be sensibly chosen. Moving beyond the linear regime in an imminent post-doctorate, we will be conducting a complementary analysis focussed on swimmer-boundary interactions by performing computational simulations on a suspension in confinement. The end goal will be to evidence the research and discoveries detailed in this work, and to explore more exciting regimes, such as swimmers in complex confinement, swimmer-swimmer interactions, and active droplets.

Appendices

A Stresses, moments and energy in the director

This derivation for the external torque imposed on the director follows a general treatment for the stresses, moments and energy on an anisotropic fluid with generalized forces,

$\boldsymbol{g}$	External body force per unit mass,
$\boldsymbol{b}$	External body moment per unit mass,
$\boldsymbol{t}$	Surface force per unit area,
$\boldsymbol{l}$	Surface moment per unit area.

The derivation follows a typical liquid-crystal treatsie, similar to De Gennes & Prost.[48] The fundamental difference is in the interpretation of the anisotropic fluid; here, an anisotropic suspension exerts stresses and moments mediated by an isotropic fluid.

A.1 Momentum conservation of an Anisotropic Fluid

The linear momentum conservation equation was derived in the main text as equation (1.8). Repeated here it states

$$\rho\dot{\boldsymbol{u}} = \rho\boldsymbol{F} + \nabla\cdot\boldsymbol{\sigma}. \tag{A.1}$$

In a similar fashion to the main text, we can write the equation for angular momentum balance,

$$\frac{\mathrm{D}}{\mathrm{D}t}\int\rho\Big(\boldsymbol{x}\times\boldsymbol{u}\Big)\,\mathrm{d}V = \int_V\rho\Big(\boldsymbol{x}\times\boldsymbol{F}+\boldsymbol{B}\Big)\,\mathrm{d}V + \int_S\Big(\boldsymbol{x}\times\boldsymbol{t}+\boldsymbol{m}\Big)\,\mathrm{d}S. \tag{A.2}$$

Rewriting the surface force vector $\boldsymbol{t}$ and surface moment vector $\boldsymbol{m}$ using

$$\boldsymbol{t} = \boldsymbol{n}\cdot\boldsymbol{\sigma}, \qquad \boldsymbol{l} = \boldsymbol{n}\cdot\boldsymbol{\pi}, \tag{A.3}$$

we obtain for the surface integral,

$$\begin{aligned}\int_S\epsilon_{ijk}x_jt_k + m_i\,\mathrm{d}S &= \int_S\epsilon_{ijk}x_j\sigma_{\gamma k}n_\gamma + \pi_{\gamma i}n_\gamma\,\mathrm{d}S\\ &= \int_V\partial_\gamma[\epsilon_{ijk}x_j\sigma_{\gamma k}+\pi_{\gamma i}]\,\mathrm{d}V\\ &= \int_V\epsilon_{ijk}x_j\sigma_{\gamma k,\gamma}+\epsilon_{ijk}\sigma_{jk}+\pi_{\gamma i,\gamma}\,\mathrm{d}V.\end{aligned} \tag{A.4}$$

The comma in $\sigma_{\gamma k,\gamma}$ and $\pi_{\gamma i,\gamma}$ denotes the derivative with respect to the γ'th coordinate. Bringing the derivative inside the integral the left hand side of (A.2) reads,

$$\int_V \rho \epsilon_{ijk} x_j \dot{u}_k \,\mathrm{d}V = \int_V \epsilon_{ijk} x_j (\rho F_k + \sigma_{jk,j}) \,\mathrm{d}V, \tag{A.5}$$

where we have used (A.1) to express $\dot{u}_i$ in terms of the body force and stress tensor. Bringing together the contributions of (A.4), (A.5) and reducing the integral to point form, we obtain an expression for the balance of angular momentum,

$$\rho B_i + \epsilon_{ijk}\sigma_{jk} + \pi_{ji,j} = 0. \tag{A.6}$$

Note that in an isotropic fluid, the external body moment $\boldsymbol{B}$ and couple stress tensor $\boldsymbol{\pi}$ are generally zero, reducing (A.6) to $\epsilon_{ijk}\sigma_{jk} = 0$, which would imply that the stress tensor is symmetric and returns the linear momentum equation (1.8).

A.2 Hydrostatic equilibrium of the director

The hydrostatic equilibrium for the elastic stresses acting on a microswimmer in an ordered suspension can be obtained by considering a free-energy argument for the distortion energy. The total elastic free energy $\mathcal{F}_T$ is a volume integral of the Frank free-energy, f_d, for the elastic distortions given by (1.32).

$$\mathcal{F}_T = \int_V \frac{1}{2}K_1(\nabla\cdot\mathbf{p})^2 + \frac{1}{2}K_2(\mathbf{p}\cdot\nabla\times\mathbf{p})^2 + \frac{1}{2}K_3||\mathbf{p}\times\nabla\times\mathbf{p}||^2 \ \mathrm{d}V. \tag{A.7}$$

From left to right, the three terms represent the splay, twist and bend deformations. The distortion constants K_i are typically the same order of magnitude, so we adopt the common one-constant approximation such that $K_i = K$. Observing the identity $||\boldsymbol{a}\times\boldsymbol{b}|| = ||\boldsymbol{a}||||\boldsymbol{b}|| - (\boldsymbol{a}\cdot\boldsymbol{b})^2$, with $\boldsymbol{a} = \boldsymbol{p}$ and $\boldsymbol{b} = \nabla\times\boldsymbol{p}$, the integrand can be written as

$$f_d = \frac{1}{2}K\Big[(\nabla\cdot\boldsymbol{p})^2 + ||\nabla\times\boldsymbol{p}||^2\Big]. \tag{A.8}$$

In Cartesian coordinates and utilising index notation, this is equivalent to

$$\partial_i p_i \partial_j p_j + \epsilon_{ijk}\partial_j p_k \epsilon_{imn}\partial_m p_n. \tag{A.9}$$

Here, we use Einstein notation for summation over repeated indices. Observing the identity $\epsilon_{ijk}\epsilon_{imn} = \delta_{jm}\delta_{kn} - \delta_{jn}\delta_{km}$, the second term reads

$$\partial_m p_n \partial_m p_n - \partial_n p_m \partial_m p_n.$$

Recasting indices and employing the product rule, we rewrite (A.9) as

$$\partial_i p_j \partial_i p_j + \partial_i\Big[p_i \partial_j p_j - p_j \partial_j p_i\Big].$$

This allows us to write (A.7) as the sum of a volume integral and surface integral using the divergence theorem,

$$\mathcal{F}_T = \int_V \frac{1}{2}K\partial_i p_j \partial_i p_j \,\mathrm{d}V + \int_A \frac{1}{2}K\Big(p_i\partial_j p_j - p_j\partial_j p_i)n_i \,\mathrm{d}S \tag{A.10}$$

where n_i is the unit normal vector pointing out the volume. The surface integrand represents a saddle-splay term and can be shown to be a null Lagrangian; these terms do not contribute to the bulk energy.[96] Where there is strong anchoring at boundaries, the effect of the saddle-splay term is to impose boundary conditions on the director which we include when we solve the boundary value problem. Consequently, we disregard the surface integral from $\mathcal{F}_T$, leaving us with just the bulk distortion energy,

$$\mathcal{F}_T[\boldsymbol{p}] = \int_V f_d(\boldsymbol{p}, \nabla\boldsymbol{p})\,\mathrm{d}V, \qquad f_d(\boldsymbol{p}, \nabla\boldsymbol{p}) = \frac{1}{2}K||\nabla\boldsymbol{p}||^2. \tag{A.11}$$

To find the conditions for static equilibrium, we minimise the functional $\mathcal{F}_T$ with respect to variations in $\boldsymbol{p}$,

$$\begin{aligned}\delta\mathcal{F}_T[\boldsymbol{p}] &= \mathcal{F}_T[\boldsymbol{p}+\delta\boldsymbol{p}] - \mathcal{F}_T[\boldsymbol{p}],\\ &= \int_V \Big[f_d\Big(\boldsymbol{x}, \boldsymbol{p}+\delta\boldsymbol{p}, \nabla\boldsymbol{p}+\delta\nabla\boldsymbol{p}\Big) - f_d\Big(\boldsymbol{x}, \boldsymbol{p}, \nabla\boldsymbol{p}\Big)\Big]\,\mathrm{d}V,\\ &= \int_V \delta\boldsymbol{p}\cdot\nabla_p f_d(\boldsymbol{p}, \nabla\boldsymbol{p}) + \delta\nabla\boldsymbol{p}\cdot\nabla_{p'} f_d(\boldsymbol{p}, \nabla\boldsymbol{p}) + \mathcal{O}\Big(\nabla_p^2, \nabla_{p'}^2\Big)\,\mathrm{d}V.\end{aligned}$$

In the final line, we have expanded f_d by Taylors theorem where ∇_p indicates gradients with respect to p and similarly $\nabla_{p'}$ indicates gradients with respect to $\nabla\boldsymbol{p}$. Keeping only linear terms and minimising $\delta\mathcal{F}_T = 0$ to all variations in $\delta\boldsymbol{p}$ such that $|\boldsymbol{p}| = 1$, we obtain the static equilibrium condition which we recognise as the standard Euler-Lagrange minimisation equation,[61]

$$\frac{\partial f_d}{\partial p_i} - \frac{\partial}{\partial x_j}\frac{\partial f_d}{\partial(\partial_j p_i)} = h_i. \tag{A.12}$$

Here, $\boldsymbol{h}$ is known as the *molecular field.* Static equilibrium is obtained in the bulk when the director is parallel to $\boldsymbol{h}$. In the case of f_d as given by (A.11), the molecular field reads

$$\boldsymbol{h} = K\nabla^2\boldsymbol{p}. \tag{A.13}$$

A.3 Rate of work

Leslie's 1992[62] rate of work hypothesis stipulates that the rate at which forces and moments do work in an anisotropic fluid is absorbed by the distortion free-energy, kinetic energy and lost through viscous dissipation. Writing down these contributions gives

$$\int_V \rho(\boldsymbol{F}\cdot\boldsymbol{u}+\boldsymbol{B}\cdot\boldsymbol{w})\,\mathrm{d}V+\int_S(\boldsymbol{t}\cdot\boldsymbol{u}+\boldsymbol{l}\cdot\boldsymbol{w})\,\mathrm{d}S=\frac{\mathrm{D}}{\mathrm{D}t}\int_V\frac{1}{2}\rho\boldsymbol{u}\cdot\boldsymbol{u}+f_d+\mathcal{D}\,\mathrm{d}V. \quad \text{(A.14)}$$

Here, $\boldsymbol{w}$ is the axial vector describing the local angular velocity of a microswimmer at $\boldsymbol{x}$. Rewriting the surface integrals in (A.14) using the divergence theorem and (1.5) gives,

$$\int_S(t_iu_i+m_iw_i)\,\mathrm{d}S=\int_V(\sigma_{ji}u_{i,j}+u_i\sigma_{ji,j}+\pi_{ji}w_{i,j}+w_i\pi_{ji,j})\,\mathrm{d}V \quad \text{(A.15)}$$

From the linear momentum balance (A.1) and angular momentum balance (A.6), the RHS can be written,

$$\int_V(\sigma_{ji}u_{i,j}+u_i(\rho\dot{u}_i-\rho F_i)+\pi_{ji}w_{i,j}-w_i(\rho B_i+\epsilon_{ijk}\sigma_{jk}))\,\mathrm{d}V. \quad \text{(A.16)}$$

Observe also that,

$$\int_V \dot{u}_iu_i\,\mathrm{d}V=\frac{\mathrm{D}}{\mathrm{D}t}\int_V\frac{1}{2}u_iu_i\,\mathrm{d}V. \quad \text{(A.17)}$$

Collecting contributions from (A.16), (A.17) and substituting them into (A.14), we obtain a point form expression for the rate of change of forces, moments and work;

$$\sigma_{ij}u_{i,j} + \pi_{ij}w_{i,j} - \epsilon_{ijk}w_i\sigma_{kj} = \dot{f}_d + \mathcal{D}. \tag{A.18}$$

Here, Reynolds transport theorem was used to bring the material derivative into the integrand for f_d. To find an expression for $\dot{f}_d(p_i, p_{i,j})$, note that the material derivative for $\boldsymbol{p}$ can be written,

$$\frac{\mathrm{D}}{\mathrm{D}t}p_{i,j} = \partial_j(\dot{p}_i) - u_{k,j}p_{i,k}. \tag{A.19}$$

By the definition of $\boldsymbol{w}$ we have $\dot{p}_i = \epsilon_{ijk}p_jw_k$; using this and the chain rule allows us to write the material derivative of $f_d(p_i, p_{i,j})$ as,

$$\begin{aligned}\frac{\mathrm{D}}{\mathrm{D}t}f_d(p_i, p_{i,j}) &= \frac{\partial f_d}{\partial p_i}\dot{p}_i + \frac{\partial f_d}{\partial p_{i,j}}\frac{\mathrm{D}}{\mathrm{D}t}p_{i,j} \\ &= \epsilon_{ijk}\Big[\frac{\partial f_d}{\partial p_i}p_jw_k + \frac{\partial f_d}{\partial p_{i,\gamma}}\Big(p_{j,\gamma}w_k + p_jw_{k,\gamma}\Big)\Big] - u_{k,j}p_{i,k}\frac{\partial f_d}{\partial p_{i,j}}. \end{aligned} \tag{A.20}$$

Ericksen[97] showed that the following identity holds for any free-energy function f_d,

$$\epsilon_{ijk}\Big(p_j\frac{\partial f_d}{\partial p_i} + p_{j,\gamma}\frac{\partial f_d}{\partial p_{i,\gamma}} + p_{\gamma,j}\frac{\partial f_d}{\partial p_{\gamma,i}}\Big) = 0. \tag{A.21}$$

Inserting this identity into (A.20) gives us,

$$\dot{f}_d = \epsilon_{ijk}\Big(p_jw_{k,\gamma}\frac{\partial f_d}{\partial p_{i,\gamma}} - p_{\gamma,j}w_k\frac{\partial f_d}{\partial p_{\gamma,i}}\Big) - u_{i,j}p_{k,i}\frac{\partial f_d}{\partial p_{k,j}}. \tag{A.22}$$

Finally, inserting this into (A.18) gives us an expression for the viscous dissipation.

$$\Big(\sigma_{ij}+\frac{\partial f_d}{\partial p_{\gamma,j}}p_{\gamma,i}\Big)u_{i,j}+\Big(\pi_{k\gamma}-\epsilon_{ijk}p_j\frac{\partial f_d}{\partial p_{i,\gamma}}\Big)w_{k,\gamma}+\epsilon_{ijk}w_k\Big(p_{\gamma,j}\frac{\partial f_d}{\partial p_{\gamma,i}}+\sigma_{ij}\Big)=\mathcal{D}. \quad \text{(A.23)}$$

Given that viscous dissipation is necessarily positive, we can draw conclusions about the nature of the stresses in (A.23). Since the signs of $u_{i,j}$, w_k and $w_{k,\gamma}$ are arbitrary, the coefficients of these terms linear in $u_{i,j}$, w_k and $w_{k,\gamma}$ must necessarily sum to zero. This leads us to the conclusion that the stresses take the form,[62]

$$\sigma_{ij}=-P\delta_{ij}-p_{k,i}\mu_{jk}+\tilde{\sigma}_{ij}, \quad \text{(A.24)}$$

$$\pi_{ij}=\epsilon_{i\gamma k}p_\gamma\mu_{jk}+\tilde{\pi}_{ij}. \quad \text{(A.25)}$$

Here; $\tilde{\sigma}_{ij}$ and $\tilde{\pi}_{ij}$ are the dynamic contributions to stress where $\tilde{\sigma}_{ij}$ is known as the viscous stress; P is pressure; $\mu_{jk}=\frac{\partial f_d}{\partial p_{k.j}}$. The natural variables to use for the dynamic couple stress are the director, director angular velocity and fluid velocity gradients. By this assumption, it follows that $\tilde{\pi}_{ij}=0$.[98]

A.4 External Torque on swimmers

Here, we derive an expression for the external torque acting on a microswimmer out of elastic equilibrium due to distortion stress in the director. This torque is defined as the anti-symmetric component of the dynamic (viscous) stress tensor; $\Gamma_i=\epsilon_{ijk}\tilde{\sigma}_{kj}$. Then substituting (A.24) and (A.25) into (A.6),

$$\Gamma_i=-\epsilon_{ijk}\Big[P\delta_{jk}+p_{\gamma,k}\mu_{j\gamma}\Big]+\epsilon_{j\gamma k}\partial_j\Big(p_\gamma\mu_{ik}\Big). \quad \text{(A.26)}$$

The pressure term vanishes as a consequence of symmetry. Using again the Ericksen identity in (A.21), we can write this expression as

$$\Gamma_i = \epsilon_{ijk}\Big(p_j\frac{\partial f_d}{\partial p_k} + p_{j,\gamma}\mu_{\gamma k}\Big) + \epsilon_{j\gamma k}\partial_j\Big(p_\gamma \mu_{ik}\Big).$$

We wish to relate the dynamic stress to the static stress defined by the molecular field $h_k = \frac{\partial f_d}{\partial p_k} - \partial_\gamma \mu_{\gamma k}$, and substitution gives

$$\Gamma_i = \epsilon_{ijk}p_j h_k - \epsilon_{ijk}\Big[p_j\partial_\gamma \mu_{\gamma k} + p_{j,k}\mu_{\gamma k}\Big] + \epsilon_{j\gamma k}\partial_j\Big(p_\gamma \mu_{ik}\Big). \tag{A.27}$$

Noticing the square brackets correspond to the derivative of $p_j\mu_{\gamma k}$ we can write,

$$\Gamma_i = \epsilon_{ijk}p_j h_k - \epsilon_{ijk}\partial_\gamma\Big(p_j\mu_{\gamma k}\Big) + \epsilon_{j\gamma k}\partial_j\Big(p_\gamma \mu_{ik}\Big). \tag{A.28}$$

To resolve the last two terms, recall the conservation of linear momentum equation: $\rho\dot{u}_i = \partial_j\sigma_{ji}$. Changes of the form $\sigma_{ji} \to \sigma_{ji} + \sigma'_{ji}$ don't effect acceleration as long as $\partial_j\sigma_{ji} = 0$. Following this, we can write the final two terms as,

$$\begin{aligned}
&= \epsilon_{j\gamma k}\delta_{lj}\partial_l\Big(p_\gamma\mu_{ik}\Big) - \epsilon_{ijk}\delta_{l\gamma}\partial_l\Big(p_j\mu_{\gamma k}\Big),\\
&= \partial_l\Big(\epsilon_{l\gamma k}p_\gamma\mu_{ik} - \epsilon_{ijk}p_j\mu_{lk}\Big),\\
&= \partial_l\Big(\Big[\epsilon_{lmk}\mu_{ik} - \epsilon_{imk}\mu_{lk}\Big]p_m\Big).
\end{aligned}$$

In the final line, a derivative in ∂_i produces a product between a symmetric tensor and anti-symmetric tensor, which can be shown to be identically zero. Consequently, we can express the torque in terms of the director only as,

$$\boldsymbol{\Gamma} = \boldsymbol{p} \times \boldsymbol{h}. \tag{A.29}$$

B | Identities

B.1 Inclined Plane

In Section 5.2.2 where $\phi = \phi_0(z) + \varepsilon\phi_1(x, z)$, the following identities are used:

$$\cos\phi_0\partial_z^2\cos\phi_0 + \sin\phi_0\partial_z^2\sin\phi_0 = -\phi_0'^2 \tag{B.1}$$

$$\cos\phi_0\partial_z^2\sin\phi_0 - \sin\phi_0\partial_z^2\cos\phi_0 = \phi_0'' \tag{B.2}$$

$$\cos\phi_0\partial_z\sin\phi_0 - \sin\phi_0\partial_z\cos\phi_0 = \phi_0' \tag{B.3}$$

$$\cos\phi_0\nabla^2\Big[\phi_1\sin\phi_0\Big] - \sin\phi_0\nabla^2\Big[\phi_1\cos\phi_0\Big] = 2\partial_z\phi_1\phi_0' + \phi_1\phi_0'' \tag{B.4}$$

Theorems

Divergence Theorem

The divergence theorem relates the total rate-of-change of a vectorial quantity (flux) over the surface of a volume, to the divergence of that quantity over the volume. Formally,

$$\iint_S (\boldsymbol{n} \cdot \boldsymbol{u}) \, \mathrm{d}S = \iiint_V (\nabla \cdot \boldsymbol{u}) \, \mathrm{d}V,$$

where V is the body volume, S its surface and $\boldsymbol{n}$ the outward-facing normal.

Euler-Cauchy Stress Principle

The Euler-Cauchy stress principle states that on any surface, real or imaginary, that divides a volume element, the action of one part of the body on the other part is equivalent to the distribution of forces and moments on that surface. Formally, this allows us to write the vectorial force acting on a surface as the product between the outward normal vector to the surface, and a stress tensor.

Levi-Civita symbol

The Levi-Civita symbol expresses the relationship between a collection of numbers. In this thesis, it is primarily used to represent the vector cross product in index notation. Explicitly it is written,

$$\epsilon_{ijk} = \begin{cases} +1 & \text{if } (i, j, k) \text{ is an even permutation,} \\ -1 & \text{if } (1, j, k) \text{ is an odd permutation,} \\ 0 & \text{if } i = j, \text{ or } j = k, \text{ or } k = i. \end{cases}$$

Reynolds Transport Theorem

Reynolds transport theorem is a three-dimensional generalisation of the Leibniz integral rule which describes differentiation under the integral sign. Formally, for time derivative $\frac{d}{dt}$, it states

$$\frac{d}{dt}\int_v \boldsymbol{f} = \int_v \frac{\partial \boldsymbol{f}}{\partial t} + (\boldsymbol{u}\cdot\nabla)\boldsymbol{f}\,\mathrm{d}V.$$

Glossary

A

active stress the stress exerted on a fluid due to the activity and motility of swimming microorganisms. 11

advection the transportation of a physical quantity such as heat or matter by the motion of fluid. 11

anisotropic (of a material) having a physical property which varies under rotation. 3

apolar (of a particle), being head-tail symmetric 1

B

Bretherton constant a measurement of a particles alignment to local shear, calculated by its geometrical properties 25

brownian motion random motion of microscopic particles in a fluid due to collisions with fluid molecules 4

C

constitutive relation a relationship between two physical quantities of a material or substance. 15

crystaline (a state of matter), matter whose constituent particles form highly ordered coherent structures. 3

D

dimension the units of a measurement, e.g. length, mass, time.

dimensionless number a number, without *dimension*, which captures physical properties of a system by relating properties to one another.

E

entropy a measure of a systems energy per unit temperature unable to do useful work. 4

F

free-energy a measure of a body's (or system's) ability to cause change 1

G

gastrointestinal epithelial lining (biology) the single cell layer that forms the lining of both the large and small intestine in the colon. 2
geotaxis motion of a cell or microorganism in response to the force of gravity. 16

H

hydrodynamic concerning the mechanical properties of a fluid. 6

I

isotropic (of a material) having a physical property which is invariant under rotation. 3

K

kinematic the mechanics of motion without reference to the forces that produced that motion. 15
kinetic the action of forces in producing or changing motion 15

L

long-wavelength (of a measurable property) fluctuations that exist on a scale larger than the length scale of interest.

M

marangoni stress (physics) gradients of surface tension between a fluid and substrate which can drive microflows in the fluid. 3
micotubules (biology) the components of the cell skeleton which determine the cell shape and motility. 3
motility ability to move oneself. 4

N

Naiver-Stokes Equation the fluidic equivalent of Newtons second law. 11, 15
nematic active matter active matter formed of *apolar* particles 1

O

overdamped a physical system which is dampened beyond the threshold to prevent oscillations. 6

P

packing fraction the volume fraction at which a suspension of particles cannot be packed together any closer. 4
phase a chemically and physically homogeneous quantity of matter, e.g. gas, liquid, solid, crystaline. 3
  separation separation of matter into two or more separate phases 5
  transition transition of matter between two phases 3
phoretic (transport of particles) the movement of particles due to a field, such as concentration, interacting with the particles. 1
polar (of a particle), having head-tail structure 1
polar active matter active matter formed of *polar* particles 1

R

Reynolds Number a dimensionless number describing the relative effects of viscous to inertia forces. 16
rheology the study of the deformation of fluids, with particular interest to viscous properties 12

S

self-propelled particle are particles which propel themselves through a medium by a means other than an external surface or body force.

shear a measure of lateral shifting of fluid layers relative to one another. 11

shear thickening (thining) (physics) a non-newtonian fluid in which viscosity increases (decreases) as a response to shear gradients. 3

Smoluchowski equations (statistical physics) equations describing the time evolution of the number density of particles as they coagulate. 21

Soft matter (field of physics) physical systems which are deformed by thermal or mechanical stresses. 5

steric interactions between particles that are nonbonding in nature, e.g. volume exclusion. 4, 11

Stokes Equation a simplification of the *Navier-Stokes* equation, describing a fluid with low *Reynolds* number. 16

strain a physical measurement of relative displacement between neighbouring particles in a continuous material.

stress is a physical quantity which expresses the internal forces between neighbouring particles in a continuous material; it is measured as the force per unit area. 1

T

thermodynamics the study of the relationship between heat, work, temperature and energy in matter. 5

V

viscoelastic (physics) a non-newtonian fluid which has an elastic response to shear gradients. 2

viscosity a physical measurement of a fluids resistance to mechanical *strain*. 15

vorticity a measurement of the local rotation of a fluid. 11

Bibliography

[1] NDomer73. Starling murmuration near starved rock state park il ddz 0104. "https://www.flickr.com/photos/8987884@N07/2173889463". Licensed with CC BY-NC-ND 2.0. To view a copy of this license, visit https://creativecommons.org/licenses/by-nc-nd/2.0/.

[2] Henry Lager. School of sardines at moalbal, philipines. https://www.conartix-photo.ch/galleries/ix-567.

[3] Fernan Federici. Confocal microscopy of fluorescent bacteria (bacillus subtilis). "https://www.flickr.com/photos/21951502@N08/5937639152". Licensed with CC BY-NC-ND 2.0. To view a copy of this license, visit https://creativecommons.org/licenses/by-nc-nd/2.0/.

[4] Alissa Eckert Medical Illustrator. Phil 23242: Extended-spectrum ß-lactamase-producing (esbl) escherichia coli bacteria. "https://phil.cdc.gov/Details.aspx?pid=21915". Licensed with CC BY-NC-ND 2.0. To view a copy of this license, visit https://creativecommons.org/licenses/by-nc-nd/2.0/.

[5] Žiga Kos and Miha Ravnik. Elementary flow field profiles of micro-swimmers in weakly anisotropic nematic fluids: Stokeslet, stresslet, rotlet and source flows. *Fluids*, 3(1):15, 2018.

[6] Pooja Chandrakar, Minu Varghese, S Ali Aghvami, Aparna Baskaran, Zvonimir Dogic, and Guillaume Duclos. Confinement controls the bend instability of three-dimensional active liquid crystals. *Physical Review Letters*, 125(25):257801, 2020.

[7] Amin Doostmohammadi and Julia M Yeomans. Coherent motion of dense active matter. *European Physical Journal Special Topics*, 227(17), 2019.

[8] Tyler N Shendruk, Amin Doostmohammadi, Kristian Thijssen, and Julia M Yeomans. Dancing disclinations in confined active nematics. *Soft Matter*, 13(21):3853–3862, 2017.

[9] Tamás Vicsek and Anna Zafeiris. Collective motion. *Physics reports*, 517(3-4):71–140, 2012.

[10] John Toner, Yuhai Tu, and Sriram Ramaswamy. Hydrodynamics and phases of flocks. *Annals of Physics*, 318(1):170–244, 2005.

[11] M Cristina Marchetti, Jean-François Joanny, Sriram Ramaswamy, Tanniemola B Liverpool, Jacques Prost, Madan Rao, and R Aditi Simha. Hydrodynamics of soft active matter. *Reviews of Modern Physics*, 85(3):1143, 2013.

[12] David Saintillan. Rheology of active fluids. *Annual Review of Fluid Mechanics*, 50:563–592, 2018.

[13] Gerhard Gompper, Roland G Winkler, Thomas Speck, Alexandre Solon, Cesare Nardini, Fernando Peruani, Hartmut Löwen, Ramin Golestanian, U Benjamin Kaupp, Luis Alvarez, et al. The 2020 motile active matter roadmap. *Journal of Physics: Condensed Matter*, 32(19):193001, 2020.

[14] John Toner and Yuhai Tu. Flocks, herds, and schools: A quantitative theory of flocking. *Physical review E*, 58(4):4828, 1998.

[15] Christopher Dombrowski, Luis Cisneros, Sunita Chatkaew, Raymond E Goldstein, and John O Kessler. Self-concentration and large-scale coherence in bacterial dynamics. *Physical review letters*, 93(9):098103, 2004.

[16] Yashodhan Hatwalne, Sriram Ramaswamy, Madan Rao, and R Aditi Simha. Rheology of active-particle suspensions. *Physical review letters*, 92(11):118101, 2004.

[17] Andrey Sokolov and Igor S Aranson. Physical properties of collective motion in suspensions of bacteria. *Physical review letters*, 109(24):248109, 2012.

[18] Jennifer Galanis, Daniel Harries, Dan L Sackett, Wolfgang Losert, and Ralph Nossal. Spontaneous patterning of confined granular rods. *Physical review letters*, 96(2):028002, 2006.

[19] Arshad Kudrolli, Geoffroy Lumay, Dmitri Volfson, and Lev S Tsimring. Swarming and swirling in self-propelled polar granular rods. *Physical review letters*, 100(5):058001, 2008.

[20] Nitin Kumar, Harsh Soni, Sriram Ramaswamy, and AK Sood. Flocking at a distance in active granular matter. *Nature communications*, 5(1):1–9, 2014.

[21] Andreas Walther and Axel HE Müller. Janus particles. *Soft Matter*, 4(4):663–668, 2008.

[22] Andreas Walther and Axel HE Muller. Janus particles: synthesis, self-assembly, physical properties, and applications. *Chemical reviews*, 113(7):5194–5261, 2013.

[23] Jeffrey L Moran and Jonathan D Posner. Phoretic self-propulsion. *Annual Review of Fluid Mechanics*, 49:511–540, 2017.

[24] Babak Vajdi Hokmabad, Ranabir Dey, Maziyar Jalaal, Devaditya Mohanty, Madina Almukambetova, Kyle A Baldwin, Detlef Lohse, and Corinna C Maass. Stop-and-go droplet swimmers. *arXiv preprint arXiv:2005.12721*, 2020.

[25] Luca Giomi, Tanniemola B Liverpool, and M Cristina Marchetti. Sheared active fluids: Thickening, thinning, and vanishing viscosity. *Physical Review E*, 81(5):051908, 2010.

[26] Arijit Ghosh, Weinan Xu, Neha Gupta, and David H Gracias. Active matter therapeutics. *Nano Today*, 31:100836, 2020.

[27] Tim Sanchez, Daniel TN Chen, Stephen J DeCamp, Michael Heymann, and Zvonimir Dogic. Spontaneous motion in hierarchically assembled active matter. *Nature*, 491(7424):431–434, 2012.

[28] Stephan Herminghaus, Corinna C Maass, Carsten Krüger, Shashi Thutupalli, Lucas Goehring, and Christian Bahr. Interfacial mechanisms in active emulsions. *Soft matter*, 10(36):7008–7022, 2014.

[29] Tamás Vicsek, András Czirók, Eshel Ben-Jacob, Inon Cohen, and Ofer Shochet. Novel type of phase transition in a system of self-driven particles. *Physical review letters*, 75(6):1226, 1995.

[30] Michael E Cates and Julien Tailleur. Motility-induced phase separation. *Annu. Rev. Condens. Matter Phys.*, 6(1):219–244, 2015.

[31] R Aditi Simha and Sriram Ramaswamy. Hydrodynamic fluctuations and instabilities in ordered suspensions of self-propelled particles. *Physical review letters*, 89(5):058101, 2002.

[32] Alexandre P Solon, Joakim Stenhammar, Michael E Cates, Yariv Kafri, and Julien Tailleur. Generalized thermodynamics of motility-induced phase separation: phase equilibria, laplace pressure, and change of ensembles. *New Journal of Physics*, 20(7):075001, 2018.

[33] Trevor GrandPre, Katherine Klymko, Kranthi K Mandadapu, and David T Limmer. Entropy production fluctuations encode collective behavior in active matter. *arXiv preprint arXiv:2007.12149*, 2020.

[34] Sho C Takatori and John F Brady. Forces, stresses and the (thermo?) dynamics of active matter. *Current Opinion in Colloid & Interface Science*, 21:24–33, 2016.

[35] Howard C Berg. *Random walks in biology.* Princeton University Press, 1993.

[36] Wen Yan and John F Brady. The swim force as a body force. *Soft Matter*, 11(31):6235–6244, 2015.

[37] M Ben Amar and LJ Cummings. Fingering instabilities in driven thin nematic films. *Physics of Fluids*, 13(5):1160–1166, 2001.

[38] Karsten Kruse, Jean-François Joanny, Frank Jülicher, Jacques Prost, and Ken Sekimoto. Asters, vortices, and rotating spirals in active gels of polar filaments. *Physical review letters*, 92(7):078101, 2004.

[39] Jean-Baptiste Caussin, Alexandre Solon, Anton Peshkov, Hugues Chaté, Thierry Dauxois, Julien Tailleur, Vincenzo Vitelli, and Denis Bartolo. Emergent spatial structures in flocking models: a dynamical system insight. *Physical review letters*, 112(14):148102, 2014.

[40] Sumesh P Thampi, Ramin Golestanian, and Julia M Yeomans. Instabilities and topological defects in active nematics. *EPL (Europhysics Letters)*, 105(1):18001, 2014.

[41] Charles W Wolgemuth. Collective swimming and the dynamics of bacterial turbulence. *Biophysical journal*, 95(4):1564–1574, 2008.

[42] Vijay Narayan, Sriram Ramaswamy, and Narayanan Menon. Long-lived giant number fluctuations in a swarming granular nematic. *Science*, 317(5834):105–108, 2007.

[43] Julia K Parrish and William M Hamner. *Animal groups in three dimensions: how species aggregate*. Cambridge University Press, 1997.

[44] Knut Drescher, Jörn Dunkel, Luis H Cisneros, Sujoy Ganguly, and Raymond E Goldstein. Fluid dynamics and noise in bacterial cell–cell and cell–surface scattering. *Proceedings of the National Academy of Sciences*, 108(27):10940–10945, 2011.

[45] Kevin D Young. The selective value of bacterial shape. *Microbiology and molecular biology reviews*, 70(3):660–703, 2006.

[46] Arnold JTM Mathijssen, Amin Doostmohammadi, Julia M Yeomans, and Tyler N Shendruk. Hotspots of boundary accumulation: dynamics and statistics of micro-swimmers in flowing films. *Journal of The Royal Society Interface*, 13(115):20150936, 2016.

[47] Silvio Bianchi, Filippo Saglimbeni, and Roberto Di Leonardo. Holographic imaging reveals the mechanism of wall entrapment in swimming bacteria. *Physical Review X*, 7(1):011010, 2017.

[48] Pierre-Gilles De Gennes and Jacques Prost. *The physics of liquid crystals*. Number 83. Oxford university press, 1993.

[49] Daniela Pimponi, Mauro Chinappi, Paolo Gualtieri, and Carlo Massimo Casciola. Hydrodynamics of flagellated microswimmers near free-slip interfaces. *Journal of Fluid Mechanics*, 789:514–533, 2016.

[50] Paul C Martin, Olivier Parodi, and Peter S Pershan. Unified hydrodynamic theory for crystals, liquid crystals, and normal fluids. *Physical Review A*, 6(6):2401, 1972.

[51] Sumithra Sankararaman and Sriram Ramaswamy. Instabilities and waves in thin films of living fluids. *Physical review letters*, 102(11):118107, 2009.

[52] Kenta Ishimoto. Jeffery orbits for an object with discrete rotational symmetry. *Physics of Fluids*, 32(8):081904, 2020.

[53] Rayan Chatterjee, Navdeep Rana, R Aditi Simha, Prasad Perlekar, and Sriram Ramaswamy. Fluid flocks with inertia. *arXiv preprint arXiv:1907.03492*, 2019.

[54] David J Acheson. Elementary fluid dynamics, 1991.

[55] DF Katz and L Pedrotti. Geotaxis by motile spermatozoa hydrodynamic reorientation. *Journal of Theoretical Biology*, 67(4):723–732, 1977.

[56] Stephen O'Malley and Martin A Bees. The orientation of swimming biflagellates in shear flows. *Bulletin of mathematical biology*, 74(1):232–255, 2012.

[57] Arnold JTM Mathijssen, Amin Doostmohammadi, Julia M Yeomans, and Tyler N Shendruk. Hydrodynamics of micro-swimmers in films. *Journal of Fluid Mechanics*, 806:35–70, 2016.

[58] Sangtae Kim and Seppo J Karrila. *Microhydrodynamics: principles and selected applications*. Courier Corporation, 2013.

[59] Michael D Graham. *Microhydrodynamics, Brownian motion, and complex fluids*, volume 58. Cambridge University Press, 2018.

[60] Kenta Ishimoto. Helicoidal particles and swimmers in a flow at low reynolds number. *Journal of Fluid Mechanics*, 892, 2020.

[61] Izrail Moiseevitch Gelfand, Richard A Silverman, et al. *Calculus of variations*. Courier Corporation, 2000.

[62] Frank M Leslie. Continuum theory for nematic liquid crystals. *Continuum Mechanics and Thermodynamics*, 4(3):167–175, 1992.

[63] Masahiro Ito, Naoya Terahara, Shun Fujinami, and Terry Ann Krulwich. Properties of motility in bacillus subtilis powered by the h+-coupled motab flagellar stator, na+-coupled motps or hybrid stators motas or motpb. *Journal of molecular biology*, 352(2):396–408, 2005.

[64] Jörn Dunkel, Sebastian Heidenreich, Knut Drescher, Henricus H Wensink, Markus Bär, and Raymond E Goldstein. Fluid dynamics of bacterial turbulence. *Physical review letters*, 110(22):228102, 2013.

[65] Linda Turner, Liam Ping, Marianna Neubauer, and Howard C Berg. Visualizing flagella while tracking bacteria. *Biophysical journal*, 111(3):630–639, 2016.

[66] CS Allen, Jacky FC Loo, Samuel Yu, SK Kong, and Ting-Fung Chan. Monitoring bacterial growth using tunable resistive pulse sensing with a pore-based technique. *Applied microbiology and biotechnology*, 98(2):855–862, 2014.

[67] Michaela E Sharpe, Philippe M Hauser, Robert G Sharpe, and Jeffery Errington. Bacillus subtilis cell cycle as studied by fluorescence microscopy: constancy of cell length at initiation of dna replication and evidence for active nucleoid partitioning. *Journal of bacteriology*, 180(3):547–555, 1998.

[68] Alys Jepson, Jochen Arlt, Jonathan Statham, Mark Spilman, Katie Burton, Tiffany Wood, Wilson CK Poon, and Vincent A Martinez. High-throughput characterisation of bull semen motility using differential dynamic microscopy. *PloS one*, 14(4):e0202720, 2019.

[69] David M Woolley, Rachel F Crockett, William DI Groom, and Stuart G Revell. A study of synchronisation between the flagella of bull spermatozoa, with related observations. *Journal of Experimental Biology*, 212(14):2215–2223, 2009.

[70] PJ Bredderman and RH Foote. Alteration of cell volume in bull spermatozoa by factors known to affect active cation transport. *Experimental cell research*, 66(1):190–196, 1971.

[71] L-O Drevius. Bull spermatozoa as osmometers. *Reproduction*, 28(1):29–39, 1972.

[72] Feng Liu, Yihong Wu, and Li Zeng. Swimming characteristics of chlamydomonas reinhardtii. *Journal of Coastal Research*, 104(SI):455–464, 2020.

[73] Corbyn Jones, Mauricio Gomez, Ryan M Muoio, Alex Vidal, Anthony Mcknight, Nicholas D Brubaker, and Wylie W Ahmed. The stochastic force dynamics of a model microswimmer–chlamydomonas reinhardtii. *arXiv preprint arXiv:2011.12415*, 2020.

[74] Guillermo J Amador, Da Wei, Daniel Tam, and Marie-Eve Aubin-Tam. Fibrous flagellar hairs of chlamydomonas reinhardtii do not enhance swimming. *Biophysical Journal*, 2020.

[75] Veikko F Geyer, Pablo Sartori, Benjamin M Friedrich, Frank Jülicher, and Jonathon Howard. Independent control of the static and dynamic components of the chlamydomonas flagellar beat. *Current Biology*, 26(8):1098–1103, 2016.

[76] Lin Wei Jong, Takayuki Fujiwara, Hisayoshi Nozaki, and Shin-ya Miyagishima. Cell size for commitment to cell division and number of successive cell divisions in multicellular volvocine green algae tetrabaena socialis and gonium pectorale. *Proceedings of the Japan Academy, Series B*, 93(10):832–840, 2017.

[77] Ron Milo, Paul Jorgensen, Uri Moran, Griffin Weber, and Michael Springer. Bionumbers—the database of key numbers in molecular and cell biology. *Nucleic acids research*, 38(suppl_1):D750–D753, 2009.

[78] Avraham Be'er, Bella Ilkanaiv, Renan Gross, Daniel B Kearns, Sebastian Heidenreich, Markus Bär, and Gil Ariel. A phase diagram for bacterial swarming. *Communications Physics*, 3(1):1–8, 2020.

[79] Felix Kempf, Romain Mueller, Erwin Frey, Julia M Yeomans, and Amin Doostmohammadi. Active matter invasion. *Soft matter*, 15(38):7538–7546, 2019.

[80] Javier Urzay, Amin Doostmohammadi, and Julia M Yeomans. Multi-scale statistics of turbulence motorized by active matter. *Journal of Fluid Mechanics*, 822:762–773, 2017.

[81] Sumesh P Thampi, Ramin Golestanian, and Julia M Yeomans. Velocity correlations in an active nematic. *Physical review letters*, 111(11):118101, 2013.

[82] Ashish B. George and Kirill S Korolev. Chirality provides a direct fitness advantage and facilitates intermixing in cellular aggregates. *PLoS computational biology*, 14(12):e1006645, 2018.

[83] Martin Mühling, Nicholas Harris, Amha Belay, and Brian A Whitton. Reversal of helix orientation in the cyanobacterium arthrospira 1. *Journal of Phycology*, 39(2):360–367, 2003.

[84] E Ben Jacob, Yakir Aharonov, and Yoash Shapira. Bacteria harnessing complexity. *Biofilms*, 1(4):239–263, 2004.

[85] Henry C Fu, Thomas R Powers, Roman Stocker, et al. Bacterial rheotaxis. *Proceedings of the National Academy of Sciences*, 109(13):4780–4785, 2012.

[86] Navaneeth K Marath and Ganesh Subramanian. The effect of inertia on the time period of rotation of an anisotropic particle in simple shear flow. *Journal of Fluid Mechanics*, 830:165–210, 2017.

[87] Tomas Rosén, Yusuke Kotsubo, Cyrus K Aidun, Minh Do-Quang, and Fredrik Lundell. Orientational dynamics of a triaxial ellipsoid in simple shear flow: Influence of inertia. *Physical Review E*, 96(1):013109, 2017.

[88] Santhan Chandragiri, Amin Doostmohammadi, Julia M Yeomans, and Sumesh P Thampi. Active transport in a channel: stabilisation by flow or thermodynamics. *Soft matter*, 15(7):1597–1604, 2019.

[89] *This is an Open Access article distributed under the terms of the Creative Commons Attribution License (http://creativecommons.org/licenses/by/4.0), which permits unrestricted use, distribution, and reproduction in any medium, provided the original work is properly cited.*

[90] Tobias Struubing, Amir Khosravanizadeh, Andrej Vilfan, Eberhard Bodenschatz, Ramin Golestanian, and Isabella Guido. Wrinkling instability in 3d active nematics. *Nano letters*, 20(9):6281–6288, 2020.

[91] Rodrigo Ledesma-Aguilar and Julia M Yeomans. Enhanced motility of a microswimmer in rigid and elastic confinement. *Physical review letters*, 111(13):138101, 2013.

[92] Liana Vaccari, Daniel B Allan, Nima Sharifi-Mood, Aayush R Singh, Robert L Leheny, and Kathleen J Stebe. Films of bacteria at interfaces: three stages of behaviour. *Soft Matter*, 11(30):6062–6074, 2015.

[93] Hongfei Chen and Jean-Luc Thiffeault. Effective diffusivity of a microswimmer in a lattice. In *APS Division of Fluid Dynamics Meeting Abstracts*, pages P19–012, 2021.

[94] MATLAB. *9.10.0.1684407 (R2021a) Update 3*. The Mathworks, Inc., Natick, Massachusetts, 2021.

[95] J Einarsson, BM Mihiretie, A Laas, S Ankardal, JR Angilella, D Hanstorp, and B Mehlig. Tumbling of asymmetric microrods in a microchannel flow. *Physics of Fluids*, 28(1):013302, 2016.

[96] Iain W Stewart. *The static and dynamic continuum theory of liquid crystals: a mathematical introduction*. Crc Press, 2019.

[97] Jerald L Ericksen. Conservation laws for liquid crystals. *Transactions of the Society of Rheology*, 5(1):23–34, 1961.

[98] Frank M Leslie. Some constitutive equations for anisotropic fluids. *The Quarterly Journal of Mechanics and Applied Mathematics*, 19(3):357–370, 1966.